2020

# Analyzing Resistance to Design Chemical Inhibitors of AAA Proteins

Rudolf Pisa


# ANALYZING RESISTANCE TO DESIGN CHEMICAL INHIBITORS OF AAA PROTEINS

A Thesis Presented to the Faculty of

The Rockefeller University

in Partial Fulfillment of the Requirements for

the degree of Doctor of Philosophy

by

Rudolf Pisa

June 2020

# ANALYZING RESISTANCE TO DESIGN CHEMICAL INHIBITORS OF AAA PROTEINS

Rudolf Pisa, Ph.D.

The Rockefeller University 2020

Chemotype-specific resistance is a major factor limiting the efficacy of molecularly targeted therapeutics. Analyses of resistance mechanisms to drugs reveal that mutations conferring resistance often arise in the drug's binding sites. As selective binding of inhibitors to their protein targets is mediated by specific interactions of the inhibitor with the protein backbone and side chains, mutations that disrupt these interactions can lead to resistance. Identifying resistance-conferring alleles can thus reveal and suggest the biochemical determinants of the drug's selectivity and potency. In this thesis, I explore how mutations in active sites of proteins can be leveraged to understand inhibitor binding and to design selective chemical inhibitors.

In my thesis work I focus on the design of chemical probes for proteins from the AAA (ATPase Associated with diverse cellular Activities) superfamily, for which only a few inhibitors are available. As the number of inhibitor-bound models of AAA proteins is also limited, the key protein-inhibitor interactions needed for design of probes for these proteins are not known. I have developed an approach - Resistance Analysis During Design - that involves testing selected heterocyclic scaffolds against wild-type protein and constructs with engineered mutations that retain enzymatic activity. These analyses, along with computational docking, can guide optimization of inhibitor potency

and selectivity. We used this approach to design the pyrazolylpyrrolopyrimidine-based spastazoline - the first potent and selective chemical probe for spastin, a microtubule-severing AAA protein needed for cell division and intracellular vesicle transport. I confirmed the predicted binding mode of spastazoline analogs by X-ray crystallography and used these high-resolution structural models, along with biochemical analyses of spastin mutant alleles, to design an allele-specific inhibitor of spastin. Further, I show that RADD can be used to analyze the binding modes of diaminotriazole-based chemical inhibitors that are chemically unrelated to spastazoline. I also identified a more potent, diaminotriazole-based analog and used our approach to show that it binds spastin's active site in a different orientation in comparison to the starting compound. The distinct binding modes of these compounds predicted by RADD also match the high-resolution models I generated using X-ray crystallography. Together, these data show how analyses of resistance can be useful at the early stages of the inhibitor design process.

In summary, the work in my thesis outlines how mutations in active sites of proteins can be identified and how they could facilitate inhibitor design. I discuss how the binding models of spastin inhibitors I developed can inform on the design of new inhibitors for other AAA proteins and suggest experiments that could be valuable to advance these efforts. I also propose how analyses of resistance to chemical inhibitors could be valuable for designing drugs against which resistance might be less likely to arise.

Věnováno babičce Anně Sochnové.

“ Původ a vznik nových věcí záleží mnohdy na náhodných okolnostech, které s vlastním problémem nemají naprosto nic společného. ”

- Otto Wichterle

## ACKNOWLEDGEMENTS

First and foremost, I would like to thank my parents, grandparents, my brother and all family members who helped me get here. You were my first teachers who lit the spark and passion for science and you unconditionally supported me every step of the way. I couldn't have done it without you.

I wish to express sincere gratitude to my advisor, Tarun Kapoor. Thank you for the opportunity to work in your research group, for providing an intellectually stimulating workplace and for your mentorship and friendship in and out of the lab. Your immense knowledge across scientific subjects, your curiosity and drive to pursue cutting-edge research have been truly inspiring! Thank you for your patience and for teaching me how to evaluate experiments critically and within the boundaries of data. I will be forever in your debt for making me a better scientist and for setting me on this path.

I would also like to thank the members of my faculty advisory committee - Jue Chen, Hiro Funabiki and Derek Tan. I am extremely grateful for your advice and guidance you provided during our annual meetings and beyond. Many thanks to Adam Frost for flying across the country to be the external examiner for my thesis.

I would also like to extend my thanks to members of the Kapoor lab for their support and camaraderie over the years. Your encouragement and help was invaluable

to this work. In particular, thank you Tommaso for being a great friend and mentor. Thank you for your generosity and encouragement throughout the years. I will forever cherish the memories of our long nights in the lab, explosions in the hoods and the most marvellous lessons in italian swearwordship.

I would also like to thank Carolina and Deena for their generous support and advice throughout my PhD. I had a blast working with you and your expertise was instrumental in getting us to the finish line.

I want to especially thank Vicky for being the best partner and friend. I could not have done it without your support, love and patience at all times.

# TABLE OF CONTENTS

## INDEX OF FIGURES

**Chapter 4.**

**Chapter 5.**



**Chapter 6.**



**Chapter 7.**

## INDEX OF TABLES

## ABBREVIATIONS USED

| | |
|---|---|
| AAA | ATPases Associated with diverse cellular Activities |
| ATP | Adenosine-5'-triphosphate |
| NADH | β-Nicotinamide adenine dinucleotide, reduced |
| DTT | 1,4-dithiothreitol |
| TCEP | Tris(2-carboxyethyl)phosphine |
| BSA | Bovine serum albumin |
| DMSO | Dimethyl sulfoxide |
| HEPES | (4-(2-hydroxyethyl)-1-piperazineethanesulfonic acid) |
| MES | 2-(N-morpholino)ethanesulfonic acid |
| Tris | Tris(hydroxymethyl)aminomethane |
| $O.D._{600}$ | Optical density at 600nm |
| nm | nanometer |
| nM | $nanomol.L^{-1}$ |
| MT | Microtubule |
| LDH | D-Lactic dehydrogenase |
| PK | Pyruvate kinase |
| PEP | Phospho(enol) pyruvic acid |
| PMSF | Phenylmethylsulfonyl fluoride |
| IPTG | Isopropyl-beta-D-thiogalactoside |
| MPD | 2-methyl-2,4-pentanediol |
| PEG4000 | Polyethylene glycol 4000 |
| s.d. | Standard deviation |
| SD | Standard deviation |
| EGFP | Enhanced green fluorescent protein |
| CENPE | Centromeric protein E |
| $IC_{50}$ | Concentration needed to achieve 50% inhibition |
| $LD_{50}$ | Concentration needed to achieve 50% viability |
| NMR | Nuclear magnetic resonance |
| LC/MS | Liquid Chromatography/Mass Spectrometry |
| ESI/MS | Electrospray ionization mass spectrometry |
| FC | Fold change |

## Chapter 1: Study introduction and objectives.

In this chapter I will introduce two main topics. 1) I will present inhibitor design strategies for members of the AAA (ATPases associated with diverse cellular activities) protein family. In particular, I will focus on how resistance-conferring mutations could be leveraged for the design of potent and selective chemical probes for these proteins. 2) I will discuss examples of chemical strategies that have been employed to overcome resistance to molecularly-targeted therapeutics.

### The AAA family of proteins.

Living cells perform a formidable number of reactions to maintain the chemistry of life. Majority of the reactions that maintain cellular homeostasis are mediated and regulated by protein macromolecules such as enzymes. For example, proteins in the AAA (ATPases associated with diverse cellular activities) superfamily perform functions in diverse cellular processes such as DNA replication (Bleichert et al., 2017), ribosome biogenesis (Kressler et al., 2012a), protein homeostasis (van den Boom and Meyer, 2018), maintenance of microtubule networks or membrane organelle organization (Kapitein and Hoogenraad, 2015; Roll-Mecak and McNally, 2010). Many AAA-mediated functions, such as cargo transport by the microtubule-dependent AAA motor dynein or remodelling of microtubule filaments by the AAA protein spastin, can occur within minutes to seconds in cells, making them challenging to study. Chemical inhibitors that act on similar timescales could therefore be useful to dissect these dynamic

mechanisms. However, chemical inhibitors are not available for most AAA proteins, in part because the inhibitor-target interactions needed to design these compounds are not known.

AAA proteins typically function as oligomeric assemblies (e.g. hexamers) of AAA domains, the defining feature of this superfamily, and bind nucleotides at the interface of a pair of these domains (Figure 1.1A) (Erzberger and Berger, 2006). The AAA active site not only is highly conserved across the superfamily, but can also undergo large-scale nucleotide-dependent motions. For example, the ATP hydrolysis-dependent translocation of a protein substrate by the AAA protein Yme1 results in up to >10Å increase in the distance between key residues in adjacent AAA domains (Puchades et al., 2017). Therefore, it is also difficult to determine which of the different active site conformational states adopted by AAA proteins contribute to chemical inhibitor binding and specificity.

**The AAA domain as a target of chemical inhibitors.**

The defining and conserved feature of AAA proteins is the nucleotide-binding unit called the AAA domain. The AAA domain is composed of N-terminal αβα core (often referred to as the large AAA subdomain) and α-helical bundle at the C-terminus (referred to as the small AAA subdomain (Figure 1.1B). The nucleotide binding site is located in a cleft near the hinge region that links the large and small AAA subdomains (Figure 1.1B). The adenine base of the nucleotide is positioned to form hydrogen-bonding interactions with backbone NH amide and carbonyl oxygen of a

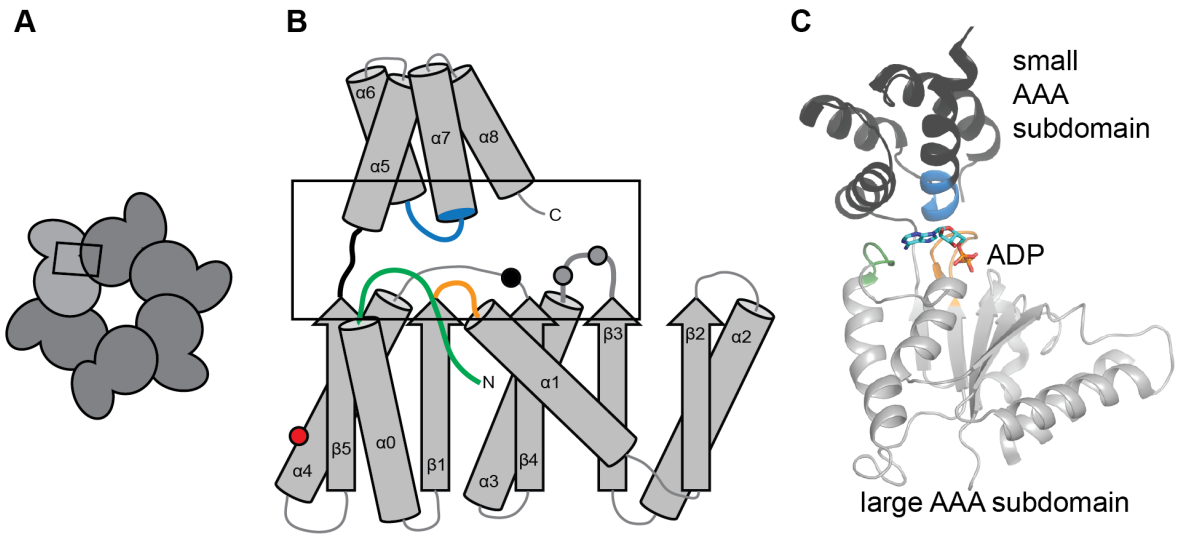


**Figure 1.1. Structural features of AAA proteins.**

(**A**) Schematic of a hexameric AAA protein. AAA domains (gray and black) and the position of the ATP-binding site (black rectangle) are shown. (**B**) Topology diagram of AAA domain. ATP-binding site is indicated (black rectangle). Nucleotide binding motifs and residues are highlighted (N-terminal loop (N-loop) - green, Walker A motif - orange, Walker B acidic residues - grey circles, sensor-I residue - black circle, sensor-II region - blue, hinge - black loop, arginine finger - red circle). (**C**) Schematic of AAA domain (ribbon representation) of fidgetin-like 1 (FIGL1) AAA protein with bound ADP nucleotide (stick representation, carbon atoms in cyan). Nucleotide-binding motifs are highlighted (N-terminal loop - green, Walker-A loop - orange, sensor-II helix- blue). PDB: 3D9B.

residue in the N-terminal loop (also referred to as the N-loop). The sugar moiety typically faces outward from the pocket and the phosphates are positioned near the Walker A residues (also known as the P-loop motif) at the tip of the β1 sheet. Two acidic residues of the Walker B motif that are crucial for β and γ phosphate binding and hydrolysis are located at the tip of the β3 sheet proximal to the P-loop (Figure 1.1B). The coordination of γ phosphate is also aided by conserved polar residues referred to as the sensor-I and -II (Guenther et al., 1997) that are located at the tip of the β4 strand and the base of helix-7, respectively (Figure 1.1B). Another conserved feature of the nucleotide binding site of AAA proteins is an arginine residue at the end of helix 4 of the large AAA subdomain in the neighboring AAA subunit that is required to form the hydrolysis-competent AAA complex (Figure 1.1B). This residue is often termed the arginine finger (R-finger) after analogous arrangement of residues in complexes of small GTPases with their GAPs (GTPase Activating Proteins (Scheffzek et al., 1997)). These conserved residues and motifs are important for AAA function and have been extensively studied in a number of AAA proteins. Although structural and functional studies of nucleotide binding and hydrolysis by AAA proteins are available, we currently lack robust inhibitor-bound models for the majority of these proteins. As inhibitor-protein binding models for many AAA proteins are not available, it is difficult to determine which active site residues could be leveraged for optimizing inhibitor binding, potency and selectivity.

**Inhibitors of AAA proteins.**

For a few AAA proteins, chemical inhibitors that block ATPase activity have been identified by screening compound libraries. These include ciliobrevins, which inhibit the microtubule-based motor protein dynein (Firestone et al., 2012; Steinman et al., 2017), ribozinoindoles, which inhibit the ribosome biogenesis factor Mdn1 (Chen et al., 2018; Kawashima et al., 2016), MSC1094308, an allosteric inhibitor of membrane remodelling AAA protein VPS4 (Pöhler et al., 2018) and a number of chemical inhibitors that block functions of ubiquitin-dependent proteolysis factor p97/VCP (also known as cdc48 in yeast) (Chou et al., 2011; Magnaghi et al., 2013). In the case of p97/VCP, structural models are available for inhibitors that bind at an allosteric site (e.g. UPCDC30245, (Banerjee et al., 2016)), and the active site (e.g. CB-5083, (Tang et al., 2019)). In addition, inhibitor activity analyses of p97/VCP mutant alleles identified in cells resistant to the CB-5083 inhibitor indicate that this compound binds in one of the two AAA domains of the protein (Anderson et al., 2015). Similarly, binding sites of ribozinoindoles are suggested by a sensitivity-conferring and several resistance-conferring point mutations that cluster at the boundary of AAA3 and AAA4, two adjacent AAA domains in the Mdn1 polypeptide (Kawashima et al., 2016). However, it is unclear whether these mutations confer resistance or sensitivity through direct interactions with the compounds or by longer-range indirect mechanisms. Developing robust binding models are needed not only to understand how inhibitor resistance or sensitivity can emerge through mutations, but also to decipher how selective and potent inhibition can be achieved.

**Inhibitor specificity.**

Developing useful chemical inhibitors hinges on addressing specificity. As binding sites of small molecules can be conserved among related members of protein families (e.g. AAA proteins), specificity of inhibitors must be optimized to ensure they act on the desired target (Kapoor and Miller, 2017). In general, specific binding of inhibitors to their targets can be achieved by engineering interactions with unique combinations of residues found in inhibitor-binding sites. Identifying compound binding modes that interact with unique conformers of the target can also be leveraged to achieve high inhibitor specificity (e.g. inhibitor binding to inactive conformations of protein kinases or to “induced fit” kinase conformations that only form upon specific interaction with the compounds (Crawford et al., 2018; Schindler et al., 2000)). Developing inhibitors targeting allosteric sites is also a potential strategy to achieve specificity as these sites are often unique to their target and are less likely to be found in other proteins. However, identifying allosteric binders is challenging as allosteric pockets are less conserved and generalizable strategies and assays to confirm inhibitor binding at these sites are often lacking.

A powerful approach for the design of specific chemical inhibitors against engineered target proteins is the “bump-hole” method (Islam, 2015; Lopez et al., 2014). In this approach, a “hole” is introduced in the active site of the target by replacing an amino acid with a large hydrophobic side chain (e.g. phenylalanine) with a smaller residue (e.g. alanine or glycine). A complementary modification of the inhibitor (“bump”)

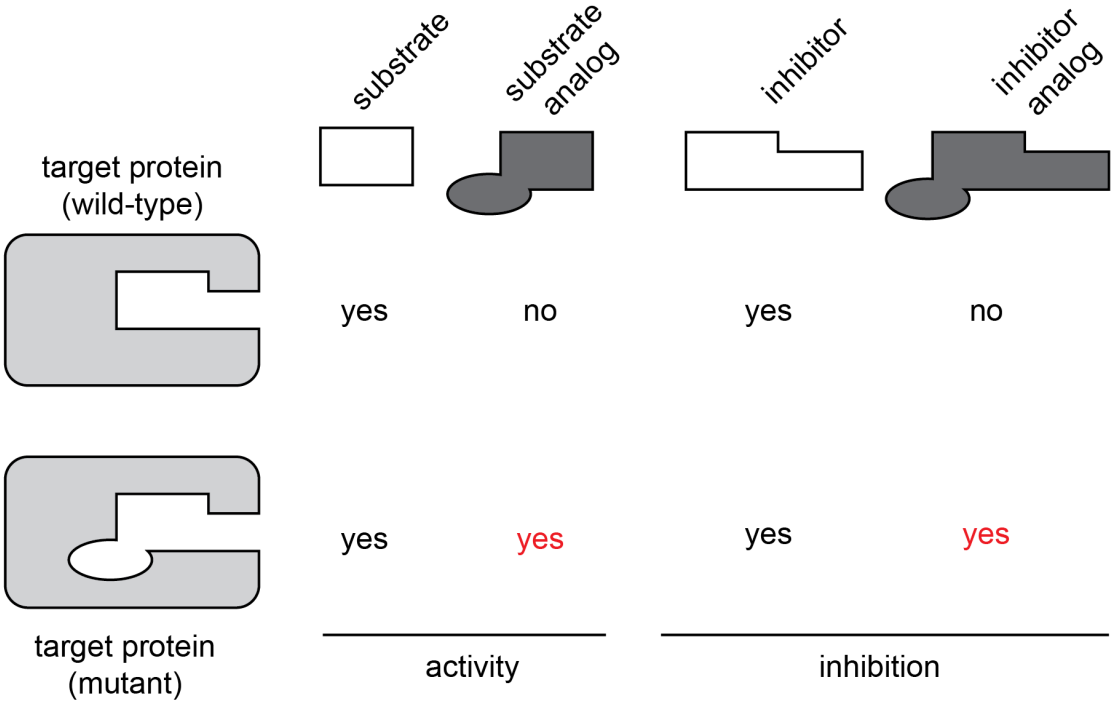


**Figure 1.2. Schematic of the "bump-hole" approach.**
Specific binding of substrate or inhibitor analogs (dark gray boxes, top) to the target protein (light gray, left) can be achieved by engineering mutation(s) in the active site and designing complementary modifications of the substrate or the inhibitor (empty boxes, top). Engineered mutations have to maintain target protein activity and allow specific binding of the modified substrate or inhibitor.

is then designed to achieve the specific binding of the “bumped” compound to the mutant allele with a “hole” (Figure 1.2). This strategy was developed in parallel to efforts to engineer protein-ligand pairs that focused on altering the specificity of enzymes (e.g. GTPases or ATPases) for non-native substrates (Hwang and Miller, 1987; Kapoor and Mitchison, 1999; Powers and Walter, 1995; Shah et al., 1997). These approaches were applied to several protein families and led to engineering allele-specific inhibitors for a number of protein targets including kinases, GPCRs, cyclophilins, PARPs or BET proteins (Baud et al., 2014; Belshaw et al., 1995; Bishop et al., 2000; Morgan et al., 2015; Urban and Roth, 2015).

**Assessing inhibitor specificity.**

Inhibitor specificity can be determined by a number of techniques *in vitro* and in cells. In vitro biochemical approaches commonly employ parallel assays with purified recombinant proteins (e.g. kinase profiling) (Ferguson and Gray, 2018; Goldstein et al., 2008; Karaman et al., 2008). These assays can provide useful indications of compound specificity between proteins in the same family as well as proteins from different families (e.g kinases, GPCR, proteases). However, the major disadvantage of these techniques is the limited number of targets that can be tested and the inherent limitations posed by using recombinant systems as they are unlikely to fully recapitulate the cellular milieu (e.g. the complex native assemblies of proteins, local concentrations of substrates or alternative proteoforms and post-translational modifications).

Affinity pulldowns from cellular lysates and/or substrate-specific-labeling techniques combined with mass spectrometry can provide more comprehensive profiling of targets of chemical inhibitors in cells in comparison to the reconstituted in vitro assays. In general, these approaches rely on reactive, promiscuous probes that are employed to label or pull-down interacting molecules in intact cells or cellular lysates (e.g. reactive ATP analogs that can bind ATP-binding proteins). Tagged or enriched molecules can then be quantified by in-gel fluorescence imaging or chromatography and mass-spectrometry (Cravatt et al., 2008). As inhibitors can outcompete the binding of such reactive probes, these techniques can thus be leveraged to assess inhibitor specificity and to reveal the target(s) of inhibitors in cells. These approaches can provide comprehensive profiling of inhibitors' cellular targets, potency and specificity. However the proteome-wide assessment of all possible targets often cannot be achieved due to limitations of the reactive probes (for example many probes are available for enzyme active sites but not allosteric sites) as well as the inherent limitations of the readout techniques (e.g. limited ionization of transmembrane proteins in mass-spectrometry).

**Leveraging resistance to validate and design potent and selective chemical inhibitors.**

Analysis of chemotype-specific resistance can be leveraged for assessing inhibitor specificity and for validating inhibitor's targets in cells (Kapoor and Miller, 2017). The "gold standard" of target validation is achieved when a resistance-conferring

mutation is identified and can protect against the inhibitor in biochemical as well as cellular assays (Kapoor and Miller, 2017). To identify these mutations our laboratory developed an approach, termed “DrugTargetSeq”, which combines selections of resistant clones, transcriptome sequencing, computational discovery of drug resistance-conferring mutations, and genome editing to confirm and validate cellular targets of drugs (Kasap et al., 2014; Wacker et al., 2012). When these mutations do not disrupt protein activity, they can be introduced in cells to systematically examine on-target and off-target activities of chemical inhibitors (Kapoor and Miller, 2017). On-target, inhibitor-induced phenotypes can be identified as those observed in cells expressing the wild-type protein but not in those expressing the allele with the resistance-conferring mutation (Kapoor and Miller, 2017). Identifying resistance-conferring mutations can be valuable not only for identifying and validating targets of inhibitors in cells but can also reveal key protein-inhibitor interactions needed for inhibitor design and optimization.

Binding of inhibitors to their targets is driven by the complementary steric and electrostatic interactions that determine potency and specificity of the inhibitor to the binding site in the target. Resistance-conferring mutations are often found in these drug-binding sites. These mutations can cause changes in shape and electrostatics of the protein-inhibitor interaction interfaces that can directly or indirectly (e.g. via allostery) contribute to drug resistance. Therefore, testing protein mutant alleles of the target protein with chemical inhibitors can reveal inhibitor-target interactions that contribute to binding. Combining these analyses with computational modeling and structure-activity

relationships of selected inhibitor scaffold can even help to decipher the inhibitor orientation in the binding site. These analyses can be especially valuable in the absence of structural models for inhibitor-protein complexes and can be useful for developing robust inhibitor-binding models needed for compound design and optimization.

**Strategies to identify and anticipate resistance to chemical inhibitors.**

Emergence of resistance is a major factor limiting the efficacy of molecularly-targeted anti-cancer drugs in the clinic. Therefore, understanding the molecular basis of chemotype-specific drug resistance is critical for developing effective therapeutics. In particular, the specific mutations or other changes (e.g truncations) of the target protein that confer resistance can help identify inhibitor-target interactions to guide design of potent and selective inhibitors. Uncovering resistance mechanisms to chemical inhibitors can help in understanding their mechanism of action in cells and can also provide hypotheses for improving clinical outcomes and new strategies for therapy (e.g. multi-drug combination therapy).

Molecularly targeted therapeutics have transformed cancer therapy but resistance to these anti-cancer drugs often arises in the clinic (Holohan et al., 2013). To identify the genetic lesions that cause resistance, sequencing analyses of samples at remission stages of the disease are commonly used (Gorre et al., 2001; Kobayashi et al., 2005; Murtaza et al., 2013). Identifying resistance-conferring genetic lesions and establishing in vitro and biochemical assays to confirm the mechanism of resistance are

crucial steps for the design of new inhibitors to overcome resistance. However, this process can be time-consuming and may lead to substantial delay before the new drugs that overcome resistance can reach the clinic. Integrating analyses of resistance early in drug development could be valuable for at least three reasons. First, testing candidate compounds before they progress to the clinic could be used to identify scaffolds that leverage binding modes against which resistance is less likely to arise (e.g. drugs interacting with conserved residues that cannot be mutated without disrupting activity of the target). Second, preclinical identification of alleles that confer resistance to candidate drugs could help guide the design of new drugs that overcome resistance in parallel to clinical testing of the initial candidate (Drilon et al., 2017a). Third, identifying drugs with non-overlapping resistance mechanisms could be leveraged for establishing drug combinations that could prevent or substantially delay the emergence of drug resistance (Imamovic and Sommer, 2013; Zhao et al., 2016). However, addressing resistance is not commonly incorporated in the drug development process and we also lack systematic analyses of resistance for many drugs in the clinic. In the following sections I will discuss chemical strategies to overcome resistance with a particular emphasis to cancer. For reviews and approaches to overcome resistance in other systems (e.g. resistance to antibiotics in bacteria or resistance to antiviral therapies) see (Anstett et al., 2017; Baym et al., 2016; Martin and Siliciano, 2016; Yelin and Kishony, 2018)

**Overcoming resistance by designing reversible inhibitors with distinct binding modes.**

Advances in cancer research, and especially cancer genomics, have revealed a myriad of molecular aberrations that can promote cancer growth and cause disease (Paez et al., 2004; Sawyers, 1999). These studies identified specific genetic lesions in a number of cancers that provide suitable candidates for developing molecularly-targeted anti-cancer therapeutics. For example, chronic myelogenous leukemias are commonly characterized by the Philadelphia chromosome translocation (Nowell and Hungerford, 1960, 1961; Rowley, 1973; Witte et al., 1980), reviewed in (Sawyers, 1999). This translocation event between chromosomes 9 and 22 places Abelson tyrosine kinase 1 (Abl1) gene on chromosome 9 under the control of highly expressing Breakpoint Cluster Region (BCR) gene on chromosome 22. The translocation results in expression of the BCR-ABL fusion gene product that is constitutively active in cells, acts oncogenically and can cause leukemias (Ben-Neriah et al., 1986).

Phenylaminopyrimidine-based compounds, such as imatinib (STI-571 or Gleevec™), bind in the nucleotide-binding pocket of Abl1 kinase and block its kinase activity (Schindler et al., 2000; Zimmermann et al., 1997). Treatment of Philadelphia-chromosome-positive cancers with imatinib has dramatically improved disease outcomes in the clinic (Druker et al., 2006). However, disease remission associated with resistance to imatinib is often observed (O'Hare et al., 2007). The predominant mechanism of resistance to imatinib identified in the clinic, which is also the most studied, involves acquired on-target point mutations in the kinase domain (KD)

of BCR-ABL (Gorre et al., 2001). In fact, although many mutations in the KD are observed in the clinic, the majority of mutations responsible for resistance to imatinib are found at a handful of “hotspot” positions such as the gatekeeper residue T315 (Shah et al., 2002). Mutations identified at these “hotspot” sites, such as the T315I or E255Y substitutions, have been shown to prevent binding of the compound in cells and *in vitro* (Shah et al., 2002). These data, along with structural and biochemical characterization of BCR-ABL-inhibitor complexes suggest that residues at the “hotspot” sites contribute to drug binding by making direct inhibitor-protein interactions (Nagar et al., 2002; Schindler et al., 2000). Interestingly, recent data also indicate that differential binding of imatinib to wild-type and mutant Abl1 alleles may also be due to distinct “induced-fit” conformational equilibria of the inhibitor-bound wild-type and mutant complexes (Agafonov et al., 2014; Wilson et al., 2015).

To address the chemotype-specific resistance to imatinib, new drugs were developed that can block the activity of imatinib-resistant BCR-ABL alleles. For example, dasatinib (BMS-354825 or Sprycel™) blocks the kinase activity of 14 out of 15 clinically relevant BCR-ABL mutants in cell culture models (Shah et al., 2004). Structural studies indicate that both dasatinib and imatinib bind Abl1 kinase in the canonical nucleotide-binding site but do so in distinct orientations (Figure 1.3A). The different binding modes of dasatinib and imatinib have been proposed to explain the differential sensitization imatinib-resistance-conferring mutations to these compounds (Shah et al., 2004). In addition, biochemical and structural analyses also reveal that the two compounds can preferentially bind distinct conformations of the kinase. This has also

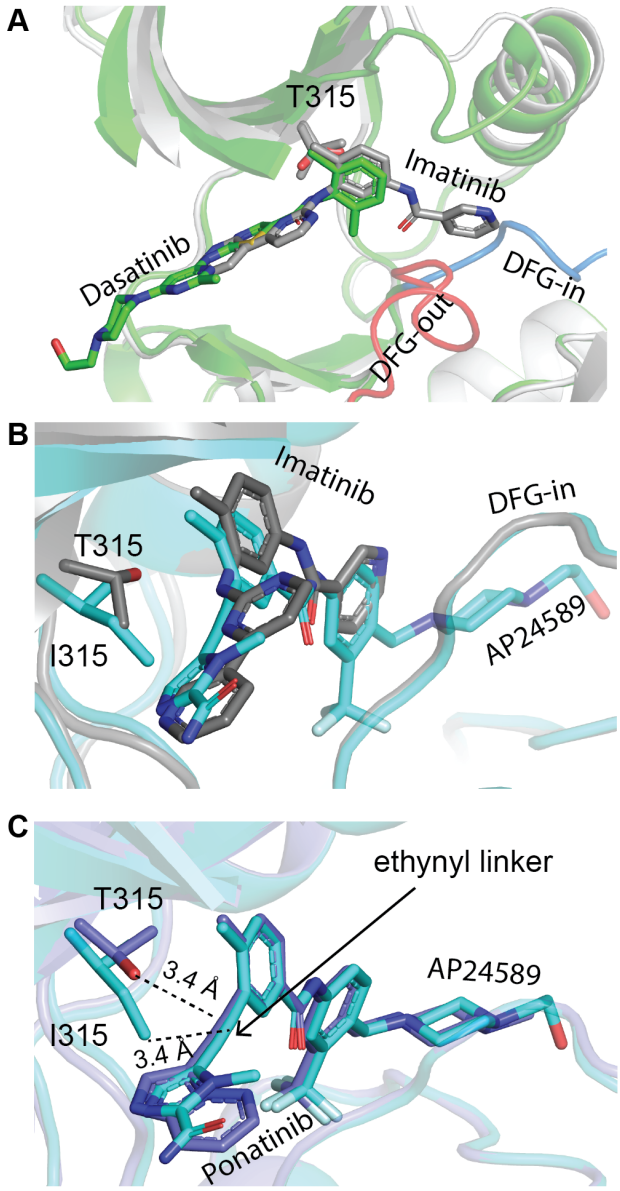


**Figure 1.3. Overcoming resistance with rational design of chemical inhibitors.**
(**A**) Structural models of Abl1 kinase in complex with imatinib (pdb: 1FPU, gray) and dasatinib (pdb:2GQG, green) shows distinct inhibitor binding mode in the active site. Gatekeeper residue (T315) and 'activation loops are highlighted (DFG-in - blue, DFG-out - red). (**B**) Structural models of Abl1 kinase (WT) in complex with imatinib (pdb:1FPU, gray) and Abl1-T315I kinase allele in complex with ponatinib analog AP24589 (pdb:3OY3, cyan). Gatekeeper residues (T315 and I315) are indicated (stick representation). (**C**) Structural models of Abl1-WT-ponatinib (pdb: 3OXZ, cyan) and Abl1-T315I-AP24589 (pdb: 3OY3, purple) complexes. Shortest distances between the ethynyl linker and the gatekeeper residue side-chains are indicated.

been suggested to contribute to differential sensitization of these drugs to subsets of resistance-conferring mutant alleles (Burgess et al., 2005). Specifically, imatinib binds the “inactive-DFG-out” conformation of Abl1 kinase (Nagar et al., 2002; Schindler et al., 2000), whereas dasatinib can bind the protein in both conformations (i.e. “inactive-DFG-out” and “active-DFG-in” conformations (Shah et al., 2004; Tokarski et al., 2006). These data suggest why mutations destabilizing the inactive conformation can confer resistance to imatinib without directly interacting with the inhibitor (Azam et al., 2003; Shah et al., 2002). However, the most common mutation that occurs at the gatekeeper “hotspot” residue (T315I) prevents binding of both imatinib and dasatinib.

Compounds such as ponatinib and AZD824 have been recently reported to block the activity of the gatekeeper mutant T315I (O’Hare et al., 2009; Ren et al., 2013). These inhibitors were identified from screening campaigns against Abl-T315I mutant protein and were optimized by medicinal chemistry approaches using structure-activity-relationship analyses (Huang et al., 2010). These compounds potently inhibit both wild-type and T315I alleles of BCR-ABL as well as a number of other resistant alleles with mutations in the Abl1 active site (O’Hare et al., 2009). Crystal structures of ponatinib and its analogs bound to Abl1 and other kinases reveal that these compounds bind their targets, including wild-type (WT) and T315I alleles of BCR-ABL, in the DFG-out conformation - similar to that of imatinib (Zhou et al., 2011). Interestingly, the structures of ponatinib analogs bound to WT and T315I alleles show that the distances between the side chains of the gatekeeper residues (T315 and I315) and the ethynyl linker in ponatinib, which replaces the pyrimidine core of imatinib, are

not substantially altered in the two structures (shortest distances between the residues and the compound: 3.4 Å in both structures - Figure 1.3B, C). These data suggest that the ethynyl linker, although proximal to the gatekeeper residue, does not substantially interact with the atoms of the gatekeeper side-chains. Taken together, these analyses show how identifying and testing mutant alleles that confer resistance to targeted anti-cancer drugs can help to guide the design of reversible inhibitors with distinct binding modes to overcome resistance.

Combining preclinical analyses of resistance and compound testing is becoming a successful approach to predict and overcome resistance to targeted therapy (Drilon et al., 2017a). For example, entrectinib and LOXO101 (also known as larotrectinib or Vitrakvi™) are first-generation ATP-competitive inhibitors for treatment of NTRK-driven cancers (Ardini et al., 2016; Drilon et al., 2017b, 2018; Hyman et al., 2017). In fact, entrectinib has been recently approved by the FDA and larotrectinib is currently undergoing late-stage clinical trials for cancer (Laetsch et al., 2018). However, acquired resistance to these inhibitors ultimately emerges (Drilon et al., 2016; Russo et al., 2016). Additionally, resistance to larotrectinib was studied by directed mutagenesis in cell culture models of NTRK-driven cancers (Drilon et al., 2017a). These studies revealed a number of mutations that preclude binding of larotrectinib and entrectinib in the active site of NTRK kinases. In particular, mutations were found at the solvent-exposed loop in the kinase active site (e.g. G595R and G667C in TrkA, G623R in TrkC) and in the activation loop of the xDFG motif (e.g. G667C in TrkA) (Drilon et al., 2017a). These mutations are homologous to resistance-conferring mutations to distinct

inhibitors of other oncogenic kinases (e.g. ALK1 and ROS1 (Awad et al., 2013; Gainor et al., 2016)). Structural and modeling studies confirm that TrkA constructs with resistance-conferring mutations in the active site, such as G595R and G667C, can prevent binding of larotrectinib and other tyrosine kinase inhibitors with anti-NTRK activity (Drilon et al., 2017a). Testing compound libraries against these mutant constructs led to the identification and design of new inhibitors that can bind and block the kinase activity of the mutant alleles. In particular, a series of 13-membered macrocycles based on larotrectinib scaffold were identified and shown to potently inhibit TrkA alleles that are resistant to the parental compound (Drilon et al., 2017a). One of these candidates (LOXO-195) was rapidly progressed to the first stage of clinical trials in parallel to larotrectinib. Selected patients that developed resistance to prior larotrectinib therapy were treated with LOXO-195 and showed tumor regression associated with on-target inhibition (Drilon et al., 2017a). These remarkable results show that incorporating resistance analyses early in the design process can be valuable for developing anti-cancer therapeutics that can address emerging drug resistance.

**Overcoming resistance by designing reactive inhibitors with irreversible mode of action.**

Mutations of the gatekeeper residue is a common mechanism of resistance to drugs targeting the nucleotide-binding site in oncogenic kinases (Blencke, 2004; Daub et al., 2004). This residue is located near the exocyclic amine at C6 of the adenine base of the ATP nucleotide in the kinase active site. The side-chain of the gate-keeper

residue determines the access to a hydrophobic pocket adjacent to the ATP site that is commonly targeted by chemical inhibitors (Zuccotto et al., 2010). In fact, the gatekeeper residue was shown to act as an important filter in the kinase ATP-binding sites that determines inhibitor selectivity (Cohen et al., 2005; Liu et al., 1999). Unsurprisingly, mutations of the gatekeeper residue can confer resistance to a number of drugs that bind in the ATP-binding site of oncogenic kinases. For example, the gatekeeper mutation T790M in EGFR (Epidermal Growth Factor Receptor) kinase is the most common resistance-conferring allele that arises upon sustained treatment of EGFR-driven cancers by EGFR-targeting small molecule drugs such as gefitinib or erlotinib (Kobayashi et al., 2005; Pao et al., 2005). However, in contrast to the T315I gatekeeper mutation in BCR-ABL, which prevents imatinib binding, the T790M gatekeeper mutation does not substantially block the binding of the quinazoline-based anti-EGFR drugs gefitinib or erlotinib (Yun et al., 2008). Interestingly, the T790M mutant kinase was found to bind ATP with substantially increased affinity, which was proposed to contribute to drug resistance mechanisms against these drugs (Yun et al., 2008).

To overcome the challenge of developing reversible and ATP-competitive inhibitors against the “high-ATP-affinity” T790M allele, inhibitors containing an electrophilic moiety that can react with a cysteine in the active site were developed. These compounds can potently block the activity of the T790M mutant EGFR as they form a covalent bond with cysteine (C797) in the active site that substantially increases the inhibitor’s occupancy in comparison to reversible inhibitors (Engelman et al., 2007; Li et al., 2007, 2008; Zhou et al., 2009). Optimizing interactions between these

electrophilic inhibitors (e.g. tool compound WZ4002 (Zhou et al., 2009) or the clinical drug osimertinib (Cross et al., 2014)) and the methionine side-chain of the mutant gatekeeper residue (T790M) can even help to reduce the unwanted effects of wild-type EGFR inhibition in noncancerous tissues (Zhou et al., 2009). Together, these studies illustrate how targeting cysteines in active sites of proteins can be leveraged for overcoming resistance to molecularly targeted anti-cancer drugs.

**Overcoming resistance by designing inhibitors targeting allosteric binding sites.**

The efficacy of ATP-competitive or covalent inhibitors can be compromised by mutations in the active site that inevitably arise upon prolonged treatment and that can prevent binding of these agents (Thress et al., 2015). A complementary strategy to targeting the ATP-binding site is to design inhibitors that can bind in a distinct pocket on the protein (e.g. an allosteric site). As the allosteric sites did not evolve to interact with common substrates such as ATP they are not as highly conserved as substrate-binding sites and are often unique to each protein. Inhibitors targeting allosteric sites can achieve exquisite selectivity as residues in these pockets are unlikely to be conserved even between proteins from the same family. For example, allosteric inhibitors targeting drug-resistant alleles of EGFR and BCR-ABL kinase have recently been developed (Jia et al., 2016; Wylie et al., 2017). These compounds are highly specific to their targets and importantly, they can block the activity of resistant alleles with mutations in the active site (Jia et al., 2016; Wylie et al., 2017). However, mutations in the allosteric sites can also lead to acquired resistance to drugs targeting these pockets, especially when

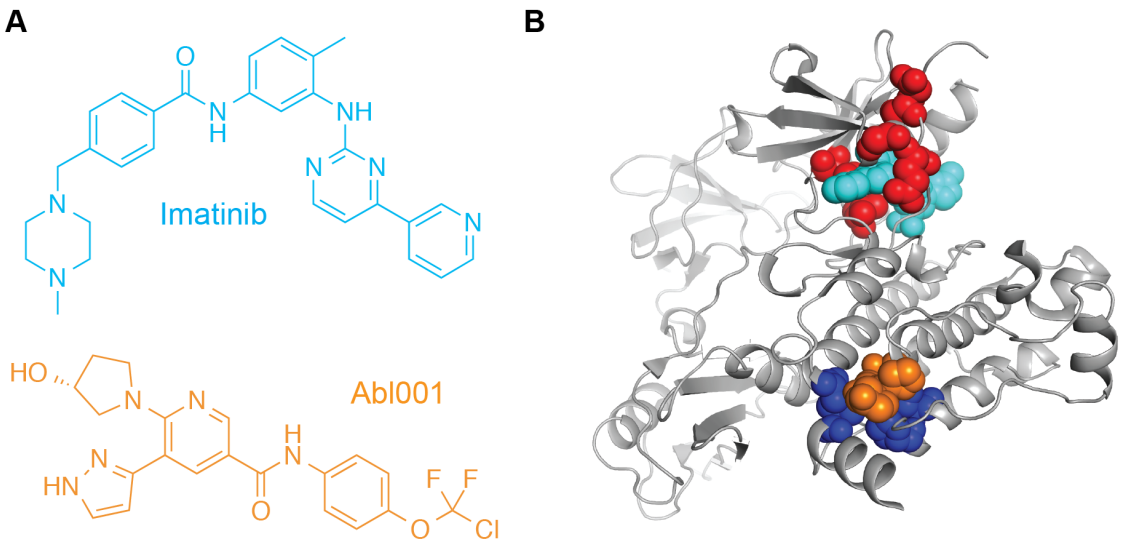


**Figure 1.4. Inhibitors with non-overlapping resistance profiles to overcome drug resistance.**

(**A**) Chemical structures of Abl kinase inhibitors. ATP-competitive inhibitor (imatinib, cyan) and allosteric inhibitor (Abl001, orange) are shown. (**B**) Schematic of Abl kinase with inhibitors (sphere representation) bound in the active site (cyan) and the allosteric site (orange). Residues that can be mutated without loss of protein activity and that confer resistance to inhibitors in the active site (red spheres) or the allosteric site (blue spheres) are also shown.

the drugs are used as a monotherapy (Wylie et al., 2017). Interestingly, the resistance-conferring mutations to allosteric compounds are distinct to the mutations that confer resistance to inhibitors that bind in the active-site (Wylie et al., 2017). Therefore, as concomitant acquisition of two distinct mutations in a cell is less likely, dual targeting of allosteric and active sites has been proposed to limit the emergence of resistance (Wylie et al., 2017).

Abl001 is the first allosteric inhibitor of BCR-ABL that reached the clinic (Schoepfer et al., 2018) (Figure 1.4A). In vitro studies of resistance to Abl001 reveal that mutations in the myristate allosteric pocket, which is the proposed binding site of the inhibitor, can confer resistance and block binding of Abl001 (Wylie et al., 2017) (Figure 1.4B). However, treatment of BCR-ABL-transformed cells with combination of allosteric and ATP-site inhibitors significantly reduces the occurrence of any resistant clones (Wylie et al., 2017). Pre-clinical studies corroborate these findings and indicate that combining inhibitors with non-overlapping “resistance-signatures” may be a possible strategy to reduce the emergence of drug resistance in the clinic. Therefore, identifying combinations of drugs that have distinct binding modes and patterns of resistance could be a potential strategy to improve molecularly-targeted anti-cancer therapies against which resistance inevitably arises.

Similar strategy has been recently employed to target the oncogenic signalling through mTOR kinase. mTOR kinase plays critical roles in the PI3K/Akt/mTOR pathway that is commonly upregulated in cancer (Vivanco and Sawyers, 2002). Inhibitors that bind mTOR in the FRB-binding site (rapalogs) or the ATP-binding site (TOR kinase

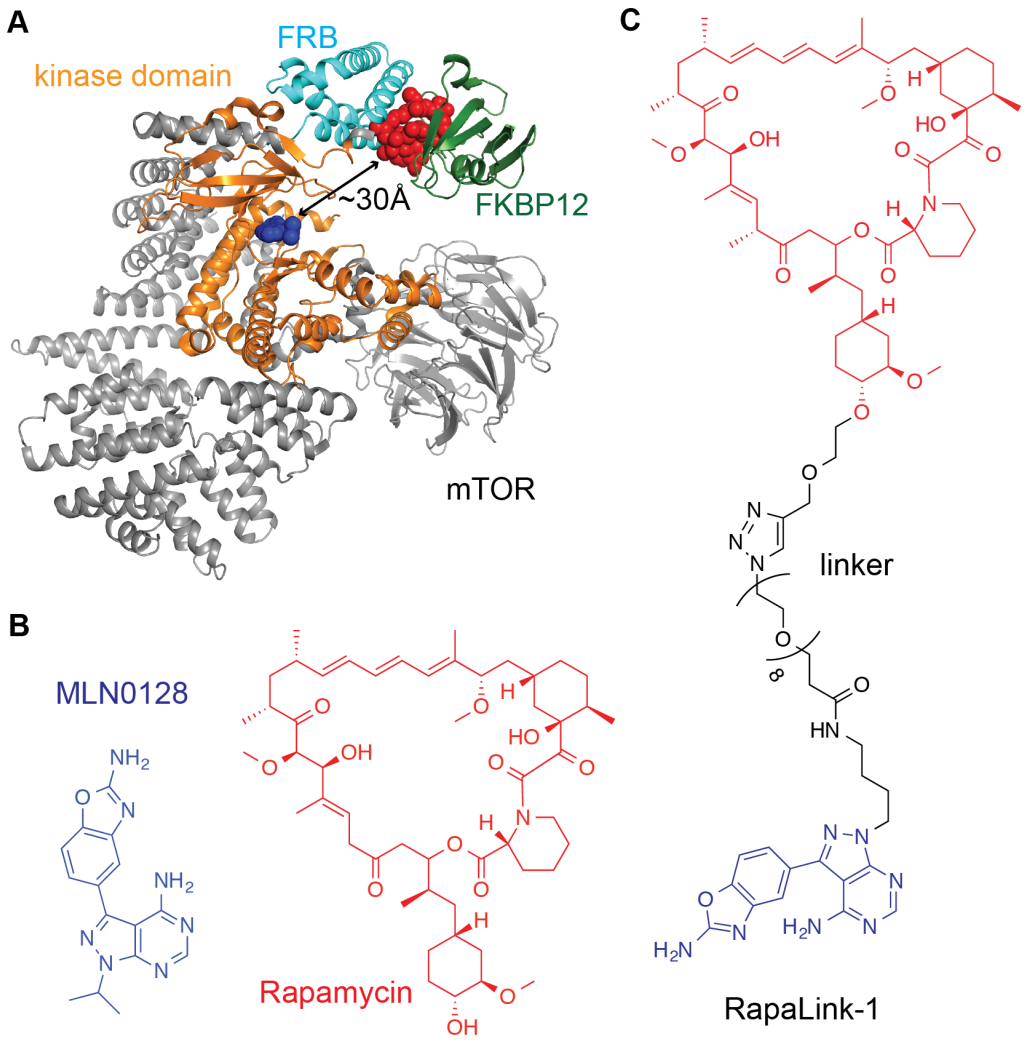


**Figure 1.5. Bivalent inhibitors to overcome drug resistance.**

(**A**) Model of mTOR kinase (gray, constructed from 4JT5 and 1FAP co-crystal structural models). FKBP12 (green), FRB (cyan) and kinase (orange) domains are indicated. Inhibitors bound in the kinase active site and the FRB-site are also shown (blue and red spheres). (**B**) Chemical structures of mTOR inhibitors binding in the active site (MLN0128, blue) and the FRB-site (rapamycin, red). (**C**) Chemical structure of the bivalent mTOR inhibitor (RapaLink-1).

inhibitors - TORKis, Figure 1.5A, B) could provide therapeutic opportunity and were evaluated in clinical trials (Basu et al., 2015; Wagle et al., 2014a). However, resistance mutations in the binding sites of these drugs can arise and confer resistance (Rodrik-Outmezguine et al., 2016; Wagle et al., 2014b). To address the acquisition of resistance, Shokat and colleagues have demonstrated an elegant approach that exploits dual inhibition of the FRB- and ATP-binding sites of the mTOR kinase using a bivalent “chimeric” compound (Rodrik-Outmezguine et al., 2016). This inhibitor, termed Rapalink-1 (Figure 1.5C), has a covalent linker between the rapalog and the TORKi moieties so that the compound can bind the FRB- and ATP-sites simultaneously. The concomitant binding of the two binding pockets by Rapalink-1 potently blocks mTOR activity and limits cancer cell proliferation (Rodrik-Outmezguine et al., 2016). Interestingly, cells with mutations in the FRB- and ATP-binding sites can be inhibited by the Rapalink-1 compound even though this “double mutant” allele confers resistance to rapalogs, TORKis as well as their combinations. It will be interesting to compare whether Rapalink-1 treatment could also limit the emergence of on-target resistance in comparison to treatment with individual inhibitors or their combinations (i.e. unlinked rapalogs and TORKis) (Rodrik-Outmezguine et al., 2016).

**Thesis outline.**

Molecularly-targeted small molecule drugs have revolutionized anti-cancer therapy but resistance to these agents often arises. In chapter 1 I outlined how understanding of chemotype-specific mechanisms of resistance can help design new drugs to overcome the resistance. Together, these studies provide a foothold for my thesis research to establish approaches for developing chemical inhibitors of AAA proteins that integrate analysis of resistance during the design process.

In chapter 2 I describe our efforts to develop spastazoline, the first potent and selective inhibitor of a microtubule-severing AAA protein spastin. To design this inhibitor, we tested selected heterocyclic scaffolds against wild-type spastin and constructs with engineered mutations in the nucleotide-binding site that do not substantially disrupt ATPase activity. We describe how active and functionally silent mutant alleles of AAA proteins can be identified and show how they can be leveraged to guide inhibitor optimization. These studies also identified spastazoline-resistance-conferring point mutations in spastin. Spastazoline, along with the matched inhibitor-sensitive and inhibitor-resistant cell lines we generated, were used in parallel experiments to dissect spastin-specific phenotypes in dividing cells. Together, our findings suggest how chemical probes for AAA proteins, along with inhibitor resistance-conferring mutations, can be designed and used to dissect dynamic cellular processes.

The topic of chapter 3 is the design of an allele-specific inhibitor of spastin. To develop this compound I first solved high-resolution crystal structures of spastazoline

analogs bound to spastin. These structures match our predicted models and are consistent with observations that mutations of a P-loop residue, such as asparagine-to-cysteine, confer resistance to spastin inhibitors. These analyses suggested that modifications of the quinazoline core of the inhibitor could restore the activity of the compound against the spastin allele with a cysteine mutation in the P-loop. We identified a fluoro-quinazoline analog that potently and selectively inhibited this spastin allele. I solved a crystal structure of the fluoro-analog bound to the cysteine mutant that confirmed the predicted interaction. Together, these studies show that tuning electrostatics rather than sterics can be a useful strategy to design allele-specific inhibitors of AAA proteins.

In chapter 4 I describe an approach, which we name RADD (resistance analysis during design) that uses data from tests of compound activity against constructs with engineered mutations to identify inhibitor-target interactions. We apply RADD to predict the binding mode for diaminotriazole-based chemical inhibitors of spastin that are chemically unrelated to spastazoline. We also identify more potent analogs and use our approach to show that they bind the spastin's active site in a different orientation in comparison to the starting compound. The distinct binding modes of these diaminotriazole-based compounds predicted by RADD match the high-resolution models I generated using X-ray crystallography. Together, these data provide a framework for how mutations in active sites of proteins could facilitate inhibitor design.

In chapter 5 I present the discovery of a mutant allele of VCP/p97 AAA ATPase that can bind and hydrolyze an unnatural nucleotide. This study provides an overview of

nucleotide substrate preferences of VCP/p97 protein alleles with mutations in the active site and shows how specificity to N6-modified ATP analogs can be engineered. The mutant allele-substrate pair identified in this study can be useful to study the function of individual AAA domains in complex assemblies of AAA proteins.

How is evolution of new traits, such as acquired resistance to drugs in cancer, influenced by the genetic and epigenetic variations in cells? In chapter 6, I present my efforts to address this question. I studied how aberrant chromosome numbers in cancer cells can impose distinct constraints on the emergence of drug resistance. For these studies I focused on GSK923295, a drug targeting mitotic kinesin CENPE that was evaluated in clinical trials for cancer, and performed unbiased selections to isolate drug-resistant clones in diploid and near-haploid cancer cell lines. In diploid cells I identified single-point mutations that can suppress inhibitor binding. Interestingly, I discovered a genomic deletion in GSK923295-resistant haploid cells that disrupts the CENPE gene. In contrast to diploid cells, CENPE is not essential in haploid cells, and thus this genomic deletion can confer resistance. These findings indicate that different chromosome copy numbers in cells can lead to distinct modes of chemotype-specific resistance.

Discussion of results in my thesis and suggested future experiments are included in chapter 7.

## Chapter 2: Designing a chemical inhibitor for the AAA protein spastin using active site mutations.

*Note to readers: the results discussed in this chapter arose from a collaboration with my colleagues in the Kapoor laboratory, Dr Tommaso Cupido and Megan E Kelley. Closely related version of our work has been published in Cupido T, Pisa R et al., Nat. Chem. Biol., 2019, 15, 444-452; DOI:10.1038/s41589-019-0225-6. I include this work here as it sets the stage for studies presented in the following chapters. Except for work explicitly credited to others, I performed experiments and analysis presented in this chapter.*

### Introduction.

In humans, the AAA superfamily (ATPases associated with diverse cellular activities) has ~100 proteins whose functions have been linked to a wide range of cellular processes, including cell division, cytoskeleton organization, and organelle biogenesis (Erzberger and Berger, 2006). As AAA proteins carry out functions that can occur within minutes to seconds, chemical probes that inhibit their activities in cells on similarly fast timescales can be valuable tools to dissect these dynamic mechanisms (Lampson and Kapoor, 2006). Currently, we have well-characterized selective chemical probes for only a handful of AAA proteins, such as dynein, a microtubule-based motor protein, midasin, a ribosome biogenesis factor, and valosin-containing protein (VCP), a regulator of ubiquitin-dependent proteolysis (Chou et al., 2011; Firestone et al., 2012;

Kawashima et al., 2016; Magnaghi et al., 2013). However, chemical inhibitors of most AAA proteins are not available.

In principle, chemical inhibitors of AAA proteins can be identified that target either the nucleotide-binding site or an allosteric site. An allosteric inhibitor-binding site has been characterized for VCP and the vacuolar protein sorting-associated protein 4 (VPS4) (Banerjee et al., 2016; Pöhler et al., 2018). However, it is unclear whether an equivalent site exists in other AAA proteins. Targeting the nucleotide-binding site could represent a more general strategy; however, designing selective nucleotide-competitive inhibitors of AAA proteins is challenging for at least three reasons. First, the active site is conserved across the AAA superfamily (Beyer, 1997). Second, this site in AAA proteins can undergo activity-associated conformational transitions that substantially alter its overall shape (Puchades et al., 2017). Third, we lack structural data for any eukaryotic AAA protein bound to a nucleotide-competitive inhibitor. These data can be crucial for structure-based inhibitor design (Davis et al., 2003).

Spastin, fidgetin, and katanin are AAA proteins closely related at the level of sequence and are collectively referred to as microtubule-severing enzymes (Roll-Mecak and McNally, 2010). Biochemical assays have shown that spastin and katanin can sever microtubules into smaller filaments in an ATP-hydrolysis-dependent manner (McNally and Vale, 1993; Roll-Mecak and Vale, 2005). On the basis of these findings, models have been proposed for how microtubule-severing enzymes contribute to the assembly, disassembly, or maintenance of microtubule-based structures in axons and dendrites, primary cilia, and dividing cells (Sharp and Ross, 2012). In addition, recent

studies have suggested a role for spastin in the biogenesis and function of the nuclear envelope and membrane organelles, such as lysosomes and endosomes (Allison et al., 2013, 2017; Vietri et al., 2015). Thus far, the only chemical proposed to target a microtubule-severing enzyme in cells is a purine-based compound that can pull-down katanin from cellular lysates (Kuo et al., 2016). However, the direct and specific inhibition of katanin by this compound has not been demonstrated (Kuo et al., 2016), and it is unclear how useful chemical probes for microtubule-severing proteins can be developed.

It is now emerging that analyses of resistance-conferring mutations can help establish the direct physiological targets of chemical inhibitors (Han et al., 2017; Kapoor and Miller, 2017; Wacker et al., 2012). In addition, resistance-conferring mutations can be leveraged for determining on- and off-target inhibitor-induced phenotypes (Kapoor and Miller, 2017). We reasoned that mutations in drug binding sites could also be useful during the early steps of inhibitor development when unoptimized compounds (for example, screening hits), without robust models for inhibitor-target interactions need to be evaluated. Thus far, resistance-conferring mutations have been typically identified using genetics-based screens that rely on selection of growth in tractable systems, as has been the case for cytotoxic chemical inhibitors of AAA proteins (Anderson et al., 2015; Kawashima et al., 2016). However, identifying mutations in AAA proteins that do not impair function but confer inhibitor resistance can be challenging.

Here we use protein structure and sequence analyses to design mutant alleles of spastin that retain ATPase activity. Testing selected heterocyclic scaffolds against

wild-type protein and constructs with these mutations, along with computational docking, helped design spastazoline, a pyrazolyl-pyrrolopyrimidine-based inhibitor of spastin. In addition, we identified a spastazoline-resistance-conferring point mutation in spastin. Spastazoline-induced phenotypes were examined in cells expressing either wild-type spastin or an allele with a resistance-conferring point mutation. Together, these studies reveal how spastin-specific cell division phenotypes can be analyzed using chemical probes and cognate resistance-conferring mutations.

**Results.**

**Mutant alleles of spastin that retain ATPase activity.**

To design mutant alleles of spastin, we focused on the nucleotide-binding pocket. We selected *Drosophila melanogaster* spastin (hereafter Dm-spastin), as it is a biochemically well-characterized microtubule-severing enzyme (Roll-Mecak and Vale, 2008). We first compared the sequences of the AAA domains in Dm-spastin and four related AAA proteins: human fidgetin-like protein 1 (Hs-FIGL1), human VPS4B, mouse VCP/p97 (Mm-VCP/p97, which has two AAA domains (D1 and D2) and is identical to the human protein) and *Xenopus laevis* katanin (*Xl*-katanin) (Figure 2.1A). These proteins were selected as recombinant forms of either their AAA domains or constructs with ATPase activity had been previously reported (Loughlin et al., 2011; Merrill and Hanson, 2010; Rouiller et al., 2002). Using available structural data (*Dm*-spastin, *Hs*-FIGL1, *Hs*-VPS4B and *Mm*-VCP) (Banerjee et al., 2016; Gonciarz et al., 2008; Karlberg et al., 2008; Roll-Mecak and Vale, 2008; Scott et al., 2005) or homology-based

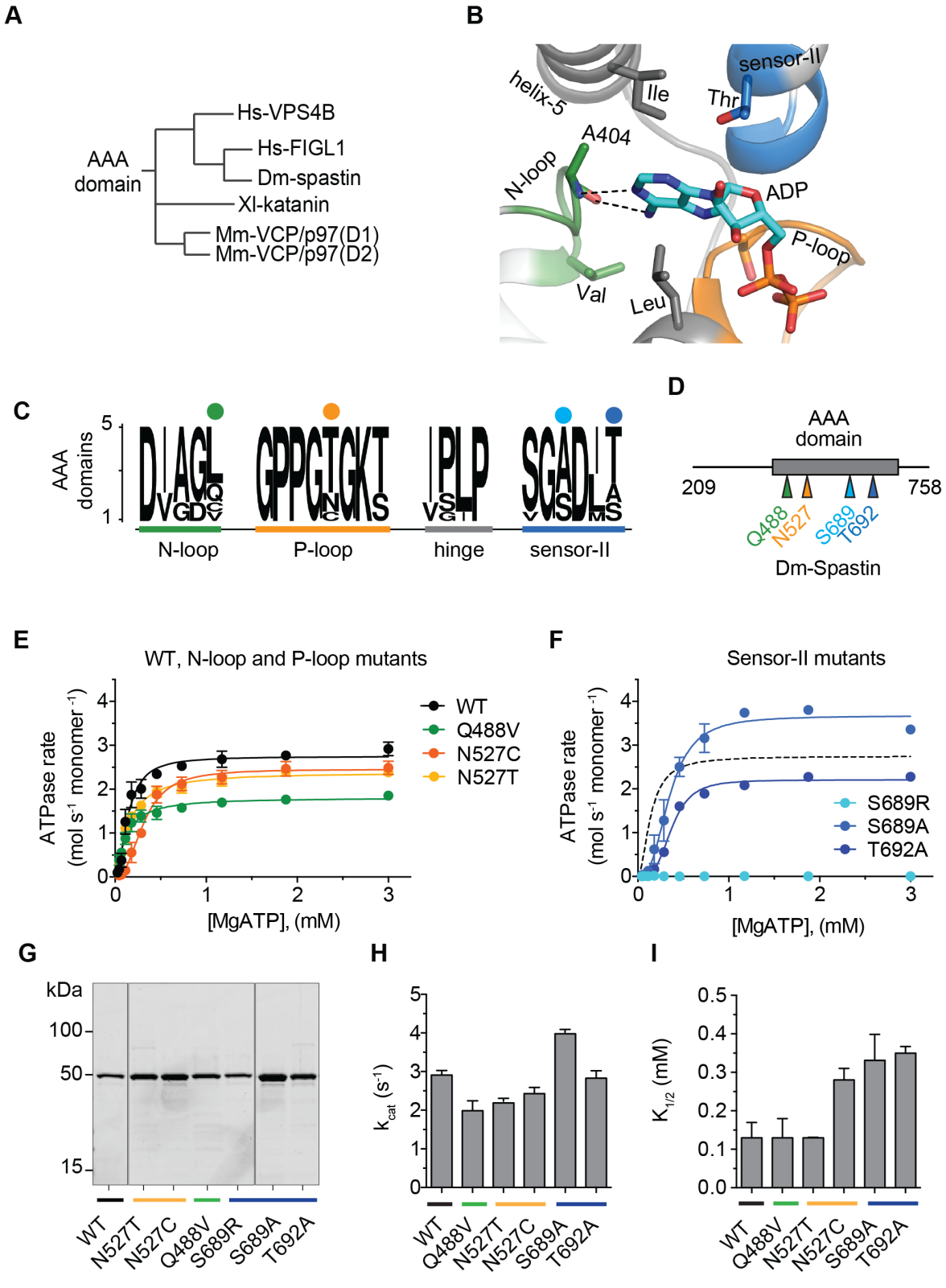


**Figure 2.1. Identifying and characterizing variability hot-spot mutations in spastin**

**Figure 2.1. Identifying and characterizing variability hot-spot mutations in spastin.** (**A**) A sequence similarity tree diagram of the AAA domains of Hs-VPS4B, Xl-katanin, Dm-spastin, Hs-FIGL1, and D1 and D2 domains of Mm-VCP/p97 (for details see Table 2.1). (**B**) Structural model (ribbon diagram) of the nucleotide-binding site in FIGL1 (PDB: 3D8B) showing adenosine-5′ diphosphate (ADP, stick representation), structural motifs (N-loop, green; P-loop, orange; helix 5, gray; sensor-II, blue; hinge, gray), and selected residues within ~6 Å of the adenine. Predicted hydrogen-bonding interaction between the nucleotide and the backbone atoms of a residue in the N-loop are also shown (black dashed lines). (**C**) A modified "sequence logo" diagram for residues in the nucleotide-binding site of five AAA domains. Four variability hot-spot residues are indicated (colored circles). The relevant structural motifs in the nucleotide-binding site are also highlighted. (**D**) Schematic shows the AAA domain (light gray box), the first and last residues of the Dm-spastin construct (not to scale), and the residues that were mutated in Dm-spastin's AAA domain (colored arrows). (**E**, **F)** ATP-concentration dependence of the steady-state activity of wild-type (WT) and mutant Dm-spastin constructs, analyzed using an NADH-coupled assay. Rates were fit to the Michaelis–Menten equation for cooperative enzymes (average ± s.d., n=3). For comparison, data for the WT protein (from **E**, dashed line) are also shown in **F**. (**G**) SDS-PAGE analysis of purified wild-type (WT) and mutant Dm-spastin constructs (Coomassie blue). (**H, I**) Catalytic turnover number ($k_{cat}$; **H**) and the ATP concentration required for half-maximal velocity ($K_{1/2}$; **I**) of recombinant Dm-spastin constructs. Data represent average ± s.d. (n=3). Measured values for these parameters are provided in Table 2.1. The corresponding structural motifs for the mutated residues are color-coded as in **B, C, D**. *Note - a subset of assays in this figure were performed by Dr Tommaso Cupido, postdoctoral fellow in the Kapoor lab.*

**A**

| | Mm-VCP/p97 (D1) | Mm-VCP/p97 (D2) | Xl-katanin | Hs-FIGL1 | Dm-spastin |
|---|---|---|---|---|---|
| Mm-VCP/p97(D1) | 100.00 | 38.24 | 41.00 | 36.72 | 37.11 |
| Mm-VCP/p97(D2) | 38.24 | 100.00 | 42.18 | 37.92 | 35.32 |
| Xl-katanin | 41.00 | 42.18 | 100.00 | 49.45 | 48.16 |
| Hs-FIGL1 | 36.72 | 37.92 | 49.45 | 100.00 | 50.37 |
| Dm-spastin | 37.11 | 35.32 | 48.16 | 50.37 | 100.00 |

**B**

| | N-loop | P-loop | hinge | helix-5 | sensor-II |
|---|---|---|---|---|---|
| Dm-spastin | DIAG**Q** | []PPG**N**GKTL | []V--P | []-L-[] | SG**S**D-T |
| Hs-FIGL1 | DIAGV | []PPGTGKTL | []I--P | []-I-[] | SGAD-T |
| Xl-katanin | DIADL | []PPGTGKTL | []I--P | []-L-[] | SGAD-T |
| Mm-VCP/p97(D1) | DIGGC | []PPGTGKTL | []I--P | []-I-[] | VGAD-A |
| Mm-VCP/p97(D2) | DIGGL | []PPGCGKTL | []I--P | []-I-[] | SGAD-T |

**C**

| Dm-spastin | $K_{1/2}$ (mM) | $k_{cat}$ ($s^{-1}$) | Hill coefficient | $k_{cat}/K_{1/2}$ ($mM^{-1}$ $s^{-1}$) |
|---|---|---|---|---|
| WT | 0.15 (0.05) | 2.8 (0.2) | 2.1 (0.4) | 19.9 (5.0) |
| Q488V | 0.12 (0.04) | 1.8 (0.1) | 1.4 (0.2) | 16.0 (3.6) |
| N527T | 0.15 (0.01) | 2.4 (0.1) | 1.4 (0.2) | 15.7 (0.9) |
| N527C | 0.31 (0.02) | 2.5 (0.2) | 2.6 (0.5) | 7.9 (0.2) |
| S689A | 0.35 (0.06) | 3.7 (0.1) | 2.8 (0.2) | 10.7 (1.8) |
| S689R | n.d. | n.d. | n.d. | n.d. |
| T692A | 0.37 (0.01) | 2.2 (0.1) | 3.6 (0.6) | 5.9 (0.2) |

**Table 2.1. Analysis of primary sequence similarity in AAA proteins and characterization of Dm-spastin variability hot-spot mutants**

(**A**) Pairwise sequence identity matrix, generated using multiple sequence alignment in Clustal Ω, for the five AAA domains in the indicated AAA proteins. (**B**) Alignment of five structural motifs in AAA domains of four AAA proteins (VCP/p97 has two AAA domains). The residues that are < 6 Å from the adenine in 3D8B structure (FIGL1) were selected and aligned with residues at equivalent positions in the other four AAA proteins. This alignment was used to generate the logo diagram in Figure 2.1. Dashes indicate residues that are not shown as they are > 6 Å from the adenine, and closed square brackets indicate sequence gaps of variable length. Selected non-conserved amino acid positions are highlighted (variability hotspots, colored as in Figure 2.1). (**C**) Analysis of the steady-state ATPase activity of Dm- spastin wild-type (WT) and mutant constructs (see Figure 2.1). Values for enzyme activity parameters are provided (average, n = 3, s.d. in parentheses). Rates were plotted against MgATP concentration and data were fit to the Michaelis-Menten equation for cooperative enzymes (see Methods). The data from each experiment were fit separately and the values, as determined by the fitting, were averaged. *Note - a subset of assays in this figure were performed by Dr Tommaso Cupido, postdoctoral fellow in Kapoor lab.*

models (*Xl*-katanin; see Methods for details), we identified residues that were likely to be within ~6Å of adenine (Figure 2.1B). These residues are located in five structural motifs of the AAA domain, named the amino (N)-terminal loop (N-loop), the phosphate-binding loop (P-loop), the hinge motif, helix 5, and the sensor-II (Figure 2.1B).

As expected for a conserved active site, most of these residues are invariant across the five AAA proteins examined. However, we noted four amino acid positions - one in the N-loop, one in the P-loop, and two in the sensor-II motif - that have substantially diverged (Figure 2.1C). These residues, which we name “variability hotspot” residues, contribute in large part to the sequence variation in these nucleotide-binding motifs across the AAA proteins (Table 2.1A, B). Sequence alignment of the five structural motifs of the nucleotide-binding site in AAA domains indicates that these variability hotspot residues can be identified across this protein superfamily (Table 2.1B). We hypothesized that a residue at a variability hotspot position could be replaced with a residue from the equivalent position in a related AAA protein, to obtain an active-site mutant that retains enzymatic activity.

To test this hypothesis, we generated recombinant constructs of wild-type Dm-spastin and Dm-spastin carrying mutations at the variability hotspot residues, and characterized their steady-state ATP-hydrolysis activity (Figure 2.1D-I). In addition to the wild-type protein, five of the six mutant constructs were active (Figure 2.1E, F, H, I and Table 2.1C provide additional enzyme activity parameters). Only one construct, with a mutation at a sensor-II variability hotspot residue (S689R), yielded an inactive

recombinant protein (Figure 2.1F). Dm-spastin had a catalytic activity ($k_{cat}$) of ~3 $s^{-1}$ (Figure 2.1E, H). The five active mutants had $k_{cat}$ values within ~1.5-fold of the wild-type protein, ranging from ~2 $s^{-1}$ for the N527T mutant to ~4 $s^{-1}$ for the S689A mutant (Figure 2.1E, F, H). The ATP concentrations required for half-maximal enzymatic velocity ($K_{1/2}$) were also within a narrow range, from ~0.1 mM (wild type, Q488V, and N527T) to ~0.4mM (S689A) (Figure 2.1E, F, I). Together, these data indicate that swapping variability hotspot residues can yield AAA protein alleles that retain catalytic activity.

**A starting chemical scaffold to design spastin inhibitors.**

To find chemical starting points for the design of spastin inhibitors, we examined conserved features of the nucleotide-binding site. We noted a pattern of two hydrogen bonds between the adenine and the backbone of a residue in the N-loop in several AAA proteins (for example, A404 in FIGL1 (PDB: 3D8B), Figure 2.1B and 2.2A). Therefore, we selected and tested a collection of 33 chemically diverse kinase inhibitors, which are heterocyclic scaffolds that could mimic these hydrogen bonding interactions, against AAA proteins (Table 2.2).

To profile the inhibitory activity and selectivity of these compounds, we generated recombinant forms of Hs-FIGL1, Mm-VCP, and Xl-katanin, and characterized their steady-state ATPase activities (Figure 2.2B, C). Consistent with other reports, we found $K_{1/2}$ values for ATP hydrolysis to be in the high micromolar range (Figure 2.2D, E) (Chou et al., 2011; Whitehead et al., 2013). Whereas the $k_{cat}$ varied >50-fold (Mm-VCP:

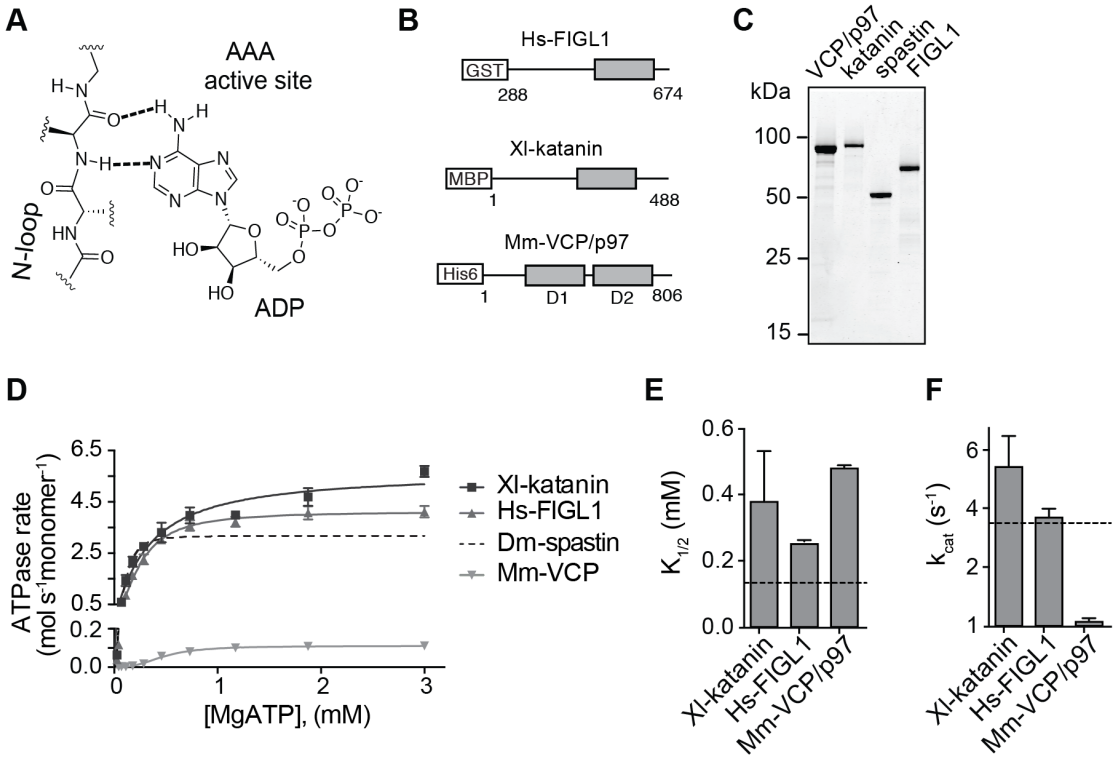


**Figure 2.2. Characterizing AAA proteins related to spastin.**

(**A**) Schematic for the predicted hydrogen-bonding interactions (dashed lines) between adenine and the N-loop in AAA proteins. (**B**) Schematic shows the AAA domain (light gray boxes), tags for affinity purification (white boxes), and the first and last residues of four AAA protein constructs (not to scale). (**C**) SDS-PAGE analysis of purified recombinant AAA proteins, including Dm-spastin, Mm-VCP/p97, Xl-katanin, Hs-FIGL (Coomassie blue). (**D, E, F**) ATP-concentration dependence of the steady-state activity of four AAA protein constructs, analyzed using an NADH-coupled assay. Rates were fit to the Michaelis–Menten equation for cooperative enzymes (average ± s.d., n = 3). (**E**) ATP concentration required for half-maximal velocity ($K_{1/2}$) and (**F**) catalytic turnover ($k_{cat}$) of three AAA proteins. For comparison the corresponding data for Dm-spastin are also shown; dashed line).

## Table 2.2. Selected compounds tested against AAA proteins.

| Figure 2.3A entry | structure | name | International Chemical Identifier | PDB | Vendor (catalog number) |
|---|---|---|---|---|---|
| 1 | 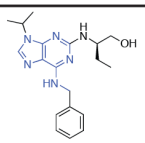 | Seliciclib | BTIHMVBBUGXLCJ-OAHLLOKOSA-N | 2A4L | LC Laboratories (R-1234) |
| 2 | 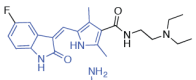 | Sunitinib | WINHZLLDWRZWRT-ATVHPVEESA-N | 3G0E | LC Laboratories (S8877) |
| 3 | 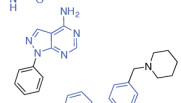 | PP3 | KKDPIZPUTYIBFX-UHFFFAOYSA-N | 4GKH | Tocris (2794) |
| 4 | 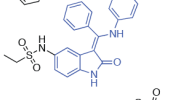 | Hesperadin | GLDSKRNGVVYJAB-DQSJHHFOSA-N | 2BFX | synthesized |
| 5 | 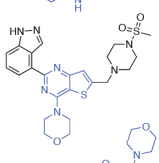 | Pictilisib | LHNIIDJUOCFXAP-UHFFFAOYSA-N | 2WXP | LC Laboratories (G-9252) |
| 6 | 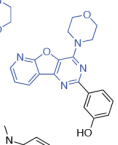 | PI-103 | TUVCWJQQGGETHL-UHFFFAOYSA-N | 4L23 | LC Laboratories (P-9099) |
| 7 | 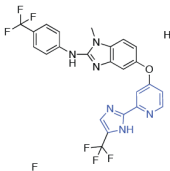 | CHIR265 | YABJJWZLRMPFSI-UHFFFAOYSA-N | 5CT7 | Selleck (S2161) |
| 8 | 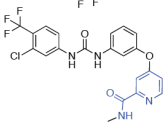 | Sorafenib | MLDQJTXFUGDVEO-UHFFFAOYSA-N | 1UWH | Selleck (S7397) |
| 9 | 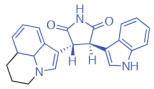 | Tivantinib | UCEQXRCJXIVODC-PMACEKPBSA-N | 3RHK | Selleck (S2753) |
| 10 | 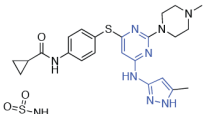 | Tozasertib | GCIKSSRWRFVXBI-UHFFFAOYSA-N | 4AF3 | LC Laboratories (T-2304) |
| 11 | 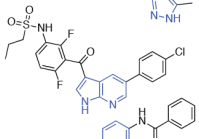 | Vemurafenib | GPXBXXGIAQBQNI-UHFFFAOYSA-N | 4RZV | ChemScene (CS-0216) |
| 12 | 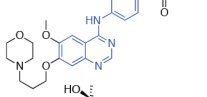 | ZM-447439 | OGNYUTNQZVRGMN-UHFFFAOYSA-N | 2VRX | Tocris (2458) |
| 13 | 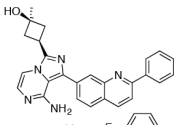 | Linsitinib | PKCDDUHJAFVJJB-UHFFFAOYSA-N | N.A. | Selleck (S1091) |
| 14 (compound 2.2) | 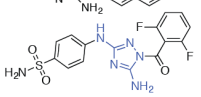 | JNJ-7706621 | KDKUVYLMPJIGKA-UHFFFAOYSA-N | 5USY | ApexBio (A4115) |
| 15 | 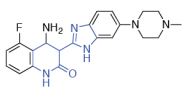 | Dovitinib | KCOYQXZDFIIGCY-ZZEZOPTASA-N | 5A46 | Selleck (S1018) |

## Table 2.2 cont'd

| Figure 2.3A entry | structure | name | International Chemical Identifier | PDB | Vendor (catalog number) |
|---|---|---|---|---|---|
| **16** | 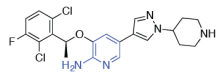 | (R)-crizotinib | KTEIFNKAUNYNJU-LBPRGKRZSA-N | 4ANQ | Active Biochemicals (A-1031) |
| **17** | 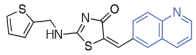 | Ro-3306 | XOLMRFUGOINFDQ-YBEGLDIGSA-N | 4EOI | Cayman Chemical (15149) |
| **18** | 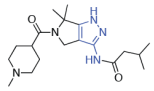 | PHA-793887 | HUXYBQXJVXOMKX-UHFFFAOYSA-N | 2WPA | Selleck (S1487) |
| **19** | 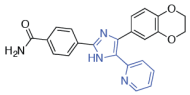 | D4476 | DPDZHVCKYBCJHW-UHFFFAOYSA-N | 3TZM | Sigma (D4476) |
| **20** | 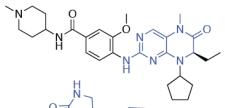 | BI2536 | XQVVPGYIWAGRNI-JOCHJYFZSA-N | 2RKU | Selleck (S1109) |
| **21** | 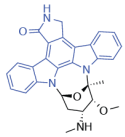 | Staurosporine | HKSZLNNOFSGOKW-FYTWVXJKSA-N | 5E8W | Sigma (S4400) |
| **22** | 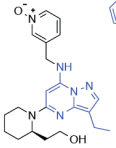 | Dinaciclib | PIMQWRZWLQKKBJ-SFHVURJKSA-N | 4KD1 | Cayman Chemical (14707) |
| **23** | 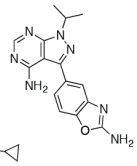 | INK-128 | GYLDXIAOMVERTK-UHFFFAOYSA-N | N.A. | Selleck (S2811) |
| **24 (compound 2.1)** | 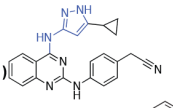 | Compound 4 | NVMCVWOODOWOLT-UHFFFAOYSA-N | 3F6X | synthesized (RP149) |
| **25** | 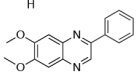 | AG-1296 | QNOXYUNHIGOWNY-UHFFFAOYSA-N | N.A. | Cayman Chemical (10010592) |
| **26** | 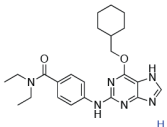 | NU-6140 | XHEQSRJCJTWWAH-UHFFFAOYSA-N | N.A. | Cayman Chemical (17271) |
| **27** | 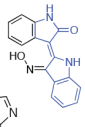 | Indirubin-3'-monoxime | LDEWQRSYYHTQRA-UHFFFAOYSA-N | 1Q41 | Cayman Chemical (13314) |
| **28** | 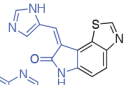 | C16/PKR inhibitor | VFBGXTUGODTSPK-FPYGCLRLSA-N | 4QMO | Cayman Chemical (15323) |
| **29** | 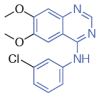 | AG-1478 | GFNNBHLJANVSQV-UHFFFAOYSA-N | 4FEX | Cayman Chemical (10010244) |
| **30** | 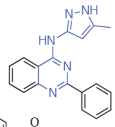 | GSK3b inhibitor XIII | JYCUVOXSZBECAY-UHFFFAOYSA-N | 2JC6 | Enzo Life Science (124-0001) |
| **31** | 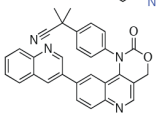 | ATRi (ETP-46464) | DPLMXAYKJZOTKO-UHFFFAOYSA-N | N.A. | Sigma (SML1321) |
| **32** | 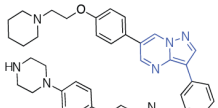 | Dorsomorphin | XHBVYDAKJHETMP-UHFFFAOYSA-N | 3H9R | MedChem Express (HY-13418) |
| **33** | 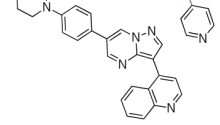 | LDN-193189 | CDOVNWNANFFLFJ-UHFFFAOYSA-N | 3Q4U | MedChem Express (HY-12071) |

~0.1 $s^{-1}$; Xl-katanin: ~5.5 $s^{-1}$; Hs-FIGL1 ~4 $s^{-1}$, Figure 2.2D, E), the $K_{1/2}$ values varied only ~3-fold (Mm-VCP: ~450 μM; Xl-katanin: ~400 μM; Hs-FIGL1: ~250 μM and Figure 2.2F). For these enzymes, the range of $K_{1/2}$ was comparable to what we found for the active Dm-spastin mutants, suggesting that variation in the hotspot residues can account for differences in how these proteins interact with the nucleotide.

We next tested the selected compounds (10μM) against Dm-spastin and the other three AAA proteins (Figure 2.3A). While most compounds did not show appreciable inhibition of any of these enzymes, we identified two compounds, one with a 4-aminopyrazolylquinazoline core (**2.1**) and the other with a 3,5-diaminotriazole core (**2.2**) that inhibited at least one AAA protein by >50% (0.5 mM ATP; Figure 2.3B, C). Both compounds **2.1** and **2.2** substantially inhibited the ATPase activity of Dm-spastin at 10 μM, and compound **2.1** also inhibited Hs-FIGL1 (Figure 2.3A). We prioritized compound **2.1** for further studies here and will examine compound **2.2** in chapter 4.

Dose-dependent analysis revealed that compound **2.1** inhibited Dm-spastin with potency in the micromolar range (Figure 2.3D, E). To examine the structure–activity relationship against AAA proteins, we synthesized and tested compound **2.1** analogs with modifications of the substituents on the pyrazolylquinazoline core (2 μM; Figure 2.3F, G). We found that compound **2.3**, in which a benzyl group replaces the phenylacetonitrile, more potently inhibited the activity of VCP/p97 compared with compound **2.1** (Figure 2.3H). By contrast, compound **2.4**, in which an N-methylpiperazine replaces the phenylacetonitrile and a phenyl replaces the cyclopropyl in the pyrazole ring, showed increased selectivity for Dm-spastin (Figure

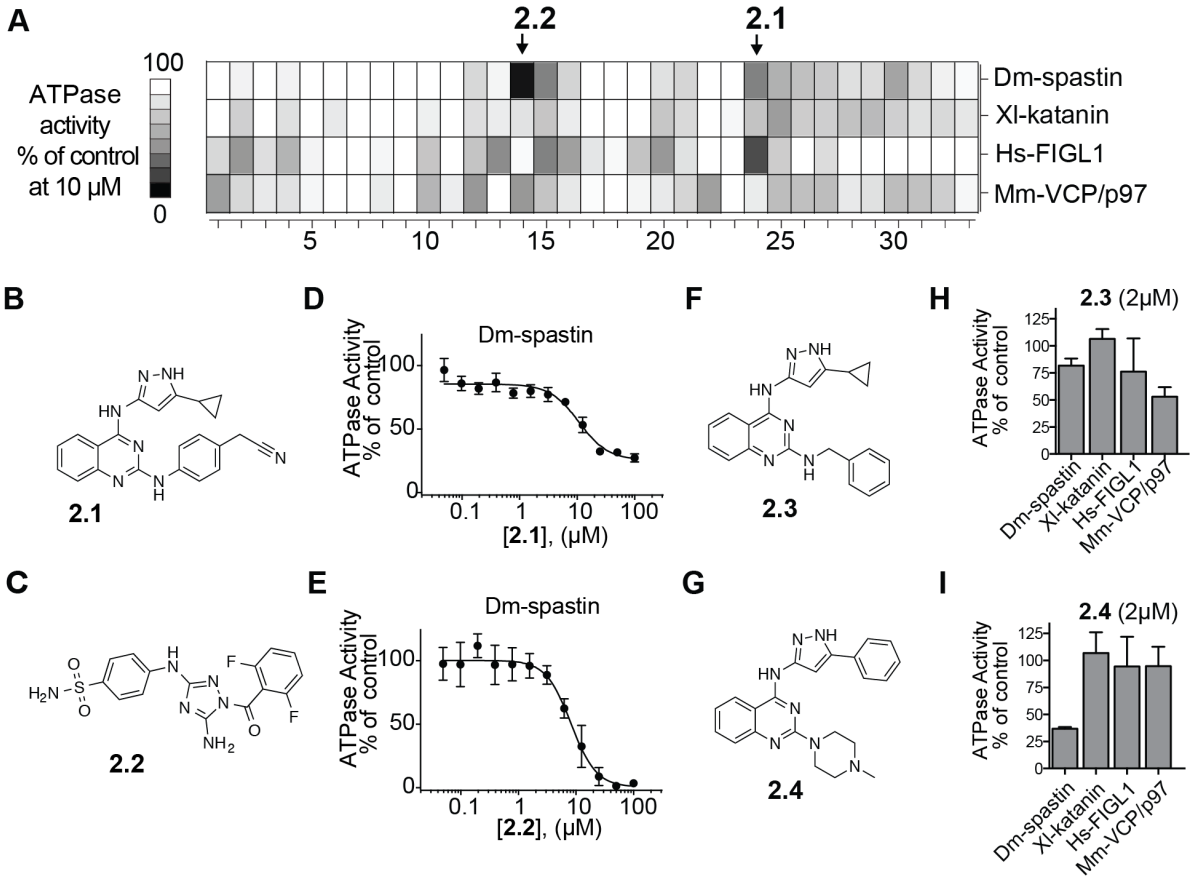


**Figure 2.3. Identifying chemical scaffolds that inhibit Dm-spastin.**

(**A**) ATPase activity of four AAA proteins in the presence of selected compounds (10μM). The heat map corresponds to percentage ATPase activity relative to DMSO control (average, n = 2, 0.5 mM MgATP). Chemical structures of all compounds tested are provided in Table 2.2. (**B, C**) Chemical structures of (**B**) compound **2.1** and (**C**) compound **2.2**. (**D, E**) Concentration-dependent inhibition of the steady-state ATPase activity of Dm-spastin by compounds **2.1** and **2.2**. Graph shows percentage residual ATPase activity values relative to DMSO control ($IC_{50}$ (**2.2**) = 6 ± 1 μM, average ± s.d., n = 3, 0.5 mM MgATP) fit to a sigmoidal dose–response equation; $IC_{50}$ value for compound **2.1** was not determined, as complete inhibition at the highest concentration tested was not observed. (**F, G**) Chemical structures of (**F**) compound **2.3** and (**G**) compound **2.4**. (**H, I**) Percentage steady-state ATPase activity of four AAA proteins in the presence of compounds **2.3** or **2.4** (2 μM, average ± s.d. ,n = 3, 0.5 mM MgATP). *Note - a subset of assays in this figure were performed by Dr Tommaso Cupido, postdoctoral fellow in the Kapoor lab).*

**A**

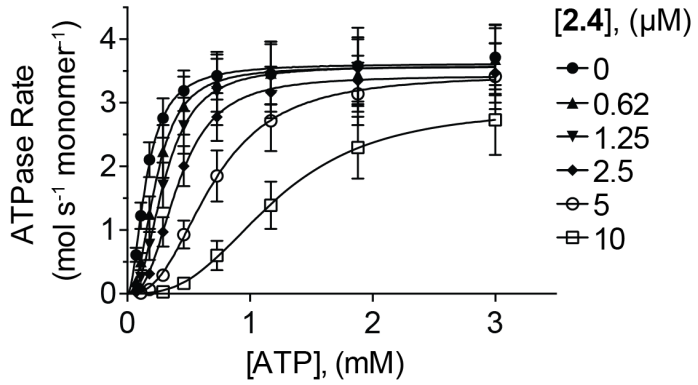


**B**

Dm-spastin-WT

| [**2.4**], (μM) | $k_{cat}$ | Hill coeff. | $K_{1/2}$ |
|---|---|---|---|
| 10 | 2.9 (2.4-3.5) | 2.9 (2.8-3.0) | 1.21 (1.15-1.27) |
| 5 | 3.4 (3.0-3.9) | 2.6 (2.6-2.5) | 0.70 (0.66-0.74) |
| 2.5 | 3.4 (3.9-3.0) | 2.7 (2.6-2.7) | 0.41 (0.40-0.43) |
| 1.25 | 3.6 (4.1-3.1) | 2.4 (2.4-2.5) | 0.31 (0.29-0.32) |
| 0.62 | 3.6 (4.1- 3.0) | 2.4 (2.3-2.5) | 0.24 (0.23-0.24) |
| 0 | 3.6 (3.1-4.2) | 1.9 (1.7-2.2) | 0.16 (0.15-0.16) |

**Table 2.3. Characterizing inhibition of spastin by compound 2.4.**

(**A**) ATP concentration-dependence of the steady- state ATPase activity of Dm-spastin at different concentrations of compound **2.4** (average, n = 2) (**B**) Values for Dm-spastin enzyme activity parameters in the presence of compound **2.4** at the indicated concentrations are provided (average, n = 2, range in parentheses). Range of MgATP concentrations tested was 0.027 to 3 mM. Steady-state ATPase activity was analyzed using an NADH-coupled assay. To calculate enzyme parameters, rates were plotted against MgATP concentration and data were fit to the Michaelis-Menten equation for cooperative enzymes. The data from each experiment were fit separately and the values, as determined by the fitting, were averaged. *Note - a subset of assays in this figure were performed by Dr Tommaso Cupido, postdoctoral fellow in Kapoor lab).*

2.3I). Testing Dm-spastin inhibition by compound **2.4** across a range of ATP concentrations revealed increases in $K_{1/2}$ at higher compound concentrations, but not substantial changes in $k_{cat}$ (Table 2.3A, B), consistent with compound **2.4** binding to the Dm-spastin nucleotide-binding site. Together, these data suggest that the pyrazolylquinazoline scaffold could provide a useful starting point for developing ATP-competitive inhibitors of spastin.

**A model for how compound 2.4 binds spastin.**

To examine how compound **2.4** binds spastin, we tested it against Dm-spastin constructs with mutations at the variability hotspot residues. We found that the mutation in the N-loop (Q488V) reduced the potency of **2.4** by ~20-fold (Figure 2.4A), whereas the mutations in the P-loop reduced potency by ~3-fold (N527C) or >35-fold (N527T) (Figure 2.4B). By contrast, mutations in the sensor-II motif led to ~2-fold reduction (T692A) or no substantial difference (S689A) in the potency of this inhibitor (Figure 2.4C). These data suggested that the P-loop and N-loop variability hotspot residues may interact with the inhibitor, and this information could be used to confirm or reject predictions from computational docking solutions.

Next, we used available Dm-spastin structural models to dock compound **2.4** into the spastin nucleotide-binding site (Roll-Mecak and Vale, 2008). Spastin structures reported to date do not have nucleotide bound, suggesting that the crystallographic models may not match the conformation that binds nucleotide-competitive inhibitors (Roll-Mecak and Vale, 2008; Taylor et al., 2012). To generate additional spastin

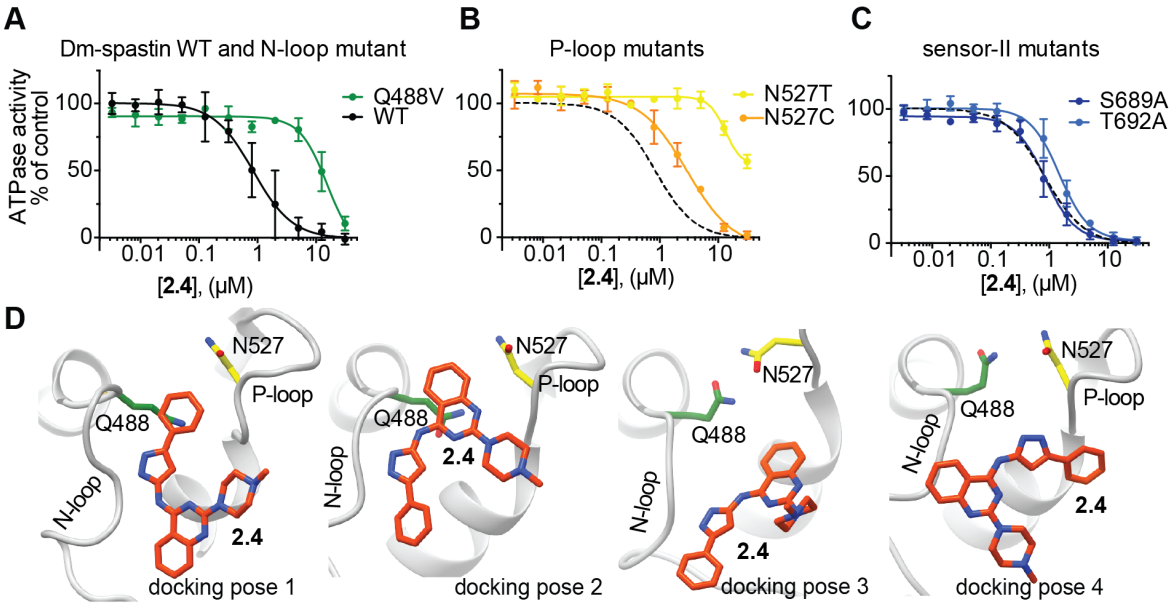


**Figure 2.4. Testing mutant constructs to build a model for the chemical inhibition of spastin.**

(**A-C**) Compound **2.4** concentration-dependent inhibition of the steady-state ATPase activity of Dm-spastin constructs with mutations at variability hotspot residues and Dm-spastin-WT. Data were fit to a sigmoidal dose-response equation and $IC_{50}$ values were calculated (Dm-spastin constructs, WT: 1.0 ± 0.6 μM; Q488V: ~12.5 μM; N527C: 2.9 ± 0.5 μM; N527T: >30 μM; S689A: 0.9 ± 0.2 μM; and T692A: 1.5 ± 0.4 μM; 0.5 mM MgATP, average ± s.d., n = 3). For comparison, analysis of the inhibition of WT (data from **A**) is also shown in **B** and **C** (dashed line). (**D**) Four computational docking poses showing compound **2.4** (stick representation, carbon atoms in orange) bound to Dm-spastin (ribbon-and-stick representation, backbone: gray ribbons) along with the Q488 (green) and N527 (yellow) variability hot-spot residues. *Note - a subset of assays in this figure were performed by Dr Tommaso Cupido (postdoctoral fellow in the Kapoor lab).*

conformations, we used molecular dynamics simulations and computationally docked compound **2.4** in the nucleotide-binding site of each spastin conformer (Amaro et al., 2018) (see Methods for details). This method yielded four models with similar docking scores for how compound **2.4** and spastin may interact (Figure 2.4D). In three of the four models, we noted adenine-like hydrogen-bonding interactions between the inhibitor aminopyrazole group and the backbone of Dm-spastin N-loop A486 (Figure 2.4D). However, only two of these docking poses had the inhibitor in close proximity to the variability hotspot residues in the N-loop and the P-loop and were therefore consistent with the potency shifts observed in the mutant spastin constructs (poses 1 and 2; Figure 2.4D).

We reasoned that the two different docking solutions could arise as a result of the chemical equivalence of the benzene rings in the quinazoline and the pyrazolyl moieties. To distinguish between these two potential binding modes we designed modifications to effectively disrupt the symmetry of the inhibitor. In particular, we synthesized compound **2.5**, in which the phenyl group in the pyrazolyl was replaced by a non aromatic tert-butyl group and the piperazine N-methyl group was shifted to the 2-position of the ring (Figure 2.5A). Compound **2.5** inhibited Dm-spastin steady-state ATPase activity (~10-fold more potently than compound **2.4**; Figure 2.5B) and also blocked Dm-spastin-dependent microtubule severing (2 μM inhibitor, 2.5C-F).
Gratifyingly, docking analysis revealed only one favored pose for compound **2.5** bound to spastin (Figure 2.5G). This model was also consistent with the data obtained by testing mutant constructs (Figure 2.5H). In this compound **2.5**-spastin model, the

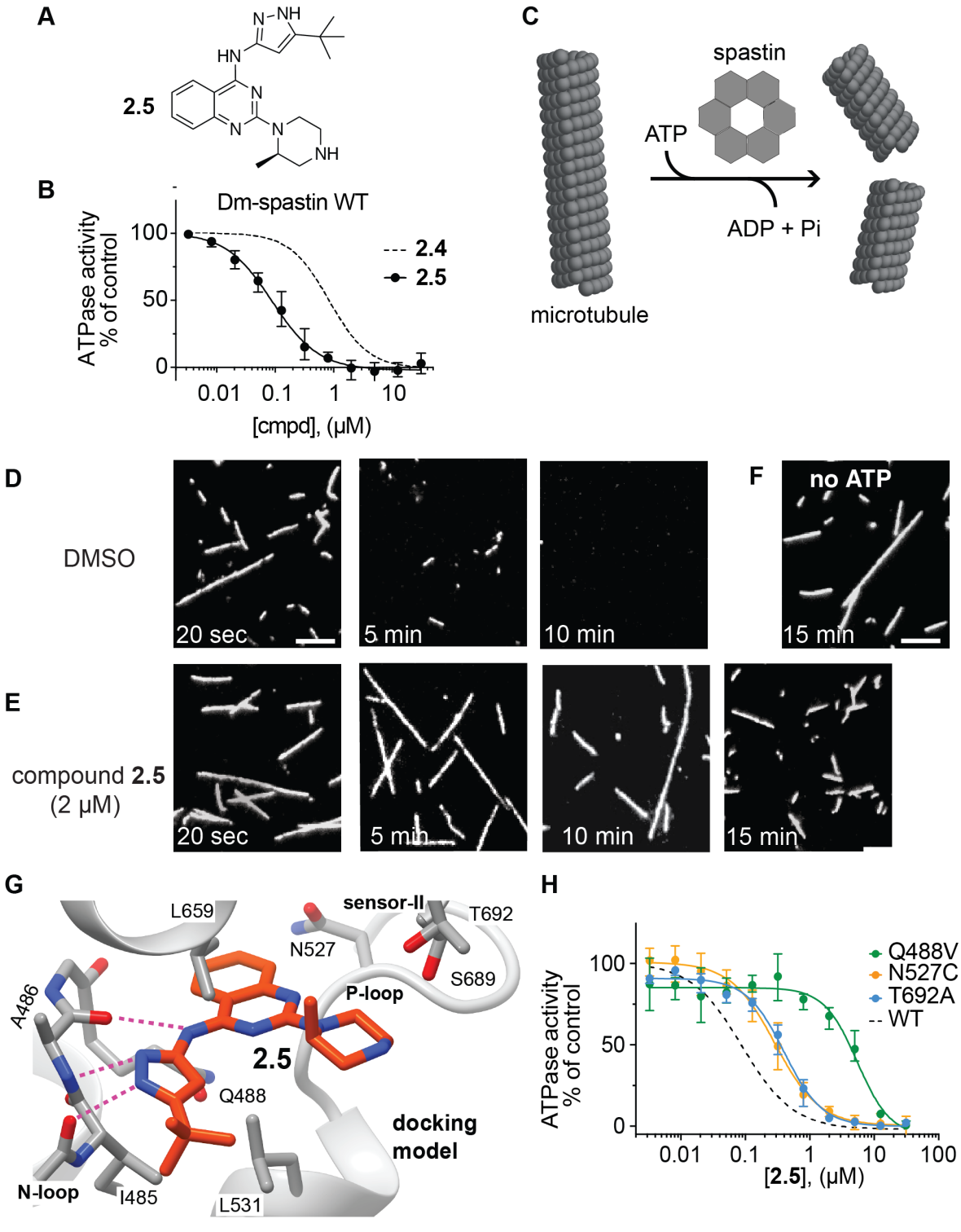


**Figure 2.5 Characterizing a potent inhibitor of Dm-spastin.**

**Figure 2.5. Characterizing a potent inhibitor of Dm-spastin.**

(**A**) Chemical structure of compound **2.5**. (**B**) Compound **2.5** concentration-dependent inhibition of the steady-state ATPase activity of Dm-spastin WT. Graph shows values fit to a sigmoidal dose–response equation. $IC_{50}$ = 106 ± 35 nM; 0.5 mM MgATP; average ± s.d., n = 3. For comparison, data for compound **2.4** are shown (from 2.4A, dashed line). (**C**) Schematic for a microtubule-severing reaction. (**D-E**) Representative fluorescence microscopy images (n = 2) of rhodamine-labeled taxol-stabilized microtubules incubated with Dm- spastin (15 nM) and DMSO (1%, **D**) or compound **2.5** (2 μM, **E**) for the indicated times in the presence of MgATP (0.5 mM), or incubated with Dm-spastin and DMSO in the absence of ATP, **F**. (**G**) Computational docking model for compound **2.5** bound to Dm-spastin. Potential hydrogen-bonding interactions between the aminopyrazole and the protein backbone are highlighted (dashed lines). Other key amino acids in Dm-spastin nucleotide-binding site are also shown. (**H**) Compound **2.5** concentration-dependent inhibition of the steady-state ATPase activity of three Dm-spastin constructs with mutations at variability hotspot residues. Graphs show average values ± s.d. (n = 3) fit to a sigmoidal dose-response equation. For comparison corresponding curve for Dm-spastin-WT is shown (dashed line, data from 2.5B). $IC_{50}$ values: Dm-spastin-WT: 0.1 ± 0.1 μM; -Q488V: 5.4 ± 1.2 μM; -N527C: 0.3 ± 0.1 μM and -T692A: 0.4 ± 0.1 μM; 0.5 mM MgATP; average ± s.d., n = 3. *Note - a subset of assays in this figure were performed by Dr Tommaso Cupido (postdoctoral fellow in the Kapoor lab).*

quinazoline core is buried in the adenine-binding pocket within van der Waals distance to the N-loop and P-loop variability hotspot residues, the piperazine group is proximal to the sensor-II helix, and the aminopyrazole group establishes a network of hydrogen-bonding interactions with the backbone of the N-loop (Figure 2.5G).

**Designing a selective inhibitor of human spastin.**

To develop a chemical probe for human spastin, we purified a recombinant form of human spastin (hereafter, Hs-spastin, Figure 2.6A, B). Hs-spastin had similar ATPase activity relative to Dm-spastin (Figure 2.6C) and was inhibited by compound **2.5**, albeit with reduced potency ($IC_{50}$ = 4.4 ± 2.1 μM, 1mM ATP; average ± s.d., n = 3; Figure 2.6D).

The inhibitor-Dm-spastin model suggests that the hydrogen at the 8-position of the quinazoline ring of compound **2.5** would be in close proximity to the N386 side chain in human spastin (equivalent to Dm-spastin N527; Figure 2.6E). An asparagine residue is rarely found at the P-loop variability hotspot position of AAA proteins (Table 2.1B). Therefore, we hypothesized that inhibitor potency and selectivity for spastin could be improved by optimizing the interaction with the N386 residue in Hs-spastin. We designed and synthesized an analog in which a pyrrolopyrimidine replaced the quinazoline core of compound **2.5**, as this would introduce an electropositive group in the position predicted to be proximal to the N386 side chain (compound **2.6**; Figure 2.6F). We found that compound **2.6** inhibited Hs-spastin with ~30-fold improved potency with respect to compound **2.5** (Figure 2.6D; $IC_{50}$ = 132 ± 55 nM, 1 mM ATP; average ±

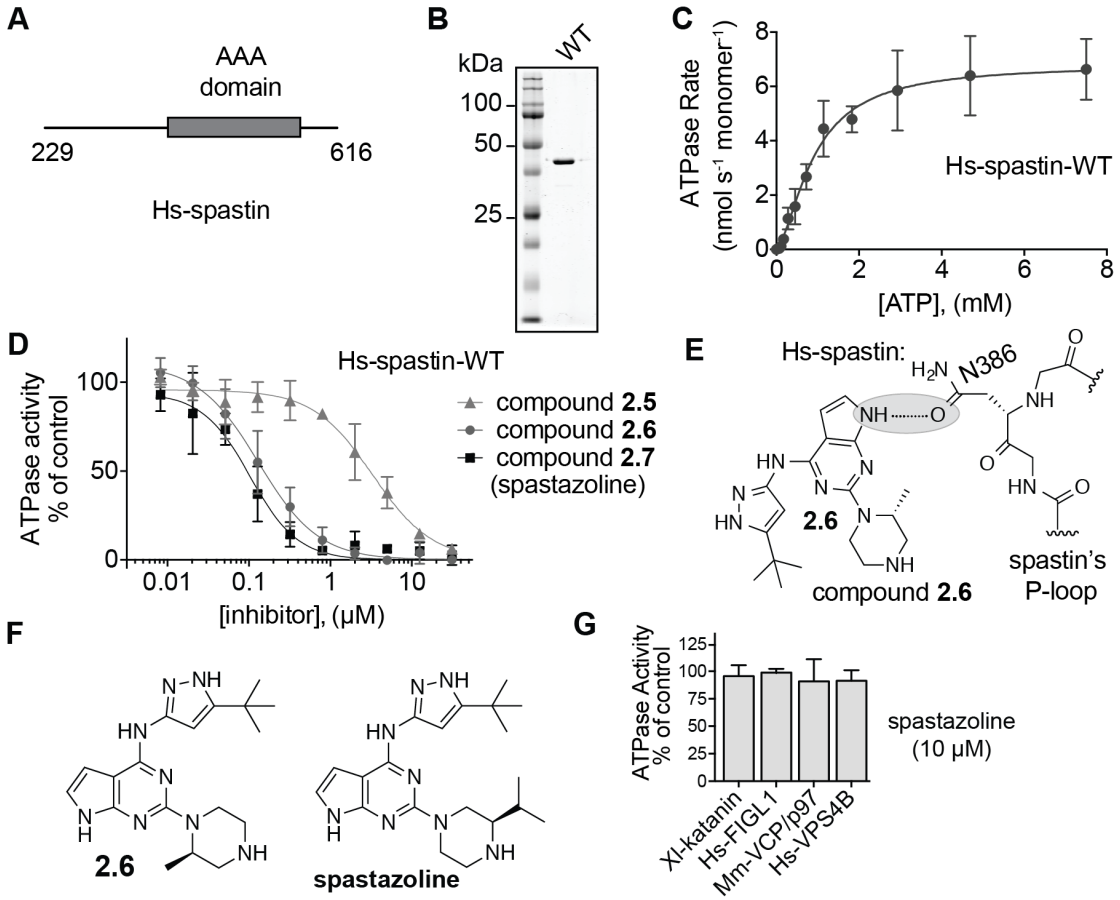


**Figure 2.6. Developing a potent and selective inhibitor of human spastin.**
(**A**) Schematic shows AAA domain (gray box, not to scale) and the first and last residues of the recombinant Hs-spastin wild-type construct. (**B**) SDS-PAGE analysis of purified recombinant wild-type (WT) Hs-spastin (Coomassie blue). (**C**) ATP concentration-dependence of the steady-state activity of the Hs-spastin WT construct analyzed using an NADH-coupled assay. Rates were fit to the Michaelis-Menten equation for cooperative enzymes and enzyme activity parameters were determined ($K_{1/2}$ = 0.9 ± 0.3 mM; $k_{cat}$ = 6.6 ± 1.8 $s^{-1}$; Hill coefficient = 1.6 ± 0.1, average ± range, n=2). (**D**) Concentration-dependent inhibition of the steady-state ATPase activity of the Hs-spastin construct by compounds **2.5**, **2.6**, and **2.7** (spastazoline). Graph shows values fit to a sigmoidal dose-response equation (average ± s.d., n = 3, 1 mM MgATP). $IC_{50}$ values (average ± s.d.; n = 3): compound **2.5**: 4.4 ± 2.1 μM; compound **2.6**: 132 ± 55 nM; spastazoline: 99 ± 18 nM. (**E**) The predicted model for compound **6** bound to spastin. (**F**) Chemical structures of compound **2.6** and spastazoline. (**G**) Percentage steady-state ATPase activity of four AAA proteins in the presence of spastazoline (10 μM, 0.5 mM MgATP; data represent average ± s.d., n = 3). *Note - a subset of assays in this figure were performed by Dr Tomasso Cupido, postdoctoral fellow in the Kapoor lab).*

s.d., n = 3). Computational docking analysis suggested two possible poses for compound **2.6** bound to spastin; however, a hydrogen-bonding interaction with the P-loop asparagine was possible in only one pose (Figure 2.7A).

As kinases are known targets of these chemical scaffolds (Statsuk et al., 2008), we examined the activity of compound **2.6** against 64 human kinases. We found that compound **2.6** inhibited only four of the 64 kinases by >50% at ~15-fold the $IC_{50}$ for Hs-spastin (2 μM, Table 2.4). To reduce off-target activity, we compared the binding modes of compound **2.6** to spastin and to kinases using available structural for data inhibitor-kinase interaction. We observed that the piperazine ring of compound **2.6** is likely to be buried in the interior of the kinase pocket but is facing the bulk solvent in our inhibitor–spastin model (Figure 2.7B). Therefore, we synthesized compound **2.7** (Figure 2.6D, F), hereafter named spastazoline, in which the 2-methyl in the piperazine group was modified to a 3-isopropyl group so as to increase steric hindrance when interacting with the kinase pocket without disrupting spastin binding. We found that spastazoline only inhibited one of the 65 kinases tested (NTRK1) by >50% (Table 2.4). Importantly, spastazoline potently inhibited Hs-spastin (Figure 2.6F; $IC_{50}$ = 99 ± 18 nM; average ± s.d.; n=3, 1mM ATP) and did not appreciably inhibit any of the related AAA proteins that we have characterized, including human VPS4B protein (10μM; Figure 2.6G). Together, these data suggest that spastazoline could be a useful chemical probe for human spastin if potential off-target effects can be systematically addressed.

We hypothesized that a mutation at N386 would disrupt the spastin–inhibitor interaction and confer resistance to spastazoline. We purified a recombinant Hs-spastin

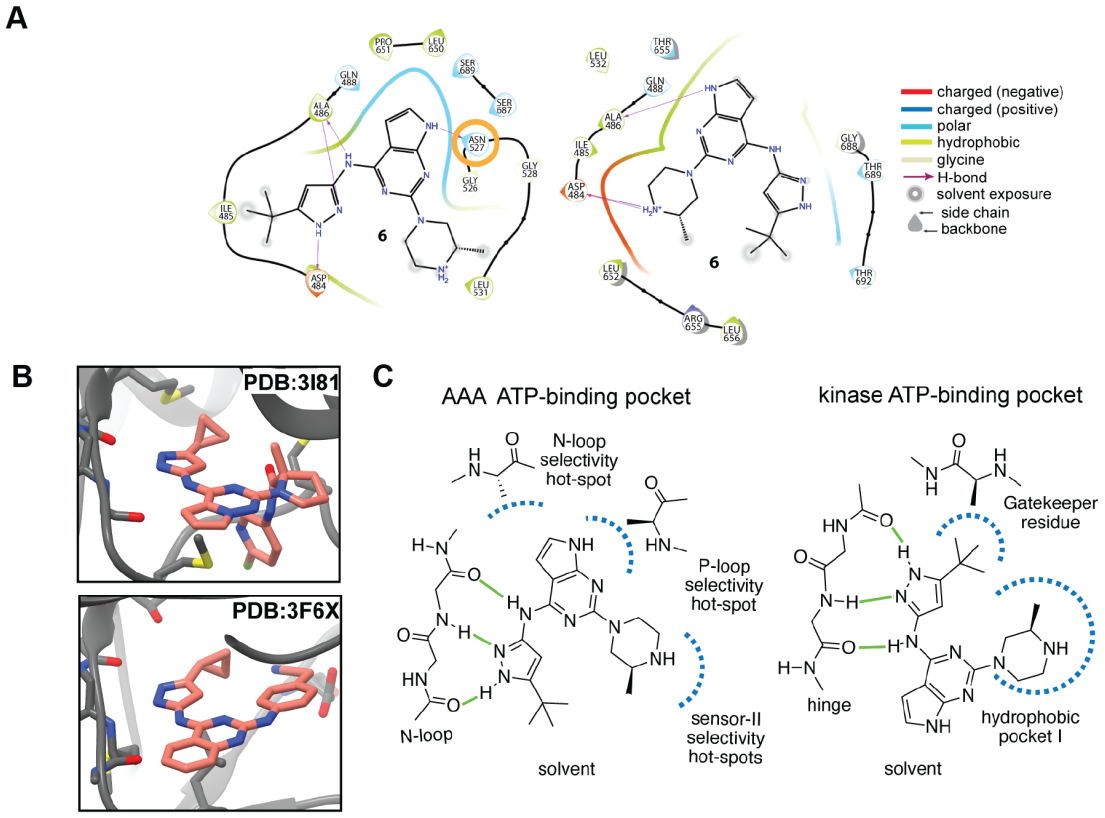


**Figure 2.7. Design of a potent Hs-spastin inhibitor.**

(**A**) Diagrams show two computational docking models for compound **2.6** bound to the Dm-spastin nucleotide-binding site. The protein residues within 3.0 Å of compound **2.6** and relevant compound-protein interactions are indicated (see legend in the figure). The position of the P-loop variability hot-spot residue is also shown (orange circle). (**B**) X-ray structural models for a 4-pyrazolyl, 2-substituted-triazine-based compound (top panel), and a 4-pyrazolyl, 2-substituted-quinazoline-based compound (bottom panel) bound to protein kinases (compounds: stick representations, carbon atoms in orange; kinase: ribbon and stick representations; PDB codes are indicated). (**C**) Schematics show likely orientations of compound **2.6** bound to AAA proteins (left) or kinases (right). Selected protein structural motifs that interact with the inhibitor are indicated. *Note - docking of compound **2.6** was performed by Dr Tommaso Cupido, postdoctoral fellow in Kapoor lab).*

| | ATP conc | Kinase | comp. 6 | comp. 7 |
|---|---|---|---|---|
| | µM | | | |
| 1 | 1000 | ABL1 | 9 | 1 |
| 2 | 1000 | AKT1 (PKB alpha) | 6 | 2 |
| 3 | 1000 | ALK | 11 | 4 |
| 4 | 1000 | AURKA (Aurora A) | -5 | 1 |
| 5 | 1000 | AURKB (Aurora B) | 0 | 6 |
| 6 | 1000 | AURKC (Aurora C) | - | 2 |
| 7 | 1000 | BTK | 10 | -3 |
| 8 | 1000 | CAMK2A (CaMKII alpha) | -2 | 6 |
| 9 | 1000 | CDK2/cyclin A | 1 | 3 |
| 10 | 1000 | CDK5/p25 | 1 | 1 |
| 11 | 1000 | CHEK1 (CHK1) | 8 | 1 |
| 12 | 1000 | CHEK2 (CHK2) | 40 | 1 |
| 13 | 1000 | CSF1R (FMS) | 20 | 19 |
| 14 | 1000 | CSNK1A1 (CK1 alpha 1) | -3 | 3 |
| 15 | 1000 | CSNK1G2 (CK1 gamma 2) | 1 | -2 |
| 16 | 1000 | CSNK2A2 (CK2 alpha 2) | -1 | 1 |
| 17 | 1000 | DYRK1A | 4 | 1 |
| 18 | 1000 | EGFR (ErbB1) | 4 | 0 |
| 19 | 1000 | EPHA2 | 1 | 0 |
| 20 | 1000 | FER | 8 | 5 |
| 21 | 1000 | FGFR1 | 17 | 16 |
| 22 | 1000 | FLT3 | 70 | 44 |
| 23 | 1000 | FLT4 (VEGFR3) | -2 | -1 |
| 24 | 1000 | FRAP1 (mTOR) | -3 | 2 |
| 25 | 1000 | GSK3A (GSK3 alpha) | 8 | 0 |
| 26 | 1000 | GSK3B (GSK3 beta) | 23 | 9 |
| 27 | 1000 | IKBKE (IKK epsilon) | 1 | -1 |
| 28 | 1000 | INSR | 5 | 9 |
| 29 | 1000 | IRAK4 | 10 | 10 |
| 30 | 1000 | JAK1 | 8 | 3 |
| 31 | 1000 | JAK2 | 6 | 1 |
| 32 | 1000 | KDR (VEGFR2) | 8 | 1 |
| 33 | 1000 | LCK | 15 | 2 |
| 34 | 1000 | LYN A | 14 | 7 |
| 35 | 1000 | MAP3K9 (MLK1) | 67 | 7 |
| 36 | 1000 | MAP4K4 (HGK) | 23 | 7 |
| 37 | 1000 | MAPK1 (ERK2) | -3 | 11 |
| 38 | 1000 | MAPK14 (p38 alpha) Direct | -4 | 8 |
| 39 | 1000 | MAPKAPK2 | 2 | 3 |
| 40 | 1000 | MARK1 (MARK) | 6 | 6 |
| 41 | 1000 | MET (cMet) | 13 | 4 |
| 42 | 1000 | MINK1 | 2 | 5 |
| 43 | 1000 | MST4 | -21 | -14 |
| 44 | 1000 | MYLK2 (skMLCK) | 2 | 3 |
| 45 | 1000 | NEK2 | 15 | 10 |
| 46 | 1000 | NTRK1 (TRKA) | 72 | 65 |
| 47 | 1000 | PAK4 | 13 | 5 |
| 48 | 1000 | PDK1 Direct | 14 | 1 |
| 49 | 1000 | PIM2 | 8 | 3 |
| 50 | 1000 | PRKACA (PKA) | 5 | 6 |
| 51 | 1000 | PRKCA (PKC alpha) | 9 | 10 |
| 52 | 1000 | PRKCA (PKC Beta I) | 20 | 2 |
| 53 | 1000 | PRKCD (PKC delta) | -1 | 8 |
| 54 | 1000 | PRKD2 (PKD2) | 8 | 4 |
| 55 | 1000 | ROCK1 | 4 | 1 |
| 56 | 1000 | RPS6KA1 (RSK1) | 31 | 16 |
| 57 | 1000 | RPS6KA2 (RSK3) | 59 | 16 |
| 58 | 1000 | RPS6KB1 (p70S6K) | 10 | 2 |
| 59 | 1000 | SGK (SGK1) | 12 | 0 |
| 60 | 1000 | SRC | 28 | 6 |
| 61 | 1000 | STK3 (MST2) | -3 | 3 |
| 62 | 1000 | TAOK2 (TAO1) | 31 | 11 |
| 63 | 1000 | TBK1 | 2 | 1 |
| 64 | 1000 | TEK (Tie2) | 12 | 1 |
| 65 | 1000 | TYK2 | 9 | 2 |

[compound] = 2 µM

< 30%

30 to 50%

> 50%

% Inhibition of control kinase activity

**Table 2.4. Activity of compound 2.6 and compound 2.7 against kinases.**

Heat-map for the inhibition of 64 human kinases by compounds **2.6** and **2.7** (2 µM). Heat map was constructed from average percent kinase activity inhibition values in the presence of the compound (n=2) normalized to DMSO control (see legend). To assess kinase activity we used the commercial Z'-LYTE platform (Thermofisher). ATP concentration in the kinase reactions was 1 mM, matching that used in all ATPase assays with Hs-spastin constructs.

construct with a N386C mutation (equivalent to the N527C mutation in Dm-spastin) and found that the ATPase activity of this mutant construct was comparable to that of wild-type Hs-spastin (Figure 2.8A,B,C). As predicted by our model, spastazoline inhibited Hs-spastin-N386C >100-fold less potently than the wild-type protein (Figure 2.8D). Additionally, we found that spastazoline did not appreciably stabilize the Hs-spastin-N386C mutant against thermal-induced denaturation ($\Delta T_m$: ~1.5°C at 200 μM; Figure 2.8E), whereas it considerably stabilized the wild-type construct ($\Delta T_m$: ~6.0°C; Figure 2.8E). Together, these data indicate that our approach not only led to a potent chemical inhibitor of spastin, but could also identify resistance-conferring mutations.

**Probing spastin function during cell division.**

To probe spastin cellular functions using spastazoline, we focused on the M87e4 spastin (containing the alternatively spliced exon 4), the most abundant spastin isoform in human cells (Claudiani et al., 2005) (Figure 2.9A). As the N386C mutation suppresses spastazoline binding in biochemical assays, we generated two HeLa cell lines in which enhanced green fluorescent protein (EGFP)-tagged spastin M87e4, either the wild-type (HeLa-WT) or mutant allele (HeLa-N386C), were introduced using the Flp-In T-REx system. We found that these transgenes were expressed at comparable levels (Figure 2.9B).

To examine spastin-dependent inhibitor-induced phenotypes, we focused on cell division. RNAi-mediated spastin knockdown has been shown to disrupt disassembly of

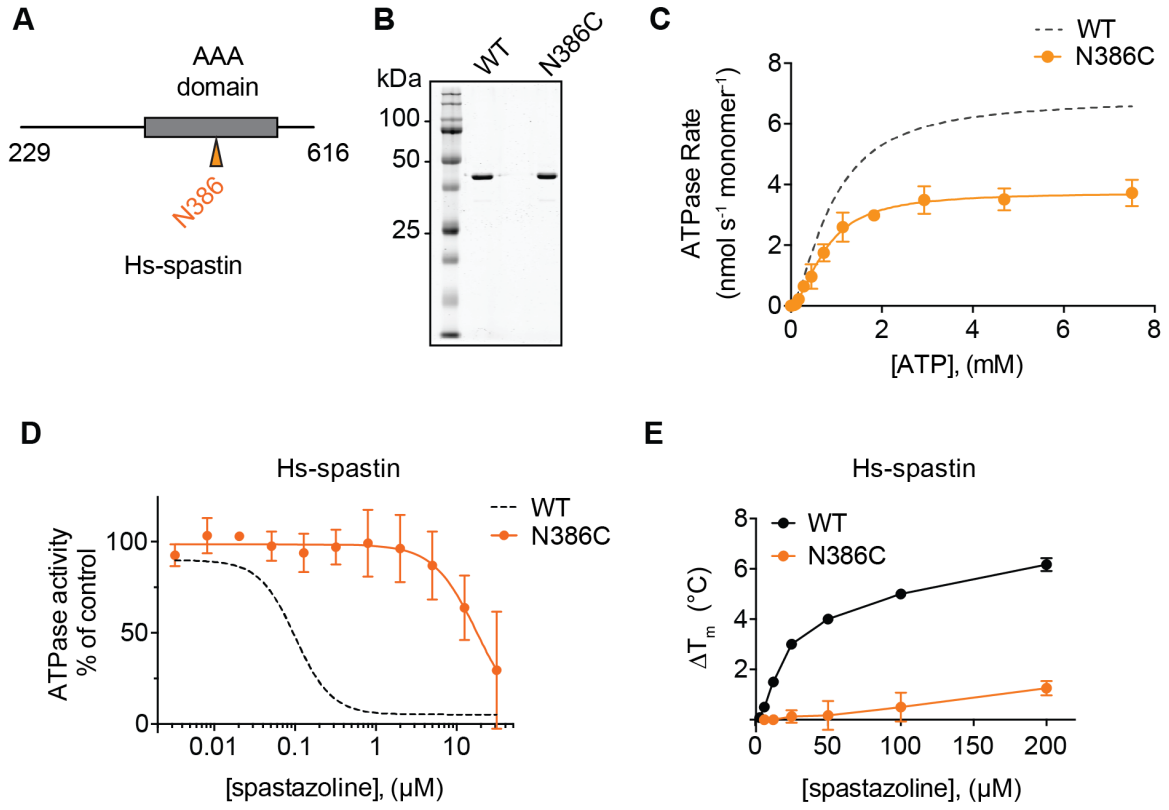


**Figure 2.8. Characterizing human spastin allele with a mutation in the P-loop variability hotspot residue (N386C).**

(**A**) Schematic shows AAA domain (gray box, not to scale) and the first and last residues of the recombinant Hs-spastin N386C mutant construct. The position of the N386C mutation is indicated with an orange arrow. (**B**) SDS-PAGE analysis of purified recombinant wild-type (WT) and N386C Hs-spastin (Coomassie blue). (**C**) ATP concentration-dependence of the steady-state activity of the Hs-spastin N386C construct analyzed using an NADH-coupled assay. Rates were fit to the Michaelis-Menten equation for cooperative enzymes and enzyme activity parameters were determined ($K_{1/2}$ = 0.7 ± 0.3 mM; $k_{cat}$ = 3.7 ± 0.9 $s^{-1}$; Hill coefficient = 1.9 ± 0.1, average ± range, n=2). (**D**) Concentration-dependent inhibition of the steady-state ATPase activity of an Hs-spastin mutant construct (N386C). Graph shows values fit to a sigmoidal dose-response equation (average ± s.d., n = 3; 1 mM MgATP). For comparison, the curve corresponding to the data for the wild-type Hs-spastin is shown (WT, dashed line; data from 2.6D). (**E**) Concentration-dependent effect of spastazoline on the heat-induced unfolding ($\Delta T_m$) of Hs-spastin WT and N386C mutant constructs analyzed using differential scanning fluorimetry (average ± s.d., n = 3). *Note - a subset of assays in this figure were performed by Dr Tommaso Cupido, postdoctoral fellow in Kapoor lab).*

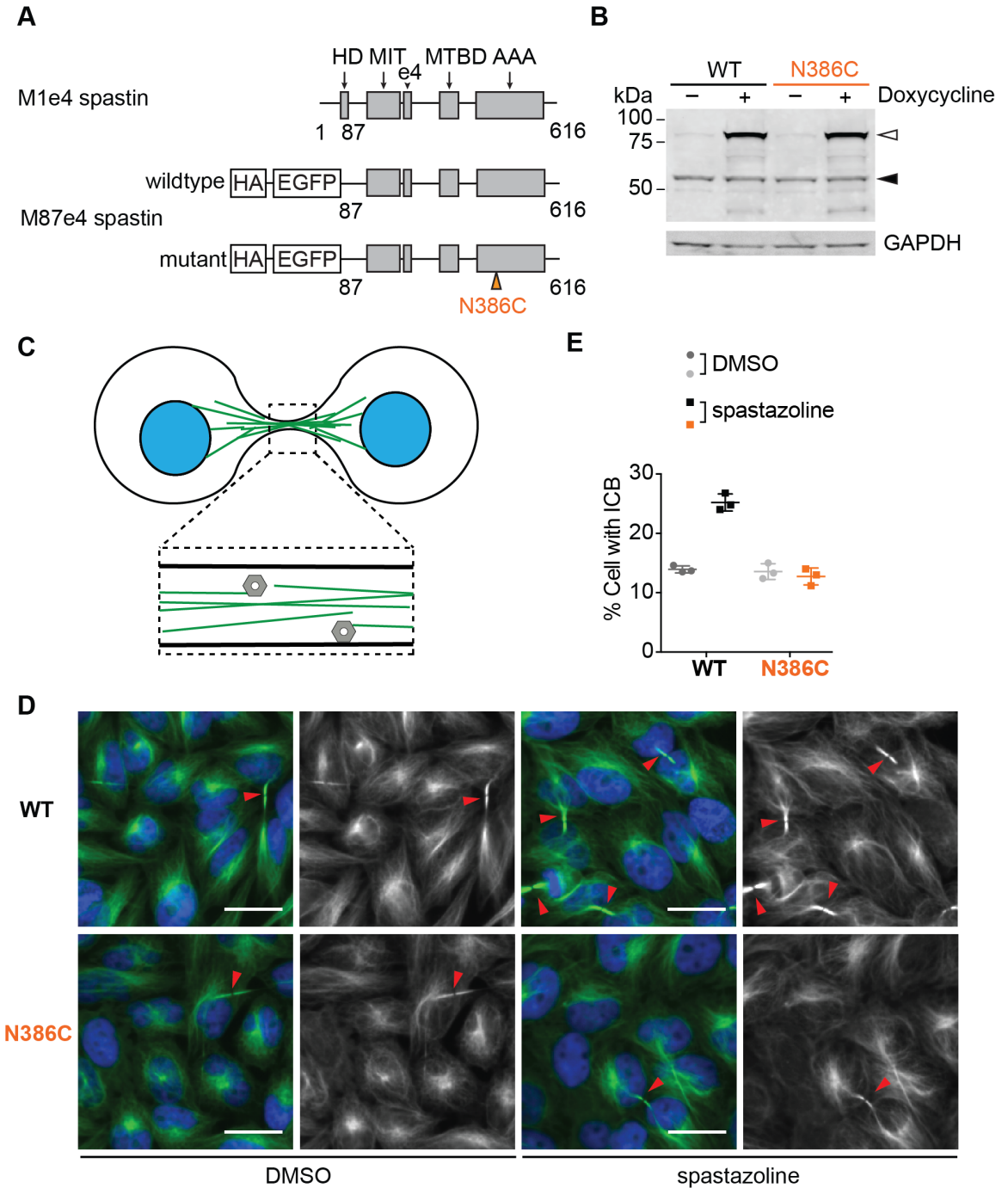


**Figure 2.9. Using spastazoline and a cognate resistance-conferring mutation to probe spastin function in cell division.**

**Figure 2.9. Using spastazoline and a cognate resistance-conferring mutation to probe spastin function in cell division.**

(**A**) Schematics for the spastin M1e4 and M87e4 isoforms. Structural domains, along with the mutation (orange arrow) and tags for the M87e4 isoform expressed in HeLa cells are indicated (not to scale). (**B**) Immunoblot analysis of HeLa cells expressing wild-type (WT) or N386C mutant (N386C) spastin M87e4 constructs. Doxycycline (1 μg/mL, 24 hours) was used to induce expression and blots were stained for spastin and GAPDH (loading control). The positions of the bands expected for the GFP-spastin constructs and the endogenous spastin (outlined and black arrows, respectively) are indicated. (**C**) Schematic for an intercellular bridge (DNA, blue; microtubules, green; spastin, gray). (**D**) Representative images of fixed, doxycycline-induced HeLa-WT and -N386C cells treated with DMSO (0.1%) or spastazoline (10 μM) for 4.5 hours, and stained for acetylated tubulin. Arrows indicate intercellular bridges. Scale bar = 10 μm. (**E**) Percentage of cells with an intercellular bridge observed in fixed HeLa-WT and N386C cells treated with DMSO (0.1%) or spastazoline (10 μM) for 4.5 h (data represent average ± s.d., n = 3; >2,500 cells analyzed per condition). *Note - a subset of assays in this figure were performed by my collaborators in the Kapoor lab, Dr Tommaso Cupido and Megan E Kelley.*

the intercellular bridge, a membrane- and microtubule-based structure that connects daughter cells during the final stage of cell division (Connell et al., 2009) (Figure 2.9C). To readily identify intercellular bridges, which are enriched in tubulin post-translational modifications associated with stable microtubules, we imaged acetylated tubulin using immunofluorescence microscopy (Figure 2.9D). Treating HeLa-WT cells with spastazoline for 4.5h (10μM) resulted in a ~2-fold increase in the number of cells with intercellular bridges compared with DMSO control (25.2 ± 1.4% versus 13.9 ± 0.6%; n=3, average ± s.d.; Figure 2.9E). Importantly, in HeLa-N386C treated with spastazoline, the number of cells with an intercellular bridge was similar to that observed in the DMSO control (13.6 ± 1.4% versus 12.7 ± 1.3%, n=3; average ± s.d.; Figure 2.9E). Together, these data indicate that spastazoline inhibits intercellular bridge disassembly by interfering with spastin activity, as the inhibitor-dependent phenotype was observed in wild-type cells but not in cells expressing the inhibitor resistance-conferring allele of spastin.

**Discussion.**

Here we report the design of spastazoline, an ATP-competitive chemical inhibitor of human spastin. We also identify a cognate resistance-conferring mutation in human spastin that, together with spastazoline, can be used to probe spastin's function in dynamic cellular processes.

Current models indicate that spastin and the endosomal sorting complex required for transport ESCRT-III, to which spastin binds (Yang et al., 2008), coordinate

microtubule disassembly with membrane constriction and fusion events during nuclear envelope reformation (Olmos et al., 2015; Vietri et al., 2015). Our data suggest that inhibition of spastin activity probably suppresses microtubule severing and thereby impairs spastin dissociation and the loss of ESCRT-III from the sites of membrane constriction. RNAi-based knockdown of VPS4 or the ESCRT-III protein, CHMP2A, results in DNA damage associated with compromised nuclear envelope integrity (Vietri et al., 2015). Consistent with these observations, we suggest that disrupting spastin activity could also result in DNA damage due to defects in cell division.

Cells depleted of spastin also show defects in the assembly, maintenance, and dynamics of intracellular membrane organelles such as endosomes and lysosomes (Allison et al., 2013, 2017). As the effects of chronic spastin depletion probably accumulate over several hours, the ability to control spastin activity on much faster timescales with spastazoline would be useful to examine intracellular trafficking of membrane organelles. Mutations in the spastin gene are linked to inherited neurodegenerative conditions called hereditary spastic paraplegias (Blackstone et al., 2011), and targeting spastin has been proposed as a therapeutic strategy for Alzheimer's disease (Zempel et al., 2013). In post-mitotic neurons, DNA damage associated with spastin inhibition is not likely, and therefore pharmacological inhibition of spastin in models for neurodegenerative diseases should be further explored. Spastazoline is also likely to be a valuable tool for these studies.

A critical step in our inhibitor-design approach is identifying amino acids in the target protein that can be mutated to alter the shape and electrostatics of the

inhibitor-binding site, without substantially disrupting the protein's activity. In the case of spastin, we find that variability hotspot residues in the nucleotide-binding pocket can be swapped to introduce mutations to generate alleles that retain biochemical activity. Variability hotspot mutations that reduce inhibitor potency are likely to identify direct inhibitor–target interactions and can be used to optimize compound potency and selectivity. Testing compounds against wild-type and mutant alleles can help select the most likely inhibitor–target binding mode from the solutions yielded by computational docking methods.

In principle, the mutagenesis-based approach we used to develop spastazoline could help design inhibitors of targets for which high-resolution structural data for inhibitor–protein interactions are not readily available, or the inhibitor-bound conformation states are not known. Additional studies will be needed to determine whether variability hotspot residues can be identified and swapped to design functionally silent mutations for protein–protein interactions or other nonenzymatic sites that can be targeted by chemical inhibitors.

## Chapter 2 - Methods.

### Plasmids.

*Homo sapiens* spastin vector for expression in HeLa cells.

Hs-spastin can be expressed as at least four isoforms (M1 with exon 4, M1 without exon 4, M87 with exon 4, and M87 without exon 4) (Mancuso and Rugarli, 2008). The wild-type (WT, isoform M87 with exon 4, with N-terminal HA- and EGFP-tags) spastin plasmid used to generate cell lines was a gift from C. Campsteijn (Oslo University Hospital). Wild-type and mutant spastin M87e4 open reading frames were subcloned into the pcDNA-5.0/FRT/TO vector (ThermoFisher) using HindIII and NotI restriction sites.

*Homo sapiens* spastin vector for expression in bacteria.

The complementary DNA sequence for Hs-spastin (residues 229–616, numbered according to NCBI RefSeq: NP_055761.2) used for protein expression in *E.coli* was PCR amplified from the ORFeome collection (Dharmacon) and cloned into a pGEX-6P1 vector using BamHI and NotI restriction sites.

*Drosophila melanogaster* spastin vector.

The vector (pDEST15-spastin-D.melanogaster) used for Dm-spastin expression was a gift from A. Roll-Mecak (NIH) and had been previously used in (Roll-Mecak and Vale, 2008).

We note that in this construct, consisting of residues 209–758, there is a deletion at residues 311–372 (corresponding to exon 3 of *Drosophila* spastin). However, the overall

residue numbering used is that for full-length Dm-spastin isoform A (Uniprot: Q8I0P1), as in previous publications (Roll-Mecak and Vale, 2008).

*Xenopus laevis* katanin vector.

MAL-c5x-X.laevis p60 (full length, NCBI RefSeq: NP_001084226.1) was a gift from R. Heald (UC Berkeley).

*Mus musculus* VCP/p97 vector.

pQE9-His-p97 (identical to Homo sapiens VCP protein, full length, NCBI RefSeq: NP_009057.1, Ile206Val variant) was obtained from Addgene (G. Warren, plasmid #14666).

*Homo sapiens* FIGL1 vector. The cDNA for Hs-FIGL1 (residues 288–674, NCBI RefSeq: NP_001036227.1) was PCR amplified from the ORFeome collection and cloned into a pDEST15 vector using the ApaI site and InFusion technology (Clontech).

*Homo sapiens* VPS4B vector.

The cDNA for the sequence Hs-VPS4B (full length, NCBI RefSeq: BC039574.1) was PCR amplified from the ORFeome collection and cloned using the NdeI and EcoRI restriction sites into a pET-SUMO vector (gift from Dr. Chris Lima, MSKCC).

Vectors for mutant constructs were generated by site-directed mutagenesis (QuikChange XL Kit, Agilent, catalog no. 200517). Incorporation of the desired mutations was verified by Sanger sequencing.

**Cell lines, cell culture, and viability analyses.**

Cells expressing wild type- or mutant-tagged spastin M87e4 were generated using the T-REx HeLa Flp-In cell line according to the vendor's protocols (ThermoFisher). Genomic DNA was extracted from cells using the DNeasy Blood and Tissue kit (Qiagen), insertions were PCR amplified and sequenced. Cells were cultured in DMEM (ThermoFisher) supplemented with 10% (v/v) FBS (Sigma-Aldrich), l-glutamine (2 mM; Thermo Fisher), hygromycin B (250 µg/ml) and blasticidin (20 µg/ml) at 37 °C and 5% $CO_2$. Cells were confirmed to be mycoplasma free using a PCR-based method (Uphoff and Drexler, 2013). For western blotting, cells were cultured with or without doxycycline (1 µg/ml for 24 h) before lysis at 4 °C. The following antibodies were used: mouse monoclonal anti-spastin (1:750; Sp6C6; Abcam) and goat polyclonal anti-GAPDH (control, 1:1,000; V-18; Santa Cruz). Membranes were imaged using a LI-COR Odyssey Infrared Imager.

**Microscopy.**

Immunofluorescence analyses. Cells were plated on acid-washed coverslips (#1.5; Fisher brand catalog no. 12-545-81) coated with poly-d-lysine hydrobromide (Sigma, catalog no. P6407) and cultured for 24–48 h before fixation. For intercellular bridge analyses, spastin expression was induced (1 µg/ml doxycycline for ~24 h), and cells were treated with 10 µM spastazoline or 0.1% DMSO (solvent control) for 4.5 h and then fixed at 37 °C, using 0.5% (w/v) glutaraldehyde in PBS for 10 min. Coverslips were washed with PBS, incubated with a solution of 0.1% $NaBH_4$ for 10 min, and

blocked (blocking buffer: 2% bovine serum albumin, 0.1% (w/v) sodium azide, and 0.1% Triton X-100 in Tris-buffered saline) for 60 min. Cells were stained with mouse monoclonal anti-acetylated tubulin (Sigma catalog no. T7451; 1:1,000 dilution) for 2 h and with Texas-Red conjugated anti-mouse secondary antibody (Jackson Immunoresearch; catalog no. 715-075-020; 1:2,000 dilution) for 60 min. DNA was stained with Hoechst 33342 (ThermoFisher, catalog no. H1399).

For intercellular bridge quantification, 5x5 fields of view were acquired using a Nikon TE2000 microscope with a 40x objective (Plan Fluor, 0.6 NA) and stitched together into ~905 $\mu m^2$ images using NIS-Elements. The number of cells and intercellular bridges were detected manually.

For microtubule staining, cells were treated with 10 µM spastazoline or 0.1% DMSO (solvent control) for 4 h and then fixed at 37 °C using 4% formaldehyde in 100 mM PIPES, 10 mM EGTA, 1 mM MgCl2, and 0.2% Triton X-100, pH 6.9 for 10 min. Coverslips were blocked (blocking buffer) for 45 min before staining with anti-α-tubulin-FITC antibody (DM1A, Sigma, catalog no. F2168; 1:2,000 dilution). Confocal fluorescence images were acquired as Z-stacks with 0.3 µm step size using a Nikon TE2000 microscope with a 100x objective (Plan Apo, 1.45 NA).

**Biochemical assays.**

*Recombinant protein expression.*

Recombinant proteins were expressed in *Escherichia coli* Rosetta (DE3) pLysS cells (Merck, catalog no. 70954) grown in Miller's LB medium (LMM, Formedium, catalog no.

LMM105). For all constructs, protein expression was induced at $O.D._{600}$ = 0.6-0.8 with 0.5 mM IPTG (Goldbio). The cultures were grown at 18 °C for 12-16 h, pelleted, and resuspended in lysis buffer (buffer A, see below). All subsequent purification steps were performed at 4 °C. Cell lysis was carried out using an Emulsiflex-C5 homogenizer (Avestin, 5–6 cycles at 10,000–15,000 psi). The homogenized lysate was centrifuged at 40,000 r.p.m. for 45–60 min using a Ti45 rotor in a Beckman Coulter Optima LE-80K ultracentrifuge. All recombinant proteins were purified using multistep strategies, involving combinations of affinity, ion exchange, and size-exclusion chromatography. Specific buffers and purification conditions, optimized for yield and specific activity, are summarized.

*Dm-spastin wild type and mutants.*

Buffer A: PBS, 10 mM $MgCl_2$, 1 mM PMSF, 20 U/ml benzonase, and cOmplete EDTA-Free Protease Inhibitor Cocktail.

Buffer B1: 50 mM Tris–HCl, 500 mM KCl, 10 mM $MgCl_2$, 5 mM DTT, pH 7.5.

Buffer B2: 50 mM Tris–HCl, 300 mM NaCl, 10 mM $MgCl_2$, 5 mM DTT, 20 mM reduced glutathione, pH 8.0.

Buffer C: 50 mM Na-MES, 10% (w/v) glycerol, 10 mM $MgCl_2$, 5 mM DTT, pH 6.5.

Buffer D: 50 mM Na-MES, 2 M NaCl, 10% (w/v) glycerol, 10 mM $MgCl_2$, 5 mM DTT, pH 6.5.

Buffer E: 20 mM K-HEPES, 300 mM NaCl, 10 mM $MgCl_2$, 5 mM DTT, 15% (w/v) glycerol, pH 7.5.

Prep conditions. Briefly, the clarified lysate containing GST-Dm-spastin was incubated with a GSTrap 4B matrix (GE Healthcare) and eluted in Buffer B2. The protein solution was incubated with PreScission protease (0.1 mg ml−1) for 8–12 h, diluted 1:2.5 with Buffer C and loaded into a CaptoS cation exchange column (GE Healthcare) equilibrated in 95% Buffer C and 5% Buffer D. Fractions eluted from the ion exchange chromatography column were pooled, concentrated tenfold with an Amicon Ultra 30K MWCO centrifugal filter, and further purified over a 16/60 Superdex 200 column (GE Healthcare) in Buffer E. The eluate containing purified spastin was pooled, concentrated using an Amicon Ultra 30K MWCO centrifugal filter to at least 1 mg/ml and stored at -80 °C. PreScission cleavage left six nonnative residues at the N terminus (GPQGSK).

*Hs-spastin wild type and N386C mutant.*

Buffer A: PBS, 10 mM $MgCl_2$, 10 mM DTT, 1 mM PMSF, 5 U/ml benzonase, and cOmplete EDTA-Free Protease Inhibitor Cocktail, pH 7.4.

Buffer B: 50 mM K-HEPES, 250 mM KCl, 5 mM $MgCl_2$, 5 mM DTT, 0.1 mM PMSF, 0.005% (v/v) Triton X-100, pH 7.5.

Buffer C: 50 mM Na-MES, 10% (w/v) glycerol, 5 mM $MgCl_2$, 5 mM DTT, pH 6.5.

Buffer D: 50 mM Na-MES, 2 M NaCl, 10% (w/v) glycerol, 5 mM $MgCl_2$, 5 mM DTT, pH 6.5.

Prep conditions. Briefly, the clarified lysate containing GST-Hs-spastin was incubated with a GSTrap 4B matrix (GE Healthcare) and eluted in Buffer B supplemented with 20 mM reduced glutathione. The protein solution was incubated with PreScission protease (0.1 mg/ml) for 10-12 h, diluted 1:2 with Buffer C and loaded into a CaptoS cation

exchange column (GE Healthcare) equilibrated in 93% Buffer C and 7% Buffer D. Fractions eluted from the ion exchange chromatography column were pooled and concentrated tenfold with an Amicon Ultra 50K MWCO centrifugal filter. The protein solution was centrifuged at 20,000g for 15 min, and the soluble fraction was stored at -80 °C. PreScission cleavage left five nonnative residues at the N terminus (GPLGS).

*GST-FIGL1 (Hs-FIGL1).*

Hs-FIGL1 protein used for measurement of kinetic parameters was obtained by the following procedure (Method 1):

Buffer A: 25 mM Tris–HCl, 300 mM NaCl, 5 mM $MgCl_2$, 5 mM DTT, 1 mM PMSF, 0.01% (v/v) Triton X-100, and cOmplete EDTA-Free Protease Inhibitor Cocktail, pH 8.0.

Buffer B1: 25 mM Tris–HCl, 300 mM NaCl, 5 mM $MgCl_2$, 5 mM DTT, 0.4 mM PMSF, 0.01% (v/v) Triton X-100, pH 8.0.

Buffer B2: 25 mM Tris–HCl, 150 mM NaCl, 5 mM $MgCl_2$, 5 mM DTT, 10 mM reduced glutathione, pH 8.

Buffer C: 25 mM Tris–HCl, 75 mM NaCl, 5 mM $MgCl_2$, 5 mM DTT, pH 8.5.

Buffer D: 25 mM Tris– HCl, 500 mM NaCl, 5 mM $MgCl_2$, 5 mM DTT, pH 8.5.

Buffer E: 25 mM Tris–HCl, 150 mM NaCl, 5 mM $MgCl_2$, 5 mM DTT, 5% (w/v) glycerol, pH 7.5

Prep conditions. The clarified lysate from cells expressing GST-FIGL1 was loaded onto GSTrap 4B (GE Healthcare), washed with Buffer B1 and then Buffer D, and finally eluted with Buffer B2. Fractions containing the proteins were pooled, diluted with 1 volume of Buffer C, and loaded on a MonoQ 5/50 GL column (GE Healthcare),

equilibrated in 95% Buffer C and 5% Buffer D. The protein fractions were pooled, concentrated tenfold using an Amicon Ultra 50K MWCO centrifugal filter, and further purified over a 10/300 Superdex 200 column (GE Healthcare) in Buffer E. Fractions from size-exclusion column were concentrated to a minimum of 1 mg/ml using an Amicon Ultra 30K MWCO centrifugal filter, and stored at -80 °C.

Method 2: Buffer A: 50 mM Tris–HCl, 150 mM NaCl, 5 mM $MgCl_2$, 10 mM DTT, 0.1 mM PMSF, 0.01% (v/v) Triton X-100, 5 U/ml benzonase, and cOmplete EDTA-Free Protease Inhibitor Cocktail, pH 8.0.

Buffer B1: 25 mM Tris–HCl, 300 mM NaCl, 5 mM $MgCl_2$, 5 mM DTT, 0.1 mM PMSF, 0.01% (v/v) Triton X-100, pH 8.0.

Buffer B2: 25 mM Tris–HCl, 150 mM NaCl, 5 mM $MgCl_2$, 5 mM DTT, 10 mM reduced glutathione, pH 8.0. Buffer C: 25 mM Tris–HCl, 75 mM NaCl, 5 mM $MgCl_2$, 5 mM DTT, pH 8.5.

Buffer D: 25 mM Tris–HCl, 1 M NaCl, 5 mM $MgCl_2$, 5 mM DTT, pH 8.5.

Buffer E: 25 mM Tris–HCl, 150 mM NaCl, 5 mM $MgCl_2$, 5mM DTT, 5% (w/v) glycerol, pH 7.5.

Prep conditions. The clarified lysate from cells expressing GST-FIGL1 was incubated with sepharose glutathione beads (GE Healthcare) for 1 h, washed with Buffer B1 and eluted with Buffer B2. Fractions containing the protein were pooled, diluted with three volumes of Buffer C, and loaded on a MonoQ 5/50 GL column (GE Healthcare), equilibrated in 95% Buffer C and 5% Buffer D. The protein fractions were pooled,

concentrated tenfold using an Amicon® Ultra 50K MWCO centrifugal filter, and further purified over a 10/300 Superdex 200 column (GE Healthcare) in Buffer E. Fractions from size-exclusion column were concentrated to a minimum of 1 mg/ml using an Amicon Ultra 30K MWCO centrifugal filter, and stored at -80 °C. Hs-FIGL1 protein used for testing inhibitors was obtained with method 1 or method 2. We note that protein purity and ATPase activity were comparable between the methods (data not shown).

*MBP-katanin (Xl-katanin).*

Buffer A: 20 mM Tris–HCl, 250 mM NaCl, 5 mM $MgCl_2$, 100 µM ATP, 5 mM DTT, 10% (w/v) glycerol, 1 mM PMSF, and cOmplete EDTA-Free Protease Inhibitor Cocktail, pH 7.5.

Buffer B: 20 mM Tris–HCl, 250 mM NaCl, 5 mM $MgCl_2$, 100 µM ATP, 5 mM DTT, 10% (w/v) glycerol, pH 7.5.

Buffer C: 20 mM Tris–HCl, 50 mM NaCl, 1 mM $MgCl_2$, 5 mM DTT, 100 µM ATP, 10% (w/v) glycerol, pH 7.5.

Buffer D: 20 mM Tris–HCl, 500 mM NaCl, 5 mM $MgCl_2$, 5 mM DTT, 100 µM ATP, 10% (w/v) glycerol, pH 7.5.

Buffer E: 20 mM Na-HEPES, 250 mM NaCl, 5 mM $MgCl_2$, 5 mM DTT, 10% (w/v) glycerol, pH 7.5.

Prep conditions. The clarified lysate from cells expressing MBP-katanin was loaded onto an MBP trap column (GE Healthcare). The column was washed with 30 column volumes of Buffer B and eluted with a Buffer B supplemented with 10 mM maltose. The eluate was diluted 1:2 with Buffer C and loaded on a 16/60 MonoQ GL ion exchange

column and eluted with a gradient of Buffer D. Combined MonoQ fractions were further purified on a 10/300 Superdex 200 gel filtration column in Buffer E. The fractions containing purified MBP-katanin protein were frozen in liquid nitrogen and stored at -80°C.

*Mouse VCP/p97 (Mm-VCP).*

Mm-VCP protein used for measurement of kinetic parameters was obtained by the following procedure (Method 1):

Buffer A: 25 mM K-HEPES, 500 mM KCl, 20 mM imidazole, 2 mM DTT, 5 U/ml benzonase, and cOmplete EDTA-Free Protease Inhibitor Cocktail, pH 8.0.

Buffer B: 25 mM K-HEPES, 500 mM KCl, 20 mM imidazole, 2 mM DTT, pH 8.0.

Buffer C: 25 mM K-HEPES, 500 KCl, 1 mM $MgCl_2$, 2 mM DTT, 500 mM imidazole, pH 7.5.

Buffer D: 25 mM K-HEPES, 250 mM KCl, 1 mM $MgCl_2$, 2 mM DTT, pH 7.5.

Prep conditions. The clarified lysate from cells expressing His6-VCP/p97 was incubated with Ni-NTA beads (Qiagen) for ~40 min, and the beads were extensively washed using Buffer B. The protein was eluted with Buffer C. Fractions containing the protein were concentrated using an Amicon Ultra 50K MWCO centrifugal filter, and the concentrated protein sample was filtered through a 0.22-µm Millex-GP PES membrane and loaded on a 10/300 Superose 6 column (GE Healthcare) in Buffer D. Fractions from the size-exclusion column were concentrated using an Amicon Ultra 50K or 100K MWCO centrifugal filter, and the concentrated protein sample was stored at -80 °C.

Method 2: Buffer A: 50 mM Tris–HCl, 400 mM NaCl, 2 mM $MgCl_2$, 20 mM imidazole, 1 mM ATP, 2 mM tris(2-carboxyethyl)phosphine (TCEP), 0.025% (v/v) Triton X-100, and cOmplete EDTA-Free Protease Inhibitor Cocktail, pH 7.5 (at 25 °C).

Buffer B: 50 mM Tris–HCl, 300 mM NaCl, 40 mM imidazole, 5 mM $MgCl_2$, 1 mM TCEP, 0.01% (v/v) Triton X-100, pH 7.5 (at 25 °C).

Buffer C: 50 mM Na-HEPES, 100 mM NaCl, 5 mM $MgCl_2$, 1 mM TCEP, pH 7.5 (at 25°C).

Buffer D: 50 mM Na-HEPES, 1 M NaCl, 5 mM $MgCl_2$, 1 mM TCEP, pH 7.5 (at 25 °C).

Buffer E: 50 mM Na-HEPES, 300 mM NaCl, 5 mM $MgCl_2$, 1 mM TCEP, pH 7.5 (at 25°C).

Prep conditions. The clarified lysate in buffer A from cells expressing His6-VCP/p97 was incubated with Ni-NTA beads (Qiagen) for ~40 min, and the beads were extensively washed with Buffer B. The protein was eluted with Buffer B supplemented with 500 mM imidazole. Eluted fractions were pooled and dialyzed in Buffer C. After dialysis, the protein was loaded onto a MonoQ column 5/50 GL (GE Healthcare) and fractioned over a gradient with Buffer D. Protein was eluted at approximately 350 mM NaCl. Combined MonoQ fractions were concentrated using an Amicon Ultra 50K MWCO centrifugal filter, and the concentrated protein sample was filtered through a 0.22-µm Millex-GP PES membrane before loading onto a 10/300 Superdex 200 column (GE Healthcare) equilibrated in Buffer E. Fractions from the size-exclusion column were concentrated using an Amicon Ultra 50K or 100K MWCO centrifugal filter, and the concentrated protein sample was mixed with 15% (w/v) glycerol and stored at -80 °C. Mm-VCP/p97

protein used for testing inhibitors was obtained with method 1 or method 2. We note that protein purity and ATPase activity were comparable between the methods (data not shown).

*6XHis-SUMO-VPS4B (Hs-VPS4B).*

Buffer A: 20 mM Na-HEPES, 500 mM NaCl, 2 mM $MgCl_2$, 10% (w/v) glycerol, 0.5 mM DTT, 1 mM PMSF, 1 mM ATP, and cOmplete EDTA-Free Protease Inhibitor Cocktail, pH 7.6.

Buffer B1: 20 mM Na-HEPES, 500 mM NaCl, 2 mM $MgCl_2$, 0.5 mM DTT, 1 mM PMSF, 1 mM ATP, 15 mM imidazole, pH 7.6.

Buffer B2: 20 mM Na-HEPES, 500 mM NaCl, 2 mM $MgCl_2$, 0.5 mM DTT, 1 mM PMSF, 1 mM ATP, 400 mM imidazole, pH 7.6.

Buffer C: 25 mM Na-HEPES, 2 mM MgCl2, 1 mM DTT, pH 7.6.

Buffer D: 25 mM Na- HEPES, 1 M NaCl, 2 mM $MgCl_2$, 1 mM DTT, pH 7.6.

Buffer E: 50 mM Na-HEPES, 150 mM NaCl, 3 mM $MgCl_2$, 2 mM DTT, pH 7.6.

Prep Conditions. The clarified lysate from cells expressing 6xHIS-SUMO-VPS4B was incubated with Ni-NTA beads for 1 h, and the beads were washed with 10 volumes of Buffer A and then 10 volumes of Buffer B1, and eluted with 10 volumes of Buffer B2. The protein-containing solution was diluted with 2.5 volumes of diluted Buffer A (1:1 in $H_2O$), loaded onto a MonoQ column 5/50 GL (GE Healthcare) equilibrated in Buffer C, and fractioned over a gradient with Buffer D. Combined MonoQ fractions were concentrated using an Amicon Ultra 30K MWCO centrifugal filter, and the concentrated protein sample was filtered through a 0.22-μm Millex-GP PES membrane before loading

onto a 10/200 Superdex 200 column (GE Healthcare) equilibrated in Buffer E. Fractions from size-exclusion column were concentrated using an Amicon Ultra 30K MWCO centrifugal filter and concentrated protein sample was mixed with 10% (w/v) glycerol and stored at -80 °C.

**Analyses of ATPase activity.**

Steady-state ATPase activity of AAA proteins was determined using the NADH-coupled assay. For all analyses, the time course of fluorescence decrease was measured using a Synergy NEO Microplate Reader ($\lambda_{ex}$ = 340 nm, 440 nm emission filter). Fluorescence values were plotted against time and fit by linear regression to obtain a rate of fluorescence decrease. The ATPase rate was calculated from rates of fluorescence decrease using ADP calibration curve. Percent inhibition of the ATPase activity was calculated by normalizing the rate of fluorescence decrease in the presence of compounds to DMSO control. GSK923295 compound stocks were made using DMSO. The rate from a control reaction with no ATP (background rate of fluorescence decrease) was subtracted from all rates. The assay buffers (listed below) were based on literature precedents, as available (Chou et al., 2011; Roll-Mecak and Vale, 2008; Whitehead et al., 2013).

*Assay conditions for $K_{1/2}$ and $k_{cat}$ analyses (enzyme concentrations).*

Dm-spastin wild-type and mutants (85 nM): 25 mM K-HEPES pH 7.5, 225 mM KCl, 25 mM $K_2HPO_4$, 5 mM $MgCl_2$, 2.5 mM DTT, 175 µM NADH.

Hs-spastin wild type and mutants (100 nM): 25 mM K-HEPES pH 7.5, 225 mM KCl, 25 mM $K_2HPO_4$, 5 mM $MgCl_2$, 2.5 mM DTT, 200 μM NADH.

Xl-katanin (80 nM): 25 mM K-HEPES pH 7.5, 70 mM KCl, 25 mM $K_2HPO_4$, 5 mM $MgCl_2$, 2.5 mM DTT, 175 μM NADH.

Hs-FIGL1 (50 nM): 25 mM Na-MES pH 6.5, 70 mM KOAc, 25 mM $K_2HPO_4$, 5 mM $Mg(OAc)_2$, 1 mM TCEP, 175 μM NADH.

Mm-VCP (450 nM): 25 mM K-HEPES pH 7.5, 25 mM KCl, 25 mM $K_2HPO_4$, 15 mM $MgCl_2$, 1 mM TCEP, 100–125 μM NADH.

Each buffer also contained 0.1 mg/ml BSA, 1 mM phosphoenolpyruvate, 40 U/ml lactate dehydrogenase, and 40 U/ml pyruvate kinase.

*Assay conditions for analysis of chemical inhibitors.*

While testing compounds we observed some precipitation, which we found to be dependent on buffer conditions. Replacing $K_2HPO_4$ with $(NH_4)_2SO_4$ addressed this issue. As Dm-spastin is more active than Hs-spastin, 0.5 mM MgATP was used rather than 1 mM MgATP. For each assay we included Triton X-100 to prevent non-specific aggregation (Feng and Shoichet, 2006).

*Dm-spastin wild-type and mutants:* protein 70–100 nM, 25 mM K-HEPES pH 7.5, 200 mM KCl, 20 mM $(NH_4)_2SO_4$, 5 mM $MgCl_2$, 2.5 mM DTT, 175 μM NADH.

*Hs-spastin wild-type and mutants:* protein 50 nM, 25 mM K-HEPES pH 7.5, 225 mM KCl, 2.5 mM $(NH_4)_2SO_4$, 5 mM $MgCl_2$, 2.5 mM DTT, 0.005% w/v Triton X-100, 175 μM NADH.

*Xl-katanin:* protein 70 nM, 25 mM K-HEPES pH 7.5, 70 mM KCl, 20 mM $(NH_4)_2SO_4$, 5 mM $MgCl_2$, 2.5 mM DTT, 0.005% w/v Triton X-100, 150 µM NADH.

*Hs-FIGL1:* protein 50–70 nM, 25 mM Na-MES pH 6.5, 70 mM KOAc, 20 mM $(NH_4)_2SO_4$, 5 mM $Mg(OAc)_2$, 1 mM TCEP, 0.005% w/v Triton X-100, 150 µM NADH.

*Mm-VCP/p97:* protein 300-450 nM, 50 mM K-HEPES pH 7.5, 25 mM KCl, 20 mM $(NH_4)_2SO_4$, 15 mM $MgCl_2$, 1 mM TCEP, pH 7.5, 100 µM NADH.

*Hs-VPS4B:* protein 80 nM, 25 mM Na-HEPES pH 7.5, 25 mM KOAc, 2.5 mM $(NH_4)_2SO_4$, 2 mM $MgCl_2$, 1 mM TCEP, 0.01% (v/v) Triton X-100, 150 µM NADH.

Each buffer also contained: 0.1 mg/ml BSA, 1 mM phosphoenolpyruvate, 30 U/ml lactate dehydrogenase, 30 U/ml pyruvate kinase.

**Equations used for data fitting.**

As ATPase activity of spastin and other AAA proteins exhibit a sigmoidal dependence on ATP concentration (Eckert et al., 2012) we analyzed the enzyme activity of recombinant enzymes using a modified Michaelis-Menten equation, which included a Hill coefficient. In particular, to determine the enzyme activity parameters of spastin constructs we fitted rates from steady state ATPase data to equation (1).

$$V = ATPase\ rate = \frac{V_{max}\, x^h}{K_{1/2}^h + x^h} \quad (1)$$

In this equation $V_{max}$ denotes the maximum ATPase rate, h is the Hill coefficient, x denotes ATP concentration and $K_{1/2}$ is the ATP concentration required for half maximal

enzyme rate and has units of concentration (e.g. mM). We adopted the $K_{1/2}$ annotation to distinguish this constant from the standard Michaelis constant $K_M$. Catalytic turnover number ($k_{cat}$) was calculated by dividing the $V_{max}$ value by the concentration of enzyme in the assay.

**Compound $IC_{50}$ calculation.**

For each experiment, values of percent inhibition of ATPase activity were calculated (0.5-1% DMSO was used as a vehicle control), plotted against concentration of compound, and the data were fit using a sigmoidal dose-response curve (Equation 2) using Prism software to determine the $IC_{50}$. The $IC_{50}$ values from at least three independent experiments were averaged and standard deviations were calculated.

$$Y = \%\ ATPase\ rate\ relative\ to\ DMSO\ control = (Y_{min}) + \frac{(Y_{max} - Y_{min})}{1+10^{(logIC50-x)h}} \qquad (2)$$

In this equation x denotes concentration of the compound and h is the Hill coefficient.

**Differential scanning fluorimetry.**

These experiments were carried out on a C1000 Touch Thermal cycler CFX-96 instrument (GE Healthcare). Purified Hs- spastin wild-type or Hs-spastin N386C mutant were diluted to 16 μM in a buffer containing 50 mM $K_2HPO_4$, 200 mM KCl, 2 mM $MgCl_2$, and 2 mM DTT, pH 7.4. Spastazoline was diluted in this buffer supplemented with 4% (v/v) DMSO and SYPRO Orange (1:250 dilution), and an equal volume was added to the Hs-spastin solution (assay concentrations: compound, 6.25 μM to 200 μM;

Hs-spastin, 8 μM; DMSO, 2%). Assays were conducted in a 96-well plate (Hard-shell HSP9665 Bio- Rad). The temperature was linearly increased with a step of 0.5 °C for 55 min, from 25 °C to 95 °C, and fluorescence readings were taken at each interval (excitation 490 nm, emission 590 nm). Melting temperatures were recorded as the minimum value of the first derivative of the fluorescence versus temperature curves.

**In vitro microtubule-severing assays.**

A fluorescence-based assay was adapted from similar assays reported previously (Ziółkowska and Roll-Mecak, 2013). Briefly, X-rhodamine-labeled, taxol (Sigma, catalog no.T7402)-stabilized microtubules (from bovine brain, prepared as in (Kapitein et al., 2008)) were diluted in buffer A (20 mM K-HEPES, 30 mM KCl, 5 mM $MgCl_2$, 2 mM TCEP, 0.2 mg/ml BSA, 0.01% Triton X-100). Compound **2.5** (2 μM, 1% DMSO final) and MgATP (0.5 mM) in buffer A were added and the mixture was incubated for 5 min. Dm-spastin was diluted to 150 nM in buffer B (50 mM K-HEPES, 300 mM KCl, 10 mM $MgCl_2$, 1 mM TCEP, 10% glycerol, 0.01% Triton X-100, pH 7.5) and then added to the mixture (final concentration: 15 nM). Aliquots were removed at selected time points, fixed, and imaged using a Zeiss Axiovert 200M wide-field microscope equipped with a Zeiss 100x/1.45 NA α-Plan Fluor objective and an EMCCD camera (iXon DU-897, Andor Technology).

**Computational methods.**

*Note - these experiments were performed jointly with Dr Tommaso Cupido (a postdoctoral fellow in the Kapoor lab).*

Analysis of nucleotide-binding sites of AAA proteins. We used a three-dimensional structural alignment to compare the residue composition of the ATP-binding site in selected AAA proteins (Dm-spastin, Xl-katanin, Hs-FIGL1, Mm-VCP/p97). We used available structural models for Dm-spastin (PDB: 3B9P), Hs-FIGL1 (PDB: 3D8B, chain A), the D1-AAA domain (PDB: 5FTK, chain A, residues 200–477), and the D2-AAA domain (residues 471– 761) of human VCP/p97. Since no structural models for katanin was available at the beginning of these studies, homology models were generated for the ATPase domains of these proteins using Bioluminate (version 2.3, Schrödinger, LLC). Xl-katanin (residues 200–486, Uniprot reference sequence Q9PUL2) was modeled using 3D8B_A, 3VFD_A, and 3B9P_A as templates. To identify the amino acid residues lining the adenine-binding pocket in these proteins the atom coordinates from the structural or homology models were aligned to the coordinates of ADP-bound Hs-FIGL1 using UCSF Chimera (Pettersen et al., 2004). Hs-FIGL1 residues within 6 Å of the adenine were selected and the corresponding residues were identified in the ATPase domains of Dm-spastin, Xl-katanin and Mm-VCP/p97.

**Inhibitor docking.**

*Note - these experiments were performed jointly with Dr Tommaso Cupido (a postdoctoral fellow in the Kapoor lab)*

The molecular dynamics system was set up for Dm-spastin (PDB: 3B9P) using the Protein Preparation Wizard in Maestro (Schrödinger Release 2016.1). First, all non-protein atoms in the PDB file were kept, and the protein loops with no coordinates were modeled using Uniprot: Q8I0P1 as reference sequence. Hydrogen atoms were added to the protein structure, and the protonation states of ionizable residues were assigned for pH 7.0. This structure was neutralized with KCl ions, additional KCl ions were placed to reproduce a salt concentration of 0.15 M, and the system was solvated with an orthorhombic box of simple point charge water molecules using the Desmond package in Maestro (Desmond Molecular Dynamics System, version 4.6, D. E. Shaw Research).

To generate the molecular dynamics atomic trajectory, the standard system relaxation protocol provided in Maestro was used, followed by 100 ns of NPT molecular dynamics (300 K, 1.01325 bar), during which atomic positions were recorded every 50 ps. To maintain the pressure and temperature of the system, isotropic position scaling and the Nosè–Hoover chain thermostat methods were used with relaxation times of 2 ps and 1 ps, respectively. A RESPA integrator scheme was employed (step: 2.0 fs for bonded interactions; 2 fs for van der Waals and short-range electrostatic interactions; 6 fs for long-range electrostatic interactions). Short-range electrostatic interactions were cut off at 9.0 Å. For the ensemble docking procedure all non-protein atoms were removed from the 5,000 molecular dynamics frames and the spastin structures from each frame were aligned to remove translational and rotational movement of the macromolecule. One hundred representative frames were selected using the molecular dynamics-trajectory

clustering methods in Schrödinger, based on the coordinates of the nucleotide-binding site residues. To remove overlap of the atoms' van der Waals radii, representative structures were minimized using 25 iterations of the Polak–Ribière conjugated gradient method or until the root mean square of the gradient of the energies was <0.05 kJ mol−1 Å−1, using OPLS2003e force field and a cut-off of 20 Å for the electrostatic interactions and 8 Å for the van der Waals interactions. Molecular docking was performed on the resulting 100 structures using the XGlide script with the OPLS2003e force field and Schrödinger's GlideScore multi-ligand scoring function (Friesner et al., 2006). A box of 22 Å was placed, centered approximately at the P-loop residues of Dm-spastin. Grids for docking calculations were obtained with the grid generation module in Schrödinger. A scaling factor of 0.8 was applied to the atom radii for every atom with assigned partial charge <0.25. The AROMATIC_H-BONDS option was set true. The major tautomer at pH 7.0 of compound **2.4** [1-methyl-4-(4-((5-phenyl-1H-pyrazol-3-yl) amino)quinazolin-2-yl)piperazin-1-ium] was calculated using the LigPrep panel in Maestro. For docking, the REWARD_INTRA_HBONDS, SAMPLE_RINGS, HBOND_DONOR_AROMH, FORCEPLANAR, and AROMATIC_H-BONDS options were set true, and a scaling factor of 0.75 was applied to atom radii for every atom with assigned partial charge <0.15. Compound **2.5** ((R)-4-(4-((5-(tert- butyl)-1H-pyrazol-3-yl)amino)quinazolin-2-yl) -3-methylpiperazin-1-ium) and compound **2.6** ((R)-4-(4-((5-(tert-butyl) -1H-pyrazol-3-yl)amino)-7H-pyrrolo [2,3-d]pyrimidin-2-yl)-3-methylpiperazin-1-ium) were docked using an analogous procedure.

**Chemical synthesis information**

Solvents were purchased from Sigma-Aldrich. Reactions were run in capped round bottom flasks or screw capped glass vials stirred with Teflon®-coated magnetic stir bars. Evaporation of solvents was accomplished using a Büchi rotary evaporator, equipped with a dry ice-acetone condenser, at 5-50 mm Hg (25-50°C). Experiments were monitored by thin layer chromatography or liquid chromatography mass spectrometry. The maintenance of 40°C to 150°C reaction temperatures was accomplished by using an oil bath. Products obtained as solids or oils were dried under vacuum. Compounds were purified using column chromatography (silica gel, Acros cat#360050010) or preparative thin layer chromatography (TLC, Analtech cat# 04011), as necessary. Analytical TLC was performed using Whatman 250 micron aluminum backed UV F254 precoated silica gel flexible plates. Subsequent to elution, ultraviolet illumination at 254 nm allowed for visualization of UV active materials. Staining with basic potassium permanganate solution or iodine vapors allowed for further visualization.

**Compound characterization**

Proton nuclear magnetic resonance spectra ($^1$H-NMR) were recorded on Bruker Avance DPX400, spectrometer operating at 400.13 MHz, carrying a BBFO probe, or a Bruker Avance II MHz spectrometer (600 MHz) with a 5 mm TXI probe. All observed proton absorptions are reported as δ in units of parts per million (ppm) relative to

tetramethylsilane (δ 0.0) using the signal of tetramethylsilane itself or the residual solvent signal as an internal standard: dimethylsulfoxide-d6 (δ 2.49, quintet at 25ºC). Multiplicities are reported as follows: s (singlet), d (doublet), t (triplet), q (quartet), dd (doublet of doublets), dt (doublet of triplets), td (triplet of doublets), m (multiplet), or br. s. (broad signal). Coupling constants are reported as a J value in Hertz. The number of protons (n) for a given resonance is indicated by nH, and is based on spectral integration values. Liquid chromatography mass spectral analyses were obtained using a Waters Acquity H-Class UPLC/MS with QDa mass spectrometer. The system used a eλ Photodiode Array Detector detector, and a Symmetry® C18 (3.5 micron) 2.1 x 50 mm column for separation (mobile phase for positive mode: solvent A: water with 0.1% formic acid, solvent B: acetonitrile with 0.1% formic acid). Values are reported in units of mass to charge (m/z).

The following abbreviations are used in this section: ACN = acetonitrile; DCM = dichloromethane; DIEA (Hunig base) = diisopropylethylamine; EtOAc = ethyl acetate; eq = equivalents; EtOH = ethanol; HCl = hydrochloric acid; HEX = hexane; MeOH = methanol; MTBE = methyl *tert*-butyl ether; rt = room temperature; TFA = trifluoroacetic acid; THF = tetrahydrofurane.

**Synthetic procedures**

*Note - compound synthesis and characterization were performed jointly with Dr Tommaso Cupido (a postdoctoral fellow in the Kapoor lab).*

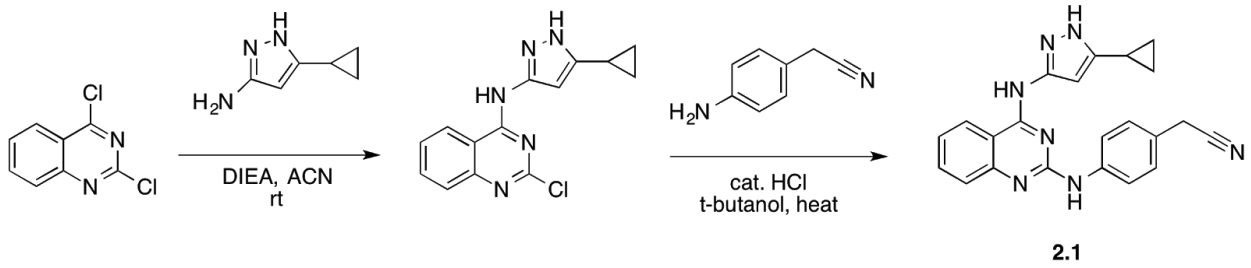


**2.1**

Synthesis of compound **2.1**,

2-(4-((4-((5-cyclopropyl-1H-pyrazol-3-yl)amino)quinazolin-2-yl)amino)phenyl)acetonitrile.

Step 1. To a stirring solution of 2,4-dichloro-quinazoline (200 mg, ~1.0 mmol) and DIEA (~0.75 eq) in ACN (2 mL) in a round bottom glass flask at rt, a solution of 5-cyclopropyl-1H-pyrazol-3-amine (135 mg, ~1.1 mmol) and DIEA (~0.75 eq) in ACN (2 mL) was added dropwise. After 24 hours an equal volume of water was added and the mixture stirred for 2 h at rt. The product was recovered by filtration and washed in a sequential manner with approximately 5 mL of the following solvents: 1- cold ACN, 2- water:ACN (4:1), 3- aqueous HCl (pH ~3), 4- water:ACN (4:1), 5- aqueous sodium hydroxide (pH ~10), 6- hexane. After drying, a solid was recovered: 2-chloro-N-(5-cyclopropyl-1H-pyrazol-3-yl)quinazolin-4-amine (intermediate-2.1). MS-ESI [M+1]: expected 285.7, found 286.5.

Step 2. Without further purification, intermediate-2.1 from step 1 (60 mg, ~0.21 mmol) was dissolved in tert-butanol (3 mL), and a solution of 2-(4-aminophenyl)acetonitrile (1.5 eq) in tert-butanol (0.5 mL) was added to the mixture. 37% HCl in water (10 µl) was added and the reaction was heated at 110ºC while stirring. After 6h, the solvent was evaporated and hexane (2 ml) was added. The precipitated product was recovered by

filtration, recrystallized from EtOAc:Hexane (4:1 v/v), and dried to obtain compound **2.1**, 2-(4-((4-((5-cyclopropyl-1H-pyrazol-3-yl)amino)quinazolin-2-yl)amino)phenyl)acetonitrile as HCl salt. MS-ESI [M+1]: expected 381.4, found 382.3.

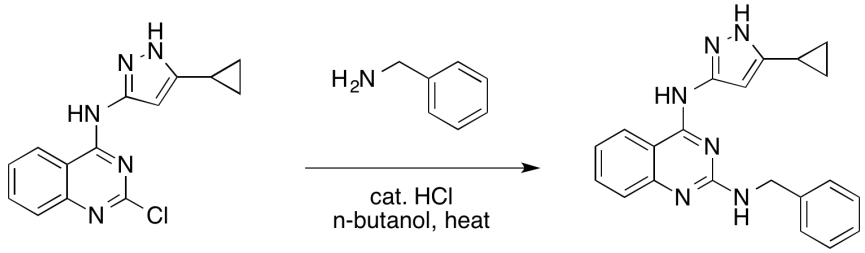


Synthesis of compound **2.3**.

[N2-benzyl-N4-(5-cyclopropyl-1H-pyrazol-3-yl)quinazoline-2,4-diamine]. Without further purification, intermediate-2.1 (60 mg, ~0.21 mmol) was dissolved in n-butanol (3 mL), and a solution of benzylamine (1.1 eq) in n-butanol (0.5 mL) was added to the mixture. 37% HCl in water (10 µl) was added and the reaction was heated at 110ºC while stirring. Once starting material was consumed (~3 h), one half of the volume was evaporated and the mixture was cooled to rt. Water (1 mL) was added and the precipitated product was recovered by filtration, and washed in a sequential manner with the following solvents: 1- water:ACN (3:7 v/v, 5 ml), 2- water (5 ml), 3- hexane (5 ml), 4- water:MeOH (1:1 v/v, 1 mL), and then dried to obtain compound **2.3** as HCl salt. MS-ESI [M+1]: expected 357.4, found 357.6.

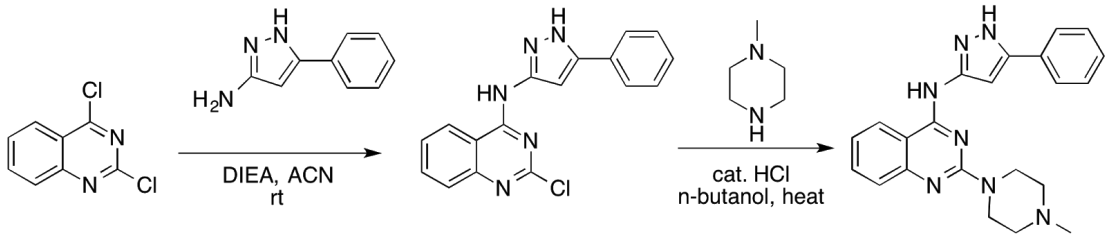


Synthesis of compound **2.4**,

2-(4-methylpiperazin-1-yl)-N-(5-phenyl-1H-pyrazol-3-yl)quinazolin-4-amine.

Step 1. To a stirring solution of 2,4-dichloro-quinazoline (200 mg, ~1.0 mmol) and DIEA (~1.6 eq) in ACN (1 mL) in a round bottom glass flask at rt, a solution of 5-phenyl-1H-pyrazol-3-amine (160 mg, ~1.0 mmol) and DIEA (~0.4 eq) in ACN (1 mL) was added dropwise. After 48 hours an equal volume of water was added and the mixture stirred for 2 h at rt. The product was recovered by filtration and washed in a sequential manner with approximately 5 mL of the following solvents: 1- cold ACN, 2- water:ACN (4:1), 3- aqueous HCl (pH ~3), 4- water:ACN (4:1), 5- aqueous sodium hydroxide (pH ~10), 6- hexane. After drying, a solid was recovered: compound 15, 2-chloro-N-(5-phenyl-1H-pyrazol-3-yl)quinazolin-4-amine. MS-ESI [M+1]: expected 321.8, found 322.7.

Step 2. Without further purification, intermediate from step 1 (60 mg, ~0.19 mmol) was dissolved in n-butanol (3 mL), and N-methylpiperazine (2.0 eq) was added. 37% HCl in water (10 µl) was added and the reaction was heated at 130ºC while stirring. After 12 h, one half of the volume was evaporated, EtOAc (5 ml) was added, and the solution stirred at rt for ~1h. A precipitate was collected, washed with EtOAc:MeOH (5:1, v/v, 2

ml), and dried to obtain compound **2.4** as a HCl salt. MS-ESI [M+1]: expected 385.5, found 387.0.

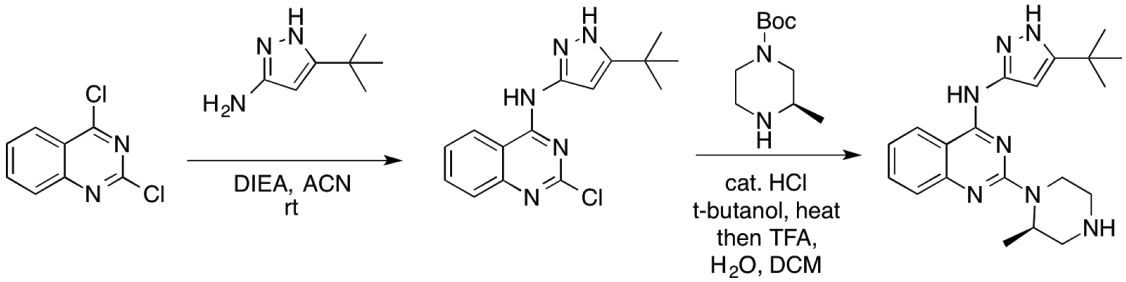


Synthesis of compound **2.5**,

[(R)-N-(5-(tert-butyl)-1H-pyrazol-3-yl)-2-(2-methyl-piperazin-1-yl)quinazolin-4-amine].

Step 1. To a stirring solution of 2,4-dichloro-quinazoline (200 mg, ~1.0 mmol) and DIEA (~1.6 eq) in ACN (1 mL) in a round bottom glass flask at rt, a solution of 5-(tert-butyl)-1H-pyrazol-3-amine (1.0 eq) and DIEA (~0.4 eq) in ACN (1 mL) was added dropwise. After 12 hours an equal volume of water was added and the mixture was stirred for 2 h at rt. The product was recovered by filtration and washed in a sequential manner with approximately 5 mL of the following solvents: 1- cold ACN, 2- water:ACN (4:1), 3- aqueous HCl (pH ~3), 4- water:ACN (4:1), 5- aqueous sodium hydroxide (pH ~10), 6- hexane. After drying, a solid was recovered: compound 16, N-(5-(tert-butyl)-1H-pyrazol-3-yl)-2-chloroquinazolin-4-amine. MS-ESI [M+1]: expected 301.8, found 302.8.

Step 2. Without further purification, 60 mg of compound from step 1 (~0.2 mmol) was dissolved in n-butanol (2.5 mL) and 10 µl of 37% HCl in water were added while stirring

at rt. Then, tert-butyl (R)-3-methylpiperazine-1-carboxylate (0.25 mmol, 1.5 eq) was dissolved in n-butanol (0.5 mL) and added to the mixture. The reaction was heated at 110ºC for 12 h while stirring and then cooled down to rt. The excess solvent was evaporated under reduced pressure, and the product of the reaction was washed with hexane, and dried. The solid residue was washed with aqueous HCl (pH ~3) for 15 min while stirring. A precipitate was collected, dissolved in a mixture of DCM:TFA:$H_2O$ (5:4.5:0.5) and stirred for 1 h at rt. The solvent was evaporated under reduced pressure and the product washed with diethylether twice. A precipitate was collected, dissolved in aqueous sodium hydroxide (pH ~12) and extracted with EtOAc. The organic solution was washed with brine, dried over $Na_2SO_4$, and filtered. The volume of EtOAc solution containing the desired product was reduced to 1.0 ml and the product precipitated by adding 20 µl of 37% HCl in water, washed once with EtOAc (5 mL), once with acetone (1 mL), and finally dried to obtain compound **2.5** as HCl salt, in ~15% total yield.

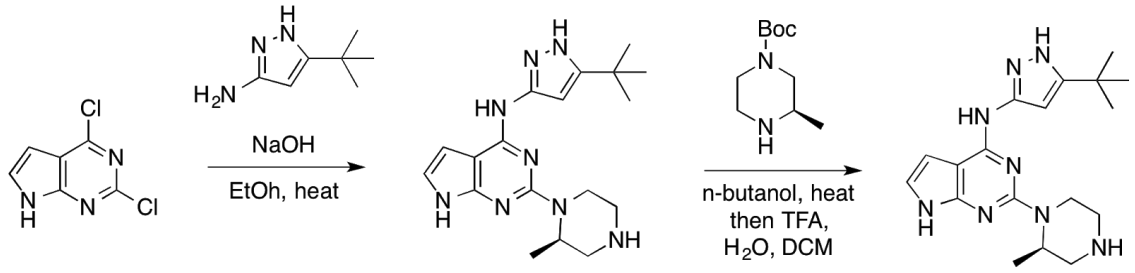


Synthesis of compound **2.6**,

[(R)-N-(5-(tert-butyl)-1H-pyrazol-3-yl)-2-(2-methylpiperazin-1-yl)-7H-pyrrolo[2,3-d]pyrimidin-4-amine].

Step 1. To a stirring solution of 5-(tert-butyl)-1H-pyrazol-3-amine (80 mg, ~0.57 mmol) in ethanol (2.0 mL) and 5 M sodium hydroxide (0.05 mL) in a round bottom glass flask, a solution of 2,4-dichloro-7H-pyrrolo[2,3-d]pyrimidine (100 mg, ~0.53 mmol) in ethanol (1 mL) was added. The mixture was heated to reflux for 12 h while stirring. Then, the solvent was evaporated under reduced pressure and the residue was washed several times with aqueous HCl (pH ~3), and then with aqueous sodium hydroxide (pH ~10). The solid was dried, dissolved in ethyl acetate and purified using flash silica gel chromatography, using a gradient of HEX:EtOAc to obtain N-(5-(tert-butyl)-1H-pyrazol-3-yl)-2-chloro-7H-pyrrolo[2,3-d]pyrimidin-4-amine. MS-ESI [M+1]: expected 290.8, found 291.4.

Step 2. Intermediate from step 2 (~0.17 mmol) was dissolved in n-butanol (2 mL). Tert-butyl (R)-3-methylpiperazine-1-carboxylate (~2 eq) and 10 µl of DIEA were added, and the reaction heated at 110ºC while stirring until consumption of starting material (3-4 h). The solvent was evaporated and the solid residue was washed with aqueous HCl (pH ~2) once, and extracted with DCM. The organic solution was washed with aqueous sodium hydroxide (pH ~12), brine, dried over MgSO4, and filtered. Then, the solvent was evaporated, and the residue was dissolved in a mixture of DCM:TFA:H2O (5:4.5:0.5) while stirring at rt for 1h. The solvent was evaporated and the product washed with diethyl ether twice and precipitated in diethyl ether overnight at rt. A solid was collected by centrifugation, dissolved in aqueous sodium hydroxide (pH ~12), and extracted with EtOAc. The organic layer containing the desired product was washed with brine, dried over MgSO4, and filtered. After evaporation of the solvent, the residue

was dried to afford (R)-N-(5-(tert-butyl)-1H-pyrazol-3-yl)-2-(2-methylpiperazin-1-yl)-7H-pyrrolo[2,3-d]pyrimidin-4-amine as free base.

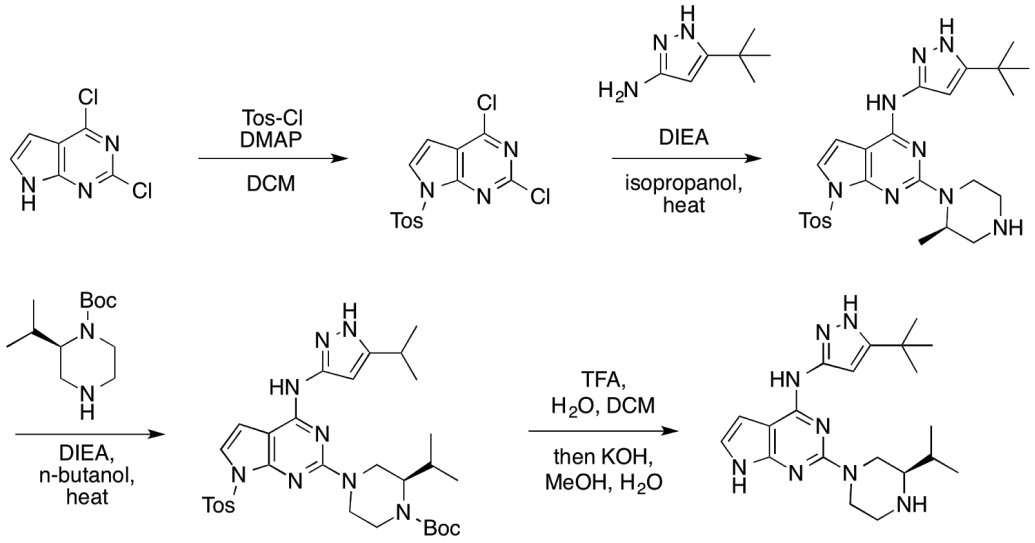


Synthesis of compound **2.7** (spastazoline), [(R)-N-(5-(tert-butyl)-1H-pyrazol-3-yl)-2-(3-isopropylpiperazin-1-yl)-7H-pyrrolo[2,3-d]pyrimidin-4-amine].

Step 1. To a stirring solution of 2,4-dichloro-7H-pyrrolo[2,3-d]pyrimidine (300 mg, ~1.6 mmol) in DCM (10 mL) at rt, a solution of tosyl chloride (1.2 eq) was added dropwise, and the mixture was stirred for 2 hrs. The crude reaction was washed with 5% $NaHCO_3$, extracted with EtOAc, dried over $Mg_2SO_4$, and purified with silica gel chromatography in a gradient of Hexane:EtOAc to obtain 2,4-dichloro-7-tosyl-7H-pyrrolo[2,3-d]pyrimidine.

Step 2. To a stirring solution of compound 2,4-dichloro-7-tosyl-7H-pyrrolo[2,3-d] pyrimidine (~0.54 mmol) in tert-butanol (5 mL) a solution of 5-(tert-butyl)-1H-pyrazol-3-amine (1.2 eq) in isopropanol was added, followed by DIEA (2.5 eq), and the solution was heated at 60 ºC for 3 hrs while stirring. The solvent was evaporated and the crude residue was purified by silica gel chromatography in a gradient of Hexane:EtOAc to obtain N-(5-(tert-butyl)-1H-pyrazol-3-yl)-2-chloro-7-tosyl-7H-pyrrolo[2,3-d]pyrimidin-4-amine.

Step 3. Intermediate from step 2 (~0.22) was dissolved in n-butanol (2 mL), and tert-butyl (R)-2-isopropylpiperazine-1-carboxylate (~2 eq) and 15 µl of DIEA were added, and the reaction heated at 110ºC while stirring, until consumption of starting material (3-4 h). The solvent was evaporated and the residue was purified with silica gel chromatography to afford tert-butyl-(R)-4-(4-((5-(tert-butyl)-1H-pyrazol-3-yl)amino)-7-tosyl-7Hpyrrolo[2,3d]pyrimidin-2-yl)-2-isopropylpiperazine-1-carboxylate.

Step 4. Intermediate from step 3 was first treated with a mixture of TFA:DCM:H2O (4.5:5:0.5; 3 mL) for 30 min. The solvent was evaporated and the residue was triturated with diethyl ether and filtered to recover an off-white precipitate. The precipitate was then treated with 0.5 M KOH in MeOH:H2O (7:3; 5 mL) for 3 h at 50 ºC. The crude was extracted with EtOAc, dried over $Mg_2SO_4$ and purified using preparative TLC, using neutral alumina with DCM:MeOH as solvent (9:1), to obtain (R)-N-(5-(tert-butyl)-1H-pyrazol-3-yl)-2-(3-isopropylpiperazin-1-yl)-7H-pyrrolo[2,3-d]pyrimidin-4-amine, compound **2.7**.

**Compounds characterization data.**

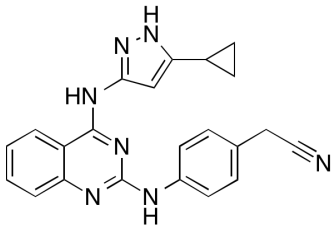

Compound **2.1**.

2-(4-((4-((5-cyclopropyl-1H-pyrazol-3-yl)amino)quinazolin-2-yl)amino)phenyl)acetonitrile hydrochloride salt. Molecular weight (MW) expected for $C_{22}H_{19}N_7$: 381.4; MS-ESI [M+1]: found 382.5. $^1$H NMR (400 MHz, DMSO-$d_6$) δ 12.60 (br. s. 1H), 11.45 (br. s. 1H), 10.49 (br. s. 1H), 8.65 (d, J = 6.8, 1H), 7.85 (t, J = 7.8, 1H), 7.64 (d, J = 8.2, 1H), 7.59 (br. s. 2H), 7.48 (m, 1H), 7.43 (d, J= 7.9, 2H), 6.21 (br. s. 1H), 4.09 (s, 2H), 1.87 (td, J = 8.6, 4.4, 1H), 0.96 (d, J = 8.1, 2H), 0.60 (s, 2H). $^{13}$C NMR (600 MHz, DMSO-$d_6$) δ 158.45, 152.64, 146.83, 146.67, 146.27, 140.36, 136.57, 135.84, 129.24, 125.25, 124.97, 124.66, 119.62, 118.32, 110.96, 96.18, 22.48, 8.37, 7.41.

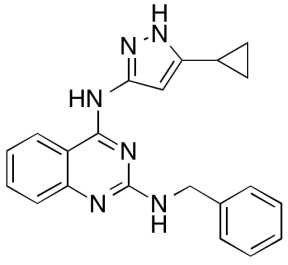

Compound **2.3**

N2-benzyl-N4-(5-cyclopropyl-1H-pyrazol-3-yl)quinazoline-2,4-diamine hydrochloride salt. MW expected for $C_{21}H_{20}N_6$: 356.4; MS-ESI [M+1]: found 357.2. $^1$H NMR (400 MHz, DMSO-$d_6$) δ 13.30 (s, 1H), 12.60 (s, 1H), 11.45 (s, 1H), 8.75 (s, 1H), 8.63 (d, J = 8.2, 1H), 7.83 (t, J = 7.7, 1H), 7.56 (d, J = 8.3, 1H), 7.46 – 7.27 (m, 5H), 6.14 (s, 1H), 1.83 (s, 1H), 0.88 (d, J = 7.9, 2H), 0.77 (s, 1H), 0.47 (s, 1H). $^{13}$C NMR (600 MHz, DMSO-$d_6$) δ 158.36, 153.67, 146.51, 146.24, 139.88, 138.58, 135.96, 128.99, 128.08, 127.59, 127.14, 125.12, 124.91, 117.37, 110.27, 95.59, 44.53, 8.36, 7.12.

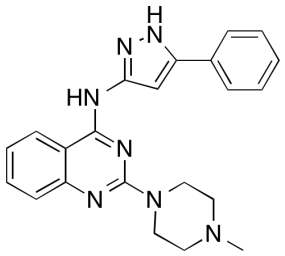


Compound **2.4**

2-(4-methylpiperazin-1-yl)-N-(5-phenyl-1H-pyrazol-3-yl)quinazolin-4-amine hydrochloride salt. MW expected for $C_{22}H_{23}N_7$ 385.5, MS-ESI [M+1]: found 386.2. $^1$H NMR (600 MHz, DMSO-$d_6$) δ 11.63 (br. s. 1H), 11.31 (br. s., 1H), 8.68 (d, J = 13.2, 1H), 8.09 (br. s., 1H), 7.93 (m, 1H), 7.81 (d, J = 12.7, 1H), 7.54 (m, 1H) 7.51 (t, J = 12.6, 2H), 7.41 (t, J = 12.6, 2H), 7.05 (s, 1H), 4.89 (m, 2H), 3.70-3.50 (m), 3.25 (m, 2H), 2.80 (s, 3H). $^{13}$C NMR (600 MHz, DMSO-$d_6$) δ. 158.17, 152.50, 146.61 143.43 140.92 135.92, 129.80, 129.60, 128. 92, 127.13, 125.66, 124.83, 118.63,110.26, 97.08, 51.84, 42.96, 42.36.

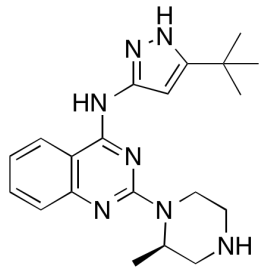

Compound **2.5**.

(R)-N-(5-(tert-butyl)-1H-pyrazol-3-yl)-2-(2-methylpiperazin-1-yl)quinazolin-4-amine hydrochloride salt. MW expected for $C_{20}H_{27}N_7$: 365.5; MS-ESI [M+1]: found 366.0. $^1$H NMR (400 MHz, DMSO-$d_6$) δ 13.36 (s, 1H), 11.54 (s, 1H), 10.04 (d, J = 10.5, 1H), 9.73 (d, J = 11.0, 1H), 8.66 (d, J = 8.3, 1H), 8.26 (d, J = 8.4, 1H), 7.87 (t, J = 7.8, 1H), 7.49 (t, J = 7.7, 1H), 6.45 (s, 1H), 5.19 (s, 1H), 4.92 (d, J = 14.6, 1H), 3.63 (t, J = 13.5, 1H), 3.33 (d, J = 15.5, 3H), 3.13 (d, J = 11.3, 1H), 1.50 (d, J = 7.0, 3H), 1.32 (s, 9H). $^{13}$C NMR (600 MHz, DMSO-$d_6$) δ 157.84, 153.64, 151.91, 145.52, 140.54, 135.78, 125.61, 124.79, 118.35, 110.27, 95.87, 46.65, 45.67, 42.20, 37.52, 31.32, 30.39, 15.66.

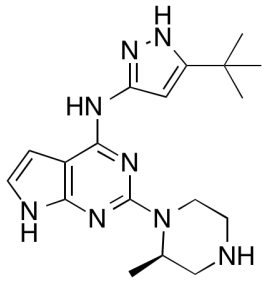

Compound **2.6**.

(R)-N-(5-(tert-butyl)-1H-pyrazol-3-yl)-2-(2-methylpiperazin-1-yl)-7H-pyrrolo[2,3-d]pyrimidin-4-amine. MW expected for $C_{18}H_{26}N_8$: 354.5; MS-ESI [M+1]: found 355. $^1$H NMR (600

MHz, DMSO-$d_6$) δ 11.93 (s, 1H), 10.91 (s, 1H), 9.50 (s, 1H), 6.63 (m, 3H), 4.46 (dd, J = 33.1, 11.8, 2H), 2.92 (d, J = 10.8, 1H), 2.71 (dt, J = 30.1, 10.2, 3H), 2.40 (t, J = 11.2, 1H), 1.30 (s, 9H), 1.02 (d, J = 6.0, 3H). $^{13}$C NMR (600 MHz, DMSO-$d_6$) δ 159.12, 153.63, 153.45, 152.35, 148.48, 118.41, 99.75, 96.91, 93.90, 60.20, 52.45, 50.61, 45.74, 45.04, 31.27, 30.46, 19.91, 0.64.

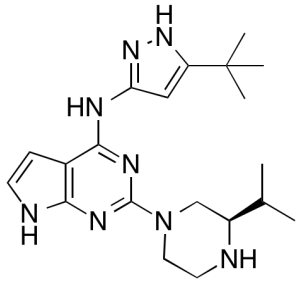


Compound **2.7**., (spastazoline)

(R)-N-(5-(tert-butyl)-1H-pyrazol-3-yl)-2-(3-isopropylpiperazin-1-yl)-7H-pyrrolo[2,3-d]pyrimidin-4-amine. MW expected for $C_{20}H_{30}N_8$: 382.5, MS-ESI [M+1]: found 383.5. $^1$H NMR (600 MHz, DMSO-$d_6$) δ 11.92 (s, 1H), 10.90 (s, 1H), 9.44 (s, 1H), 6.73 (br. s. 1H), 6.64 (br. s. 1H), 6.51 (br. s. 1H), 4.47 (dd, J = 65.1, 12.1, 2H), 4.04 (q, J = 7.1, 1H), 2.96 (d, J = 10.8, 1H) 2.70 (dt, J = 50.1, 2.5, 2H), 2.3 (m, 1H), 1.77 (m, 1H), 1.61 (m, 1H), 1.29 (s, 9H), 0.96 (dd, J = 2.3, 4.7, 6H). $^{13}$C NMR (600 MHz, DMSO-$d_6$) δ 159.44, 153.61, 152.50, 152.38, 148.65, 118.37, 100.01, 99.76, 96.92, 60.67, 48.61, 45.95, 45.61, 31.45, 31.19, 30.46, 19.70, 19.42.

## Chapter 3: Designing Allele-Specific Inhibitors of Spastin, a Microtubule-Severing AAA Protein.

*Noter to readers: A closely related version of this work was published in Pisa R et al., 2019, J. Am. Chem. Soc., 141, 5602-5606; DOI: 10.1021/jacs.8b13257. Except for results explicitly credited to others, I performed all experiments and analysis.*

### Introduction.

Chemical inhibitors that specifically block the function of a selected protein allele can be useful tools to examine complex and dynamic cellular processes (Islam, 2015). Early examples of engineering of allele–ligand pairs focused on modifications of nucleotide analogues to specifically bind a mutant GTPase or ATPase (Hwang and Miller, 1987; Kapoor and Mitchison, 1999; Powers and Walter, 1995; Shah et al., 1997). In parallel, a similar strategy called the bump-hole approach was developed that introduced mutations in the protein's active site to create a pocket ("hole") that can accommodate an inhibitor with a modification ("bump") (Belshaw et al., 1995; Lopez et al., 2014). The shape complementarity between the inhibitor and the mutant allele can be achieved by even subtle compound modifications (e.g., hydrogen to methyl substitution) that are sufficient to provide substantial improvements in selectivity toward the mutant protein allele (Baud et al., 2014; Belshaw et al., 1995). For several protein families, including cyclophilins (Belshaw et al., 1995), kinases (Bishop et al., 2000), GPCRs (Urban and Roth, 2015), PARPs (Morgan et al., 2015), and BET proteins (Baud

et al., 2014), we have a wealth of high-resolution structural data for how different chemical scaffolds bind active sites, and as a result, the design of allele-selective inhibitors of these proteins has been possible. However, for many enzyme families, such as the ATPases associated with diverse cellular activities (AAA) superfamily, we lack these critical data, and designing allele-specific chemical inhibitors has been difficult.

There are ~100 AAA proteins in humans, and several of these enzymes have essential functions (Erzberger and Berger, 2006). The improper function of AAA proteins has also been linked to a wide range of diseases, including Alzheimer's disease and related dementias (Hazan et al., 1999; Zempel et al., 2013) and cancer (Anderson et al., 2015; Assimon et al., 2019). Additionally, therapeutic agents targeting AAA proteins have recently entered clinical trials (Anderson et al., 2015). Therefore, selective chemical inhibitors would be useful probes for normal physiology and disease. These proteins typically function as oligomeric assemblies (e.g., hexamers) of conserved AAA domains, which bind ATP at their interface (Wendler et al., 2012). Furthermore, the AAA active site can undergo large-scale nucleotide-dependent rearrangements (Puchades et al., 2017), and as a result, it is unclear which of the different conformational states of the active site can contribute to chemical inhibitor binding and specificity.

Here we focus on spastin, a microtubule-severing AAA protein needed for cell division and organelle transport (Allison et al., 2013; Connell et al., 2009; Vietri et al., 2015). We report high-resolution structures of wild-type and mutant alleles of spastin

bound to chemical inhibitors that we have developed (Cupido et al., 2019). Our structural data and activity analyses of spastin mutants reveal that the interaction between an engineered cysteine residue in the active site and a fluoro-substituted pyrazolylaminoquinazoline-based compound can be leveraged for the design of allele-specific inhibitors of spastin.

**Results.**

**Crystal structure of the wild-type spastin bound to a pyrazolylquinazoline-based inhibitor.**

As high-resolution structural data can facilitate the rational design of selective chemical probes, we first sought to obtain an X-ray crystal structure of an inhibitor-bound AAA protein. We characterized a truncated construct including spastin's AAA domain (amino acids 445–758, *Drosophila melanogaster* spastin, hereafter denoted as spastin-AAA-WT; Figure 3.1A, B), as only this portion of spastin is well-resolved in the structures of its apo form (Roll-Mecak and Vale, 2008; Taylor et al., 2012). This construct is not an active ATPase, but gel filtration and differential scanning fluorimetry revealed that it is a stable monomer in solution that retains the ability to bind nucleotides (Figure 3.1C-F).

We recently described the development of spastazoline, a potent and selective inhibitor of spastin (Cupido et al., 2019). Here we examined the binding of the spastin-AAA-WT construct to compound **3.1** (Figure 3.2A; this compound is also referred to as compound **2.5** in chapter 2), a pyrazolylaminoquinazoline-based analogue

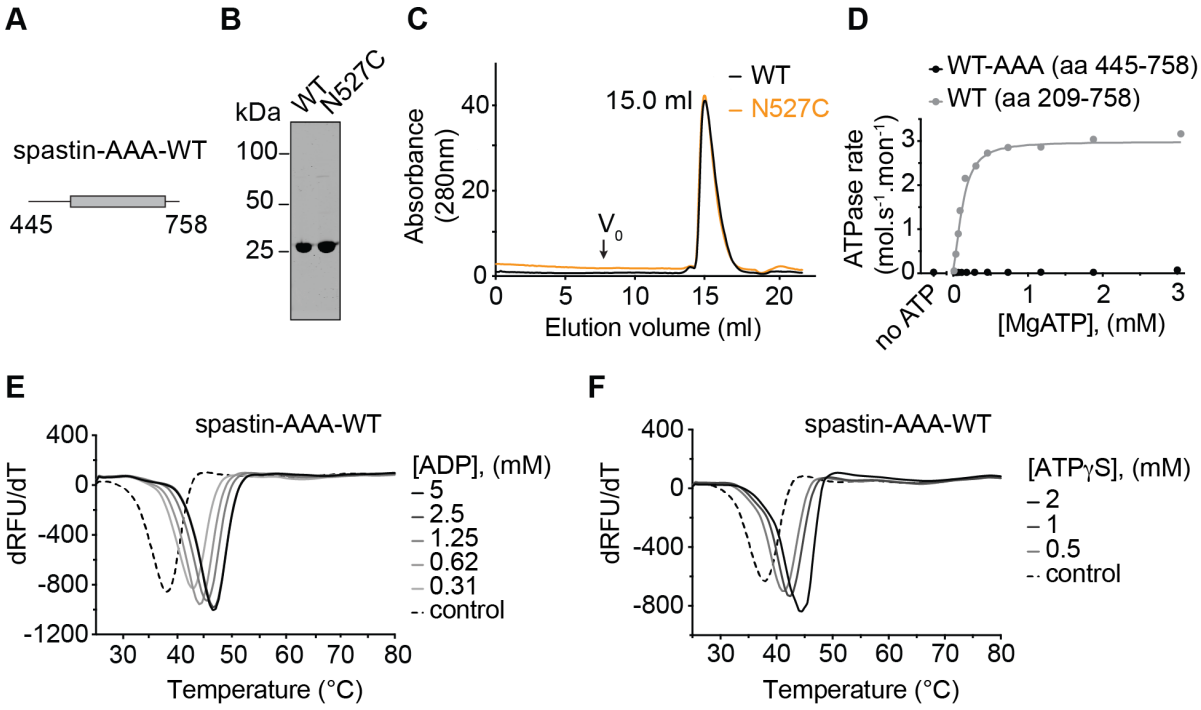


**Figure 3.1. Biochemical characterization of spastin-AAA constructs.**

(**A**) Schematic shows the truncated recombinant construct (*Drosophila melanogaster* spastin, aa 445-758, hereafter denoted as spastin-AAA). The AAA domain (gray box) and first and last residues of the construct are indicated. (**B**) SDS-PAGE analysis (Coomassie blue) of purified spastin-AAA wild-type (WT) and mutant (N527C) constructs. (**C**) Size-exclusion chromatography trace (Superdex 200 column) for spastin-AAA-WT and -N527C constructs with volume at elution peak indicated. $V_0$, void volume. (**D**) ATP concentration-dependence of the steady-state activity of spastin-AAA-WT construct, analyzed using an NADH-coupled assay (average, n = 2). For comparison, the curve for an ATPase active spastin construct (*Drosophila melanogaster* spastin, aa 209-758, hereafter denoted as spastin-WT) is shown (gray). (**E-F**) Differential scanning fluorimetry analysis of the melting temperature of spastin-AAA-WT construct in the presence of ADP (**E**, n = 2; observed $\Delta T_m$ ~8.0 °C at highest concentration tested: 5 mM ADP) and a nucleotide analog (**F**, n = 2; $\Delta T_m$ ~5.0 °C at highest concentration tested: 2 mM ATPγS). Data from one representative experiment are shown for each nucleotide.

of spastazoline. We found that compound **3.1** binds this construct with submicromolar affinity in an isothermal titration calorimetry assay ($K_d$ = 312 ± 300 nM, n = 4; Figure 3.2B). In addition, differential scanning fluorimetry revealed concentration-dependent stabilization of the spastin-AAA-WT construct against heat-induced denaturation by compound **3.1** ($\Delta T_m$ = ~6.0 °C at highest concentration tested, 100 μM compound **3.1**, Figure 3.2C).

Next, we set up cocrystallization trials of spastin-AAA-WT with compound **3.1**. We obtained diffracting crystals and determined the structure of the spastin-AAA-WT–compound **3.1** complex at ~2.4 Å resolution using molecular replacement (Table 3.1). This structural model contains a clear density that can be assigned to compound **3.1** in a pocket between the αβα core of the large AAA subdomain and the α-helical bundle of the small AAA subdomain (Figure 3.2D).

In this structural model, the 4-aminopyrazolyl moiety of compound **3.1** is positioned to form two hydrogen-bonding interactions with Ala-486's carbonyl oxygen and nitrogen atoms in spastin's N-loop. These interactions likely mimic the hydrogen bonds made by adenine in the active site. The pyrazole heterocycle is also aligned to form a third potential hydrogen-bonding interaction with the Asp-484 backbone carbonyl oxygen (Figure 3.2E). The pyrazolylaminoquinazoline core of compound **3.1** is sandwiched between the hydrophobic residues projecting from spastin's large and small AAA subdomains (Ile-485, Leu-531, and Leu-659; Figure 3.2E). In addition, the quinazoline is positioned to interact with residues in the N-loop and P-loop motifs (e.g., Gln-488 and Asn-527; Figure 3.2E).

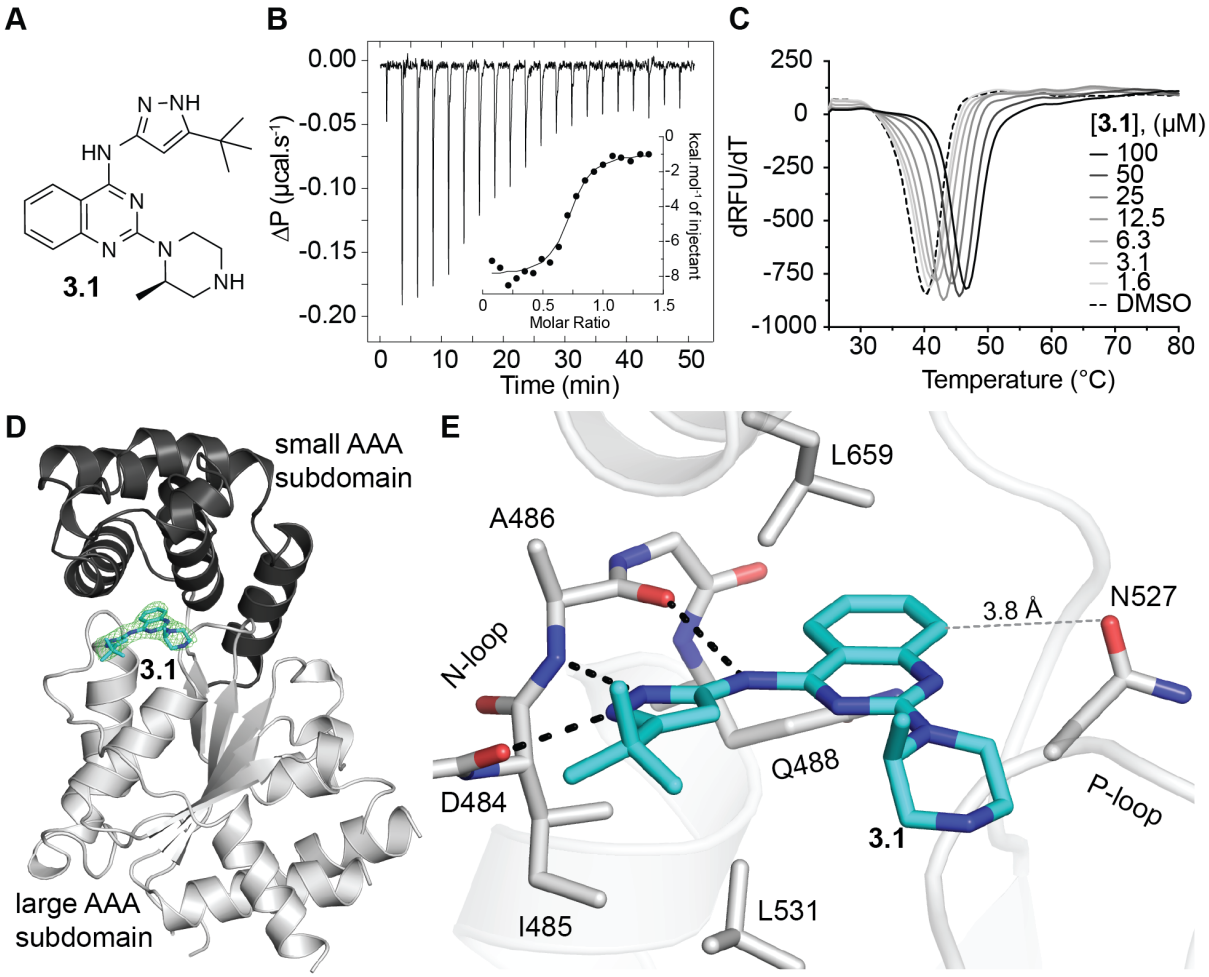


**Figure 3.2. X-ray structure of wild-type spastin bound to compound 3.1, a pyrazolylaminoquinazoline-based spastin inhibitor.**

(**A**) Chemical structure of compound **3.1**. (**B**) Isothermal titration calorimetry analysis of compound **3.1**'s binding to spastin-AAA-WT ($K_d$ = 312 ± 300 nM, average ± s.d., n = 4). (**C**) Compound **3.1** concentration-dependent changes in melting temperature of the spastin-AAA-WT construct analyzed using differential scanning fluorimetry (n = 2; observed $\Delta T_m$ = ~6.0 °C at highest concentration tested, 100 μM compound **3.1**, data from one experiment are shown). (**D**) Crystal structure of the spastin-AAA-WT−compound **3.1** complex (stick and ribbon representation). Spastin's large and small AAA subdomains are highlighted in gray and black, respectively. The composite omit electron density map around compound **3.1** contoured at 3σ is also shown ($mF_o - DF_c$; green mesh). (**E**) View of compound **3.1** from the entrance of spastin's ATP-binding site. Selected residues proximal to the inhibitor (<4 Å) and predicted hydrogen-bonding interactions (black dashed lines) are indicated. Distance between the C8 carbon of compound's **3.1** quinazoline and the carbonyl oxygen of the Asn-527 side chain is indicated (gray dashed line).

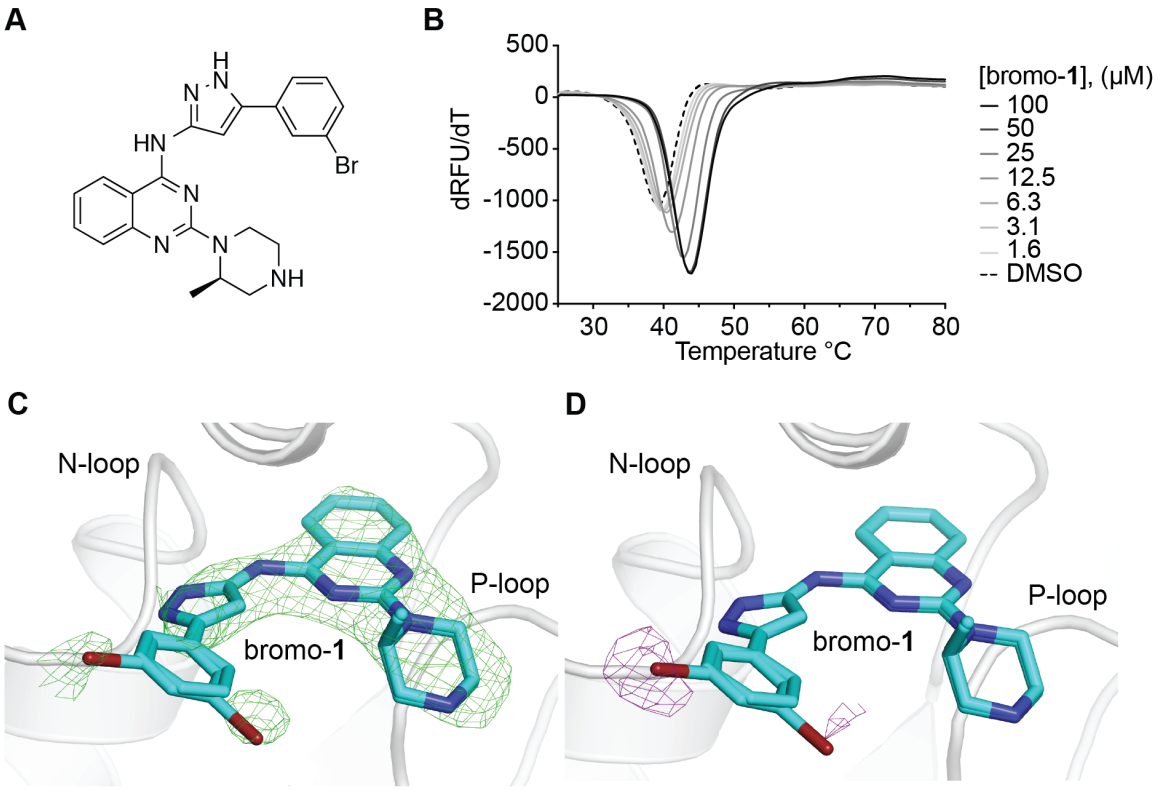


**Figure 3.3. X-ray structure of wild-type spastin bound to bromo-1, a pyrazolylaminoquinazoline-based spastin inhibitor.**

(**A**) Chemical structure of bromo-**1**. (**B**) Bromo-**1** concentration-dependent changes in melting temperature of the spastin-AAA-WT construct analyzed using differential scanning fluorimetry ($\Delta T_m$ = 4.3 ± 0.3 °C at highest concentration tested, 100 μM bromo-**1**, average ± range, n = 2; data from one experiment are shown). (**C-D**) Crystal structure of the spastin-AAA-WT-bromo-**1** complex (stick and ribbon representation). View of bromo-**1** **f**rom the entrance of spastin's ATP-binding site is shown. (**C**) The composite omit electron density map around bromo-**1** contoured at 2.5σ is shown ($mF_o - DF_c$; green mesh). (**D**) View of bromo-**1** from the entrance of spastin's ATP-binding site. (**D**) Bromine anomalous signal contoured at 3σ is shown (purple mesh).

**Crystal structure of wild-type spastin bound to a brominated pyrazolylquinazoline-based compound.**

To unambiguously confirm the orientation of quinazoline-based inhibitors in the active site we synthesized a pyrazolylquinazoline-based analog of compound **3.1** that has a meta-bromophenyl in place of the tert-butyl moiety on the pyrazolyl ring (hereafter referred to as bromo-**1**, Figure 3.3A). Determining structural model of this analog bound to spastin using X-ray crystallography should help confirm the inhibitor binding mode as bromine can be located unequivocally via anomalous scattering (Hendrickson, 1991; Tiefenbrunn et al., 2014).

We next examined binding of bromo-**1** to spastin-AAA-WT using differential scanning fluorimetry. Similar to compound **3.1**, these analyses revealed that bromo-**1** dose-dependently stabilizes the spastin-AAA-WT construct against heat-induced denaturation ($\Delta T_m$ = 4.3 ± 0.3 μM, average ± range, n=2, Figure 3.3B). Next, we set up crystallization trials of bromo-**1** and spastin-AAA-WT. We obtained diffracting crystals and determined the structure of the spastin-WT-bromo-**1** complex at 2.5 Å using molecular replacement (Table 3.1). We observed density in the active site that we could assign to the compound (Figure 3.3C). In addition, we detected anomalous signal near the N-loop motif, which could be assigned to the bromine substituent on the phenylpyrazolyl moiety (Figure 3.3D). In fact, we observe two peaks in the anomalous signal, which likely correspond to two predominant conformations of the meta-bromophenyl ring (Figure 3.3D). In this structural model, the orientation of both conformers of bromo-**1** match the binding mode of compound **3.1** we determined for

spastin-AAA-WT-compound **3.1** complex (Cα root-mean-square deviation [RMSD] ~0.24 Å, WT-compound **3.1** versus WT-bromo-**1**). Taken together, these data reveal how pyrazolylaminoquinazoline-based compounds interact with residues in the AAA active site.

**Designing and characterizing analogs of compound 3.1.**

Next, we examined whether the structures of spastin-AAA-WT–compound **3.1** and bromo-**1** complexes could guide the design of allele-specific inhibitors. The structures reveal that the side-chain amide of Asn-527 in the P-loop is proximal to the quinazoline's C8 hydrogen (the distance between the compound **3.1**'s C8 and the Asn-527 carbonyl oxygen is 3.8 Å; Figures 2.2E and 2.4A). We have reported that modifications of the quinazoline's C8 led to inhibitors with improved potency and selectivity toward human spastin (Cupido et al., 2019). Therefore, to probe the inhibitor interaction with the side-chain amide of Asn-527, we synthesized three analogues of compound **3.1** with modifications at C8 (compounds **3.2**–**3.4**; Figure 3.4B). These compounds were synthesized using established procedures (Statsuk et al., 2008). In compound **3.2**, we replaced the benzene ring of the quinazoline with a pyrrole so that the C–H bond is replaced by the N–H hydrogen-bond donor. In compound **3.3**, a pyridopyrimidine places a hydrogen-bond acceptor at C8, and in compound **3.4** the polarity at C8 is reversed, as fluorine replaces the hydrogen. We generated an ATPase-active spastin construct (amino acids 209–758, hereafter called spastin-WT) and tested its inhibition by these compounds. While the potency of compound **3.2** did

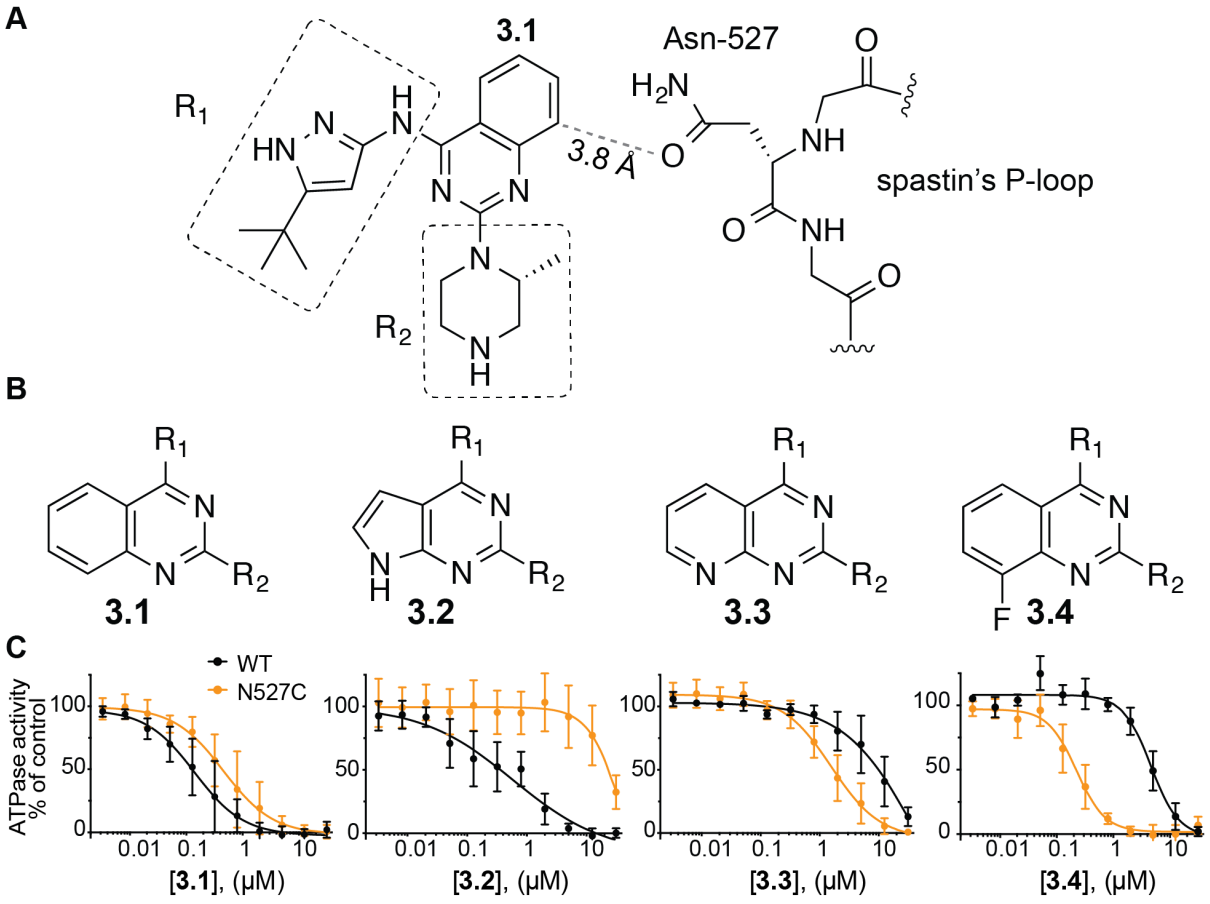


**Figure 3.4. Designing analogues of compound 3.1 to probe inhibitor interactions with a residue in spastin's P-loop.**

(**A**) Schematic of compound **3.1** in the ATP-binding site of spastin. Distance between quinazoline's C8 of compound **3.1** and Asn-527 side chain carbonyl oxygen is indicated. (**B**) Chemical structures of compound **3.1** analogues. (**C**) Concentration-dependent inhibition of spastin's ATPase activity (aa 209-758; wild-type, black; N527C mutant, orange) by compounds **3.1**-**3.4**. Percentage residual ATPase activity values relative to DMSO control were fit to a sigmoidal dose-response equation and $IC_{50}$ values were calculated ($IC_{50}$: WT-cmpd **3.1** = 0.21 ± 0.21 μM; N527C-cmpd **3.1** = 0.70 ± 0.81 μM; WT-cmpd **3.2** = 0.50 ± 0.48 μM; N527C-cmpd **3.2** = ~21 ± 5 μM; WT-cmpd **3.3** = 13.9 ± 9.8 μM; N527C-cmpd **3.3** = 1.91 ± 1.56 μM; WT-cmpd **3.4** = 4.84 ± 1.46 μM; N527C-cmpd **3.4** = 0.23 ± 0.11 μM.average ± s.d., n = 4, 0.5 mM MgATP). As complete inhibition of the spastin-N527C allele by compound **3.2** was not observed at the highest concentration tested, the $IC_{50}$ values for this compound were calculated by constraining the bottom parameter of the fit to 0. *Note - a subset of the ATPase assays in this figure were performed by Dr T. Cupido, postdoctoral fellow in the Kapoor laboratory).*

not substantially change, compounds **3.3** and **3.4** inhibited the wild-type spastin nearly 100-fold less potently (Figure 3.4C, black traces), indicating the importance of interactions between the quinazoline's C8 hydrogen and the side-chain amide of the Asn-527 residue.

We have found that the asparagine-527 can be mutated to a cysteine without disrupting spastin's ATPase activity (Cupido et al., 2019). Therefore, we reasoned that it could be suitable for the development of allele-specific inhibitors and tested analogues of compound **3.1** against the spastin-N527C construct. Compound **3.2** does not potently inhibit the ATPase activity of this spastin allele (Figure 3.4C, orange traces). However, compounds **3.3** and **3.4** more potently inhibit the spastin-N527C allele in comparison with the wild-type protein, with compound **3.4** being ~20-fold selective for the mutant allele (Figure 3.4C).

**Structural model of spastin-N527C bound to 8-fluoroquinazoline-based compound.**

To examine the structural basis for the selectivity of compound **3.4** for the spastin-N527C allele, we cocrystallized the spastin-AAA-N527C construct with compound **3.4** and determined the structure at ~2.2 Å resolution (Figure 3.5A and Table 3.1). The quinazoline core of compound **3.4** is positioned in the pocket with an orientation nearly identical to that of compound **3.1** (Figure 3.5B). The side-chain β-carbon and sulfur atoms of the Cys-527 residue also adopt similar positions as the β- and γ-carbon atoms of the Asn-527 residue in the structure of the wild-type protein with

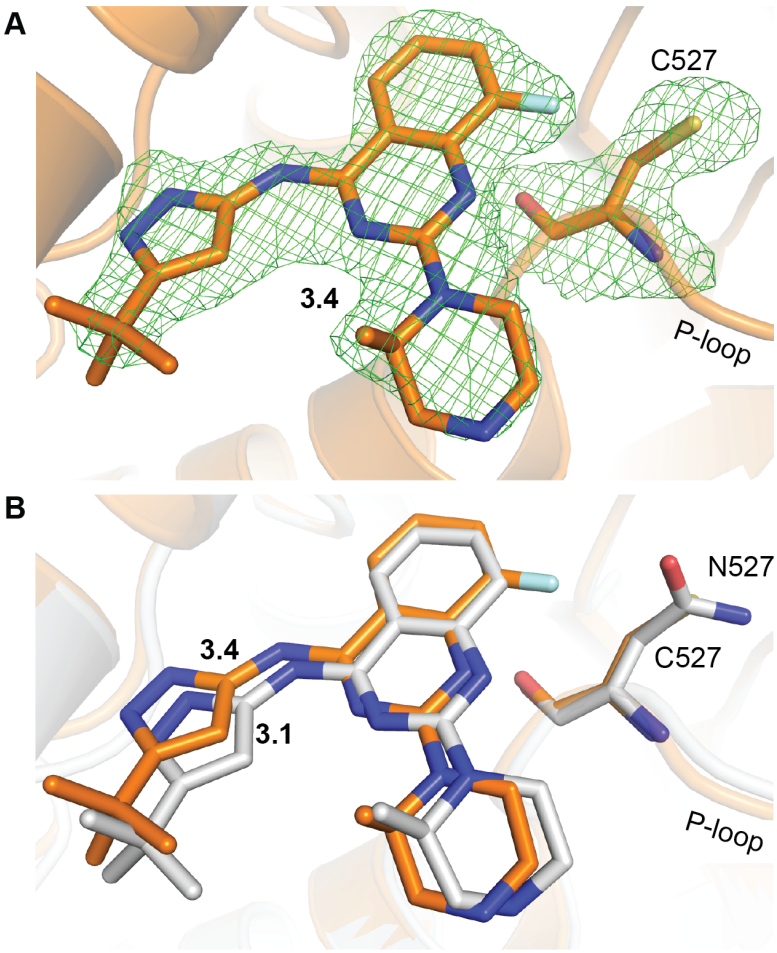


**Figure 3.5. X-ray structure of the spastin-N527C−compound 3.4 complex.**
(**A**) View of compound **3.4** in the active site of the spastin-N527C-compound **3.4** complex (stick and ribbon representation, carbon atoms in orange). The omit electron density map around the inhibitor and the Cys-527 residue contoured at 3σ is also shown ($mF_o - DF_c$, green mesh). (**B**) Overlay of wild-type (gray) and N527C (orange) spastin structures with bound compounds (**3.1** - gray; **3.4** -orange).

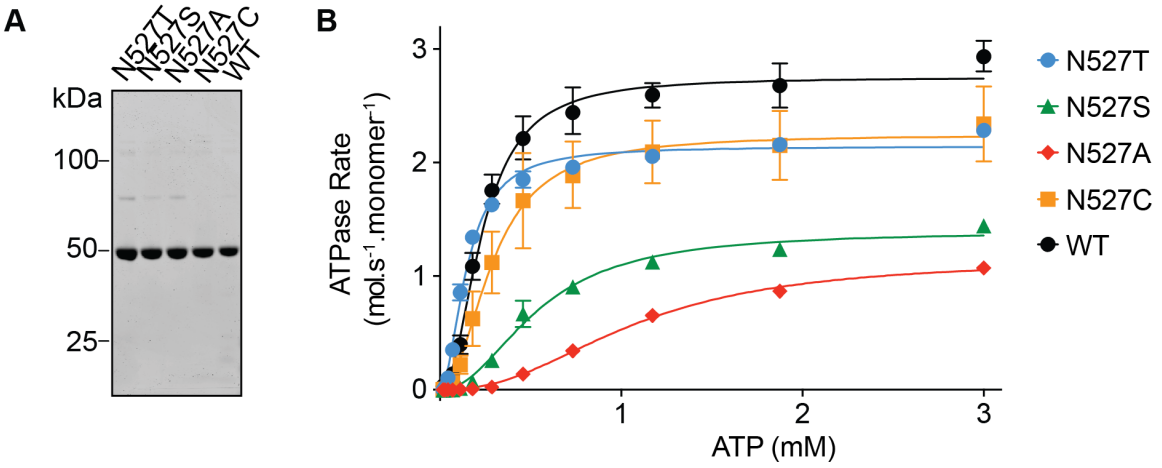


**C**

| | N527T | N527S | N527A | N527C | WT |
|---|---|---|---|---|---|
| $k_{cat}$ ($s^{-1}$) | 2.14 ± 0.02 | 1.39 ± 0.02 | 1.15 ± 0.06 | 2.24 ± 0.28 | 2.76 ± 0.13 |
| Hill coefficient | 1.93 ± 0.16 | 2.15 ± 0.19 | 2.36 ± 0.28 | 2.12 ± 0.09 | 2.01 ± 0.23 |
| $K_{1/2}$ (mM) | 0.15 ± 0.01 | 0.54 ± 0.05 | 1.07 ± 0.03 | 0.30 ± 0.04 | 2.23 ± 0.01 |

**Figure 3.6. Biochemical characterization of spastin wildtype and constructs with mutations of the 527 residue.**

(**A**) SDS-PAGE analysis (Coomassie blue) of purified recombinant spastin constructs (aa 209-758). (**B**) ATP-concentration dependence of the steady-state activity of wild-type (WT) and mutant spastin constructs, analyzed using an NADH-coupled assay. Rates (average ± s.d., n = 3) were fit to the Michaelis-Menten equation for cooperative enzymes (see Methods for details). (**C**) Enzyme activity parameters for recombinant wild-type and mutant spastin constructs (aa 209-758). Values for the catalytic turnover number ($k_{cat}$), the Hill coefficients and the ATP concentration required for half-maximal enzymatic rate ($K_{1/2}$) of the spastin constructs (average ± s.d., n = 3) were determined by fitting the enzyme rates from the NADH-coupled steady state assay to equation 1 (see Methods for details).

bound compound **3.1** (Figure 3.5B). The structure of the spastin-AAA-N527C–compound **3.4** complex shows clearly resolved density around the 8-fluoro atom that points toward the Cys-527 residue (Figures 3.5A, B). In principle, the cysteine side chain can form a covalent bond with the fluoro-substituted heterocycle. Our structural model indicates that this is not the case.

Organic fluorines can engage in n−π* interactions with carbonyl groups in protein-backbone amides as well as with carbonyls in the side chains of asparagine and glutamine residues (Kamer et al., 2013; Pollock et al., 2015). In addition, interactions of fluorine with sulfur-containing hydrophobic side chains, such as cysteine and methionine, have also been shown to contribute to compound binding (Bauer et al., 2016; Lange et al., 2015; Murray et al., 2008). To examine the interactions of compound **3.4** with residue 527, we generated three spastin constructs with mutations at this site (spastin-N527A, -S, and -T, Figure 3.6A) and tested their ATPase activities (Figure 3.6B). The catalytic turnover number ($k_{cat}$) and the ATP concentration required for half-maximal enzyme rate ($K_{1/2}$) of the N527T construct are within ~1.5-fold of those for the wild-type protein (Figure 3.6C). In contrast, the N527A and N527S mutant constructs have lower $k_{cat}$ (~3-fold) and higher $K_{1/2}$ (~5–7-fold) compared with wild-type spastin (Figure 3.6C). Next, we tested the inhibition of these mutant alleles by compound **3.4**. We found that the N527A, -S, and -T mutant constructs are inhibited ~15–100-fold less potently than the N527C allele, consistent with the importance of the fluorine–cysteine interaction (Figure 3.7A). As the N527S and N527A mutants have substantially lower enzyme activities than the wild-type construct, we also tested binding

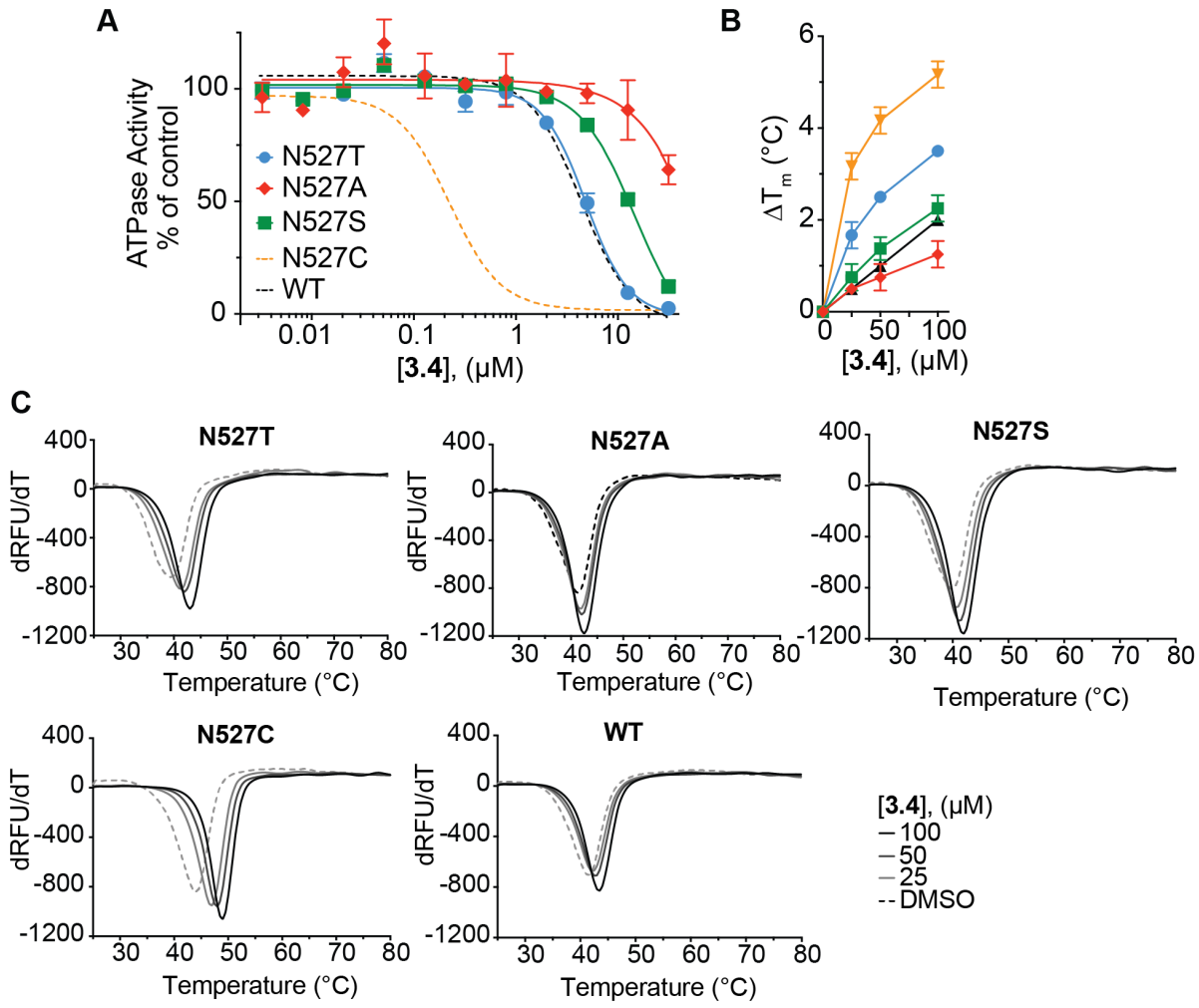


**Figure 3.7. Analyses of compound 3.4's binding to mutant spastin constructs.** (**A**) Concentration-dependent inhibition of N527 mutant alleles of spastin with compound **3.4**. For comparison, data for the wild-type and N527C mutant alleles (data from Figure 3.4C) are shown as dashed lines. Percentage residual ATPase activity values relative to DMSO control (average ± s.d., n = 3, 0.5 mM MgATP) were fit to a sigmoidal dose-response equation and $IC_{50}$ values were calculated ($IC_{50}$ (**3.4**): N527T = 4.87 ± 0.54 μM; N527S = 14.5 ± 0.7 μM). $IC_{50}$ values were not determined for the spastin-N527A allele as complete inhibition was not observed at the highest compound concentration tested. (**B, C**) Compound **3.4** concentration-dependent changes in melting temperature of the spastin-WT, -N527C, -N527T, -N527S and -N527A constructs (aa 209-758) analyzed using differential scanning fluorimetry (**B**, n = 2, 25, 50 and 100 μM compound **3.4**, 1% DMSO was used as a vehicle control). Data from one representative experiment for each construct are shown (**C**).

of compound **3.4** to the mutant alleles using differential scanning fluorimetry. We observed dose-dependent stabilization of the N527C mutant allele by compound **3.4**. Gratifyingly, we observed substantially reduced stabilization of the N527A, -S, and -T constructs (Figure 3.7B, C). Taken together, these data suggest that binding of compound **3.4** to the N527C mutant protein is likely due to favorable stereoelectronic interactions of the fluorine atom with the Cys-527 residue.

**Discussion.**

Designing the bump–hole approach involves two steps. First, binding sites of proteins need to be modified using mutations that do not disrupt activity. Our structural and biochemical data show how a spastin mutant allele alters the inhibitor's binding site while retaining ATPase activity. In principle, the P-loop residue at an equivalent site in other AAA proteins may also be similarly mutated to generate active alleles. Second, complementary modifications of an inhibitor need to be designed. Our studies reveal how a fluorine modification of a spastin inhibitor can generate a mutant-allele-selective compound. However, we find that compounds **3.1** and **3.4** are selective for spastin and do not inhibit the activity of four other closely related AAA proteins (i.e., Fidgetin-like 1, katanin, VPS4B, and VCP/p97; Figure 3.8A, B). Therefore, without substantial additional structure–activity analyses, this compound cannot be used to develop the bump–hole approach for other AAA proteins. As other chemical scaffolds that target the active site of AAA proteins have now been identified and more X-ray data are becoming available (Anderson et al., 2015; Tang et al., 2019), structure-guided approaches may

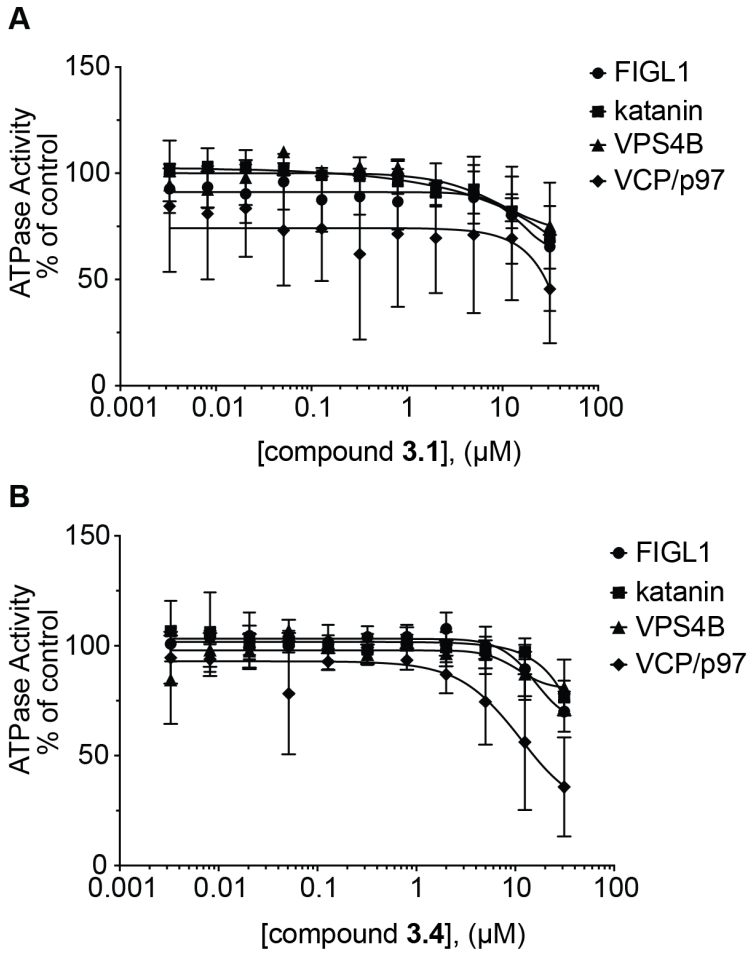


**Figure 3.8. Determining selectivity of compounds 3.1 and 3.4 against four AAA proteins.**

(**A**) Compound **3.1** and (**B**) compound **3.4** concentration-dependent inhibition of the steady-state ATPase activity of four AAA proteins related to spastin (Fidgetin-like 1 (FIGL1), katanin, VPS4B and VCP/p97; n = 2, 0.5 mM MgATP). $IC_{50}$ values were not determined as complete inhibition was not observed at the highest compound concentration tested. *Note - a subset of the ATPase assays in this figure were performed by Dr T. Cupido, postdoctoral fellow in the Kapoor laboratory).*

be used to identify suitable scaffolds. Together, our data suggest that tuning stereoelectronics may be effective for designing allele-specific chemical probes for AAA proteins based on these other scaffolds.

As mammalian cells express at least two isoforms of spastin that share a common AAA domain (Claudiani et al., 2005), allele-specific inhibitors will be powerful tools to dissect spastin's isoform-specific functions. Errors in spastin function have been linked to essential processes such nuclear envelope reformation during cell division and ER–endosome organization (Allison et al., 2017; Vietri et al., 2015). In addition, protein knockdown studies indicate that amyloid-β toxicity can be suppressed by loss of spastin function (Zempel et al., 2013). The allele-specific inhibitors reported here could be valuable starting points to develop chemical tools to evaluate the roles of spastin isoforms in cellular context.

**Table 3.1** | Data collection and refinement statistics.

| *spastin-AAA:*<br>*ligand:*<br>*pdbID:* | WT<br>compound **1**<br>**6NYV** | WT<br>Bromo-**1** | N527C<br>compound **4**<br>**6NYW** |
|---|---|---|---|
| **Data collection** | | | |
| Space group | $P6_5$ | $P6_5$ | $P6_5$ |
| Cell dimensions | | | |
| *a*, *b*, *c* (Å) | 79.2, 79.2, 97.1 | 79.5, 79.5, 97.9 | 78.5, 78.5, 96.5 |
| $\alpha, \beta, \gamma$ (°) | 90, 90, 120 | 90, 90, 120 | 90, 90, 120 |
| Resolution (Å) | 50.0-2.42 (2.46-2.42)* | 29.5-2.48 (2.54 – 2.48)* | 50.0-2.19 (2.23 – 2.19)* |
| $R_{merge}$ | 0.069 (0.656) | 0.013 (0.186) | 0.074 (0.595) |
| $\langle I \rangle / \sigma I$ | 53.6 (4.00) | 23.5 (3.07 | 38.5 (2.56) |
| Completeness (%) | 99.9 (100.0) | 99.6 (95.1) | 99.9 (100.0) |
| Multiplicity | 19.5 (19.4) | 19.4 (18.9) | 7.7 (7.5) |
| Total reflections | 256544 | 242124 | 134250 |
| Unique reflections | 13136 | 12493 | 17457 |
| CC1/2 | 99.5 (94.7) | 99.4 (79.2) | 99.2 (89.1) |
| | | | |
| **Refinement** | | | |
| Resolution (Å) | 39.61-2.43 | 25.21-2.50 | 39.35-2.19 |
| No. reflections | 13098 (1291) | 12179 (1212) | 17412 (1727) |
| No. refl. for Rfree | 1291 (129) | 1215 (125) | 1728 (170) |
| $R_{work}$ / $R_{free}$ | 0.1996/0.2448 | 0.2134/0.2690 | 0.1907/0.2304 |
| No. atoms | 2129 | 2123 | 2229 |
| Protein | 2031 | 2050 | 2065 |
| Ligands/ion | 40 | 73 | 57 |
| Water | 58 | 0 | 107 |
| *B*-factors | | | |
| Protein | 64.74 | 78.17 | 51.73 |
| Ligand/ion | 65.68 | 86.31 | 54.12 |
| Water | 68.81 | | 55.46 |
| R.m.s. deviations | | | |
| Bond lengths (Å) | 0.003 | 0.006 | 0.005 |
| Bond angles (°) | 0.82 | 0.86 | 0.67 |
| Clashscore | 10.12 | 6.85 | 5.47 |
| Rotamer Outliers | 0.51 | 1.02 | 1.47 |
| Ramachandran Favored (%) | 97.82 | 96.36 | 98.15 |
| Ramachandran Allowed (%) | 2.18 | 3.64 | 1.85 |
| Ramachandran Outliers (%) | 0.00 | 0.00 | 0.00 |

*Data in brackets indicate the high-resolution shell.

## Chapter 3 - Methods.

### Vectors for recombinant protein expression.

Vector for expression of *D. melanogaster* wild-type protein (residues 209-758, pDEST15-spastin-*D.melanogaster*) was obtained from Dr. Antonina Roll-Mecak (Roll-Mecak and Vale, 2008). The P-loop N527C, T, S and A mutants were generated by site-directed mutagenesis (Quikchange XL Kit, Agilent) using the pDEST15-spastin-*D.melanogaster* vector as template and verified by Sanger sequencing. Vector for expression of *X. laevis* katanin was obtained from Dr Rebecca Heald (UC Berkeley) (Loughlin et al., 2011). Plasmids for expression of mouse VCP/p97, human Fidgetin-like 1 and human VPS4B proteins were generated as described in (Cupido et al., 2019). Vector for expression of the spastin AAA domain was generated using standard molecular biology techniques. Briefly, the coding sequence for *D.melanogaster* AAA domain (spastin-AAA, residues 445-758) was PCR amplified (CloneAmp HiFi, Clontech) from pDEST15-spastin-*D.melanogaster* plasmid and cloned into pDEST15 vector using AscI and ApaI sites to generate N-terminal GST-fusion constructs. Full coding sequences for all recombinant constructs were verified by Sanger sequencing.

### Protein expression and purification.

*D.melanogaster* spastin (residues 209-758) wild-type and mutants, *Hs*-FIGL1, *Xl*-katanin, *Hs*-VPS4B and *Mm*-VCP/p97 were expressed, purified and assayed as described (Cupido et al., 2019; Roll-Mecak and Vale, 2008). All reagents were

molecular biology grade or better and were purchased from Sigma Aldrich unless indicated otherwise.

*D.melanogaster* spastin AAA domain (residues 445-758) wild-type and mutant constructs were expressed and purified as follows. Briefly, *E.coli* Rosetta cells were grown in Miller's LB medium (LMM, Formedium, cat #LMM105) to $O.D._{600}$ ~ 0.8 at 30°C, chilled to 18°C and the protein expression was induced with 0.5 mM IPTG (GoldBio, cat#I2481) overnight (14-16 hours). The cells were re-suspended in lysis buffer (50 mM Tris.HCl pH = 8.0, 400 mM NaCl, 10 mM $MgCl_2$, 1 mM PMSF, 5 mM β-mercaptoethanol, 0.001% triton-X and 1 tablet of Roche complete protease inhibitor cocktail per 50 ml of buffer), supplemented with 0.1 µg / ml lysozyme and 5 U / ml benzonase followed by lysis using a probe sonicator or Emulsiflex-C5 homogenizer (Avestin, 5-10 cycles at 10-15 kPsi). The lysate was spun at 45,000 rpm for 45 min at 4°C in Ti-45 rotor using Beckman Coulter Optima LE-80K ultracentrifuge. The clarified supernatant was incubated with glutathione agarose resin (GoldBio, cat#G-250-10) for 1 hr. Beads were washed with ~300 ml of wash buffer (50 mM Tris.HCl pH = 8.0, 400 mM NaCl, 10 mM $MgCl_2$, 5 mM β-mercaptoethanol) and the protein was eluted by on-beads cleavage using PreScission protease. Cleaved protein was diluted 2-fold with low salt buffer (20 mM Tris.HCl pH = 8.2, 40 mM NaCl, 5 mM $MgCl_2$, 5 mM β-mercaptoethanol), loaded onto HiTrap™ Q HP column (GE Healthcare) and eluted with high salt buffer (20 mM Tris.HCl pH = 8.0, 500 mM NaCl, 5 mM $MgCl_2$, 5 mM β-mercaptoethanol). Both constructs eluted around 180-200 mM NaCl. The protein was further purified over a HiLoad 16/60 Superdex 200 column (GE Healthcare) in SEC buffer (20 mM

HEPES-NaOH pH = 7.4, 100 mM NaCl, 5 mM $MgCl_2$, 2 mM TCEP, 25 mM $(NH_4)_2SO_4$) and the selected fractions were concentrated using Amicon 30 kDa MWCO device to 10-20 mg $ml^{-1}$. The PreScission cleavage did not leave any non-native residues at the N terminus.

**Analyses of ATPase activity.**

Steady-state ATPase activity of Dm-spastin (aa 209-758) was analyzed using the NADH-coupled assay. The time course of fluorescence decrease corresponding to the consumption of the NADH was measured using a Synergy NEO Microplate Reader ($\lambda_{ex}$ = 340 nm, 440 nm emission filter). The fluorescence values were plotted against time and fit by linear regression to obtain a rate of fluorescence decrease. The ATPase rate was calculated from the background (no ATP) corrected rates of fluorescence decrease using an ADP calibration curve. Percent inhibition of the ATPase activity was calculated by normalizing the rate of background-corrected fluorescence decrease in the presence of compounds to DMSO control. Final conditions for spastin wild type and N527 mutants (protein concentration: 50-75 nM): 25 mM HEPES-KOH pH 7.5, 225 mM KCl, 20 mM $(NH_4)_2SO_4$, 5 mM $MgCl_2$, 2.5 mM DTT, 0.005% triton-X, BSA 0.1 mg/ml, 175-200 μM NADH, 1 mM phosphoenolpyruvate, 15-30 U/ml lactate dehydrogenase, 15-30 U/ml pyruvate kinase. All ATPase assays were performed in the presence of 0.5 mM MgATP. Equations used for data fitting are described in Chapter 2 - Methods section. All solution stocks for testing compound activity were made in DMSO.

**Differential Scanning Fluorimetry.**

These experiments were carried out on a C1000 Touch Thermal cycler CFX-96 instrument (GE Healthcare). Spastin-WT, -N527C, T, S and A (aa 209-758) or spastin-AAA-WT and -N527C (aa 445-758) recombinant constructs were diluted to a final concentration of 7-10 µM in 25 mM HEPES-KOH (pH 7.5), 225 mM KCl, 5 mM $MgCl_2$, 20 mM $(NH_4)_2SO_4$, 2.5 mM DTT, 0.005% triton-X and assayed in a 96-well plate (Hard-shell® HSP9665 Bio-Rad). Compounds were added (0.8 µM to 100 µM, 1-2.5% DMSO). SYPRO® Orange (Sigma S5692, excitation 490 nm, emission 590 nm) was used at 1:500 to 1:1000 dilution. The temperature was linearly increased with a step of 0.5 ºC for 55 minutes, from 25 ºC to 95 ºC and fluorescence readings were taken at each interval. Melting temperatures were recorded as the minimum value of the first derivative of the fluorescence vs temperature curves (dRFU/dT).

**Isothermal titration calorimetry (ITC).**

ITC measurements were performed using a MicroCal auto-iTC200 calorimeter (MicroCal, LLC). Briefly, purified spastin-AAA-WT construct (aa 445-758) was dialyzed against 20 mM HEPES-KOH (pH 7.5, at 4ºC), 100 mM NaCl, 5mM $MgCl_2$, 50 mM $(NH_4)_2SO_4$, 1 mM TCEP, for 12 h at 4 °C. A solution of compound (100 µM) dissolved in dialysis buffer was titrated into a solution of the dialyzed protein (15 µM, 200 µl) in the ITC chamber. ITC titrations were carried out at 25 ºC, while stirring at 275 rpm, by an initial injection of 0.4 µl followed by 19 injections of 1.5 µl of compound, with the duration of 4 sec (per injection) and a spacing of 150 s. The heat of dilution was

determined by independent titrations (buffer into protein) and was subtracted from the experimental data. The collected data were analyzed in the AFFINImeter software as previously described (Dumas et al., 2016), and plotted using Prism (Version 6.0, GraphPad Software Inc). Dissociation constants from each titration were obtained employing a single-site equilibrium-binding model.

**Co-crystallization of *Drosophila* spastin-AAA constructs with compounds.**

Spastin-AAA constructs (WT or N527C) were concentrated to ~20 mg/ml and mixed in 1:1 ratio with a saturated solution (~200 μM) of compound **3.1**, bromo-**1** or **3.4** in SEC buffer. Saturated solutions of compounds were prepared by dissolving the HCl salt of each compound in SEC buffer and spinning down any undissolved residue. The protein-compound complex was incubated on ice and mixed with 0.1 M Na-acetate pH 5-6.5, 2% PEG-4000, 15% MPD using a hanging drop method. The crystals were allowed to form at 14-18 °C for 2-3 days. Obtained crystals were cryo-protected in a solution of the reservoir supplemented with 20% MPD prior to flesh freezing in liquid nitrogen.

**Data collection and refinement.**

Data for all structures were collected at NSLS-II 17-ID-1 and 2 (AMX and FMX) beamlines at Brookhaven National Laboratory at 100 K, and processed with HKL2000. The resolution cutoff was determined by considering values of $R_{merge}$ (<0.7 in the high resolution shell) and I/σ (>1.5 in the high resolution shell). The structures were solved

by molecular replacement with PHASER (McCoy et al., 2007) (as part of the PHENIX software package (Adams et al., 2010)). All structures were solved from independently obtained data for individual crystals by molecular replacement using apo spastin (3B9P) as a template. The model was rebuilt and refined using COOT (Emsley et al., 2010) and phenix.refine software (Afonine et al., 2012). In all crystals the asymmetric unit contains a single molecule of the protein with the hexameric symmetry embedded in the crystal lattice. During refinement ~10% of reflections were assigned as $R_{free}$ for each dataset by the Phenix.refine software and not used in any further refinement steps. Data collection and refinement statistics are shown in Table 3.1. Simulated annealing composite omit maps were computed in Phenix from protein models without ligands and overlayed with a model with the ligand. Figures were generated in MacPyMOL (Schrodinger LLC, http://www.pymol.org) and UCSF Chimera (Pettersen et al., 2004).

The crystal structures of spastin-inhibitor complexes solved in this study have been deposited in the RCSB protein data bank (PDB: 6NYV and 6NYW).

**Chemical synthesis information**

For general procedures see Chapter 2 - Methods section.

**Compound synthesis and characterization.**

Synthetic procedures for compounds **3.1**, bromo-**1**, **3.3** and **3.4** were identical. As an example we show synthesis of compound **3.4:**

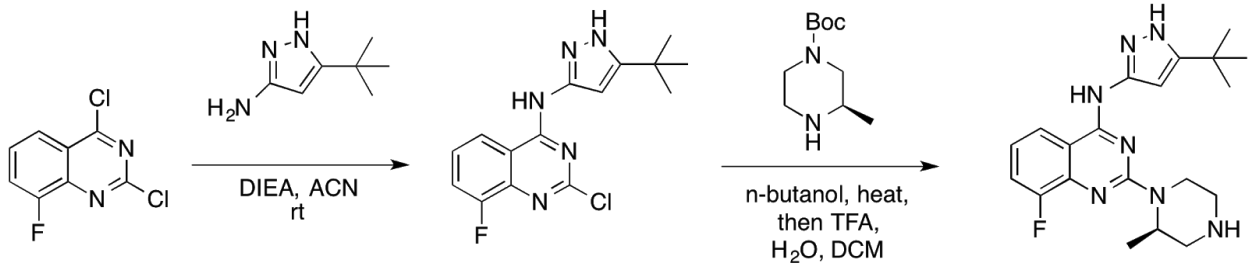


Synthesis of compound **3.4**, (*R*)-*N*-(5-(*tert*-butyl)-1*H*-pyrazol-3-yl)-8-fluoro-2-(2-methylpiperazin-1-yl)quinazolin-4-amine. *Step 1.* To a stirring solution of 5-(*tert*-butyl)-1*H*-pyrazol-3-amine (80 mg, ~0.57 mmol) and DIEA (1 eq) in ACN (2.5 mL) in a round bottom glass flask at rt, a solution of 2,4-dichloro-8-fluoroquinazoline (100 mg, ~0.5 mmol) and DIEA (1 eq) in ACN (2 ml) was added dropwise and the mixture was stirred for 36 h. Then, an equal volume of distilled water was added while stirring at rt. After 30 min, a precipitate was collected, filtered and washed in a sequential manner with approximately 5 mL of the following solvents: 1- $H_2O$:ACN (1:1), 2- aqueous sodium hydroxide (pH ~10), 3- $H_2O$:ACN (1:1), and finally dried to obtain *N*-(5-(*tert*-butyl)-1*H*-pyrazol-3-yl)-2-chloro-8-fluoroquinazolin-4-amine. MS-ESI [M+1]: expected 302.8, found 302.2. *Step 2.* Without further purification, 50 mg of this intermediate (~0.17 mmol) were dissolved in dry n-butanol (2 ml) and 10 µl of 37% HCl were added while stirring at rt. Then, *tert*-butyl (*R*)-3-methylpiperazine-1-carboxylate (0.25 mmol, 1.5 eq) was dissolved in n-butanol (0.5 ml) and added to the mixture. The reaction was heated to 100ºC for 5 h while stirring and then cooled down to rt. The excess solvent was evaporated under reduced pressure, and the product of the reaction

was washed with hexane, and dried. The solid residue was washed with aqueous HCl (pH ~3) for 15 min while stirring. A precipitate was collected, dissolved in a mixture of DCM:TFA:$H_2O$ (5:4.5:0.5) and stirred for 1 h at rt. The solvent was evaporated under reduced pressure and the product washed with diethylether twice. A precipitate was collected, dissolved in aqueous sodium hydroxide (pH ~12) and extracted with EtOAc. The organic solution was washed with brine, dried over $Na_2SO_4$, and filtered. The volume of EtOAc solution containing the desired product was reduced to 1.0 ml and the product precipitated by adding 20 µl of 37% HCl in water, washed once with EtOAc (5 mL), once with acetone (1 mL), and finally dried to obtain compound **3.4** as HCl salt, in ~15% total yield.

**Compound characterization data.**

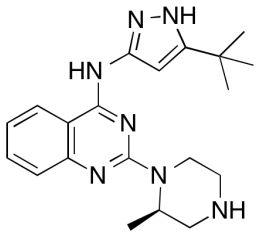


Compound **3.1** (also referred to as compound **2.5** in chapter 2).

(*R*)-*N*-(5-(*tert*-butyl)-1*H*-pyrazol-3-yl)-2-(2-methylpiperazin-1-yl)quinazolin-4-amine hydrochloride salt. Molecular weight (MW) expected for $C_{20}H_{27}N_7$: 365.5; MS-ESI [M+1]: found 366.0. $^1$H NMR (400 MHz, DMSO-$d_6$) δ 13.36 (s, 1H), 11.54 (s, 1H), 10.04 (d, *J* = 10.5, 1H), 9.73 (d, *J* = 11.0, 1H), 8.66 (d, *J* = 8.3, 1H), 8.26 (d, *J* = 8.4, 1H), 7.87 (t, *J* =

7.8, 1H), 7.49 (t, *J* = 7.7, 1H), 6.45 (s, 1H), 5.19 (s, 1H), 4.92 (d, *J* = 14.6, 1H), 3.63 (t, *J* = 13.5, 1H), 3.33 (d, *J* = 15.5, 3H), 3.13 (d, *J* = 11.3, 1H), 1.50 (d, *J* = 7.0, 3H), 1.32 (s, 9H). $^{13}$C NMR (600 MHz, DMSO-$d_6$) δ 157.84, 153.64, 151.91, 145.52, 140.54, 135.78, 125.61, 124.79, 118.35, 110.27, 95.87, 46.65, 45.67, 42.20, 37.52, 31.32, 30.39, 15.66.

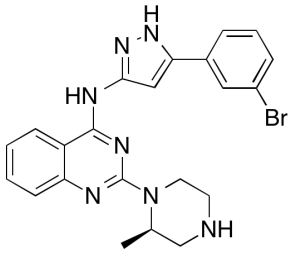


Compound bromo-**1.**

(R)-N-(5-(3-bromophenyl)-1H-pyrazol-3-yl)-2-(2-methylpiperazin-1-yl)quinazolin-4-amine

MS-ESI [M+1]: expected for $C_{22}H_{22}N_7Br$ 464.4, found 464.2+466.3 (bromine pattern).

$^1$H NMR (600 MHz, DMSO-$d_6$) δ 11.42 (s ,br, 1H), 9.53 (s, 1H), 9.10 (s, 1H), 8.60 (d, *J* = 7.26, 1H), 8.02 (s, br, 1H), 7.87 (t, *J* = 6.78, 1H), 7.79 (d, *J* = 7.74, 1H), 7.73 (d, *J* = 5.82, 1H), 7.60 (d, *J* = 7.98, 1H), 7.47 (m, 2H), 7.12 (s, 1H), 5.09 (s, br, 1H), 4.64 (d, *J* = 14.1, 1H), 3.53 (m, 1H), 3.45 (d, *J* = 12.12, 1H), 3.39 (d, *J* = 12.66, 1H), 3.33 (s, br, 1H), 3.16 (s, br, 1H), 1.45 (d, *J* = 6.96, 3H).

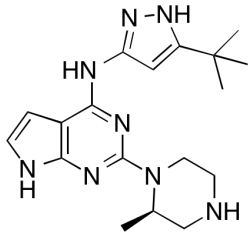

Compound **3.2.**

(*R*)-*N*-(5-(*tert*-butyl)-1*H*-pyrazol-3-yl)-2-(2-methylpiperazin-1-yl)-7*H*-pyrrolo[2,3-*d*]pyrimidin-4-amine. MS-ESI [M+1]: expected for $C_{18}H_{26}N_8$ 354.5, found 355. $^1$H NMR (600 MHz, DMSO-$d_6$) δ 11.93 (s, 1H), 10.91 (s, 1H), 9.50 (s, 1H), 6.63 (m, 3H), 4.46 (dd, *J* = 33.1, 11.8, 2H), 2.92 (d, *J* = 10.8, 1H), 2.71 (dt, *J* = 30.1, 10.2, 3H), 2.40 (t, *J* = 11.2, 1H), 1.30 (s, 9H), 1.02 (d, *J* = 6.0, 3H). $^{13}$C NMR (600 MHz, DMSO-$d_6$) δ 159.12, 153.63, 153.45, 152.35, 148.48, 118.41, 99.75, 96.91, 93.90, 60.20, 52.45, 50.61, 45.74, 45.04, 31.27, 30.46, 19.91, 0.64.

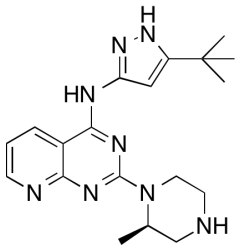


Compound **3.3**.

(*R*)-*N*-(5-(*tert*-butyl)-1*H*-pyrazol-3-yl)-2-(2-methyl-4λ$^4$-piperazin-1-yl)pyrido[2,3-*d*]pyrimidin-4-amine, hydrochloride salt. MS-ESI [MH$^+$]: expected for $C_{19}H_{26}N$ 366.5, found 367. $^1$H NMR (400 MHz, DMSO-$d_6$) δ 11.47 (s, 1H), 9.95 (d, *J* = 9.2 Hz, 1H), 9.64 (br, 1H), 9.43 (d, *J* = 8 Hz, 1H), 7.59 (t, *J* = 7.2 Hz, 1H), 6.54 (s, 1H), 5.19 (s, br, 1H), 4.81 (d, *J* = 14 Hz, 1H), 3.73-3.29 (m, br, 25H ,water contamination), 3.09 (d, *J* = 10.8 Hz, 2H), 1.52 (d, *J* = 7 Hz, 3H), 1.35 (s, 9H).

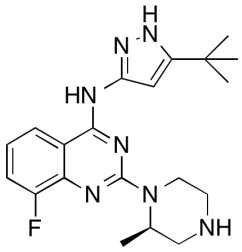

Compound **3.4**.

(*R*)-*N*-(5-(*tert*-butyl)-1*H*-pyrazol-3-yl)-8-fluoro-2-(2-methyl-4λ$^4$-piperazin-1-yl)quinazolin-4-amine, hydrochloride salt. MS-ESI [MH$^+$]: expected for $C_{20}H_{26}FN_7$ 383.5, found 384. $^1$H NMR (400 MHz, DMSO-$d_6$) δ 11.05 (s, br, 1H), 9.92 (s, br, 1H), 9.52 (s, br, 1H), 8.37 (d, *J* = 8.4 Hz, 1H), 7.63 (t, *J* = 8.4 Hz, 1H), 7.29 (m, 1H), 6.48 (s, 1H), 5.08 (s, 1H), 4.66 (d, *J* = 13.6 Hz, 1H), 3.44-3.00 (m, 4H), 1.42 (d, *J* = 7.2 Hz, 3H), 1.32 (s, 9H).

## Chapter 4: Analyzing resistance to design diaminotriazole-based inhibitors of AAA proteins.

*Note to readers: A closely related version of this work was published in Pisa R et al., Cell Chem. Biol., 2019, 26, 1-11; DOI: 10.1016/j.chembiol.2019.06.001. Except for results explicitly credited to others, I performed all experiments and analysis.*

### Introduction.

Enzyme active sites are common binding sites for chemical inhibitors, as compounds can mimic substrates or cofactors to compete for occupancy (Copeland, 2004). Active sites are typically comprised of conserved structural motifs and amino acid sequences and their overall steric and stereoelectronic features can be similar across enzymes within a protein family (Endicott et al., 2012; Wendler et al., 2012). For some protein families, such as kinases, a wealth of high-resolution structural data for how different chemical scaffolds interact with residues in conserved active sites has enabled the design of selective chemical inhibitors (Ferguson and Gray, 2018). However, the relatively low resolution (3-4 Å) of structures for many proteins, including members of AAA (ATPases associated with diverse cellular activities) family (Erzberger and Berger, 2006), can limit their use for rational inhibitor design (Davis et al., 2008) and additional approaches are needed to identify the key interactions determining inhibitor potency and specificity (Erlanson et al., 2019).

Proteins in the AAA family carry out critical tasks in various cellular processes including DNA unwinding and replication, protein unfolding or membrane remodeling (Bleichert et al., 2017; van den Boom and Meyer, 2018; McCullough et al., 2018). For a few AAA proteins, chemical inhibitors have been identified by screening compound libraries (Anderson et al., 2015; Chou et al., 2011; Firestone et al., 2012; Kawashima et al., 2016; Magnaghi et al., 2013). In most cases, the inhibitor binding sites have been mapped to the AAA domain, the core enzymatic module of AAA proteins (Wendler et al., 2012), either in the active site (Anderson et al., 2015; Cupido et al., 2019; Magnaghi et al., 2013) or in an allosteric site (Banerjee et al., 2016; Magnaghi et al., 2013; Pöhler et al., 2018). Structural models for a few inhibitor-bound AAA proteins are also now available (Banerjee et al., 2016; Boyaci et al., 2016; Pisa et al., 2019a; Tang et al., 2019). However, for many AAA proteins the key inhibitor-target interactions needed for the design of selective chemical inhibitors are not known.

We have recently focused on spastin, a microtubule-severing AAA protein whose functions have been linked to several cellular processes including nuclear envelope reformation and cytokinesis (Connell et al., 2009; Vietri et al., 2015). In addition, blocking spastin function has been shown to reduce amyloid-β toxicity in a model for Alzheimer's disease (Zempel et al., 2013). Therefore, chemical inhibitors would be valuable tools to probe spastin functions in normal physiology and disease. We recently designed spastazoline, a potent and selective inhibitor of spastin (Cupido et al., 2019). To design this pyrazolylpyrrolopyrimidine-based inhibitor, we analyzed compound activity against biochemically active mutant alleles of spastin. We reasoned that mutant

alleles that alter the potency of compounds would reveal key compound-target interactions and guide the selection of robust inhibitor-protein binding models. From a collection of heterocyclic scaffolds that could mimic key hydrogen-bonding interactions made by adenine in the AAA active site, we identified a pyrazolyl-based scaffold. Testing this compound against wild-type (WT) and mutant spastin alleles revealed key interactions that we used to select a robust model from computational docking solutions. We used the selected inhibitor-spastin binding model to design modifications of the core scaffold and generated spastazoline, a potent and selective inhibitor of spastin (Cupido et al., 2019). Structural models we generated by X-ray crystallography confirmed the predicted binding models (Pisa et al., 2019a). However, it remains unclear if our approach, which we now name RADD (for Resistance Analysis During Design), can be used to identify binding site interactions of inhibitors based on different chemical scaffolds and if the target-binding modes we predict are accurate.

Here, we focus on applying RADD to diaminotriazole-based compounds, which are chemically unrelated to spastazoline. Testing compound activity against WT and mutant spastin alleles identified key interactions that contribute to inhibitor binding. Our approach also indicated that a more potent derivative binds spastin in a distinct pose, essentially oriented ~180° relative to the starting compound. High-resolution X-ray structures of these two different diaminotriazole-based compounds confirmed the inhibitor-spastin interactions predicted by RADD. Together, these data suggest how biochemical analyses of resistance against chemical inhibitors can be leveraged to determine the key inhibitor-protein interactions in conserved active sites and can

establish potential resistance-conferring mutations in the target at the start of the inhibitor design process.

**Results.**

**Using RADD to examine binding of diaminotriazole-based and quinolinone-based inhibitors to spastin.**

In our efforts to identify different chemical scaffolds that inhibit AAA proteins we found a diaminotriazole-based compound JNJ-7706621 (hereafter referred to as compound **4.1**; also referred to as compound **2.2** in chapter 2) and a quinolinone-based compound dovitinib (also known as CHIR258 or TKI258, Figure 4.1A, B). Both compounds are known inhibitors of kinases (Lin et al., 2005; Trudel et al., 2005) and our initial screens indicated that these compounds inhibit spastin as well as other AAA proteins (Cupido et al., 2019). A dose-dependent analysis for wild-type spastin (WT) inhibition revealed an $IC_{50}$ = 5.8 ± 0.6 μM for compound **4.1** and $IC_{50}$ = 13.7 ± 0.8 μM for dovitinib (average ± s.d., n = 3, 0.5 mM MgATP, Figure 4.1C). Further analyses of spastin-WT inhibition, across a range of ATP concentrations, revealed that both compounds increased the apparent $K_{1/2}$ for ATP without altering the $k_{cat}$ (Figures 4.1D, E and Tables 4.1 and 4.2), indicating an ATP competitive mechanism of inhibition that is consistent with binding of these compounds in spastin's nucleotide-binding site.

The first step of RADD is to analyze compound activity against alleles that have mutations in the putative compound binding site of the target enzyme but retain biochemical activity. We have found that active mutant alleles of spastin can be

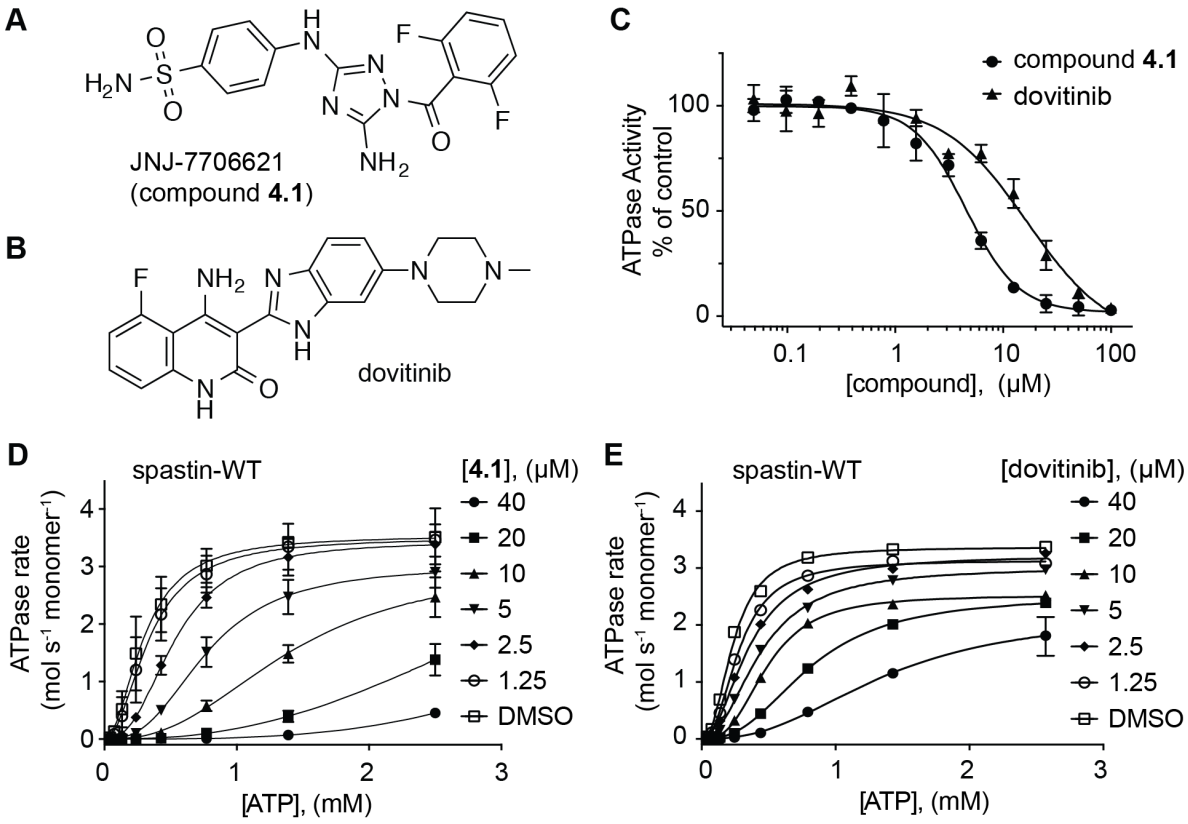


**Figure 4.1. Characterizing chemical scaffolds that inhibit spastin.**

(**A-B**) Chemical structures of diaminotriazole-based compound **4.1** (JNJ-7706621, **A**) and quinolinone-based dovitinib (**B**). (**C**) Concentration-dependent inhibition of the steady-state ATPase activity of spastin wild-type (WT) by compound **4.1** and dovitinib. Graph shows average values ± s.d. (n = 3) fit to a sigmoidal dose-response equation (compound **4.1**, $IC_{50}$ = 5.8 ± 0.6 μM; dovitinib, $IC_{50}$ = 13.7 ± 0.8 μM; average ± s.d, n = 3, 0.5 mM MgATP). (**D-E**) ATP concentration-dependence of the steady-state ATPase activity of spastin at different concentrations of compound **4.1** (**D**) and dovitinib (**E**), analyzed using an NADH-coupled assay. Average values (compound **4.1**: n = 3, error bars denote s.d.; dovitinib: n = 2, error bars denote range) were fit to the Michaelis-Menten equation for cooperative enzymes (see Methods). Enzyme activity parameters determined for each condition are provided in Tables 4.1 and 4.2.

**Table 4.1**

| [compound **4.1**], (μM) | $k_{cat}$ | Hill coefficient | $K_{1/2}$ |
|---|---|---|---|
| 40 | n.d. | n.d. | n.d. |
| 20 | n.d. | n.d. | n.d. |
| 10 | 3.1 (0.6) | 2.5 (0.2) | 1.4 (0.1) |
| 5 | 3.0 (0.3) | 2.8 (0.2) | 0.8 (0.1) |
| 2.5 | 3.5 (0.4) | 2.6 (0.2) | 0.5 (0.1) |
| 1.25 | 3.6 (0.6) | 2.2 (0.1) | 0.4 (0.1) |
| DMSO | 3.5 (0.03) | 2.2 (0.2) | 0.2 (0.01) |

**Table 4.2**

| [dovitinib], (μM) | $k_{cat}$ | Hill coefficient | $K_{1/2}$ |
|---|---|---|---|
| 40 | 2.3 (1.1) | 2.6 (0.7) | 1.4 (0.6) |
| 20 | 2.5 (0.01) | 2.5 (0.03) | 0.8 (0.1) |
| 10 | 2.5 (0.1) | 2.8 (0.1) | 0.5 (0.03) |
| 5 | 3.0 (0.6) | 2.2 (0.4) | 0.4 (0.1) |
| 2.5 | 3.2 (0.1) | 2.1 (0.3) | 0.3 (0.1) |
| 1.25 | 3.1 (0.1) | 2.3 (0.1) | 0.3 (0.03) |
| DMSO | 3.4 (0.1) | 2.3 (0.04) | 0.2 (0.01) |

**Tables 4.1 and 4.2. Characterizing chemical scaffolds that inhibit spastin.**
ATP concentration-dependence of the steady-state ATPase activity of spastin-WT (*Drosophila melanogaster* spastin, aa 209-758, see Methods for details) at different concentrations of compound **4.1** (**Table 4.1**) and dovitinib (**Table 4.2**), analyzed using a steady-state NADH-coupled assay. To calculate enzyme activity parameters, rates were plotted against ATP concentration and data were fit to the Michaelis-Menten equation for cooperative enzymes (see Methods for details). Range of ATP concentrations tested was 0.04 to 2.5 mM (dilution factor: 1.8). The data from each experiment were fit separately and the enzyme activity parameter values were determined. Average values for apparent enzyme activity parameters including $k_{cat}$, Hill coefficient and $K_{1/2}$ are provided (compound **4.1**: average, s.d. in parentheses, n = 3, n.d. = not determined; dovitinib: average, range in parentheses, n = 2).

engineered in three structural motifs in spastin's active site (the N-loop, the P-loop, and the sensor-II motif) by substituting the relatively less conserved residues, which we named variability hotspots, with residues found at equivalent positions in related AAA proteins (Cupido et al., 2019). Here, we focus on three alleles with mutations in spastin's variability hotspots (Q488V, N527C and T692A) that we had previously characterized (Cupido et al., 2019) (Figure 4.2A). We found that a sensor-II mutation (T692A) increased the potency of compound **4.1** by ~7-fold (Figure 4.2B). In contrast, mutations in the N loop (Q488V) and the P loop (N527C) hotspot residues led to less than 2-fold changes in inhibitor potency (Figure 4.2B). To further characterize binding of compound **4.1** to spastin alleles, we used differential scanning fluorimetry. For these assays we focused on a truncated construct including only spastin's AAA domain (aa: 445–758, *Drosophila melanogaster* spastin, hereafter, spastin-AAA; Figure 4.2C) that we had characterized (Pisa et al., 2019a). A dose-dependent increase in the melting temperature of spastin-AAA constructs in presence of compound **4.1** was observed (Figures 4.2D and 4.7A-D). Gratifyingly, the spastin-AAA-T692A construct was stabilized by compound **4.1** more substantially than the WT, N527C, and Q488V constructs ($\Delta T_m$: T692A ~6.2°C; WT ~4.5°C; N527C ~4.3°C; Q488V ~4.5°C, 100 μM compound **4.1**, DMSO was used as a vehicle control; Figures 4.2D and 4.7A-D) indicating that compound **4.1** binds spastin-AAA-T692A with higher affinity compared to the other alleles. These data suggest that compound **4.1** interacts with the side chain of the sensor-II hotspot residue in spastin's active site and does not substantially interact with those of the N-loop and P-loop hotspot residues (Figure 4.2E).

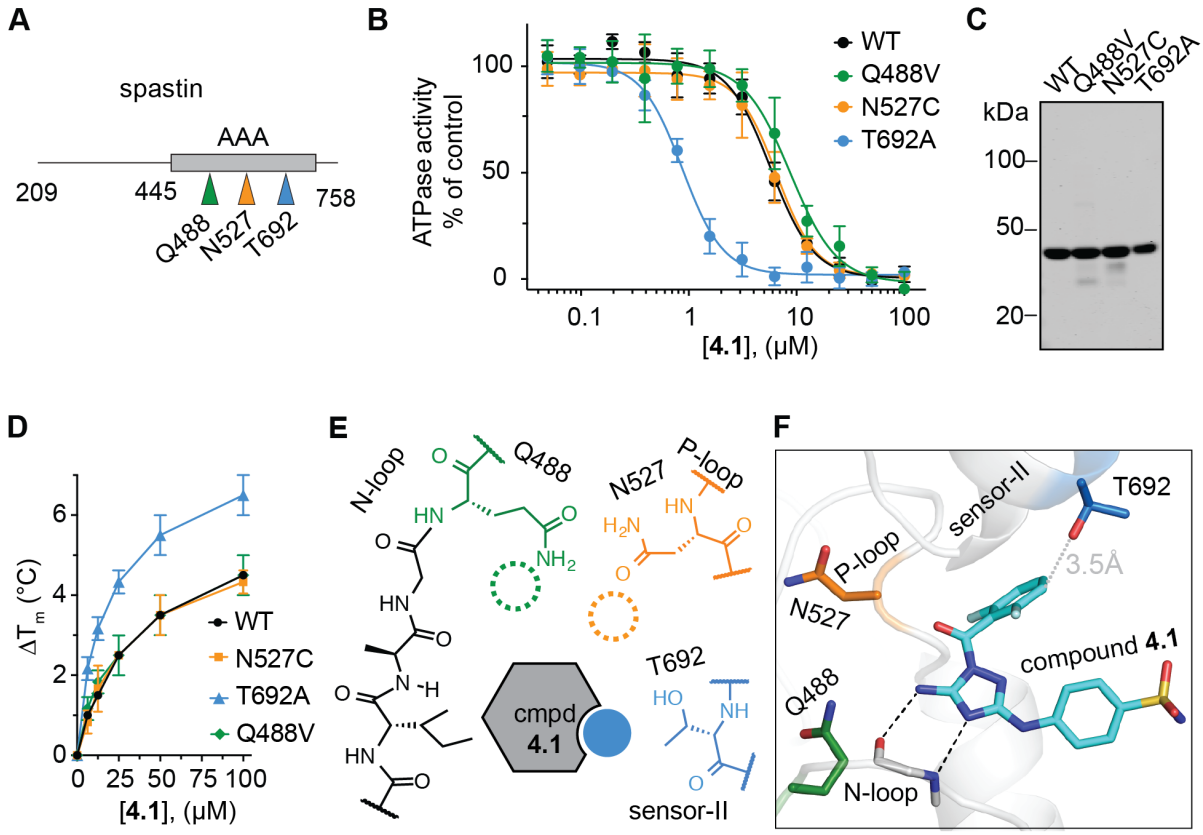


**Figure 4.2. Using RADD to analyze binding of compound 4.1 to spastin.**

(**A**) Schematic shows the AAA domain (gray box) of the recombinant spastin construct used for ATPase assays. The positions of three variability hotspot residues are highlighted (colored arrows). The first and last residues of the construct are also indicated (aa: 209–758). (**B**) Compound **4.1** concentration-dependent inhibition of the steady-state ATPase activity of three spastin constructs with mutations at variability hotspot residues (Q488V, N527C, and T692A). Graphs show average values ± SD (n = 3) fit to a sigmoidal dose-response equation. $IC_{50}$ values: spastin-WT, 5.7 ± 0.6 μM; -Q488V, 8.9 ± 0.5 μM; -N527C, 6.0 ± 1.0 μM; and -T692A, 0.9 ± 0.1 μM; average ± SD, n = 3; 0.5 mM MgATP. For comparison, analysis of the inhibition of WT (data from Figure 4.1C, black line) is also shown. (**C**) SDS-PAGE analysis (Coomassie blue) of purified spastin-AAA-WT and constructs with mutations in variability hot-spot residues (Q488V, N527C, and T692A). Legend continues on next page.

**Figure 4.2. Using RADD to analyze binding of compound 4.1 to spastin - cont'd.** (**D**) Concentration-dependent effect of compound **4.1** on the heat-induced denaturation of spastin-AAA constructs analyzed by differential scanning fluorimetry. Observed $\Delta T_m$: -WT ~4.5 °C; -N527C ~4.3 °C; -Q488V ~4.5 °C; -T692A ~6.2 °C, 100 mM compound **4.1**, average values are shown, error bars denote range, n = 2. (**E**) Schematic for predicted interactions between compound **4.1** and the variability hotspot residues based on analyses of the inhibition of spastin alleles (filled circle, predicted interaction; dashed circles, predicted weak or no interaction). (F) Computational docking model (ribbon and stick representation) of compound **4.1** in the active site of spastin that is consistent with the observed activity of the compound against spastin alleles (for details see Figure 4.3 and the Methods). Predicted hydrogen-bonding network between the diaminotriazole core of compound **4.1** and spastin's N-loop motif is shown (black dashed lines). The spastin variability hotspot residues (Gln-488, Asn-527, and Thr-692) are also shown. The distance between the compound and the side chain of the sensor-II variability hotspot residue is indicated (gray dotted line).

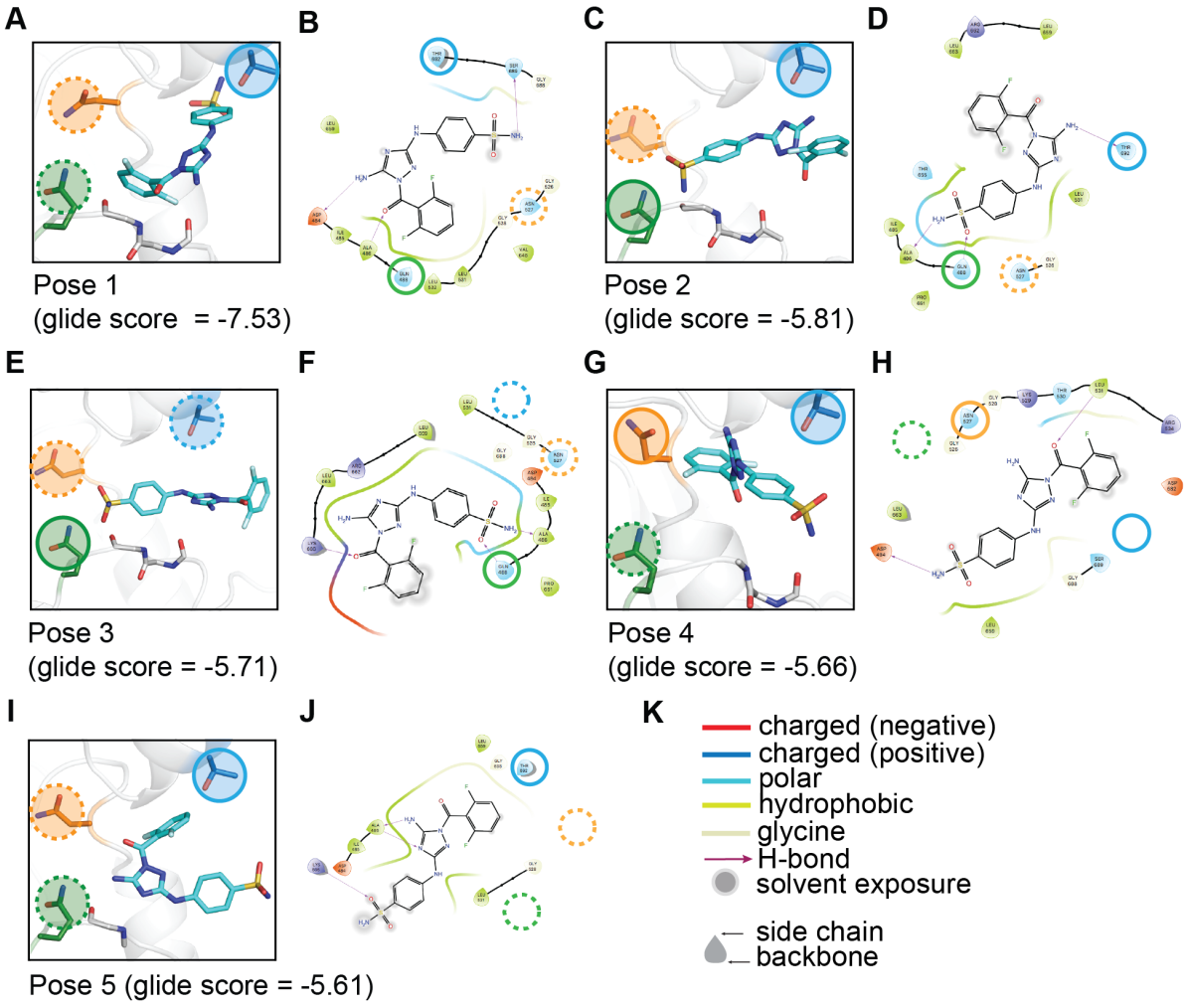


**Figure 4.3. Computational docking of compound 4.1 in spastin's active site.**
(**A**-**J**) Computational docking models for compound **4.1** bound to spastin. Five top scoring poses for compound **4.1** docked in the ATP site of spastin are shown (A, C, E, G and I). See Chapter 4 Methods for details how these models were generated. Interaction maps for each pose are also shown (B, D, F, H and J; for details see panel K). The expected positions of three variability hotspot residues are highlighted by circles (Q488 – green, N527 – orange, T692 – blue; residue-compound distance < 4 Å: full circle, > 4 Å: dotted circle). Pose 5 (**I** and **J**) is also shown in Figure 4.2. *Note - data in this figure were generated together with Dr Tommaso Cupido, postdoctoral fellow in the Kapoor laboratory.*

Next, we performed computational docking of compound **4.1** on a conformational ensemble of apo spastin (PDB: 3B9P) obtained from molecular dynamics simulations (see Methods for additional details). These analyses suggested several possible orientations of compound **4.1** in the active site (Figure 4.3) with computed docking scores within ~2 kcal/mol. In four of the five top-scoring models, compound **4.1** establishes hydrogen-bonding interactions with the protein backbone of the spastin N loop (Figure 4.3). In one of the poses, the diaminotriazole core establishes contacts with the N loop of spastin in a manner that is analogous to ATP (pose 5; Figure 4.2F and Figure 4.3I, J). We noted that in this pose compound **4.1** is also proximal to the sensor-II residue (Thr-692; side chain to compound distance, <4 Å), while the side chains of variability hotspot residues in the N loop (Gln-488) and P loop (Asn-527) are positioned further away from the compound (side chain to compound distance, >4 Å; Figure 4.2F). This pose, in which the difluorobenzoyl substituent of the compound **4.1** is proximal to the Thr-692 sensor-II side chain and the phenylsulfonamide substituent points out from the AAA domain toward the bulk solvent (Figure 4.2F), is consistent with the changes in activity of compound **4.1** observed against spastin alleles. Therefore, we rejected the other poses with similar or even more favorable docking scores as they were not consistent with analyses of inhibition of spastin alleles. This model of compound **4.1** bound in the active site of spastin is different from our RADD models for pyrazolylaminoquinazoline-based spastin inhibitors, which we have confirmed by X-ray crystallography (Cupido et al., 2019; Pisa et al., 2019a). Importantly, mutant alleles conferring resistance to the pyrazolylaminoquinazoline-based inhibitors are different

from those that alter potency of compound **4.1**, consistent with these compounds binding differently to spastin.

**Crystal Structure of Spastin-N527C Bound to Compound 4.1**

To test the binding pose for compound **4.1** predicted by our RADD approach, we sought to determine the crystal structure of the spastin-compound **4.1** complex. Our trials with the spastin-AAA WT construct in the presence of compound **4.1** did not yield any diffracting crystals. As increased thermal stability of proteins has been shown to improve the likelihood of crystallization (Dupeux et al., 2011), we examined the stability of spastin-AAA constructs against heat-induced denaturation using differential scanning fluorimetry and determined their melting temperature ($T_m$). Spastin-AAA-WT has a $T_m$ of ~38.5°C, the sensor-II mutation (T692A) does not substantially alter stability ($T_m$ ~39°C) and the N loop mutation (Q488V) causes a modest reduction of this construct's melting temperature ($T_m$ ~34.5°C) (Figure 4.4A). Remarkably, we found that the P-loop mutation (N527C) stabilizes spastin in the differential scanning fluorimetry assay ($T_m$ ~42°C) (Figure 4.4A). As compound **4.1** inhibits the ATPase activity of the N527C allele of spastin with nearly identical potency as the WT protein (Figure 4.2B, D), we set up crystallization trials of spastin-AAA-N527C in the presence of compound **4.1**.

We obtained diffracting crystals and determined the structure of the spastin-compound **4.1** complex at ~2.30 Å resolution using molecular replacement (Table 4.5). We observed a density, in the pocket between the large and small AAA subdomain (Figure 4.4B) and could assign it to the compound. In this model, the

diaminotriazole core of compound **4.1** is positioned to form a network of three hydrogen-bonding interactions with the backbone atoms of residues Asp-484 and Ala-486 in spastin's N loop (Figure 4.4C). The phenylsulfonamide substituent is proximal to a hydrophobic residue in the large AAA subdomain (Leu-531) at the entrance of the ATP-binding site and the difluorobenzoyl moiety contacts the side chain of Thr-692, the variability hotspot residue in the sensor-II motif (Figure 4.4D). In particular, one fluorine atom in the difluorobenzoyl moiety is oriented toward the Thr-692 hydroxyl group (fluorine to hydroxyl oxygen distance: ~3.2 Å; Figure 4.4E). In contrast, the N loop (Gln-488) and P loop (Cys-527) variability hotspot residues are located >4 Å away from the compound (Figure 4.4E), which is consistent with mutations at these sites not having a substantial effect on the inhibition of spastin's ATPase activity by compound **4.1**. As the Cys-527 residue is not proximal to compound **4.1**, we hypothesize that the binding mode of compound **4.1** is not altered by the N527C mutation and is likely similar in the WT protein. Together, these structural data match our RADD model for compound **4.1** bound in the active site of spastin.

**Crystal Structure of Spastin-N527C bound to Dovitinib**

To determine the binding mode of dovitinib in the active site of spastin we first examined activity of the compound against three mutant alleles of spastin with mutations at variability hotspot residues (Q488V, N527C and T692A). We found that inhibition of these alleles was not substantially altered by dovitinib (Figure 4.5A). Consistently, dovitinib only weakly stabilizes the spastin-AAA-N527C mutant against

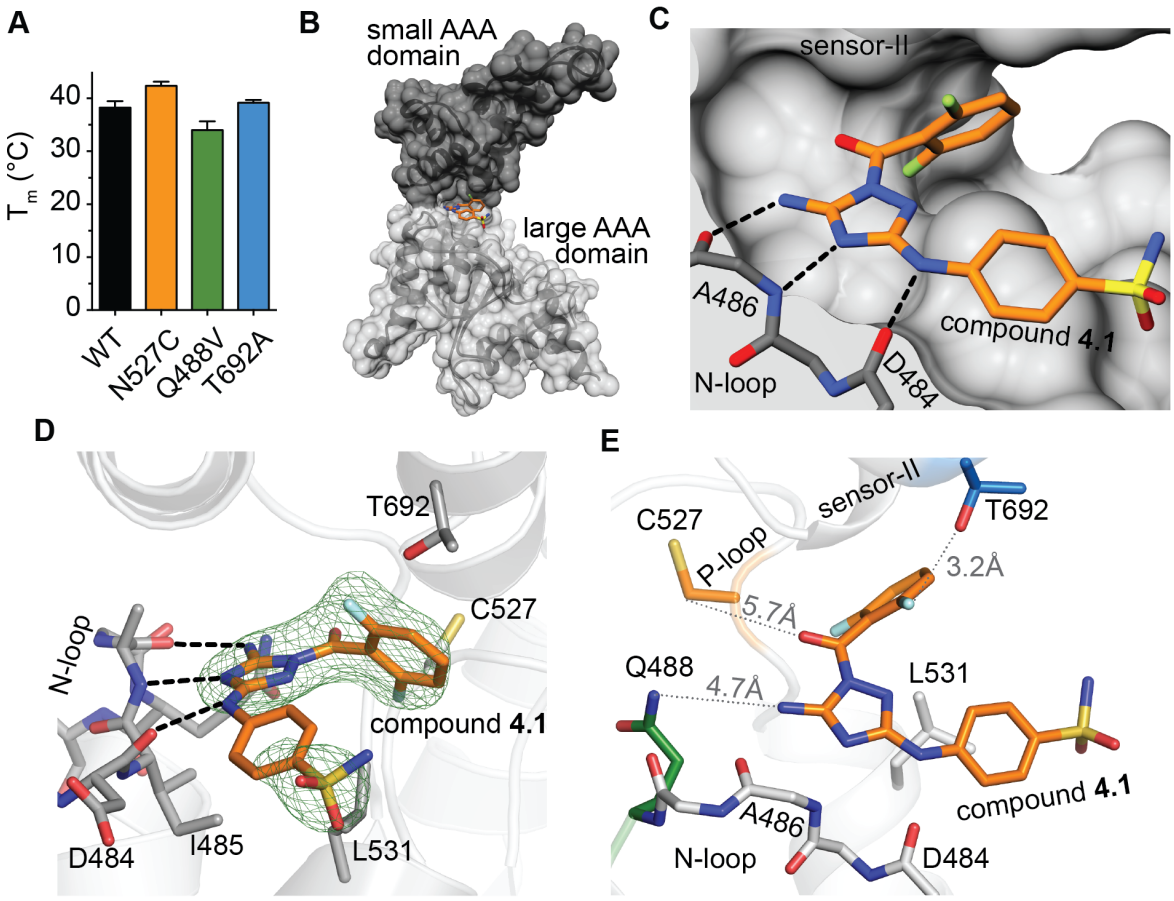


**Figure 4.4. Crystal structure of the spastin variability hotspot mutant (N527C) bound to compound 4.1 matches the RADD model.**

(**A**) Melting temperature of spastin-AAA-WT, -Q488V, -N527C and T692A constructs analyzed using differential scanning fluorimetry (n = 2; error bars denote range; observed $T_m$ for spastin-AAA-WT: ~38.5°C; -Q488V: ~34.5°C; -N527C: ~42°C; -T692A: ~39°C). (**B**) Structural model of the spastin-AAA-N527C- compound **4.1** complex (surface and stick representation, generated using UCSF Chimera). Small and large AAA subdomains are indicated (black and gray). (**C**) Compound **4.1** in the active site of spastin-N527C (surface and stick representation). Predicted hydrogen-bonding interactions are shown (black dashed lines). (**D-E**) Views of compound **4.1** in the active site of spastin-N527C. The variability hotspot residues in the N-loop, P-loop and the sensor-II motifs are highlighted (Gln-488, green; Cys-527, orange; Thr-692, blue). N-loop backbone atoms and a residue at the entrance of the active site (Leu-531) are also shown. Predicted hydrogen-bonding interactions (**D**, black dashed lines) and simulated annealing omit electron density map around compound **4.1** contoured at 3σ are shown (**D**, green mesh). Distances between the side chains of variability hotspot residues (Gln-488, Cys-527, and Thr-692) and compound **4.1** are indicated (**E**, gray dotted lines).

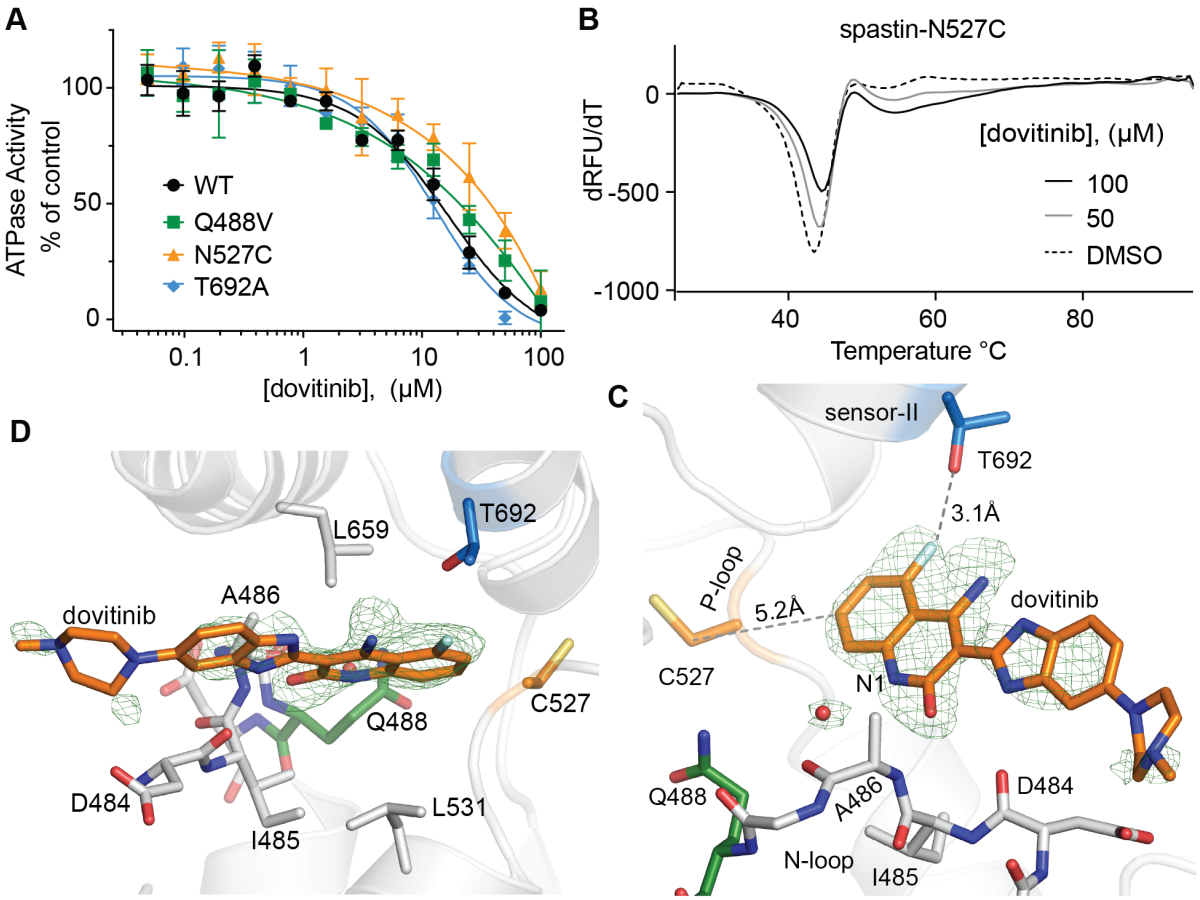


**Figure 4.5. Crystal structure of the spastin variability hotspot mutant (N527C) bound to dovitinib.**

(**A**) Concentration-dependent inhibition of spastin wild-type (WT) and three constructs with mutations at variability hotspot residues (Q488V, N527C, and T692A) by dovitinib. Graphs show average values ± s.d. (n = 3) fit to a sigmoidal dose-response equation. $IC_{50}$ values: spastin-WT, 13.7 ± 0.8 μM; -Q488V, 17.4 ± 4.5 μM; -N527C, 28.9 ± 5.3 μM; and -T692A, 11.5 ± 2.2 μM; average ± s.d., n = 3; all ATPase assays were performed at 0.5 mM MgATP. (**B**) Differential scanning fluorimetry analysis of the melting temperature of spastin-AAA-N527C construct in the presence of dovitinib ($\Delta T_m$ ~1 °C, 100 μM dovitinib, n = 2). (**C-D**) Structural model of spastin-N527C-dovitinib complex. Views of dovitinib in the active site of spastin-N527C. The variability hotspot residues in the N-loop, P-loop and the sensor-II motifs are highlighted (Gln-488, green; Cys-527, orange; Thr-692, blue). N-loop backbone atoms and residues at the entrance of the active site (Leu-531 and Leu-659) are also shown. Simulated annealing omit electron density map around dovitinib contoured at 3σ is shown (green mesh). Distances between the side chains of variability hotspot residues (Cys-527, and Thr-692) and dovitinib are indicated (**C**, gray dotted lines).

heat-induced denaturation ($\Delta T_m$ = ~1 °C at highest dose tested, 100 μM dovitinib, Figure 4.5B). Together, these data suggest that dovitinib does not substantially interact with side chains of these three variability hotspot residues.

To further characterize binding of dovitinib to spastin we setup co-crystallization trials with spastin-AAA-N527C. We obtained diffracting crystals and determined the structure of spastin-N527C-dovitinib complex at 2.4 Å resolution (Table 4.5). We observed a density in the ATP-pocket that could be assigned to the quinolinone core and the benzimidazole substituent of dovitinib (Figure 4.5C, D). However, we were not able to assign a density to the methylpiperazine moiety as it is likely oriented away from the active site and projects into the bulk solvent (Figure 4.5C, D).

In this structural model, dovitinib is positioned to make a network of hydrogen bonding interactions with the backbone amides of the N-loop residues Asp-484 and Ala-486. Interestingly, the predicted hydrogen bonding interaction between the quinolinone nitrogen (N1) and the amide carbonyl oxygen of Ala-486 is mediated by a water molecule that is well resolved in the structure (Figure 4.5C, D). This binding mode is not observed in structural models of spastin-inhibitor complexes with diaminotriazole- or quinazoline-based compounds.

Similar to the structure of spastin-N527C-compound **4.1**, the variability hotspot residues in the N-loop and P-loop are positioned further away from dovitinib and do not directly engage with the inhibitor scaffold (inhibitor-residue distance: >4 Å,Figure 4.5D). This is consistent with our analyses of dovitinib activity against spastin constructs with mutations in the N-loop and P-loop variability hotspot residues (Figure 4.5A).

Interestingly, the 5-fluoro substituent of the quinolinone ring of dovitinib is positioned proximal to the sensor-II variability hotspot residue (Thr-692, residue to compound distance: 3.5 Å, Figure 4.5C). However, this interaction is likely weak as potency of dovitinib against the sensor-II mutant allele (T692A) in the ATPase assays is not substantially altered in comparison to the wild-type protein. Taken together, these analyses show how dovitinib binds in spastin's active site. However, as dovitinib is less potent inhibitor of spastin's ATPase activity in comparison to compound **4.1** and spastazoline we did not examine dovitinib further.

**Using RADD to Examine Binding of Compound 4.1 Derivatives to Spastin**

To further examine our structural models, we synthesized and tested analogs of compound **4.1** (Figure 4.6A). We modified the difluorobenzoyl and phenylsulfonamide substituents while keeping the diaminotriazole core, as it forms a key hydrogen-bonding network with the backbone of spastin's active site residues (Figure 4.6B). Changes of the difluorobenzoyl moiety result in modest (~2-fold) changes in potency (compound **4.2**: $IC_{50}$ = 2.77 ± 0.39 μM, average ± s.d., n = 3; Figures 4.6B, C). In contrast, modifications of the phenylsulfonamide can lead to >10-fold higher potency. In particular, we identified compound **4.3**, in which a meta-N-methylamide group replaces the para-sulfonamide, which inhibits spastin with submicromolar potency ($IC_{50}$ = 0.45 ± 0.03 μM, average ± s.d., n = 3; Figure 4.6B, C). We combined substitutions from compounds **4.2** and **4.3** and synthesized compound **4.4**. This compound inhibits spastin-WT ~40-fold more potently than compound **4.1** ($IC_{50}$ = 0.23 ± 0.02 μM, average

± s.d., n = 3; Figure 4.6B, C). Additional structure activity relationships of compound **4.1** analogs binding to spastin are shown in Table 4.3.

To examine how compound **4.4** binds spastin, we used our RADD approach and tested the inhibitor against spastin constructs with mutations at variability hotspot residues in the N loop, P loop, and sensor-II motifs (Figure 4.6D). Surprisingly, we observe a different pattern of compound **4.4** activity against these mutant alleles in comparison to compound **4.1**. We found that the mutation in the N loop (Q488V) reduces compound **4.4** potency ~11-fold in comparison with the WT protein (Figure 4.6D). Similarly, the P loop mutation (N527C) reduces the potency ~4-fold (Figure 4.6D). We note that the same N-loop and P-loop mutations did not substantially alter the potency of compound **4.1** (Figure 4.2B). In contrast, the mutation of the sensor-II variability hotspot residue (T692A), which sensitizes spastin to inhibition by compound **4.1**, did not change the potency of compound **4.4** (Figure 4.6D). We also examined the direct binding of compound **4.4** to spastin-AAA mutant alleles using differential scanning fluorimetry. We found that compound **4.4** stabilizes WT and T692A constructs more substantially than the N-loop (Q488V) and P-loop (N527C) constructs (Figures 4.6E and Figure 4.7E-H). Taken together, these analyses indicate that compound **4.4** binds in the active site of spastin differently than compound **4.1** (Figure 4.6F).

To examine specificity of compound **4.4**, we tested the inhibitor against three AAA proteins related to spastin (katanin, fidgetin-like 1, and VPS4B; Figures 4.6G and Table 4.4). We found that compound **4.4** at 2 μM concentration potently inhibits spastin

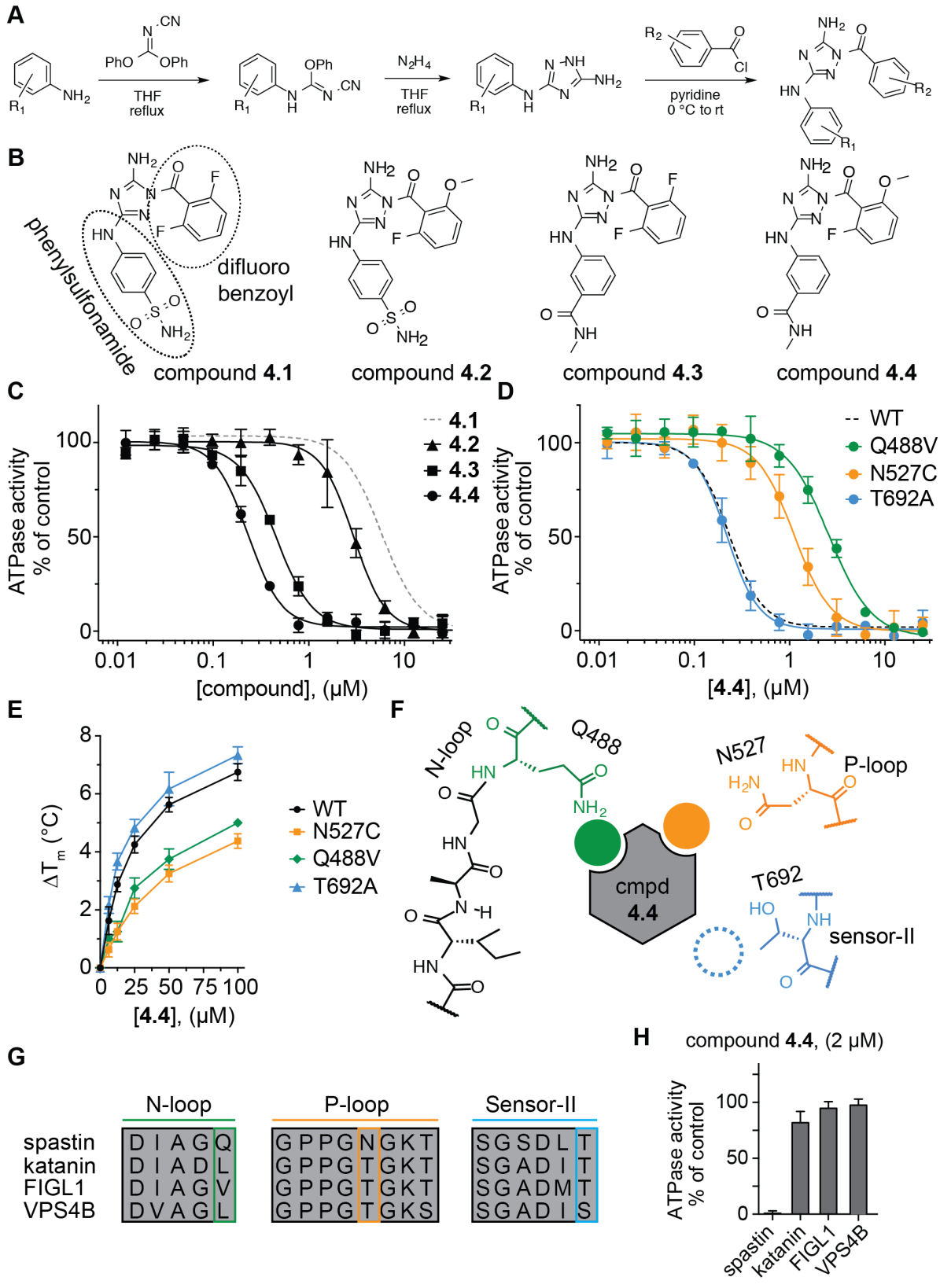


**Figure 4.6. Characterizing analogs of compound 4.1.**

**Figure 4.6. Characterizing analogs of compound 4.1.**

(**A**) Schematic for the synthesis of compound **4.1** analogs (adapted from Malerich et al, 2010). (**B**) Chemical structures of compounds **4.1**–**4.4**. (**C**) Compound concentration-dependent inhibition of the steady-state ATPase activity of spastin-WT. Graph shows average values ± s.d. (n = 3) fit to a sigmoidal dose-response equation. For comparison, the curve for compound **4.1** (data from Figure 4.1C) is also shown (gray dashed line). Compound **4.2**, $IC_{50}$ = 2.77 ± 0.39 μM; compound **4.3**, $IC_{50}$ = 0.45 ± 0.03 μM; compound **4.4**, $IC_{50}$ = 0.23 ± 0.02 μM (average ± s.d., n = 3, 0.5 mM MgATP). (**D**) Compound **4.4** concentration-dependent inhibition of the steady-state ATPase activity of three spastin constructs with mutations at variability hotspot residues (Q448V, N527C, and T692A). Graph shows average values ± s.d. (n = 3) fit to a sigmoidal dose-response equation. For comparison, the corresponding curve for spastin-WT is shown (dashed line, data from Figure 4.5C). $IC_{50}$ values: spastin-Q488V, 2.60 ± 0.15 μM; -N527C, 1.11 ± 0.21 μM; and -T692A, 0.22 ± 0.04 μM; average ± s.d., n = 3, 0.5 mM MgATP.

(**E**) Concentration-dependent effect of compound **4.4** on the heat-induced denaturation of spastin-AAA constructs analyzed by differential scanning fluorimetry. Observed $\Delta T_m$: -WT ~6.7 °C; -N527C ~4.5 °C; -Q488V ~5.0 °C; -T692A ~7.2 °C, 100 mM compound **4.4**, average values are shown, error bars denote range, n = 2. (**F**) Schematic for the expected compound **4.4** interactions with variability hotspot residues in the active site of spastin (filled circles, predicted interaction; dashed circle, predicted weak or no interaction). Variability hotspot residues in three structural motifs are shown (N-loop, green; P-loop, orange; sensor-II, blue). (**G**) Sequence alignment of nucleotide-binding motifs (N-loop, P-loop, and sensor-II) in four AAA proteins. Variability hotspot residues are highlighted (green, orange, and blue rectangles). (**H**) Percent steady-state ATPase activity of four AAA proteins in the presence of compound **4.4** (2 μM, 0.5 mM MgATP, average values are shown, error bars denote range, n = 2).

**A**

| ID | $R_1$ | $R_2$ | $IC_{50}$ (μM) |
|---|---|---|---|
| (**4.2**) | 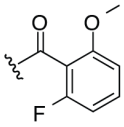 | 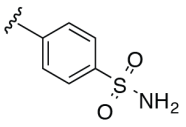 | 2.8 ± 0.4 |
| (**4.7**) | 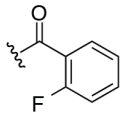 | 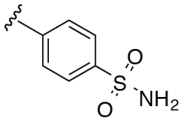 | 8.4 ± 2.7 |
| (**4.8**) | 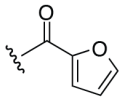 | 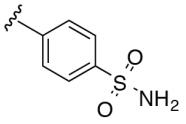 | 14.5 ± 4.7 |
| (**4.9**) | 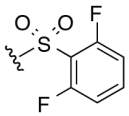 | 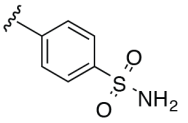 | n.d. |
| (**4.10**) | 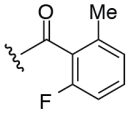 | 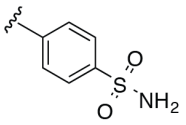 | 15.9 ± 4.1 |
| (**4.11**) | 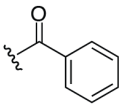 | 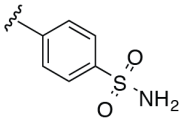 | 15.9 ± 4.1 |

| ID | $R_1$ | $R_2$ | $IC_{50}$ (μM) |
|---|---|---|---|
| (**4.3**) | 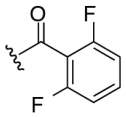 | 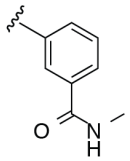 | 0.45 ± 0.03 |
| (**4.4**) | 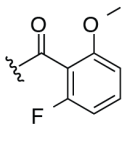 | 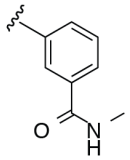 | 0.23 ± 0.02 |
| (**4.5**) | 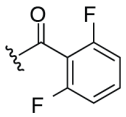 | 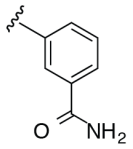 | 1.89 ± 0.41 |
| (**4.6**) | 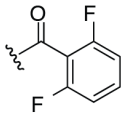 | 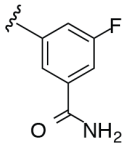 | 0.32 ± 0.11 |

core structure: 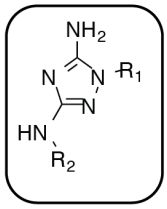

**B**

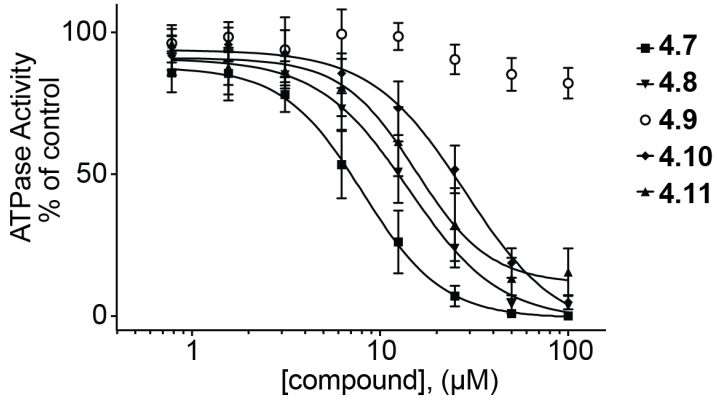


**Table 4.3. Structure-activity relationship analysis of compound 4.1 derivatives.**

**Table 4.3. Structure-activity relationship analysis of compound 4.1 derivatives.**
Ten compound **1** analogs were generated using established procedures using commercially available precursors (see Chapter 2 - Methods for details). Core structure (bottom right) and corresponding variable groups ($R_1$ and $R_2$) are shown. Compounds were tested against *Drosophila melanogaster*-spastin wild-type construct (aa 209-758) using NADH-coupled assay. Percentage residual ATPase activity values relative to DMSO control were fit to a sigmoidal dose-response equation and $IC_{50}$ values were calculated (average ± s.d, n = 3, all ATPase assays were performed at 0.5 mM MgATP, n.d. = not determined as full inhibition was not achieved at the highest concentration of the compound). Fitted curves that were used to generate the $IC_{50}$s are shown in (B). (B) Concentration-dependent inhibition of *Drosophila melanogaster*-spastin's ATPase activity (aa 209-758; wild-type) by indicated compounds. Percentage residual ATPase activity values relative to DMSO control were fit to a sigmoidal dose-response equation and $IC_{50}$ values were calculated.

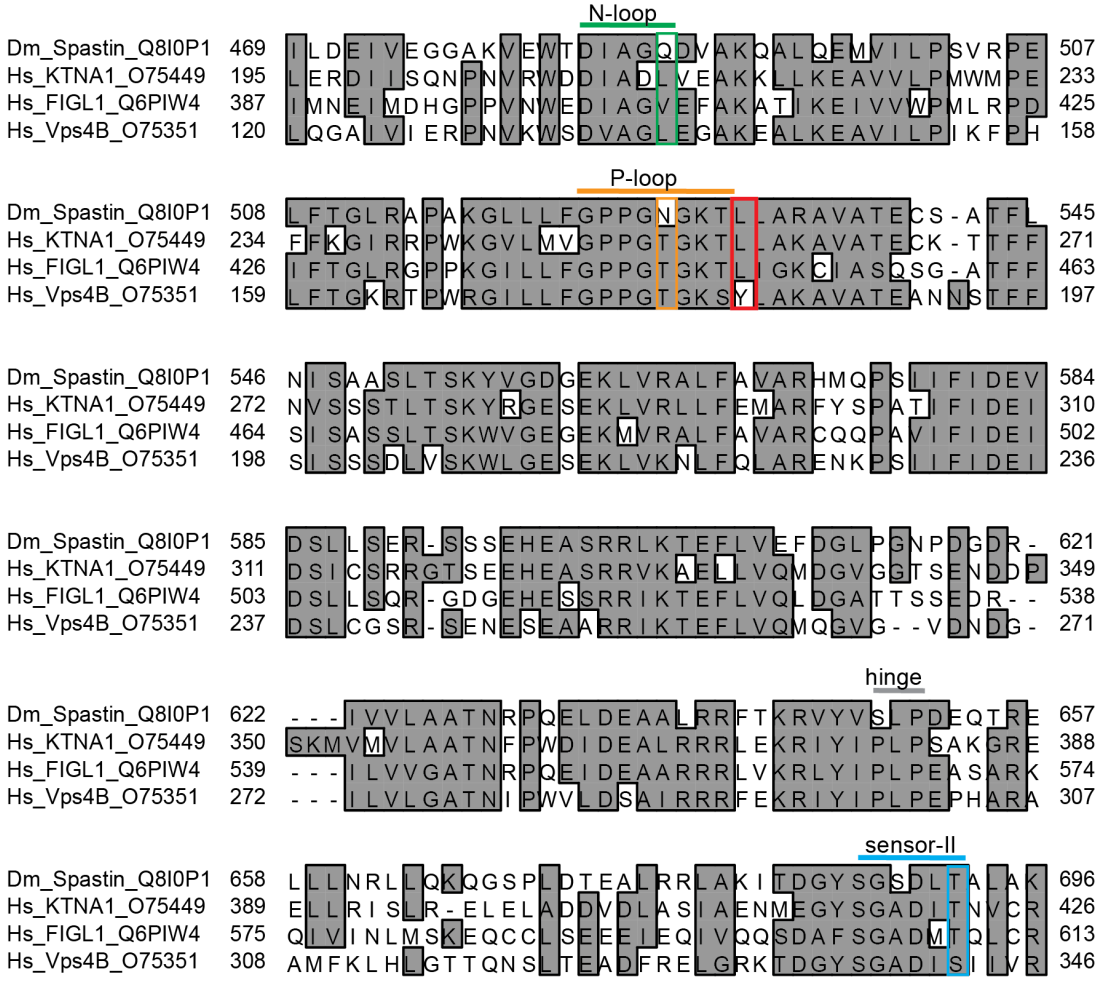


**Table 4.4. Sequence alignment of four related AAA proteins.**

Sequence alignment of the AAA domains of *D. melanogaster* spastin, human katanin, human fidgetin-like 1 (FIGL1) and human VPS4B proteins (supporting data for Figure 4.6G). Conserved ATP binding motifs are highlighted (N-loop - green, P-loop - orange, hinge - gray and sensor-II - blue). Residues at the entrance of the ATP pocket are highlighted by a red box. Variability hot-spot residues in the N-loop , P-loop, hinge and sensor-II motifs are also indicated by colored boxes.

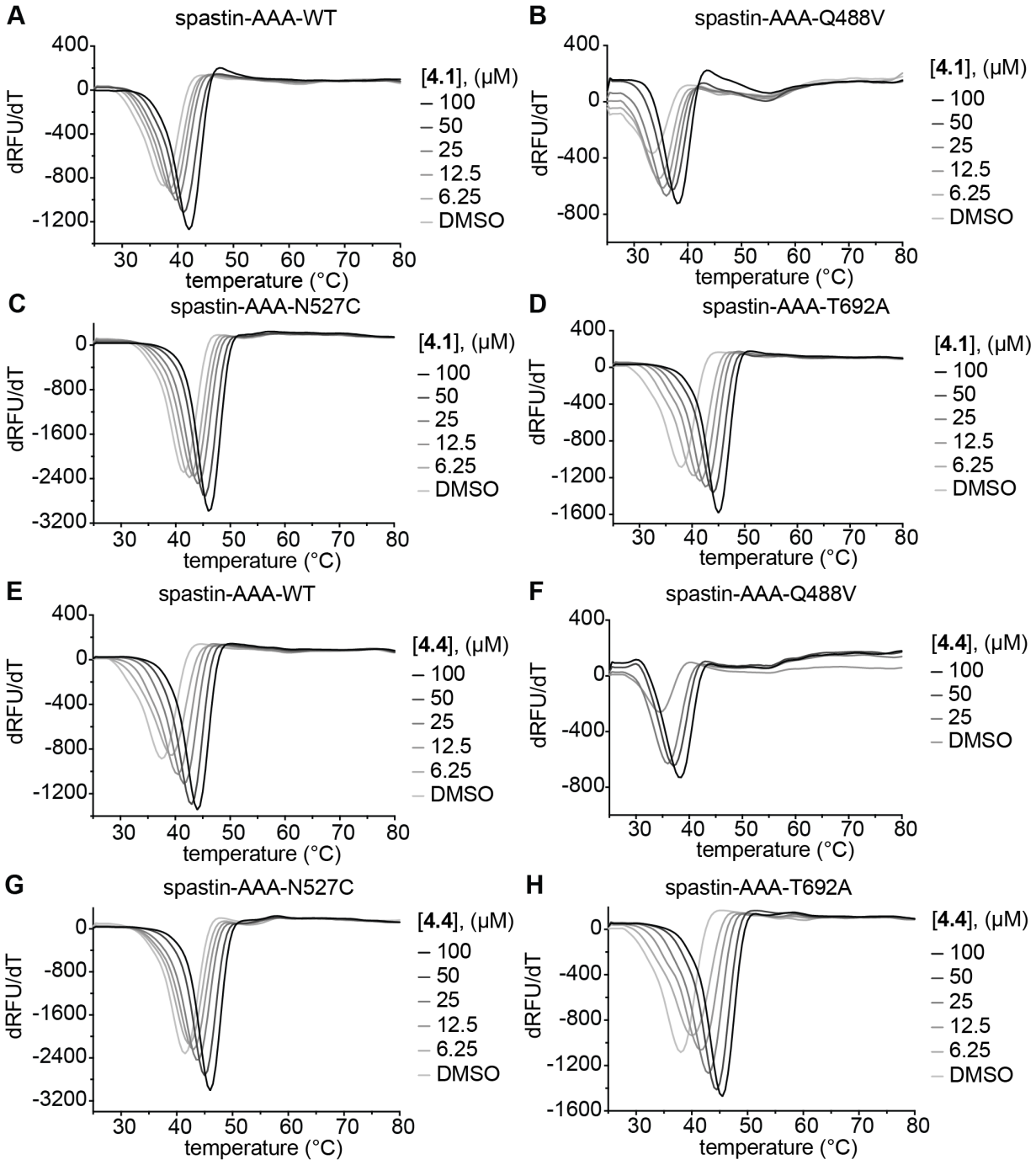


**Figure 4.7. Differential scanning fluorimetry analyses of compounds 4.1 and 4.4.** (**A**-**H**) Differential scanning fluorimetry analysis of the melting temperature of spastin-AAA constructs in the presence of compound **4.1** (**A**-**D**) and compound **4.4** (**E**-**H**). Data from one representative experiment are shown for each construct (n = 2; spastin-AAA-WT, -Q488V, -N527C and -T692A, supporting data for Figures 4.2 and 4.6).

but does not substantially inhibit the other three AAA proteins (Figure 4.6H). These analyses suggest that interactions of compound **4.4** with the unique combination of N-loop and P-loop variability residues (Gln-488 and Asn-527) in spastin contribute to the compound's potency as well as specificity against other AAA proteins. However, available structure-activity relationships for diaminotriazole-based compounds suggest that compound **4.4** likely inhibits several kinases (Lin et al., 2005; Malerich et al., 2010). Further optimization of diaminotriazole-based spastin inhibitors should be possible using our RADD models.

**Crystal Structure of Spastin-WT Bound to Compound 4.4**

To examine if the spastin-compound **4.4** interactions predicted by the RADD approach were indeed correct, we set up crystallization trials. For these experiments we chose the spastin-AAA-WT construct instead of spastin-AAA-N527C as compound **4.4** inhibits the WT protein with higher potency. Gratifyingly, we obtained crystals of spastin-AAA-WT in the presence of the inhibitor and determined the structure of the spastin-AAA-WT-compound **4.4** complex at ~1.94 Å resolution (Table 4.5). We observed a well-defined density in the active site that was assigned to the compound (Figures 4.8A, B). In this structural model, the diaminotriazole core of compound **4.4** is positioned to form hydrogen-bonding interactions with backbone amides of the residues Ala-486 and Asp-484 in spastin's N loop (Figures 4.8C, D).

Remarkably, as predicted by the RADD approach, there are several differences between the binding modes of compound **4.1** and **4.4** in spastin's active site. First, the

diaminotriazole scaffold of compound **4.4** is positioned in the active site in an orientation ~180° relative to the diaminotriazole scaffold of compound **4.1**. The exocyclic 5-amino group of the core scaffold in compound **4.4** points out of the pocket into the bulk solvent, whereas in the spastin-compound **4.1** complex it faces the inside of the ATP-binding site (Figure 4.8E). Second, compound **4.4**'s methoxy-fluorobenzoyl substituent is positioned between the P-loop and the sensor-II helix in a nearly perpendicular orientation to the difluorobenzoyl moiety of compound **4.1** (Figure 4.8E). Third, the phenyl-N-methylamide substituent of compound **4.4** is positioned in the ATP pocket and forms a π-stacking interaction with the side chain amide of the N-loop variability hotspot residue (Gln-488). In addition, the N-methylamide group of compound **4.4** is oriented between spastin's N-loop and P-loop motifs such that it can form hydrogen-bonding interactions with the backbone amide nitrogen of the N-loop residue (Gln-488) and the backbone carbonyl oxygen of the Ser-649 residue in the hinge motif (Figure 4.8D). These interactions are missing in the spastin-compound **4.1** structure and may contribute to more potent binding of compound **4.4** to spastin. Taken together, the compound-target interactions predicted by our RADD approach match the high-resolution X-ray data for the spastin-AAA-WT-compound **4.4** complex.

**Structure-guided design of a diaminotriazole-based inhibitor for spastin allele with a mutation in the P-loop variability hotspot residue (N527C)**

Our studies of pyrazolylquinazoline-based analogs of spastazoline revealed how allele-specific chemical inhibitors of spastin can be designed (see Chapter 3 and

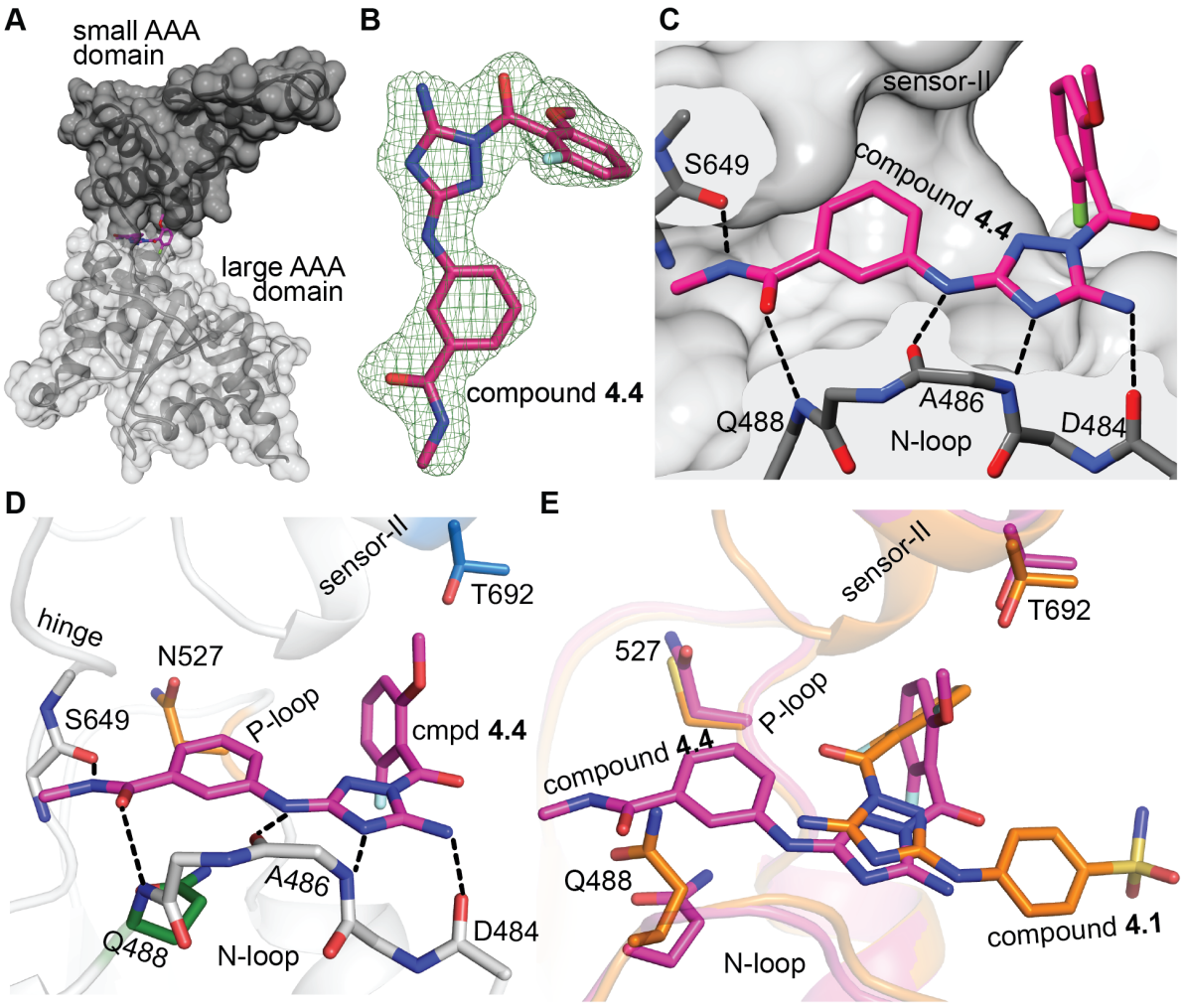


**Figure 4.8. Crystal Structure of the Spastin-WT-Compound 4.4 Complex.**
(**A**) Structural model of the spastin-AAA-WT-compound **4.4** complex (surface and stick representation). (**B**) Compound **4.4** (stick representation) and the corresponding simulated annealing composite omit electron density map contoured at 3σ is shown ($mF_o - DF_c$, green mesh). (**C** and **D**) Compound **4.4** in spastin's active site. Predicted hydrogen-bonding interactions are shown (**C** and **D**, black dashed lines). Side chains of the variability hotspot residues in the N loop (Gln-488, green), P loop (Asn-527, orange), and sensor-II (Thr-692, blue) motifs as well as the backbone atoms of the hinge residue (Ser-649) are shown (**D**). (**E**) Overlay of spastin-AAA-WT-compound **4.4** and spastin-N527C-compound **4.1** complexes. Variability hotspot residues (Gln-488, Asn-527, and Thr-692) are indicated.

(Pisa et al., 2019a)). Specifically, we identified an 8-fluoro-modified quinazoline analog that can potently and selectively inhibit the N527C allele of *D. melanogaster* spastin (Figures 3.4 and 3.5). Our structural model of the diaminotriazole-based compound **4.4** reveals that this compound binds spastin in a similar orientation as the pyrazolylquinazoline-based inhibitors (Figure 4.9A). In fact, the distance between the side chain carbonyl oxygen of the Asn-527 residue and the C5 of compound **4.4**'s aminobenzamide moiety is nearly identical to the distance between this residue and the quinazoline's C8 (Figures 4.9A and 3.2E).

Therefore, we next examined if diaminotriazole scaffold could also be used for designing allele-specific inhibitors. Guided by our 8-fluoroquinazoline-based allele-specific inhibitor of spastin we designed the diaminotriazole-based compound **4.6**, in which fluorine replaces the hydrogen at benzamide's C5 (Figure 4.9A, B). As a control we synthesized compound **4.5** that has an identical core as compound **4.6** (Figure 4.9B). We next tested these compounds against wild-type and N527C spastin constructs. We found that compound **4.5** inhibits WT spastin more potently than the N527C mutant allele (compound **4.5,** WT: $IC_{50}$ = 1.89 ± 0.41 μM; N527C: $IC_{50}$ = 11.4 ± 7.6 μM, n = 2, average ± range, Figure 4.9C). In contrast, compound **4.6** potently inhibits both alleles (compound **4.6,** WT: $IC_{50}$ = 0.32 ± 0.11 μM; N527C: $IC_{50}$ = 0.31 ± 0.07 μM, n = 2, average ± range, Figure 4.9D). These data suggest that potent diaminotriazole-based inhibitors of the spastin-N527C allele could be designed. However, as compound **4.6** also inhibits the wild-type protein, its use as a probe for spastin-N527C is limited and further modifications will be needed.

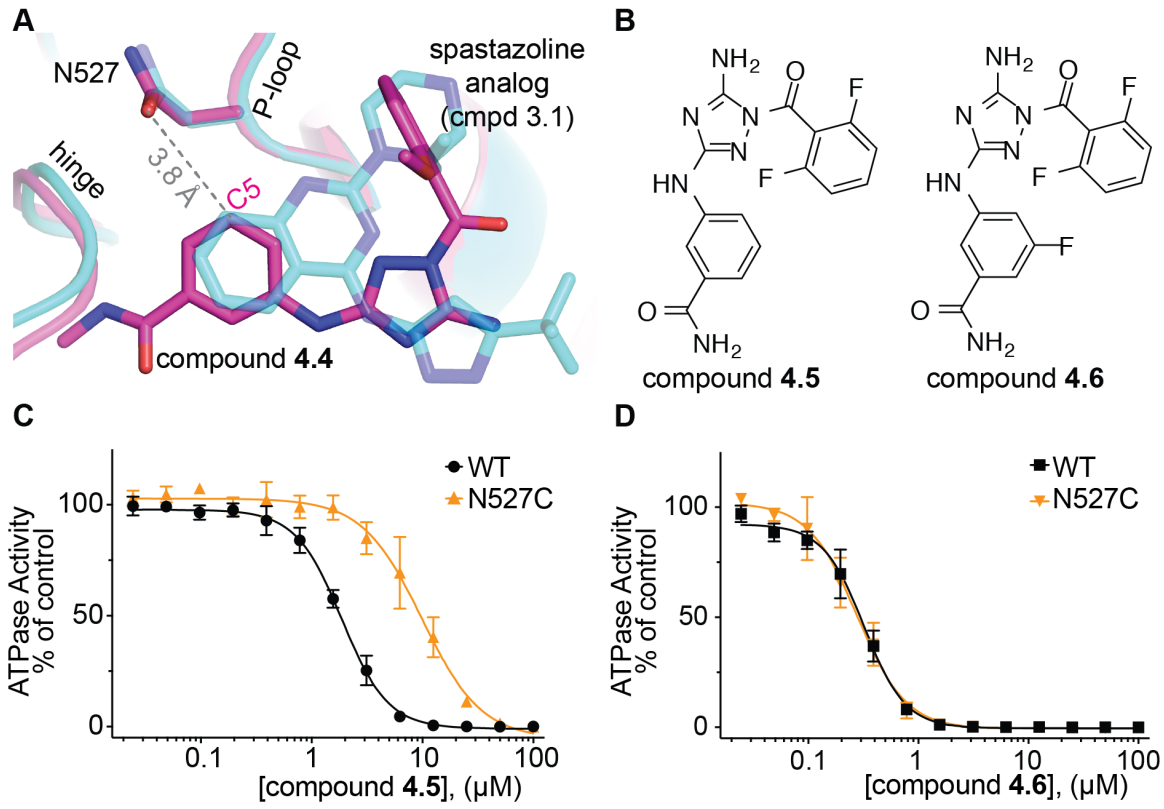


**Figure 4.9. Analysis of diaminotriazole-based compound binding to wild-type spastin and a construct with a mutation in the P-loop variability hotspot residue.** (**A**) Overlay of spastin-WT-compound **4.4** (magenta, pdbID:6P12) and spastin-WT-compound **3.1** (cyan, pdbID: 6NYV) complexes (cyan). Distance between compound **4.4**'s aminobenzamide C5 and Asn-527 side chain carbonyl oxygen is indicated (**B**) Chemical structures of compound **4.4** analogues. (**C** and **D**) Concentration-dependent inhibition of spastin's ATPase activity (aa 209-758; wild-type, black; N527C mutant, orange) by compounds **4.5** and **4.6**. Percentage residual ATPase activity values relative to DMSO control were fit to a sigmoidal dose-response equation and $IC_{50}$ values were calculated ($IC_{50}$: WT-cmpd **4.5** = 1.89 ± 0.41 μM; N527C-cmpd **4.5** = 11.4 ± 7.6 μM; WT-cmpd **4.6** = 0.32 ± 0.11 μM; N527C-cmpd **4.6** = 0.31 ± 0.07 μM, average ± range, n = 2, 0.5 mM MgATP).

**Structural Models of the Spastin Sensor-II Mutant Allele (T692A) Bound to Compounds 4.1 and 4.4**

Our findings show that a sensor-II mutation (T692A) in spastin increases the potency of compound **4.1** in the ATPase assays but does not substantially alter the potency of compound **4.4**. To examine this difference in binding we determined three additional structures, one of the spastin-AAA-T692A construct with compound **4.1** (~2.15 Å resolution, Table 4.5) and two with compound **4.4** (crystal form A, ~2.10 Å; crystal form B, ~1.93 Å, Table 4.5).

Refinement of the spastin-AAA-T692A-compound **4.1** structural model suggested that compound **4.1** can sample two conformations (Figures 4.10A). In both conformations, the diaminotriazole core is positioned to form a hydrogen-bonding network with backbone amides of the N-loop residues (Asp-484 and Ala-486). The difluorobenzoyl moieties in each of the two conformers are also nearly co-aligned and are proximal to the sensor-II motif (Figure 4.10A). Interestingly, we observe a different orientation of the phenylsufonamide moiety in the two conformers. One conformer of compound **4.1** in the spastin-AAA-T692A structure has the phenylsulfonamide proximal to Leu-531 residue of the large AAA subdomain (conformer 1; Figures 4.10A). The binding mode of this conformer is similar to the orientation of compound **4.1** we observed in the spastin-AAA-N527C-compound **4.1** co-crystal structure (Figure 4.10B). In the other conformer, the phenylsulfonamide moiety is aligned proximal to helix 5 of the small AAA subdomain and is positioned to form a hydrogen-bonding interaction between the sulfonamide NH and the backbone carbonyl oxygen of the Arg-662 residue

(conformer 2; Figures 4.10A). These interactions are not observed in the structure of spastin-N527C-compound **4.1** complex.

Next, to examine the structural basis for how compound **4.4** inhibits the WT spastin and sensor-II mutant allele (T692A) with nearly identical potency we set up crystallization trials of the spastin-AAA-T692A and compound **4.4**. Interestingly, the trials yielded two crystal forms of the spastin-T692A-compound **4.4** complex (forms A and B, Table 4.5 and Figure 4.10C). The structural model of the spastin-AAA-T692A construct in the crystal form A has nearly identical protein backbone conformation to that observed in the spastin-AAA-WT-compound **4.4** complex (Cα root-mean-square deviation [RMSD] ~0.2 Å, WT versus T692A form A; Figure 4.10D). In crystal form B, we observed small changes in the periphery of the protein in comparison with the WT complex (Cα RMSD ~1.9 Å, WT versus T692A form B; Figure 4.10D). Interestingly, the inhibitor adopts nearly superimposable conformations in these three structural models (WT and T692A forms A and B; Figure 4.10E). In both crystal forms of the spastin-AAA-T692A-compound **4.4** complex, the side chain of the sensor-II residue (Ala-692) is positioned >4 Å away from the methoxy group in compound **4.4**'s fluorobenzoyl substituent (Figures 4.10F, G). In comparison, the structure of spastin-AAA-WT-compound **4.4** complex reveals that the compound's methoxy group is proximal (<4 Å) to the sensor-II residue (Thr-692; Figure 4.10H). Taken together, our X-ray structures of inhibitor-spastin complexes show that mutations in variability hotspot residues do not disrupt the active site conformation and reveal how diaminotriazole-based inhibitors interact with spastin.

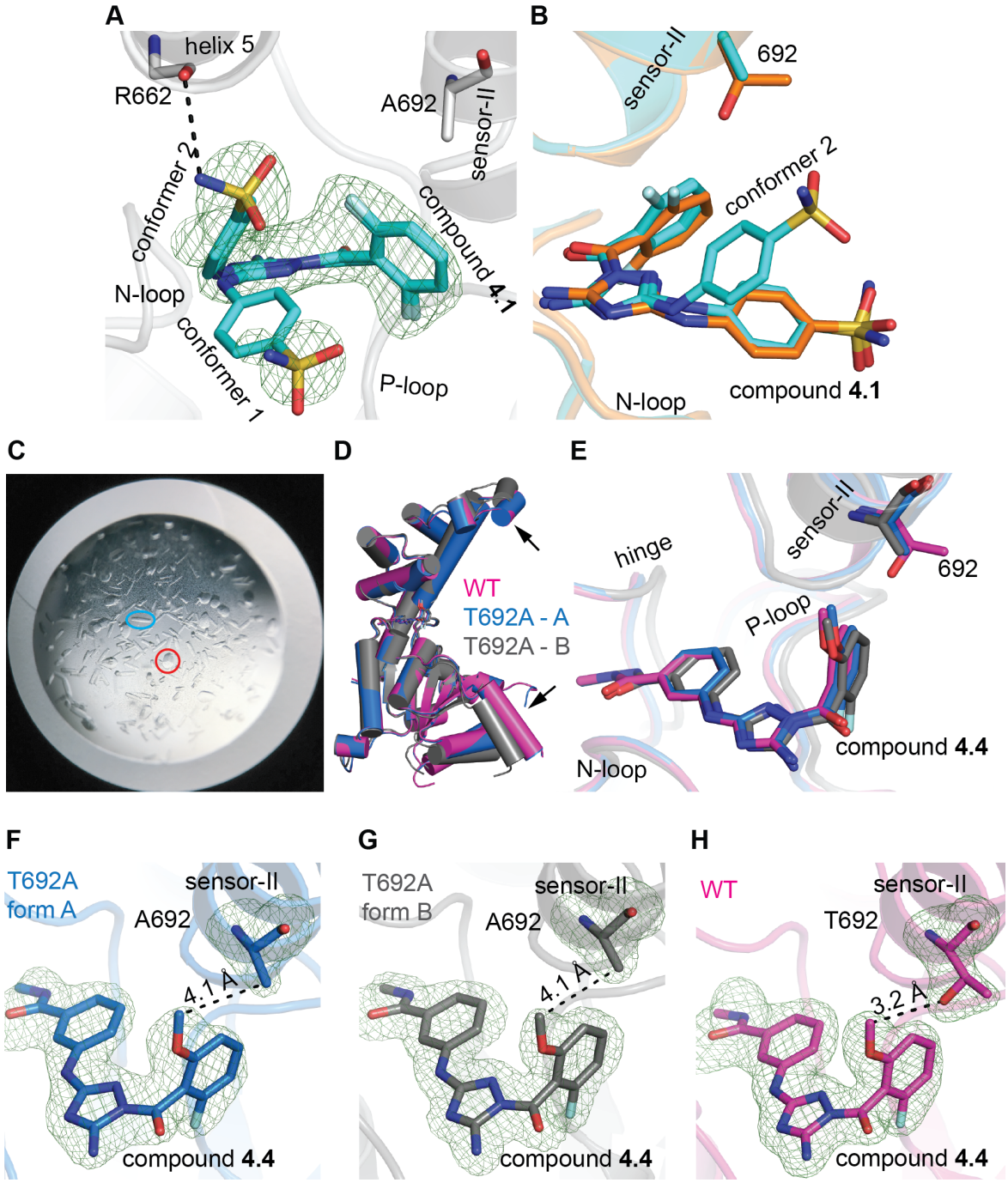


**Figure 4.10. Structural Models of the Sensor-II Variability Hotspot Mutant Allele of Spastin (T692A) Bound to Compounds 4.1 and 4.4.**

**Figure 4.10. Structural Models of the Sensor-II Variability Hotspot Mutant Allele of Spastin (T692A) Bound to Compounds 4.1 and 4.4.**

**(A)** Structural model of the spastin-AAA-T692A-compound **4.1** complex. View of two compound **4.1** conformers from the entrance of the ATP pocket is shown (ribbon and stick representation). Simulated annealing composite omit map around the compound contoured at 3σ is shown ($mF_o - DF_c$, green mesh). Side chain of the mutated variability hotspot residue (Ala-692) and the backbone atoms of a residue in the small AAA domain (Arg-662) are indicated. (**B**) Overlay of spastin-AAA-N527C-compound **4.1** (carbon atoms in orange) and spastin-AAA-T692A-compound **4.1** (carbon atoms in cyan) structural models. The side chains of the variability hotspot residues in the sensor-II motif (Thr-692, orange; Ala-692, cyan) are shown. (**C**) Two crystal forms (highlighted by colored ovals; form A - blue, form B - red) in a drop with spastin-AAA-T692A construct in the presence of compound **4.4** and crystallization buffer (0.1 M Na-acetate pH 5-7, 2% PEG-4000, 15% MPD). (**D**) Overlay of AAA domains in spastin-AAA-WT-compound **4.4** (magenta) and two crystal forms of the spastin-AAA-T692A-compound **4.4** complex (crystal form A, blue; crystal form B, gray). The displacement of helices in the periphery of the protein is indicated by black arrows. (**E**) Overlay of spastin-AAA-T692A-compound **4.4** (crystal form A, blue; crystal form B, gray) and spastin-AAA-WT-compound **4.4** (magenta) complexes is shown. The N-loop, hinge, P-loop, and sensor-II motifs are indicated. Overlays in (**D** and **E**) were generated in PyMOL using the Align function with spastin-AAA-WT-compound **4.4** complex set as the target model. (**F–H**) Views of sensor-II variability hotspot residue in the spastin-AAA-T692A-compound **4.4**, (**F**) form A, (**G**) form B, and spastin-AAA-WT-compound **4.4** (**H**) complexes. Distances between the sensor-II residue and the compounds are indicated.

**Designing compound 4.1-sensitive alleles of Fidgetin-like 1 AAA protein.**

Our analyses of spastin inhibition by diaminotriazole-based compounds suggest that variability hot-spot residues can substantially contribute to inhibitor specificity. We hypothesized that swapping variability hotspot residues in other AAA proteins to those found in spastin could lead to sensitization of these protein mutant alleles to inhibition by diaminotriazole-based inhibitors. For these experiments I decided to focus on Fidgetin-like 1 (FIGL1) AAA protein that plays a central role in DNA repair and maintenance of genomic stability (Girard et al., 2015; Yuan and Chen, 2013).

First, we examined the sequence of FIGL1 to identify variability hotspot residues in its active site (Figure 4.11A, B). These analyses reveal that the sensor-II variability hotspot is conserved in FIGL1 and spastin (Thr-609 in FIGL1 and T692 in spastin, also see Table 4.4) but the N-loop and P-loop hotspot residues have diverged in these proteins (N-loop: Val-406 in FIGL1, Gln-488 in spastin; P-loop: Thr-445 in FIGL1, N527 in spastin, Figure 4.11B and Table 4.4). We next examined if hotspot residues found in spastin could be introduced to FIGL1 to generate active mutant alleles. We expressed and purified two FIGL1 constructs with mutations in the N-loop and P-loop variability hotspot residues and characterized their steady-state ATP-hydrolysis activity (Figure 4.11C-H). We found that both constructs are active ATPases with $k_{cat}$ values within ~1.5-fold of the wild-type protein (Figure 4.11E, F, H). The ATP concentrations required for half-maximal enzymatic velocity ($K_{1/2}$) were also within a narrow range, from ~0.1 mM (wild type and T445N) to ~0.6 mM (V406Q) (Figure 4.11E, G, H). Together, these

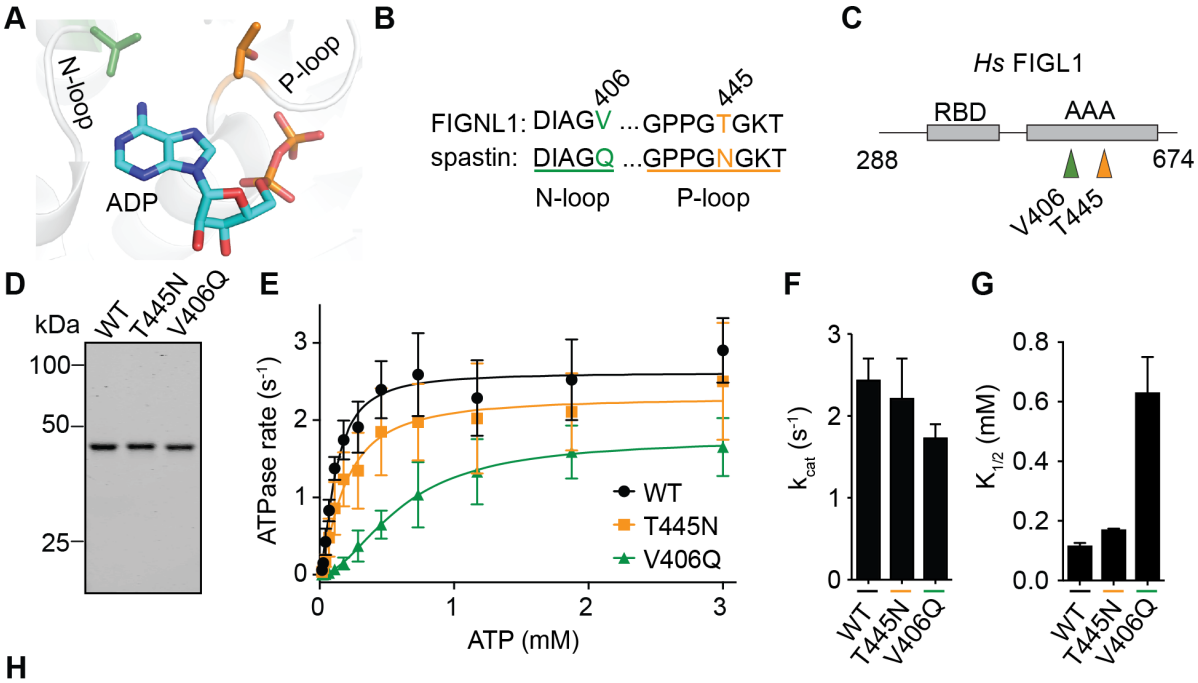


H

| | WT | V406Q | T445N | V406Q;T445N |
|---|---|---|---|---|
| $k_{cat}$ ($s^{-1}$) | 2.58 ± 0.84 | 1.73 ± 0.35 | 2.23 ± 1.01 | 2.53 ± 0.19 |
| Hill coefficient | 1.65 ± 0.27 | 1.91 ± 0.37 | 1.50 ± 0.33 | 2.03 ± 0.12 |
| $K_{1/2}$ (mM) | 0.10 ± 0.03 | 0.63 ± 0.25 | 0.17 ± 0.01 | 0.61 ± 0.01 |

**Figure 4.11. Characterizing human Fidgetin-like 1 construct with mutations in variability hotspot residues.**

(**A**) Ribbon diagram (PDB: 3D8B) of the nucleotide-binding site in human Fidgetin-like 1 (Hs-FIGL1) showing ADP (stick representation) and selectivity hotspot residues in the N-loop (green) and P-loop (orange) structural motifs. (**B**) Sequence alignment of the N-loop and P-loop motifs in the adenine-binding pocket of Hs-FIGL1 and Dm-spastin. Selectivity hotspot residues are numbered and color-coded as in **A**. (**C**) Schematic shows the AAA domain (gray box) and the Rad51 binding domain (RBD) of the recombinant construct (Hs-FIGL1). The positions of two selectivity hotspot residues are indicated (arrows). The first and last residues of the construct are numbered. (**D**) SDS-PAGE analysis of purified wildtype (WT) and mutant Hs-FIGL1 constructs (Coomassie blue). (**E**) ATP concentration-dependence of the steady-state activity of WT and mutant Hs-FIGL1 constructs, analyzed using an NADH-coupled assay. Rates were fit to the Michaelis-Menten equation for cooperative enzymes and average and range were calculated. (**F**, **G, H**) Histograms show average ± s.d. (n = 2) values for the catalytic turnover number ($k_{cat}$; **F**), and the ATP concentration required for half-maximal velocity ($K_{1/2}$; **G**) of recombinant Hs-FIGL1 constructs. Numerical values for these parameters are provided in (**H**).

data indicate that variability hot-spot residues in Fidgetin-like 1 can be mutated to yield alleles that retain catalytic activity.

Dose-dependent analyses reveal that compound **4.1** weakly inhibits wild-type Fidgetin-like 1 protein ($IC_{50}$ > 25 μM, Figure 4.12A). Our RADD and structural models of compound **4.1** bound to spastin suggest that this inhibitor likely binds in the active site of FIGL1 in a similar orientation to the one it adopts in spastin's active site (Figure 4.12B). In this model, the diaminotriazole core of compound **4.1** is positioned to make hydrogen-bonding interaction with the N-loop backbone amides (Figure 4.12B - black dashed lines). The exocyclic amine faces the N-loop variability hotspot residue, the difluorobenzoyl moiety is proximal to the P-loop and the para-sulfonamide faces away from the active site to the bulk solvent (Figure 4.12B). Next, we examined the binding of compound **4.1** to the FIGL1 constructs with mutations in the variability hotspot residues. We found that both N-loop and P-loop mutants of FIGL1 are sensitized to inhibition by compound **4.1** (25 μM, Figure 4.12C). We next generated a FIGL1 construct with two mutations, one in the N-loop and the other in the P-loop variability hotspot (V406Q;T445N, Figure 4.12D), and analyzed its activity. These tests revealed that both $k_{cat}$ and $K_{1/2}$ of the double mutant construct are more similar to the wild-type protein than the FIGL1 allele with a single mutation in the N-loop (V406Q) (Figure 4.12E). Furthermore, we found that compound **4.1** more potently inhibits the double mutant construct in comparison the wild-type and the V406Q proteins ($IC_{50}$: V406Q: 39 ± 6 μM; V406Q-T445N: 10.4 ± 2 μM, WT >25 μM, Figure 4.12F). In fact, the potency of compound **4.1** against the "spastinized" double mutant of FIGL1 is similar to the potency

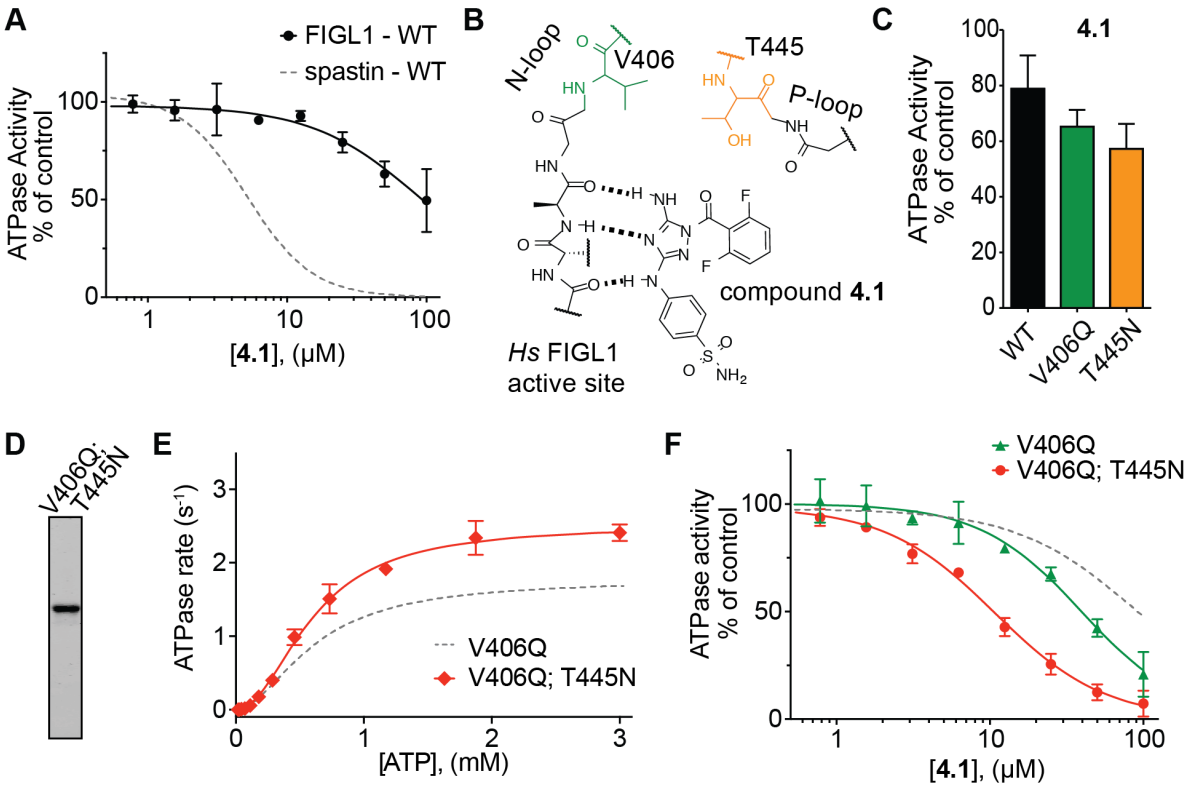


**Figure 4.12. Designing FIGL1 alleles sensitive to compound 4.1.**

(**A**) Concentration-dependent inhibition of the steady-state ATPase activity of Hs-FIGL1 by compound **4.1**. Graph shows percent residual ATPase activity values compared to DMSO control (average ± range, n = 2) fit to a sigmoidal dose-response equation. For comparison, analysis of the inhibition of Dm-spastin-WT (data from Fig. 4.1) is also shown (gray line). (**B**) Schematic for the predicted hydrogen-bonding interactions (dashed lines) between compound **4.1** and the N-loop of human FIGL1. Relative positions of the selectivity hotspot residues in the N-loop (V406, green) and P-loop (T445, orange) are highlighted. (**C**) Percent steady-state ATPase activity of Hs-FIGL1 WT and selectivity hotspot mutants in the presence of compound **4.1** (25 μM, average ± range, n = 2). (**D**) SDS-PAGE analysis (Coomassie blue) of purified double mutant Hs-FIGL1 construct (V406Q; T445N). (**E**) ATP concentration-dependence of the steady-state activity of Hs-FIGL1 double mutant construct with mutations at selectivity hotspot residues (V406; T445N) analyzed using an NADH-coupled assay. For comparison, the activity of V406Q single mutant (data in 4.11E) is also shown (gray line). Rates (average ± range, n = 2) were fit to the Michaelis-Menten equation for cooperative enzymes (for numerical values see 4.11H, see Methods for details). (**F**) Concentration-dependent inhibition of the steady-state ATPase activity of Hs-FIGL1 single mutant (V406Q) and double mutant (V406; T445N) alleles with comparable $K_{1/2}$ values by compound **4.1**. Graph shows percent residual ATPase activity values compared to DMSO control (average ± range, n = 2). Data were fit to a sigmoidal dose-response equation and $IC_{50}$ were calculated (Hs-FIGL1 constructs, V406Q: 39 ± 6 μM; V406Q;T445N: 10.4 ± 2 μM). For comparison, analysis of the inhibition of Hs-FIGL1-WT (data from **A**) is also shown (gray line).

of the compound against wild-type spastin (Figure 4.1C). Taken together, these data show that FIGL1 AAA protein can be sensitized to inhibition by a diaminotriazole-based inhibitor and suggest that our RADD approach can be applied to multiple AAA proteins.

**Discussion**

In this study, we used inhibitor analyses against spastin alleles with engineered mutations in variability hotspot residues to identify key compound-target interactions for diaminotriazole-based spastin inhibitors. Our findings reveal distinct sets of resistance-conferring residues that predict different binding modes for two chemically related compounds. Our X-ray crystallography models of the inhibitor-bound spastin complexes match the predicted binding modes. Together, these findings suggest a general approach, which we name RADD, for designing potent and selective inhibitors for AAA proteins.

Our RADD inhibitor design approach (Figure 4.13) involves the following steps. First, mutations of residues in the inhibitor binding site are engineered so that the steric and stereoelectronic properties are altered without disrupting enzyme activity. In particular, we generated active mutant alleles by replacing relatively less conserved residues in spastin's active site with residues present at equivalent positions in other AAA proteins (Cupido et al., 2019). It will be important to compare the efficiency of our approach with other techniques, such as alanine scanning (Wells and McClendon, 2007), for identifying active mutant alleles. Second, the analyses of inhibitor activity against engineered mutant alleles are used to determine the key inhibitor-target

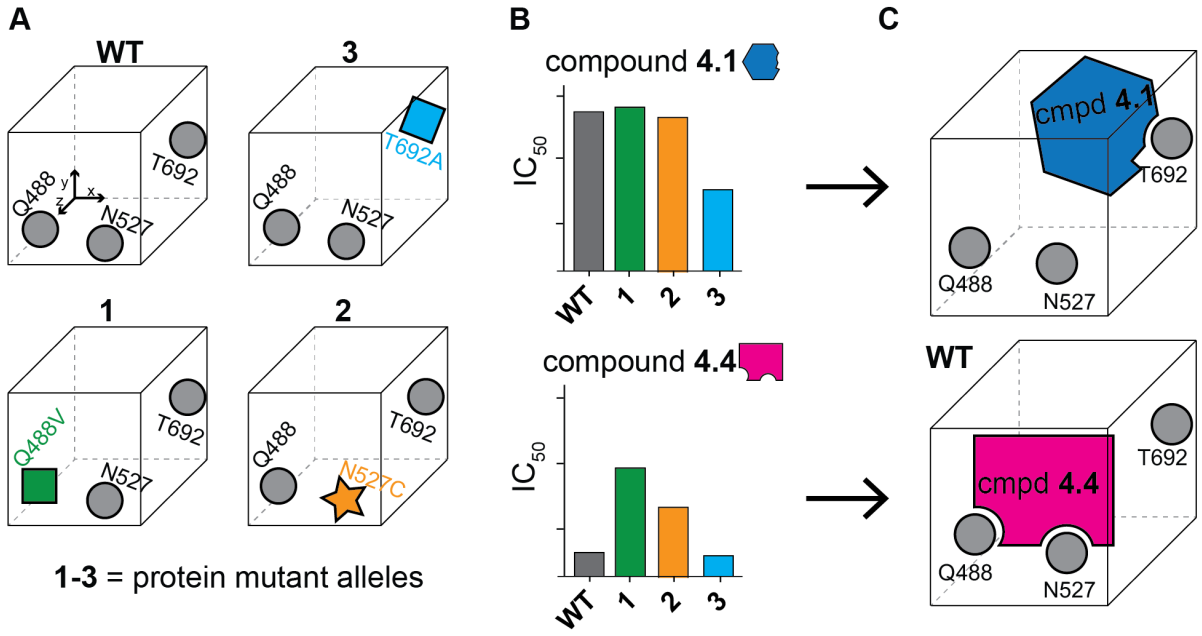


**Figure 4.13. Developing Compound-Target Binding Models Using the RADD Approach.**

(**A-C**) Schematic for the RADD approach. (**A**) Mutations that maintain biochemical activity (e.g., ATPase) but alter the shape and electrostatics of the inhibitor binding site are identified. (**B**) Analyses of inhibitor activity against the different mutant alleles reveal key inhibitor-protein contacts and guide the selection of robust binding models (**C**).

interactions. These interactions can guide the selection of robust models from computational docking solutions as rank ordering of these solutions is often difficult without additional data that characterize inhibitor binding (Chen, 2015).

During inhibitor design many analogs are often generated to optimize and improve the initial starting scaffold. X-ray crystallography is commonly employed to confirm the binding modes of a handful of these analogs in the process. Interestingly, analyses of inhibitor-target complexes suggest that even closely related compounds can bind their target differently and often reorient in the binding site. For example, moving a lactate substituent from ortho to meta position in an indole-based PPARγ agonist induces a ~180° turn over of the ligand in the binding site (Bruning et al., 2007). Similarly, closely related diphenylamide-based inhibitors of p38 MAP kinase bind to the active site in different orientations and can even bind to different conformations of the kinase (Angell et al., 2008). Our results for two diaminotriazole-based inhibitors, which bind the active site of spastin in distinct orientations, suggest that inhibitor activity analyses against protein mutant alleles can help differentiate these binding modes. In some cases, the binding modes of inhibitor analogs can be successfully predicted using computational docking methods (Shoichet and Kobilka, 2012), but these methods can be challenging when the inhibitor binding sites undergo large conformational rearrangements, as is the case with AAA proteins (Puchades et al., 2017). Testing inhibitors against active mutant alleles can provide experimental validation for poses predicted by computational methods, and help determine the compound interactions and orientations in the active site of the target protein.

Therefore, the RADD approach could be useful for monitoring compound binding at multiple stages of inhibitor development, especially in the case of protein families for which high-resolution structures of inhibitor-protein complexes are lacking.

**Table 4.5**. Crystallography data collection and refinement statistics.

| *spastin-AAA:* | N527C | T692A | WT | T692A | T692A |
|---|---|---|---|---|---|
| *ligand:* | compound **4.1** | compound **4.1** | compound **4.4** | compound **4.4** form A | compound **4.4** form B |
| *pdbID:* | **6P10** | **6P11** | **6P12** | **6P13** | **6P14** |
| **Data collection** | | | | | |
| Space group | $P6_5$ | $P6_5$ | $P6_5$ | $P6_5$ | $P6_5$ |
| Cell dimensions | | | | | |
| *a*, *b*, *c* (Å) | 79.4 79.4 97.3 | 79.5 79.5 97.2 | 80.9 80.9 96.3 | 79.7 79.7 96.9 | 105.3 105.3 65.4 |
| $\alpha$, $\beta$, $\gamma$ (°) | 90, 90, 120 | 90, 90, 120 | 90, 90, 120 | 90, 90, 120 | 90, 90, 120 |
| Resolution (Å) | 50.0-2.30 (2.34-2.30) | 50.0-2.15 (2.19-2.15) | 50.0-1.94 (1.97-1.94) | 50.0-2.10 (2.14-2.10) | 50.0-1.93 (1.96-1.93) |
| Wavelength (Å) | 0.9181 | 0.9201 | 0.9197 | 0.9201 | 0.9201 |
| $R_{merge}$ | 0.044 (0.468) | 0.035 (0.391) | 0.031 (0.450) | 0.043 (0.448) | 0.039 (0.439) |
| $\langle I \rangle / \sigma I$ | 32.2 (1.8) | 37.4 (2.7) | 52.5 (2.8) | 42.0 (2.7) | 40.7 (2.9) |
| Completeness (%) | 99.0 (99.5) | 99.8 (99.9) | 99.0 (99.2) | 99.9 (100.0) | 99.9 (100.0) |
| Multiplicity | 4.7 (4.1) | 5.5 (5.6) | 6.5 (6.7) | 5.8 (6.0) | 5.8 (6.0) |
| Total reflections | 71736 | 103752 | 168901 | 118576 | 180192 |
| Unique reflections | 15364 (783) | 18985 (940) | 26138 (1323) | 20435 (1015) | 31137 (1549) |
| CC1/2 | 100 (81.9) | 99.39 (89.6) | 99.6 (91.3) | 99.4 (86.9) | 99.8 (90.6) |
| | | | | | |
| **Refinement** | | | | | |
| Resolution (Å) | 39.7-2.30 (2.38-2.30) | 39.7-2.15 (2.23-2.15) | 40.34 – 1.94 (2.01-1.94) | 39.85 – 2.10 (2.18-2.10) | 34.47 – 1.93 (1.99 – 1.93) |
| No. reflections | 15360 (1546) | 18944 (1878) | 26123 (2613) | 20389 (2020) | 31108 (3101) |
| No. refl. for $R_{free}$ | 1548 (147) | 1889 (189) | 2615 (265) | 2048 (203) | 3091 (306) |
| $R_{work}$ / $R_{free}$ | 0.206/0.252 | 0.213/0.241 | 0.193 / 0.230 | 0.207 / 0.245 | 0.179 / 0.200 |
| No. atoms | 2120 | 2291 | 2354 | 2208 | 2199 |
| Protein | 2044 | 2046 | 2095 | 2059 | 1979 |
| Ligands/ions | 40 | 67 | 41 | 41 | 49 |
| Water | 36 | 178 | 218 | 108 | 171 |
| *B*-factors | | | | | |
| Protein | 61.51 | 55.31 | 48.00 | 50.54 | 43.94 |
| Ligand/ion | 64.98 | 52.86 | 44.57 | 45.94 | 42.02 |
| Water | 62.46 | 63.29 | 57.14 | 55.78 | 46.83 |
| R.m.s. deviations | | | | | |
| Bond lengths (Å) | 0.003 | 0.002 | 0.003 | 0.002 | 0.019 |
| Bond angles (°) | 0.64 | 0.44 | 0.58 | 0.49 | 1.58 |
| Clashscore | 4.40 | 4.12 | 4.77 | 1.94 | 2.51 |
| Rotamer Outliers | 1.00 | 0.00 | 0.98 | 0.00 | 2.05 |
| Ramachandran Favored (%) | 96.34 | 96.69 | 98.90 | 97.06 | 97.67 |
| Ramachandran Allowed (%) | 3.66 | 3.31 | 1.10 | 2.94 | 2.33 |
| Ramachandran Outliers (%) | 0.00 | 0.00 | 0.00 | 0.00 | 0.00 |

*Data in brackets indicate the high-resolution shell.

## Chapter 4 - Methods.

### Vectors for Recombinant Protein Expression.

Vector for expression of *D. melanogaster* wild-type protein (aa 209-758) was obtained from Dr. Antonina Roll-Mecak (pDEST15-spastin-D.melanogaster) (Roll-Mecak and Vale, 2008). Constructs for expression of mutant spastin alleles (Q488V, N527C and T692A; aa 209-758) were described in earlier work (Cupido et al., 2019).

Constructs for expression of *D. melanogaster* AAA domain (spastin-AAA, aa 445-758) were described in earlier work (Pisa et al., 2019a). Briefly, the coding sequence for spastin AAA domain (aa 445-758) was PCR amplified (CloneAmp HiFi, Clontech) from pDEST15-spastin-D.melanogaster (WT, Q488V, N527C or T692A) and cloned into pDEST15 vector using AscI and ApaI sites to generate N-terminal GST-fusion constructs. The coding sequences for all constructs were verified by Sanger sequencing. Sequence alignments were performed using the ClustalW algorithm in MacVector software (MacVector, Inc).

### Protein Expression and Purification.

*D. melanogaster* spastin (spastin, aa 209-758) wild-type and mutant constructs (Q488V, N527C and T692A) were expressed and purified as described earlier (Roll-Mecak and Vale, 2008). *Xl*-katanin, *Hs*-FIGL1 and *Hs*-VPS4B were purified and assayed as described earlier (Cupido et al., 2019).

*D. melanogaster* spastin AAA domain (spastin-AAA, aa 445-758) wild-type and mutant constructs (Q488V, N527C and T692A) were expressed and purified as described earlier (Pisa et al., 2019a). Briefly, *E.coli* Rosetta cells were grown in Miller's LB medium to $O.D._{600}$ ~0.8 at 30°C, chilled to 18°C and the protein expression was induced overnight (14-16 hours, 0.5 mM IPTG). The cells were resuspended in lysis buffer (50 mM Tris.HCl pH = 8.0, 400 mM NaCl, 10 mM $MgCl_2$, 1 mM PMSF, 5 mM β-mercaptoethanol, 0.001% triton-X and 1 tablet of Roche cOmplete protease inhibitor cocktail per 50 ml of buffer), supplemented with 0.1 µg / ml lysozyme and 5 U / ml benzonase and lysed using Emulsiflex-C5 homogenizer (Avestin, 5-10 cycles at 10-15 kPsi). The lysate was spun at 45,000 rpm for 45 min at 4°C in a Ti-45 rotor using Beckman Coulter Optima LE-80K ultracentrifuge. The clarified supernatant was incubated with glutathione agarose resin for 1 hr. The beads were washed with ~300 ml of wash buffer (50 mM Tris.HCl pH = 8.0, 400 mM NaCl, 10 mM $MgCl_2$, 5 mM β-mercaptoethanol) and the protein was eluted by on-bead cleavage using PreScission protease made in-house. Cleaved protein was diluted two-fold with low salt buffer (20 mM Tris.HCl pH = 8.2, 40 mM NaCl, 5 mM $MgCl_2$, 5 mM β-mercaptoethanol), loaded onto HiTrap™ Q HP (GE Healthcare) and eluted with high salt buffer (20 mM Tris.HCl pH = 8.0, 500 mM NaCl, 5 mM $MgCl_2$, 5 mM β-mercaptoethanol). All constructs eluted around 180-200 mM salt. The protein was further purified over a HiLoad 16/60 Superdex 200 column (GE Healthcare) in size exclusion buffer (20 mM HEPES-NaOH pH = 7.4, 100 mM NaCl, 5 mM $MgCl_2$, 2 mM TCEP, 25 mM $(NH_4)_2SO_4$) and the desired

fractions were concentrated using Amicon 30 kDa MWCO device to 10-20 $mg.ml^{-1}$. The PreScission cleavage did not leave any non-native residues at the N terminus.

**Analyses of ATPase Activity.**

Procedures and equations to determine ATPase activity parameters and $IC_{50}$ values of compounds are described in Methods sections of chapters 2 and 3. All ATPase assays were performed in the presence of 0.5 mM MgATP or otherwise indicated. All solution stocks for testing compound activity were made in DMSO.

**Molecular Dynamics (MD).**

*Note - molecular dynamics and compound docking analyses were performed together with Dr Tommaso Cupido.*

Molecular dynamics calculations and ensemble docking were performed as described earlier (Cupido et al., 2019). Briefly, the MD system was set up for *D. melanogaster* spastin (PDB: 3B9P) using the Protein preparation wizard in Maestro® (version 11.6.013, Schrödinger, New York). All non-protein atoms in the PDB file were kept, and the protein loops with no coordinates were modeled using Uniprot: Q8I0P1 as reference sequence. Hydrogen atoms were added to the protein structure, and the protonation states of ionizable residues were assigned for pH 7.0, using the protein preparation wizard in Maestro. This structure was neutralized with KCl ions, additional KCl ions were placed to reproduce a salt concentration of 0.15 M and the system was solvated with an orthorhombic box of simple point charge (SPC) water molecules using

the desmond package in Maestro (Desmond Molecular Dynamics System, version 4.6, D. E. Shaw Research).

To generate the MD atomic trajectory, the standard system relaxation protocol provided in Maestro® was used, followed by a 250 ns of NPT (Isothermal-Isobaric ensemble) molecular dynamics (300 K, 1.01325 bar), during which atomic positions were recorded every 50 ps. To maintain the pressure and temperature of the system, isotropic position scaling and the Nosè-Hoover chain thermostat methods 42 were used with relaxation times of 2 ps and 1 ps, respectively. A RESPA integrator scheme was employed (step: 2.0 fs for bonded interactions; 2 fs for van der Waals and short-range electrostatic interactions; 6 fs for long-range electrostatic interactions). Short-range electrostatic interactions were cut off at 9.0 A.

**Ensemble Docking Procedure.**

All non-protein atoms were removed from the 5000 molecular dynamics frames and the spastin structures from each frame were aligned to remove translational and rotational movement of the macromolecule. Starting from 2 ns of MD trajectory, 1 every 10 frames were selected (97 structures total) as representative of the entire trajectory. To remove overlap of the atoms' van der Waals radii, these structures were minimized using 20 iterations of the Polak-Ribière conjugated gradient method or until the root mean square of the gradient of the energies was < 0.05 kJ mol-1 Å-1, using OPLS2003e force field and a cut-off of 20 Å for the electrostatic interactions and 8 Å for the van der Waals interactions.

Molecular docking was performed on the 97 structures (see above) using the XGlide script in Schrodinger. The major tautomer at pH 7.0 of compound **4.1** (4-((5-amino-1-(2,6-difluorobenzoyl)-1H-1,2,4-triazol-3-yl)amino)benzene sulfonamide) was calculated using the LigPrep panel in Maestro® and energy minimized. A box of 22 Å was placed, centered approximately at the Gln-488 residue of spastin, and compound **4.1** (4-((5-amino-1-(2,6-difluorobenzoyl)-1H-1,2,4-triazol-3-yl)amino)benzenesulfonamide) was docked into the 97 spastin structures using Glide XP and the OPLS2003e forcefield with Schrodinger's GlideScore multi-ligand scoring function44. Receptor grids were generated using a scaling factor of 0.9 for the van Der Waals radii for atom with partial charge <0.25 (absolute value). For ligand docking, the options REWARD_INTRA_HBONDS, SAMPLE_RINGS, HBOND_DONOR_AROMH were set true, the FORCEPLANAR options was set false, and a scaling factor of 0.9 was applied to the van der Waals radii for atom with partial charge <0.15 (absolute value). The binding poses shown in Figure 4.3 represent five distinct poses with the highest docking scores.

**Differential Scanning Fluorimetry.**

Conditions and procedures for differential scanning fluorimetry assays presented in this chapter were identical to those described in Methods sections of chapters 3.

**Co-crystallization of *Drosophila* Spastin-AAA Constructs (aa 445-758) with Compounds.**

***Co-crystallization of Spastin with Compound 4.1.***

Spastin-AAA constructs (N527C or T692A) were concentrated to ~20 mg/ml and mixed with an equal volume of a saturated solution of compound **4.1** in size exclusion buffer (20 mM HEPES-NaOH pH = 7.4, 100 mM NaCl, 5 mM $MgCl_2$, 2 mM TCEP, 25 mM $(NH_4)_2SO_4$). The saturated solution of compound **4.1** was prepared by dissolving the compound in size exclusion buffer and spinning at 14000 rpm for 10 minutes. The protein-compound complex was then mixed with reservoir solution (0.1 M Na-acetate pH 5-7, 2% PEG-4000, 15% 2-methyl-2,4-pentanediol (MPD)) using the hanging drop method and the crystals were allowed to form at 14-18°C. The crystals were additionally soaked for ~1 hour in reservoir solution supplemented with 20% MPD and 200 μM of compound **4.1** prior to freezing in liquid nitrogen.

***Co-crystallization of Spastin with Compound 4.4***

Spastin-AAA constructs (WT or T692A) were concentrated to 10-15 mg/ml and compound **4** was added (final compound concentration ~200 μM) and the mixture was incubated on ice for ~0.5 h. The protein-compound complex was mixed with reservoir solution (0.1 M Na-acetate pH 5-7, 2% PEG-4000, 15% MPD) supplemented with 200 μM of compound **4.4** and the crystals were allowed to form at 14-18°C using the hanging drop method. Obtained crystals were cryo-protected in a solution of the reservoir supplemented with 20% MPD prior to flesh freezing in liquid nitrogen.

**Data Collection and Refinement**

Procedures for crystallographic data collection and refinement for all X-ray structural models presented in this chapter were identical to those described in the Methods section of Chapter 3. The crystal structures of spastin-inhibitor complexes solved in this chapter have been deposited in the RCSB protein data bank (PDB: 6P10, 6P11, 6P12, 6P13, 6P14).

**Chemical Synthesis Information**

For general procedures see Chapter 2 - Methods section.

JNJ-7706621 (compound **4.1**) was purchased from MedChemExpress (Cat. No.: HY-10329). Procedures for synthesis of compounds **4.2**, **4.3** and **4.4** were similar and based on previously published methods (Malerich et al., 2010). As an example, synthesis of compound **4.4** is summarized.

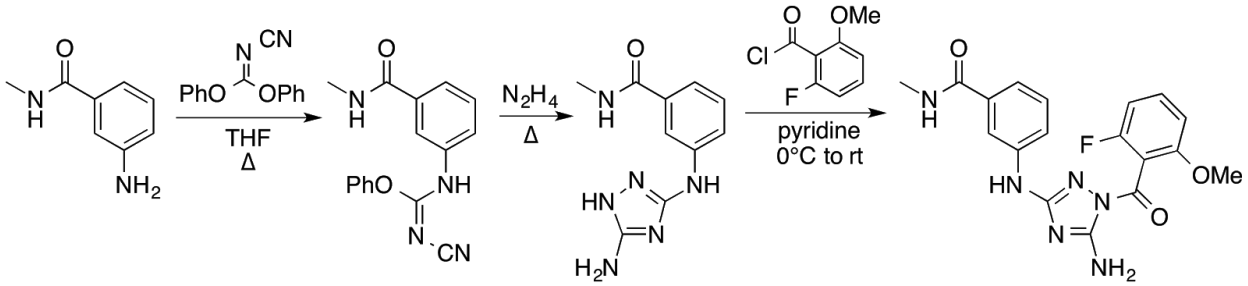


Synthesis of compound **4.4**, 3-((5-amino-1-(2-fluoro-6-methoxybenzoyl) -1H-1,2,4-triazol-3-yl)amino)-N-methylbenzamide. Step 1. 3-amino-N-methylbenzamide (0.5 g, 3.3 mmol) and diphenyl cyanocarbonimidate (1.1 eq, 0.87 g, 3.7 mmol) were dissolved in THF (3 mL) in a round bottom glass flask and refluxed overnight. Solvent was evaporated under reduced pressure using Rotary evaporator and the residue was

treated with diethylether (2x10 ml) and triturated. Crude product was dried and used directly in the next step. MS-ESI [M+1]: expected 295.3, found 295.2. Step 2. Without further purification, 0.9 g of this intermediate (~3.1 mmol) was dissolved in 1M hydrazine solution in THF (1.5 eq, 4.6 mmol, 4.6 ml) while stirring at rt. The reaction was heated at reflux for 4 h while stirring and then cooled down to rt. The excess solvent was evaporated under reduced pressure, and the product of the reaction was washed with diethylether (3x10 ml) and dried. MS-ESI [M+1]: expected 233.2, found 233.3. Step 3. 30 mg (0.13 mmol) of the crude intermediate from step 2 was suspended in ~1 ml of pyridine and 1.2 eq of 2-fluoro-6-methoxybenzoyl chloride were added dropwise while stirring on ice. The reaction was allowed to warm up to room temperature and the solvent was evaporated under flow of nitrogen. The compound **4.4** was separated from the crude mixture by silica gel chromatography in hexane/EtOAc. To obtain HCl salt, the purified compound **4.4** was dissolved in ethylacetate and precipitated by addition of 37% HCl and dried.

**Compound Characterization.**

*Note - compound synthesis and characterization were done in collaboration with Dr Tommaso Cupido, a postdoctoral fellow, and Natalie Jones, a PhD student, in the Kapoor laboratory.*

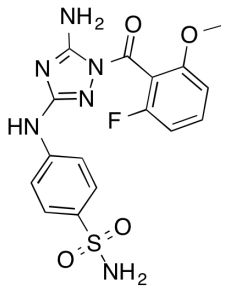

Compound **4.2.**

4-((5-amino-1-(2-fluoro-6-methoxybenzoyl)-1*H*-1,2,4-triazol-3-yl)amino)benzenesulfonamide

Molecular weight (MW) expected for $C_{16}H_{15}FN_6O_4S$: 406.4; MS-ESI [$MH^+$]: found 407.2. $^1$H NMR (600 MHz, DMSO-$d_6$) δ 9.76 (s, 1H), 7.90 (br.s., 2H), 7.58 (m, 1H), 7.56 (d, *J* = 8.6 , 2H), 7.46 (d, *J* = 8.8, 2H), 7.07 (m, 3H), 6.99 (t, *J* = 8.7, 1H), 3.82 (s, 3H).

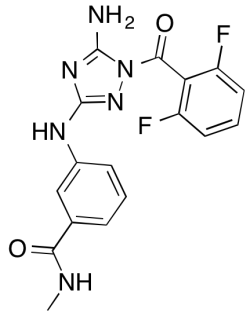

Compound **4.3**.

3-((5-amino-1-(2,6-difluorobenzoyl)-1*H*-1,2,4-triazol-3-yl)amino)-*N*-methylbenzamide

MW expected for $C_{17}H_{14}F_2N_6O_2$: 372.3; MS-ESI [$MH^+$]: found 373.0. $^1$H NMR (600 MHz, DMSO-$d_6$) δ 9.47 (s, 1H), 8.14 (d, *J* = 4.5, 1H), 7.95 (br.s., 2H), 7.76 (s, 1H), 7.70 (m, 1H), 7.49 (d, *J* = 7.5,1H), 7.31 (t, *J* = 8.3, 2H), 7.19 (m, 2H), 2.73 (d, *J* = 4.5, 3H).

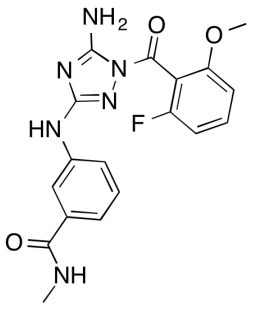

Compound **4.4**.

3-((5-amino-1-(2-fluoro-6-methoxybenzoyl)-1*H*-1,2,4-triazol-3-yl)amino)-*N*-methylbenza mide

MW expected for $C_{18}H_{17}FN_6O_3$ : 385.4; MS-ESI [$MH^+$]: found 385.1. $^1$H NMR (600 MHz, DMSO-$d_6$) δ 9.38 (s, 1H), 8.13 (d, *J* = 4.6, 1H), 7.85 (br.s., 2H), 7.73 (s, 1H), 7.53 (m, 2H), 7.17 (m, 2H), 7.03 (d, *J* = 8.4, 1H), 6.95 (t, *J* = 8.7, 1H), 3.83 (s, 3H), 2.80 (d, *J* = 4.5, 0.6H), 2.73 (d, *J* = 4.5, 2.4H).

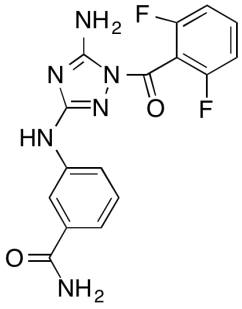

Compound **4.5.**

3-((5-amino-1-(2,6-difluorobenzoyl)-1H-1,2,4-triazol-3-yl)amino)benzamide.

MW expected for $C_{16}H_{12}F_2N_6O_2$: 358.3 , MS-ESI [$MH^+$]: found 359.1. NMR data were collected and analysis is currently undergoing. Assignments can be provided in an addendum to this thesis.

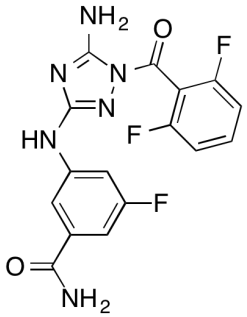

Compound **4.6.**

3-((5-amino-1-(2,6-difluorobenzoyl)-1H-1,2,4-triazol-3-yl)amino)-5-fluorobenzamide.

MW expected for $C_{16}H_{11}F_3N_6O_2$: 376.3 , MS-ESI [$MH^+$]: found 377.2. NMR data were collected and analysis is currently undergoing. Assignments can be provided in an addendum to this thesis.

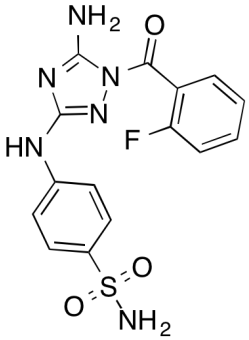

Compound **4.7.**

4-((5-amino-1-(2-fluorobenzoyl)-1H-1,2,4-triazol-3-yl)amino)benzenesulfonamide

MW expected for $C_{15}H_{13}FN_6O_3S$ 376.4; MS-ESI [MH+]: found 377.0. $^1$H NMR (600 MHz, DMSO-d6) δ 9.77 (s, 1H), 7.90 (br.s., 2H), 7.77 (t, J = 6.6, 1H), 7.68 (m, 1H), 7.59 (d, J = 8.4, 2H), 7.50 (d, J = 8.4, 2H), 7.40 (m, 2H), 7.01 (br.s., 2H).

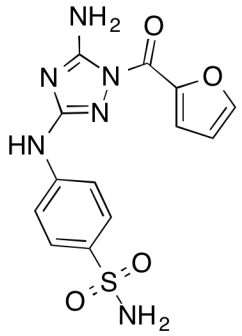

Compound **4.8.**

4-((5-amino-1-(furan-2-carbonyl)-1*H*-1,2,4-triazol-3-yl)amino)benzenesulfonamide

MW expected for $C_{13}H_{12}N_6O_4S$: 348.3, MS-ESI [$MH^+$]: found 349. $^1$H NMR (600 MHz, DMSO-$d_6$) δ 9.85 (s, 1H), 8.19 (s, 1H), 8.04 (d, *J* = 3, 1H), 7.87 (br.s., 2H), 7.77 (d, *J* = 8.4, 2H), 7.69 (d, *J* = 8.4, 2H), 7.15 (s, 2H), 6.88 (dd, *J* = 3, *J* = 1 , 1H).

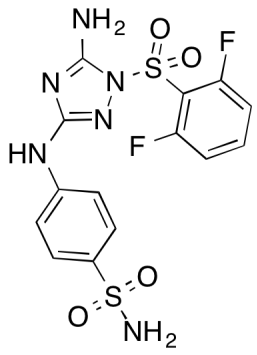

Compound **4.9.**

4-((5-amino-1-((2,6-difluorophenyl)sulfonyl)-1*H*-1,2,4-triazol-3-yl)amino)benzenesulfona mide

MW expected for $C_{14}H_{12}F_2N_6O_4S_2$: 430.4; MS-ESI [$MH^+$]: found 431.1. $^1$H NMR (600 MHz, DMSO-$d_6$) δ 9.80 (s, 1H), 7.88 (m, 1H), 7.77 (d, *J* = 8.4, 2H), 7.54 (br.s., 2H), 7.50 (d, *J* = 8.4, 2H), 7.42 (t, *J* = 9, 2H), 7.12 (br.s., 2H).

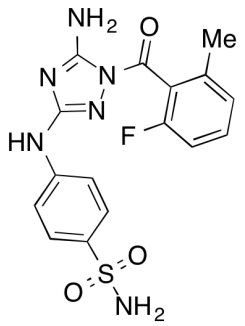

Compound **4.10.**

4-((5-amino-1-(2-fluoro-6-methylbenzoyl)-1*H*-1,2,4-triazol-3-yl)amino)benzenesulfonamide

MW expected for $C_{16}H_{15}FN_6O_3S$: 390.4; MS-ESI [$MH^+$]: found 391.1. $^1H$ NMR (600 MHz, DMSO-$d_6$) δ 9.79 (s, 1H), 7.97 (br.s., 2H), 7.56 (d, , *J* = 8.4, 2H), 7.50 (m, 1H), 7.45 (d, , *J* = 8.4, 2H), 7.22 (d, , *J* = 7.8, 2H), 7.07 (s, 2H), 2.29 (s, 3H).

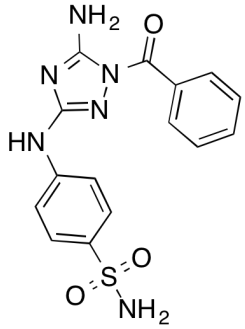

Compound **4.11.**

4-((5-amino-1-benzoyl-1*H*-1,2,4-triazol-3-yl)amino)benzenesulfonamide

MW expected for $C_{15}H_{14}N_6O_3S$: 358.4, MS-ESI [$MH^+$]: found 359.0. $^1H$ NMR (600 MHz, DMSO-$d_6$) δ 9.79 (s, 1H), 8.14 (d, *J* = 7.8, 2H), 7.88 (br.s., 4H), 7.63 (m, 5H), 7.11 (s, 2H).

## Chapter 5: Engineering AAA protein to accept an unnatural nucleotide.

*Note to readers: Results in this chapter arose from a collaboration between myself and Owen Jarman, a summer research fellow in the Kapoor laboratory. Except for results explicitly credited to others I designed and performed all experiments and analysis.*

### Introduction

VCP/p97 is a AAA protein conserved in all eukaryotic cells and plays a critical role in the regulation of a broad range of cellular processes including endoplasmic reticulum associated degradation (ERAD), the ubiquitin-proteasome system, DNA replication, mitophagy and cell division (van den Boom and Meyer, 2018; Maric et al., 2014; Ramadan et al., 2007; Tanaka et al., 2010; Wu and Rapoport, 2018). VCP/p97 belongs to a type 2 class of AAA proteins that contain two AAA domains in tandem on a single polypeptide (Erzberger and Berger, 2006). The two AAA domains in VCP/p97 (referred to as D1 and D2 domains) assemble in a side-on fashion to form functional double-stacked hexamers (DeLaBarre and Brunger, 2003; Twomey et al., 2019). Biochemical studies suggest that D1 and D2 domains are not functionally equivalent (Song et al., 2003). D1 domains have been implicated in the formation of the hexamer and do not substantially hydrolyze ATP (Wang et al., 2003). In contrast, the D2 domains contribute the majority of the ATPase activity of the complex (Chou et al., 2014) and undergo large conformational changes upon ATP hydrolysis. ATP-dependent

conformational changes in VCP/p97 have been linked to substrate processing (Rouiller et al., 2002). However, the precise contribution and interplay of the two AAA domains to the control of VCP/p97's activity are not fully understood.

Engineering nucleotide specificity has facilitated the biochemical and structural studies of many nucleotide-binding enzymes (e.g. GTPases (Hwang and Miller, 1987; Powers and Walter, 1995), kinases (Shah et al., 1997), kinesins (Kapoor and Mitchison, 1999)). This strategy, sometimes referred to as the "bump-hole" method, relies on engineering of the active site in proteins (to generate a "hole") to specifically interact with a modified substrate ("bump") that is not accepted by the wild-type protein (Islam, 2015). Engineering specificity for a non-natural substrate can allow orthogonal control of the engineered protein function in the presence of other enzymes that can bind the same natural substrate. For example, engineered kinase alleles with mutations of the gatekeeper residue in the active site can selectively utillize N6-modified analogs of adenosine 5'-triphosphate that can be leveraged to determine substrates of these proteins in cellular lysates (Shah et al., 1997). However, residues in active sites of many proteins, including proteins in the AAA family, which could be mutated to engineer substrate specificity without disrupting activity are not known.

Here, we use alanine scanning and identify a residue in the active site of AAA protein VCP/p97 that can be mutated to engineer steric complementarity to a bulky ATP analog. We show that this mutant allele can bind and hydrolyze N6-modified nucleotide that cannot be utilized by the wild-type protein. Our results suggest that mutations in the active site of a AAA protein can alter specificity for nucleotide substrate without

disrupting the ATPase activity. Such protein-nucleotide pairs could be useful for studying functions of individual AAA domains in complex assemblies of AAA proteins.

## Results

### Purification and biochemical characterization of mouse VCP/p97 protein.

To identify residues in AAA active site that could alter nucleotide specificity we focused on the VCP/p97 protein. First, to gain insight into nucleotide specificity of the wild-type VCP/p97 we tested its ATPase activity with a panel of N6-modified ATP analogs. For these assays we expressed and purified recombinant, full-length, mouse VCP/p97 protein using a multi-step protocol including affinity, ion exchange and gel filtration chromatography steps (Figure 5.1A, B, C, D). Next, we used malachite green-based assay (Biswas et al., 2009) to characterize the activity of the wild-type VCP/p97 protein. This assay relies on quantification of inorganic phosphate and can therefore be used for analyses of ATP nucleotide analogs (Figure 5.1E). We found that wild-type VCP/p97 can hydrolyze ATP analogs with smaller substituents at the N6 position of adenine (e.g N6-methyl-ATP – Figure 5.1F). In contrast, sterically bulky substituents at the N6 position such as phenyl or cyclopentyl were not tolerated and could not be efficiently hydrolyzed by the wild type protein (Figure 5.1F).

Interestingly, we found that N6-furfuryl adenosine-5'-triphosphate (also known as kinetin triphosphate, KTP) was hydrolyzed at rates similar to the ATP nucleotide (Figure 5.1F). This analog can be utilized as a neo-substrate by other ATP-binding proteins such as kinases (Hertz et al., 2013). Together, these data show that wild-type VCP/p97

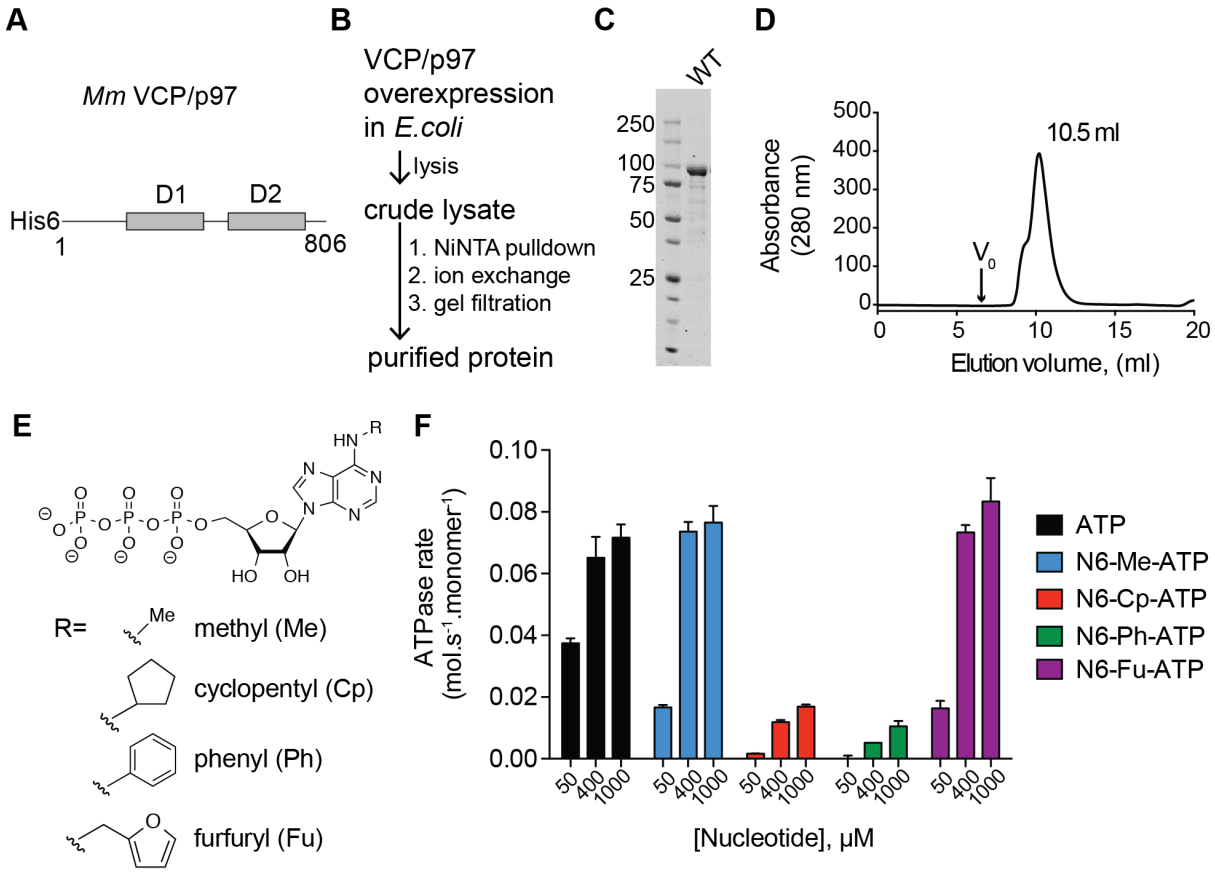


**Figure 5.1. Characterizing nucleotide specificity of wild-type VCP/p97.**
(**A**) Schematic shows the AAA domains (gray boxes, denoted D1 and D2) of the recombinant mouse VCP/p97 (*Mm* - *Mus musculus*) construct used for ATPase assays. N-terminal hexahistidine tag (His6) is also shown (not to scale). (**B**) Schematic detailing the purification of recombinant VCP/p97 constructs. (**C**) SDS-PAGE analysis of purified VCP/p97 wild-type (WT) recombinant construct. (**D**) Elution profile of wild-type VCP/p97 construct from gel filtration chromatography (Superose 6 column). $V_0$, void volume. (**E**) Chemical structures of nucleotide analogs used in this study. (**F**) Rate of nucleotide hydrolysis of mouse VCP/p97 (WT) in presence of indicated nucleotides determined using malachite green-based assay.

protein can selectively hydrolyze only a subset of N6-modified adenosine-5'-triphosphate analogs.

**Identifying and characterizing mutant alleles of VCP/p97 protein.**

Next, to identify residues in the VCP/p97 that could alter nucleotide specificity we focused on the D2 domain of the protein as it was shown to contribute the majority of the protein's ATP hydrolysis activity in biochemical assays (Chou et al., 2014). We examined residues in proximity to the N6 amine of the adenine base (N6 to residue distance: <6Å) in a structural model of VCP/p97 with bound ADP nucleotide (pdbID: 3CF0). These analyses suggested four residues in proximity of the N6 amine (L482, C522, L526 and I656, Figure 5.2A, B). We reasoned that replacing these residues with alanine could "expand" the ATP-binding pocket of VCP/p97 and alter the protein's nucleotide specificity. Therefore, we expressed and purified four recombinant proteins with alanine mutations in the active site (L482A, C522A, L526A and I656A, Figure 5.2C). We characterized ATP-hydrolysis activity of these constructs using malachite green assay and found that all four constructs were active ATPases (Figure 5.2D). These results indicate that mutations of the four residues in VCP/p97 near N6 of the nucleotide do not disrupt ATP hydrolysis activity.

Next, we tested the ATPase activity of these mutants in the presence of N6-modified ATP analogs. Similar to the wild-type protein, we found that all four mutants were able to hydrolyze N6-methyl-ATP analog with rates similar to ATP (Figure 5.3A).

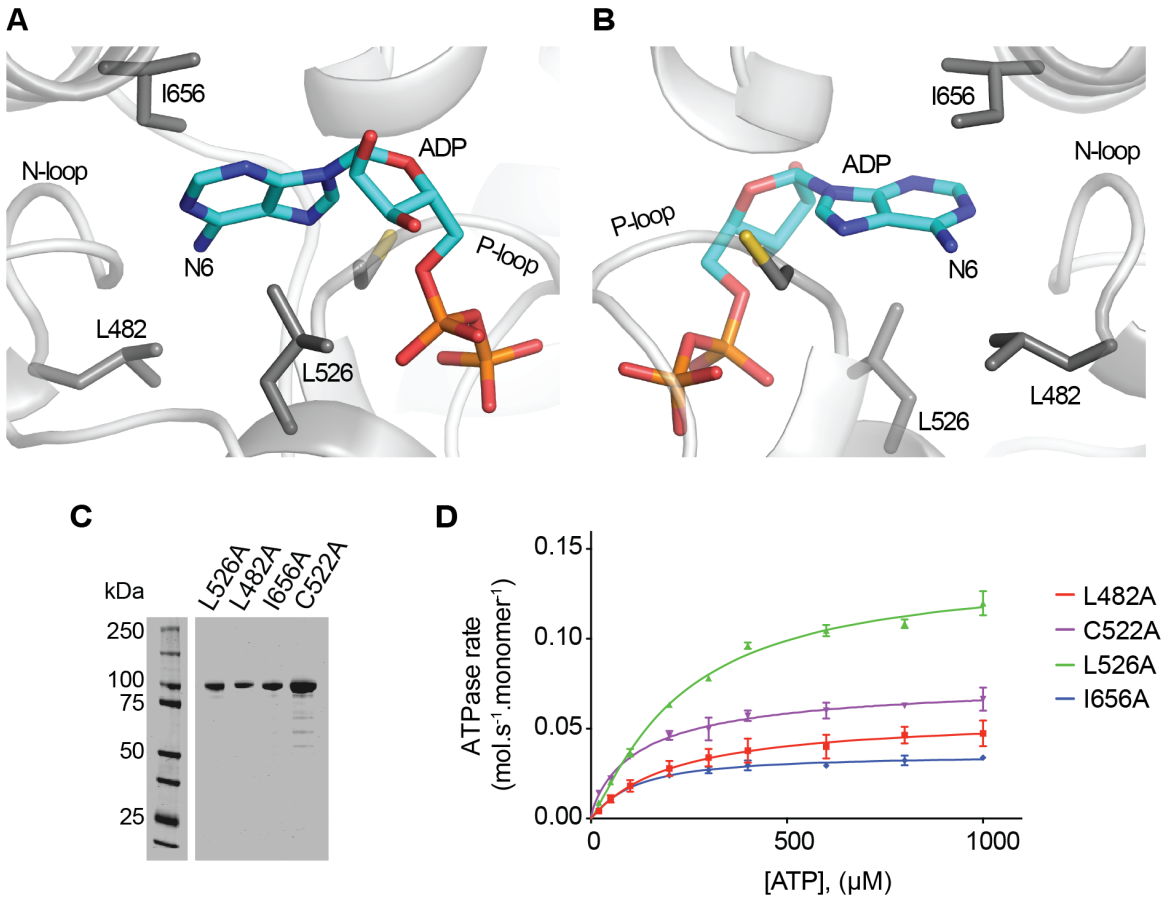


**Figure 5.2. Identifying and characterizing mutations in the active site of D2 domain in VCP/p97.**

(**A-B**) Two views of the nucleotide-binding site in VCP/p97 (PDB: 3CF0) showing adenosine-5′ diphosphate (ADP, stick representation), structural motifs (N-loop and P-loop), and selected side chains of residues within ~6 Å of adenine's N6. (**A**) - view from the front of the active site. (**B**) - view from the back of the ATP pocket. (**C**) SDS-PAGE analysis of four VCP/p97 recombinant constructs with mutations in the active site of the D2 AAA domain. (**D**) ATP-concentration dependence of the steady-state activity of four VCP/p97 protein constructs with mutations in the active site, analyzed using malachite green-based assay. Rates were fit to the Michelis-Menten equation for cooperative enzymes (average ± range, n=2). Values for enzyme activity parameters are provided in Table 5.1.

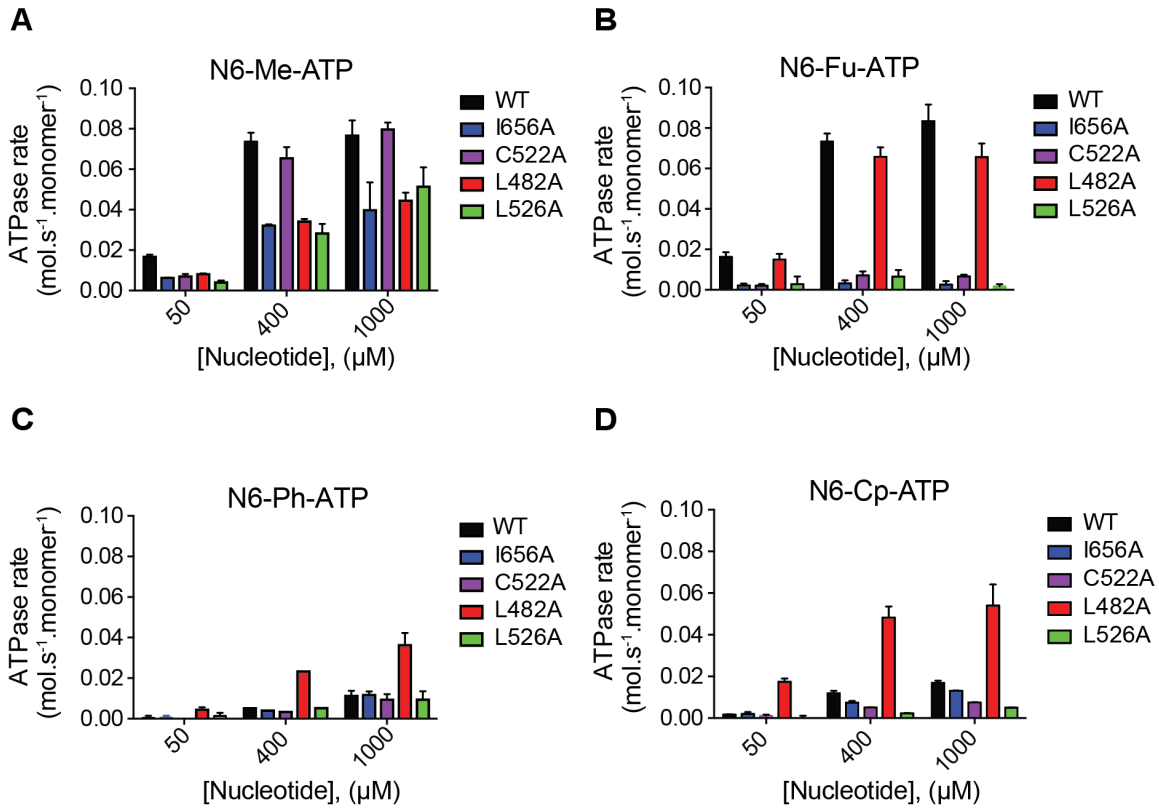


**Figure 5.3. Identifying ATP analogs that can be hydrolyzed by VCP/p97 mutant alleles.**

(**A-D**) Rates of nucleotide hydrolysis of wild-type and four mutant alleles of mouse VCP/p97 in the presence of four N6-modified ATP analogs (N6-methyl-adenosine-5'-triphosphate, N6-Me-ATP (**A**); N6-furfuryladenosine-5'-triphosphate, N6-Fu-ATP (**B**); N6-phenyladenosine-5'-triphosphate, N6-Ph-ATP (**C**) and N6-cyclopentyladenosine-5'-triphosphate, N6-Cp-ATP (**D**). Rate of nucleotide hydrolysis was determined using malachite green assay at three concentrations of each nucleotide (50, 400 and 1000 μM).

We also found that N6-furfuryl adenosine-5'-triphosphate can be hydrolyzed by the L482A mutant similar to the wild-type protein but is not accepted by the other three mutants (C522, L526 and I656, Figure 5.3B). These studies also revealed that ATP analogs with N6-phenyl and N6-cyclopentyl substitutions are not readily accepted by the wild-type and mutant constructs apart from the L482A allele (Figure 5.3C, D). Interestingly, the L482A construct can hydrolyze both N6-phenyl- and N6-cyclopentyl-modified ATP with rates nearly identical to those of the L482A protein in presence of ATP (Figure 5.2D and 5.3C, D). Therefore, we next focused on the L482A construct and characterized the concentration-dependent, steady-state hydrolysis activity of this construct along with the wild-type protein in the presence of ATP and the N6-cyclopentyladenosine -5'-triphosphate (N6-Cp-ATP) nucleotides. The L482A construct had a catalytic activity ($k_{cat}$) of 0.05 ± 0.01 $s^{-1}$ in the presence of ATP and 0.04 ± 0.01 $s^{-1}$ in the presence of N6-Cp-ATP (average ± range, n = 2 , Figure 5.4A). These $k_{cat}$ values are within ~1.5-fold of the wild-type protein (ATP: 0.07 ± 0.01 $s^{-1}$, average ± s.d., n = 3, Figure 5.4B).

The ATP concentrations required for half-maximal enzymatic velocity ($K_{1/2}$) were also within a narrow range, from 43 ± 4 μM (ATP, wild type, average ± s.d., n = 3, Figure 5.4B) to 49 ± 14 μM (N6-Cp-ATP, L482A, average ± range, n=2, Figure 5.4A) and 197 ± 52 μM (ATP, L482A, average ± range, n=2, Figure 5.4A). These results indicate that nucleotide specificity of a AAA protein can be altered by engineering mutations of selected residues in its active site.

## Discussion

Here, I report the identification of a mutant allele of VCP/p97 protein (L482A) that can selectively accept and hydrolyze N6-cyclopentyladenosine-5'-triphosphate nucleotide (N6-Cp-ATP). This N6-modified ATP analog cannot be hydrolyzed by the wild-type VCP/p97 protein and thus provides an orthogonal substrate for studying VCP/p97 functions.

Leu-482 residue maps to the variability hotspot site in the N-loop motif of the VCP/p97's D2 domain. In our work with spastin and fidgetin-like 1 AAA proteins we found that swapping residues at this site with residues found at the equivalent position in other AAA proteins can be used to generate active mutant alleles of these proteins (see chapters 2, 3 and 4). Although alanine is not commonly found at this position in AAA family (Cupido et al., 2019; Wendler et al., 2012), our studies with VCP/p97 suggest that replacing the N-loop variability hotspot residue with alanine could also afford active mutant alleles of AAA proteins.

The VCP/p97-L482A allele and its cognate nucleotide analog (N6-Cp-ATP) should be useful for studying the roles of D1 and D2 AAA domains of the protein. For example, it is not fully understood how activities of VCP/p97's D1 and D2 domains modulate the interactions with substrate proteins during the catalytic cycle. Traditionally, Walker A and Walker B mutations that block ATP binding and hydrolysis have been used to study functions of the two AAA domains in the protein (Chou et al., 2014). However, using these mutations to dissect roles of active sites that reciprocally modulate their functions, such as those in VCP/p97, can be challenging. The mutant

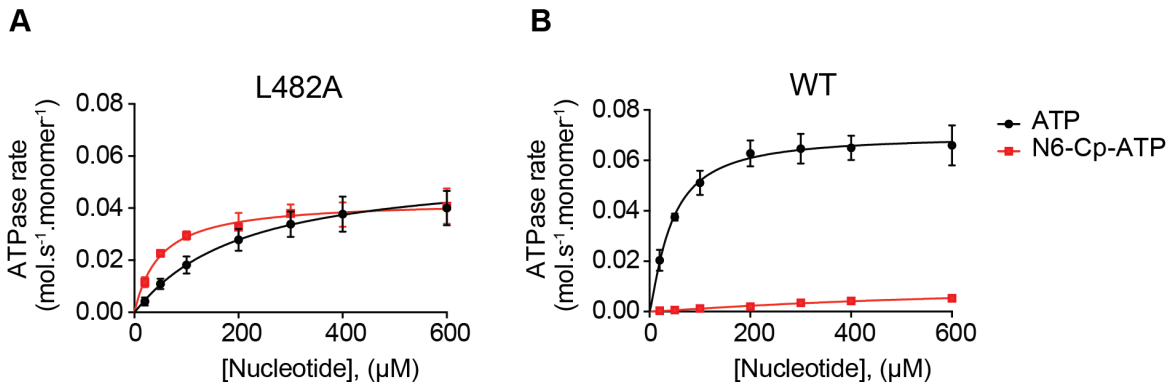


**Figure 5.4. Characterizing wild-type and L482A mutant allele of VCP.**
(**A-B**) Concentration dependence of the steady-state activity of (**A**) L482A mutant allele and wild-type (WT) (**B**) VCP in the presence of ATP and N6-Cp-ATP nucleotides analyzed using malachite green assay. Rates were fit to the Michaelis–Menten equation for cooperative enzymes (L482A: $K_{1/2}$ (ATP) = 197 ± 52 μM; $K_{1/2}$(N6-Cp-ATP) = 49 ± 14 μM; $k_{cat}$ (ATP) = 0.05 ± 0.01 $s^{-1}$; $k_{cat}$(N6-Cp-ATP) = 0.04 ± 0.01 $s^{-1}$; average ± range; n = 2. WT: $K_{1/2}$ (ATP) = 43 ± 4 μM; $k_{cat}$ (ATP) = 0.07 ± 0.01 $s^{-1}$; average ± s.d.; n = 3. $K_{1/2}$ and $k_{cat}$ values for the wild-type protein in the presence of N6-Cp-ATP could not be determined due to low nucleotide hydrolysis activity).

| ATP | L482A | C522A | L526A | I656A |
|---|---|---|---|---|
| $k_{cat}$ ($s^{-1}$) | 0.04 ± 0.01 | 0.08 ± 0.01 | 0.16 ± 0.01 | 0.04 ± 0.01 |
| Hill coefficient | 1.1 ± 0.2 | 0.7 ± 0.2 | 1.1 ± 0.1 | 1.0 ± 0.1 |
| $K_{1/2}$ (mM) | 0.20 ± 0.05 | 0.17 ± 0.07 | 0.28 ± 0.04 | 0.13 ± 0.02 |

**Table 5.1. Characterizing VCP/p97 mutant alleles.**
Concentration-dependence of the steady-state activity of L482A, C522A, L526A and I656A mutant alleles in the presence of ATP analyzed using malachite green assay. Rates were fit to the Michaelis–Menten equation for cooperative enzymes and average and range were calculated (n=2).

allele identified here does not abrogate protein activity and allows dissecting the role of nucleotide hydrolysis by the VCP's D2 domain in isolation. Therefore, this tool will be useful for establishing the roles of D1 and D2 domains for VCP/p97-mediated substrate engagement and processing.

Our result suggests a possible approach to study AAA proteins with high homology in the active site. As many AAA proteins have nearly identical active sites to VCP/p97 it should be possible to generate equivalent mutant alleles of these proteins. For example, the nuclear valosin-containing protein (NVL) is a AAA ATPase implicated in ribosome biogenesis that is homologous to VCP/p97 and has nearly identical active sites (Kressler et al., 2012b). Therefore, engineering equivalent mutations in NVL should be possible and could be used to dissect its functions in ribosome biogenesis. This approach could be especially powerful in reconstituted systems such as Xenopus egg extract, in which proteins of choice can be immunodepleted and replaced with mutant alleles. The supplied alleles can then be specifically activated by N6-Cp-ATP or inhibited by the slowly hydrolyzable analogs such as N6-Cp-ATPγS or N6-Cp-AMPPNP. This could be useful for identifying NVL's substrates during ribosome biogenesis.

In our screen for unnatural ATP analogs we identified N6-cyclopentyl ATP as a suitable substrate for the L482A allele of VCP/p97. However, it is possible that N6-cyclopentyl-ATP may not be an optimal substrate for AAA proteins in which residues diverged near the N6 of ATP. For example, FIGL1 AAA protein has a valine at this site and valine-to-alanine mutant of FIGL1 does not hydrolyze N6-Cp-ATP (Figure 5.5). To overcome these limitations, modifications to the cyclopentyl moiety or identification of

other nucleotide analogs may be needed. Nevertheless, the approach presented in this chapter provides a template for engineering nucleotide specificity of proteins in the AAA family. It will be interesting to investigate if this approach could be extended to other ATP-binding proteins with related nucleotide-binding sites such as RecA helicases or ABC transporter proteins.

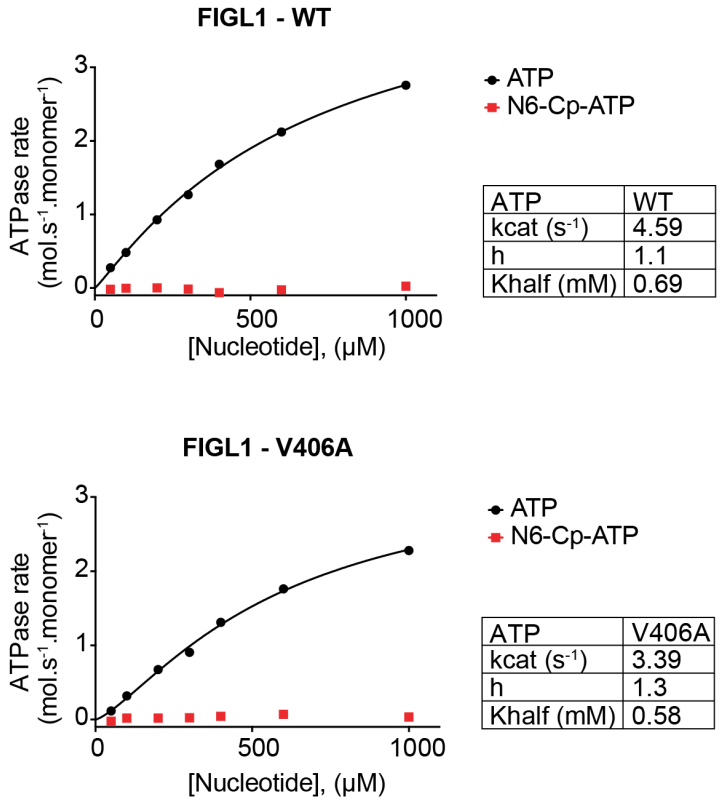


**Figure 5.5. Characterizing nucleotide-specificity of wild-type and mutant allele of FIGL1.**

(**A-B**) Concentration dependence of the steady-state activity of FIGL1 AAA protein (**A**) wild-type (WT) and (**B**) mutant allele (V406A) in the presence of ATP and N6-Cp-ATP nucleotides analyzed using malachite green assay. Rates were fit to the Michaelis–Menten equation for cooperative enzymes (values for the wild-type and mutant proteins in the presence of N6-Cp-ATP could not be determined due to low nucleotide hydrolysis activity).

**Chapter 5 - Methods.**

All biochemical reagents were obtained from Sigma-Aldrich unless specified otherwise. All recombinant proteins were expressed in *Escherichia coli* BL21 Rosetta cells (Merck) grown in LB Miller's medium (Formedium). Protein expression was induced at $O.D._{600}$= 0.6-0.8 with 0.5 mM IPTG (Goldbio), and the cultures were grown at 16 ºC for 12-16 h. All purification steps were performed on ice. Protein concentration was estimated using a Bradford assay (BioRad), and bovine serum albumin (BSA) standards. Molecular weight and purity of the recombinant protein samples were analyzed by SDS-PAGE, followed by staining with Coomassie blue (BioRad).

**His6-*Mm*-VCP/p97 purification strategy**.

Cells expressing recombinant proteins were collected by centrifugation, re-suspended in the lysis buffer (50 mM Tris-HCl, 250 mM NaCl, 20 mM imidazole, 5 mM $MgCl_2$, 1 mM tris(2-carboxyethyl)phosphine (TCEP), 0.5 mM ATP, 5 U/ml benzonase, and complete EDTA-free protease inhibitors (Roche), pH 8.0), and lysed with an Emulsiflex-C5 homogenizer (Avestin) through five cycles at 10,000-15,000 psi. The homogenized lysate was centrifuged at 40,000 rpm for 45 to 60 min using a Ti45 rotor in a Beckman Coulter Optima LE-80K ultracentrifuge. The clarified lysate was incubated with Ni-NTA beads (Qiagen) for 40 min, and the beads were extensively washed using wash buffer (50 mM Tris-HCl, 400 mM NaCl, 20 mM imidazole, 5 mM $MgCl_2$, 1 mM TCEP, pH 7.5). The protein was eluted with wash buffer supplemented with 300 mM imidazole, diluted 1:2 in low salt buffer (50 mM Na-HEPES, 150 mM NaCl,

5 mM $MgCl_2$, 2 mM TCEP, pH 7.5) and loaded onto a Mono Q column 5/50 GL (GE Healthcare). After loading the protein was eluted with a gradient of high salt buffer (50 mM Na-HEPES, 1 M NaCl, 5 mM $MgCl_2$, 2 mM TCEP, pH 7.5). The wild-type VCP/p97 protein eluted at approximately 350 mM NaCl. Combined MonoQ fractions were filtered through a 0.22-µm Millex-GP PES membrane and loaded on a 10/300 Superdex 200 column (GE Healthcare) in size exclusion buffer (25 mM Na-Hepes 150 mM NaCl, 5 mM $MgCl_2$, 2 mM TCEP, 5% (w/v) glycerol, pH 7.5). Fractions from size-exclusion column were concentrated to a minimum of 1 mg/ml using an Amicon Ultra 100K MWCO centrifugal filter, snap frozen in liquid nitrogen and stored at −80 °C.

**Analyses of nucleotide hydrolysis.**

Nucleotide hydrolysis activity was determined by quantifying the rate of phosphate release using malachite green assay by a protocol adapted from (Biswas et al., 2009). Briefly, following stock solutions were prepared:

MG = 0.13% (w/v) malachite green (Sigma – M6880) in water

PVA = 3.7% (w/v) PVA (Sigma – P8136) in water

AM = 9.15% (w/v) ammonium molybdate (Sigma – A7302) in 6M HCl

Citrate = 34% (w/v) sodium citrate (Sigma – S1804) in water

Malachite green reagent (MGR) for detection of phosphate was prepared fresh as follows. MG:water:PVA:AM solutions were mixed in 2:2:1:1 ratios (by volume) and rotated at room temperature until the solution turned yellow. The mixture was then spun for 10 min at 5000 rpm in table-top centrifuge at room temperature (rt), decanted and

the soluble supernatant was used for assays. To detect inorganic phosphate, 25 µl of enzyme reaction was mixed with 25 µl of freshly-prepared MGR reagent and the resulting solution was left incubating at rt for 1 min. Next, 1/10th of the volume (i.e. 5 µl) of citrate solution was added and the solution was mixed well. Calibration curve using phosphate standards (aqueous solutions of $K_2HPO_4$: 0 to 1000 µM) was also obtained by this procedure. Next, the time course of absorbance increase of each sample corresponding to the release of phosphate in the ATPase reaction was measured using a Synergy NEO Microplate Reader (absorbance measured @ 635nm). The absorbance values were plotted against time and fit by linear regression to obtain a rate of absorbance increase. The ATPase rate was calculated from the background (no protein) corrected rates and the phosphate calibration curve.

**Determining Enzyme Parameters.**

Enzyme parameters $K_{1/2}$, $k_{cat}$ and Hill coefficients (h) for the recombinant enzymes were determined by fitting the rates to the Michaelis-Menten equation for cooperative enzymes using Prism v.6.0 (GraphPad Software Inc) (Equation 1 - see chapter 2 for details).

## Chapter 6: Distinct mechanisms of resistance to a CENPE inhibitor emerge in haploid and diploid cells.

*Note to readers: A closely related version of this work is currently under review in Cell Chemical Biology. Results in this chapter arose from a collaboration between myself and Donovan Phua, a summer research fellow in the Kapoor laboratory. Except for results explicitly credited to others I designed and performed all experiments and analysis.*

### Introduction.

Understanding resistance to chemical inhibitors in cells is critical for improving their efficacy as therapeutics (Daub et al., 2004). Cancer cells often harbor chromosomal translocations and abnormal ploidy (Bakhoum and Cantley, 2018; Chunduri and Storchová, 2019; Gordon et al., 2012) and these differences in karyotypes can result in unique constraints on the evolution of genetic changes (Podgornaia and Laub, 2015; Starr and Thornton, 2016). For example, variations in gene copy numbers can influence epistatic interactions between alleles that results in the evolution of distinct biochemical outputs of proteins (Siddiq et al., 2017). Therefore, the emergence of drug resistance can depend on differences in cellular karyotypes and ploidy. However, for most anti-cancer drugs we lack analyses of how differences in chromosome number impacts the specific mechanisms of resistance that can emerge.

CENPE is a large (~312 kDa) plus-end directed microtubule motor that mediates interactions between kinetochores and microtubules and plays a key role in aligning chromosomes during mitosis (Kapoor et al., 2006; McEwen et al., 2001; Putkey et al., 2002; Wood et al., 1997). Genetic knockout or chemical inhibition of CENPE results in activation of the spindle assembly checkpoint, prolonged metaphase arrest, and cell death (Putkey et al., 2002; Wood et al., 2010). Therefore, CENPE has been proposed as a potential target for cancer therapeutics and chemical inhibitors of CENPE have been developed (Hirayama et al., 2015; Ohashi et al., 2015; Wood et al., 2010). In particular, GSK923295 is a potent CENPE inhibitor that was tested in phase 1 clinical trial as an anti-cancer agent (Chung et al., 2012; Lock et al., 2012). In vitro biochemical and biophysical analyses indicate that the compound binds in an allosteric pocket proximal to the ATP-binding site in the kinesin motor domain (Wood et al., 2010). Further, GSK923295 has been proposed to block the ATPase cycle of CENPE by preventing the phosphate release and locking the motor domain in a tight microtubule-bound state (Wood et al., 2010). This mechanism likely contributes to cytotoxic activity of GSK923295 against cancer cell lines. However, many cancer cells are not sensitive to the GSK923295 inhibitor (Lock et al., 2012; Wood et al., 2010) and the mechanisms of resistance against GSK923295 in cells are not well understood.

Analysis of resistance that is specific to a chemical inhibitor can also be leveraged for determining its cellular target and validating its mechanism of action (Kapoor and Miller, 2017). We have developed an approach termed “DrugTargetSeqR” that combines transcriptome sequencing, computational discovery of drug

resistance-conferring mutations, and genome editing to confirm and validate cellular targets of drugs (Kasap et al., 2014; Wacker et al., 2012). We have proposed that “gold standard” target validation is achieved when a resistance-conferring mutation is identified and shown to protect against the inhibitor in biochemical as well as cellular assays (Kapoor and Miller, 2017). However, we lack this level of analysis of the mechanism of action of GSK923295 in cancer cells.

Here, we use unbiased selections to isolate GSK923295-resistant clones in diploid or haploid cells to investigate mechanisms of resistance. We use sequencing analyses to identify genetic changes in these cells that confer resistance to the GSK923295 inhibitor, and use biochemical assays to characterize selected mutations in vitro. Our data suggest that cells with different ploidies can acquire distinct mechanisms of chemotype-specific drug resistance against the same chemical inhibitor.

**Results.**

**Identifying and characterizing cells resistant to GSK923295.**

To examine resistance to GSK923295 (Figure 6.1A) we focused on two cancer cell lines - HCT116 and KBM7. We used diploid HCT116 cells that were employed for DrugTargetSeqR (Kasap et al., 2014; Wacker et al., 2012) as selection of inhibitor-resistant clones can be efficient due to impaired DNA mismatch repair pathways in these cells (Glaab and Tindall, 1997). We used the KBM7 cell line in our analyses as these are well characterized near-haploid mammalian cells that have been used to examine recessive resistance mechanisms that could be otherwise masked in diploid or polyploid cells (Elling and Penninger, 2014; Smurnyy et al., 2014).

As a first step we confirmed that GSK923295 potently inhibits proliferation of these two cell lines (HCT116: $LD_{50}$ = 0.25 ± 0.04; KBM7: $LD_{50}$ = 0.31 ± 0.02 μM; average ± s.d.; n=3, Figure 6.1B). Next, we set up unbiased selections in HCT116 cells to identify clones resistant to the GSK923295 compound. We cultured HCT116 cells in the presence of the compound (2μM GSK923295) and in approximately two weeks observed multiple resistant colonies. We isolated and characterized two resistant clones (Figure 6.1C, see Methods for details). We tested these HCT116 clones and found they were resistant to the GSK923295 compound at concentrations up to ~85-fold higher than the $LD_{50}$ for parental cells (HCT116 cl.1: $LD_{50}$ = 20.3 ± 1.1 μM; cl.2: 21.5 ± 0.7 μM, Figure 6.1C). As KBM7 cells grow in suspension, we first optimized a cell dilution-based protocol in 96-well plates in order to select GSK923295-resistant cells (see schematic in Figure 6.2A). After ~3 weeks of selections with our cell dilution-based scheme in the

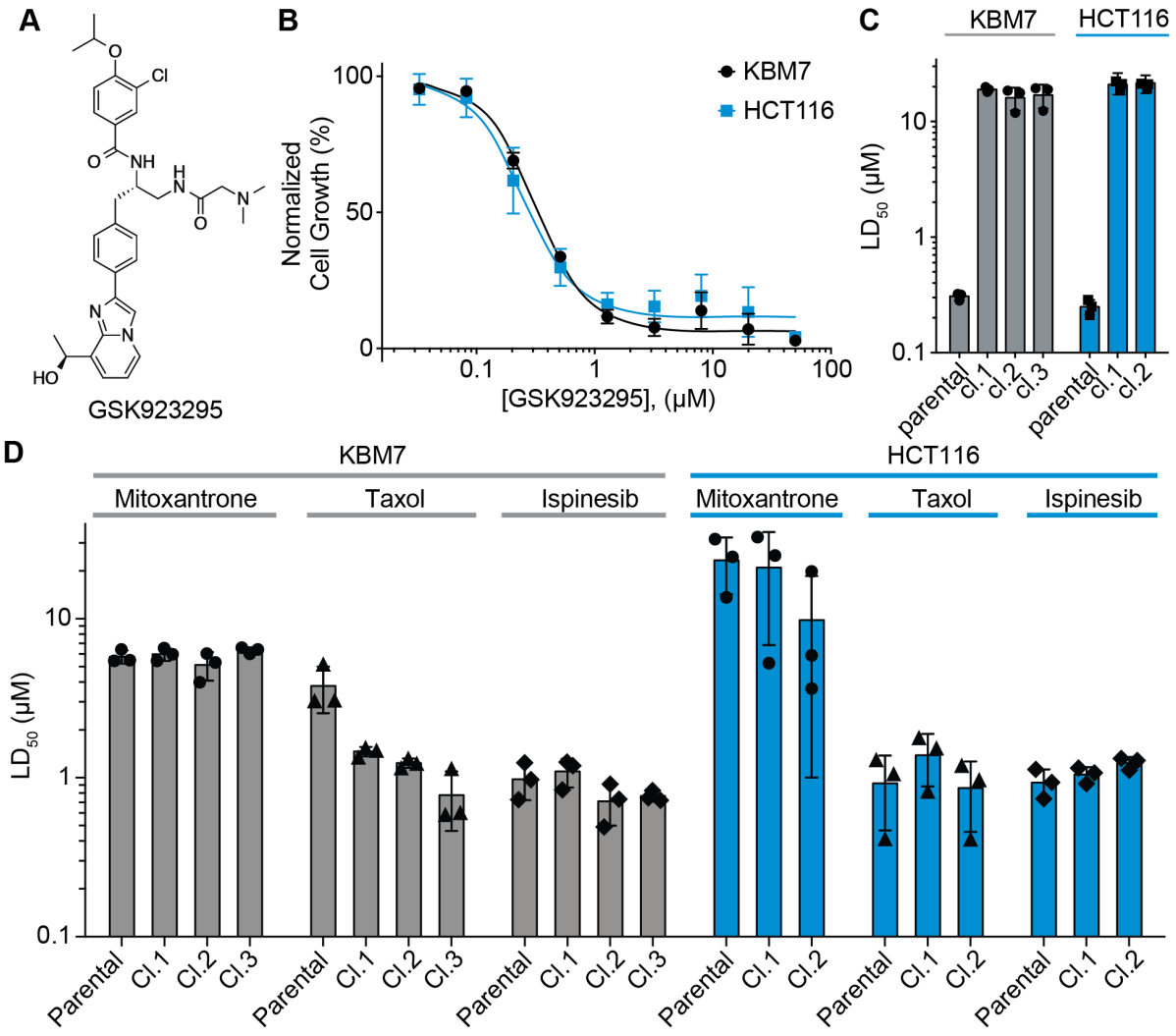


**Figure 6.1. Identifying GSK923295-resistant clones derived from HCT116 or KBM7 cells.**

(**A**) Chemical structure of CENPE kinesin inhibitor (GSK923295). (**B**) Proliferation assay showing dose-dependent response of HCT116 and KBM7 parental cells to treatment with GSK923295 inhibitor (KBM7: $LD_{50}$ = 0.31 ± 0.02 μM, HCT116: $LD_{50}$ = 0.25 ± 0.04 μM, average ± s.d., 72 hr, n=3). (**C**) Cellular viability of HCT116 and KBM7 clones after treatment with GSK923295 inhibitor (KBM7 cl.1: $LD_{50}$ = 19 ± 1 μM, cl.2: 16 ± 4 μM, cl.3: 17 ± 4 μM; HCT116 cl.1: 20 ± 1 μM, cl.2: 22 ± 1 μM, average ± s.d., 72 hr, n=3). For comparison, $LD_{50}$ values for parental cells treated with GSK923295 compound are also shown (data from Figure 7.1C). (**D**) Proliferation assay showing the effects of mitoxantrone, taxol and ispinesib on the growth of HCT116 and KBM7 parental and GSK923295-resistant cells (72 hr, n=3). Corresponding dose response curves that were used to determine the $LD_{50}$ values in (**C**) and (**D**) are provided in Fig. 6.2 and Table 6.1.

presence of the GSK923295 inhibitor (2 μM), we isolated cells from three wells in which growth was observed. We tested these KBM7 clones and found they were also resistant to the GSK923295 compound (KBM7 cl.1: 18.9 ± 1 μM, cl.2: 16.0 ± 3.6 μM, cl.3: 16.9 ± 3.9 μM, Figure 6.1C).

A range of mechanisms (e.g. upregulation of drug efflux pumps) can confer resistance to chemically-unrelated cytotoxic agents in cancer cells (Gottesman et al., 2016; Robey et al., 2018). In developing and applying DrugTargetSeqR, we have found that testing resistant clones for sensitivity to mitoxantrone, ispinesib, and taxol can help identify multi-drug response-based resistance mechanisms (Kasap et al., 2014; Wacker et al., 2012). We found that compared to parental cells, GSK923295-resistant clones derived from HCT116 or KBM7 cells did not exhibit resistance to these compounds (Figure 6.1D and 6.2B and Table 6.1). In fact, we note that KBM7 clones resistant to the GSK923295 compound exhibited modestly enhanced sensitization to the microtubule-stabilizing agent taxol (Figure 6.1D, 6.2B and Table 6.1). Taken together, these data indicate that resistance to GSK923295 exhibited by the KBM7 and HCT116 clones we isolated is chemotype-specific and not likely due to multi-drug response mechanisms.

Next, we also examined the HCT116 parental cells and resistant clones for presence of uncongressed chromosomes in metaphase, which is a typical phenotype observed in cells upon CENPE knockdown (Kapoor et al., 2006; Wood et al., 2010) (Figure 6.3A-D). We found that treatment of parental cells with GSK923295 resulted in uncongressed chromosomes in metaphase cells (Figure 6.3A,B) consistent with

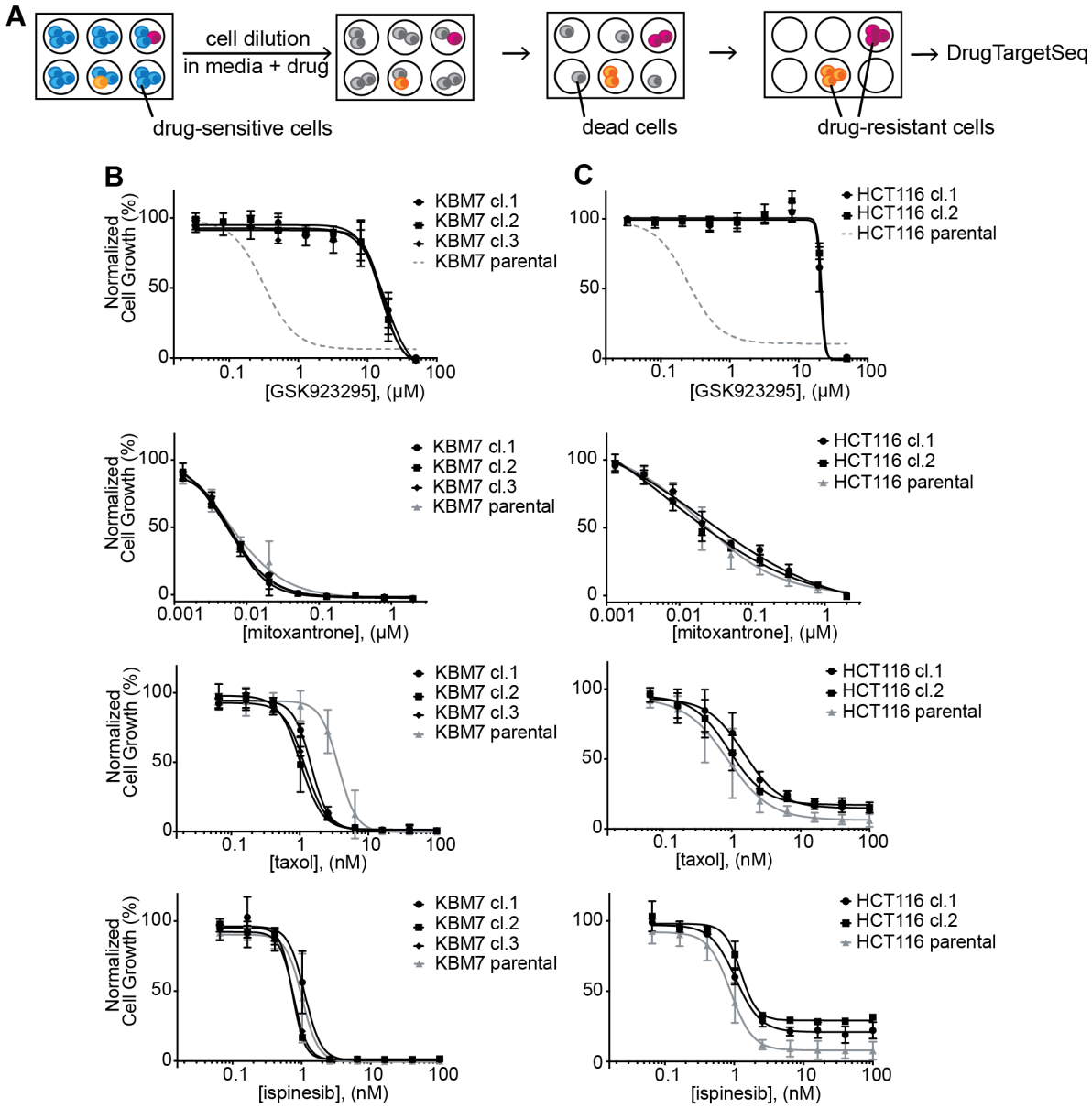


**Figure 6.2. Characterizing GSK923295-resistant clones in KBM7 and HCT116 cells. Related to Figure 6.1C and D.**

(**A**) Schematic of cell dilution-based protocol for selection of drug-resistant cells growing in suspension (e.g. KBM7). (**B-C**) Concentration-dependent inhibition of cell growth of parental and GSK923295-resistant KBM7 and HCT116 cells. Cell proliferation was determined using Alamar Blue assay (72 hr, see Methods for details). Data were fit to a sigmoidal dose-response equation and $LD_{50}$ values were determined ($LD_{50}$ values are shown in Table 6.1. For comparison, data for parental cells treated with GSK923295 are also shown (from Figure 6.1B, gray dotted lines).

**KBM7**

| LD50: | | parental | cl.1 | cl.2 | cl.3 |
|---|---|---|---|---|---|
| **GSK923295** | average | 0.31 | 18.93 | 16.03 | 16.92 |
| (μM) | SD | 0.02 | 0.95 | 3.60 | 3.92 |
| | | | | | |
| **Ispinesib** | average | 0.98 | 1.10 | 0.71 | 0.77 |
| (nM) | SD | 0.26 | 0.22 | 0.21 | 0.06 |
| | | | | | |
| **Taxol** | average | 3.78 | 1.46 | 1.24 | 0.78 |
| (nM) | SD | 1.23 | 0.10 | 0.08 | 0.32 |
| | | | | | |
| **Mitoxantrone** | average | 5.77 | 5.99 | 5.12 | 6.34 |
| (nM) | SD | 0.55 | 0.55 | 1.04 | 0.30 |

**HCT116**

| LD50: | | parental | cl.1 | cl.2 |
|---|---|---|---|---|
| **GSK923295** | average | 0.25 | 20.30 | 21.50 |
| (μM) | SD | 0.04 | 1.13 | 0.70 |
| | | | | |
| **Ispinesib** | average | 0.93 | 1.11 | 1.24 |
| (nM) | SD | 0.20 | 0.05 | 0.11 |
| | | | | |
| **Taxol** | average | 0.92 | 1.38 | 0.86 |
| (nM) | SD | 0.46 | 0.50 | 0.40 |
| | | | | |
| **Mitoxantrone** | average | 23.32 | 21.00 | 9.80 |
| (nM) | SD | 9.10 | 14.16 | 8.79 |

**Table 6.1. Characterizing GSK923295-resistant clones derived from HCT116 and KBM7 cells. (Related to Figure 6.1C and D and Figure 6.2).**

Corresponding dose response curves that were used to determine the $LD_{50}$ values in this table are provided in Figure 6.2.

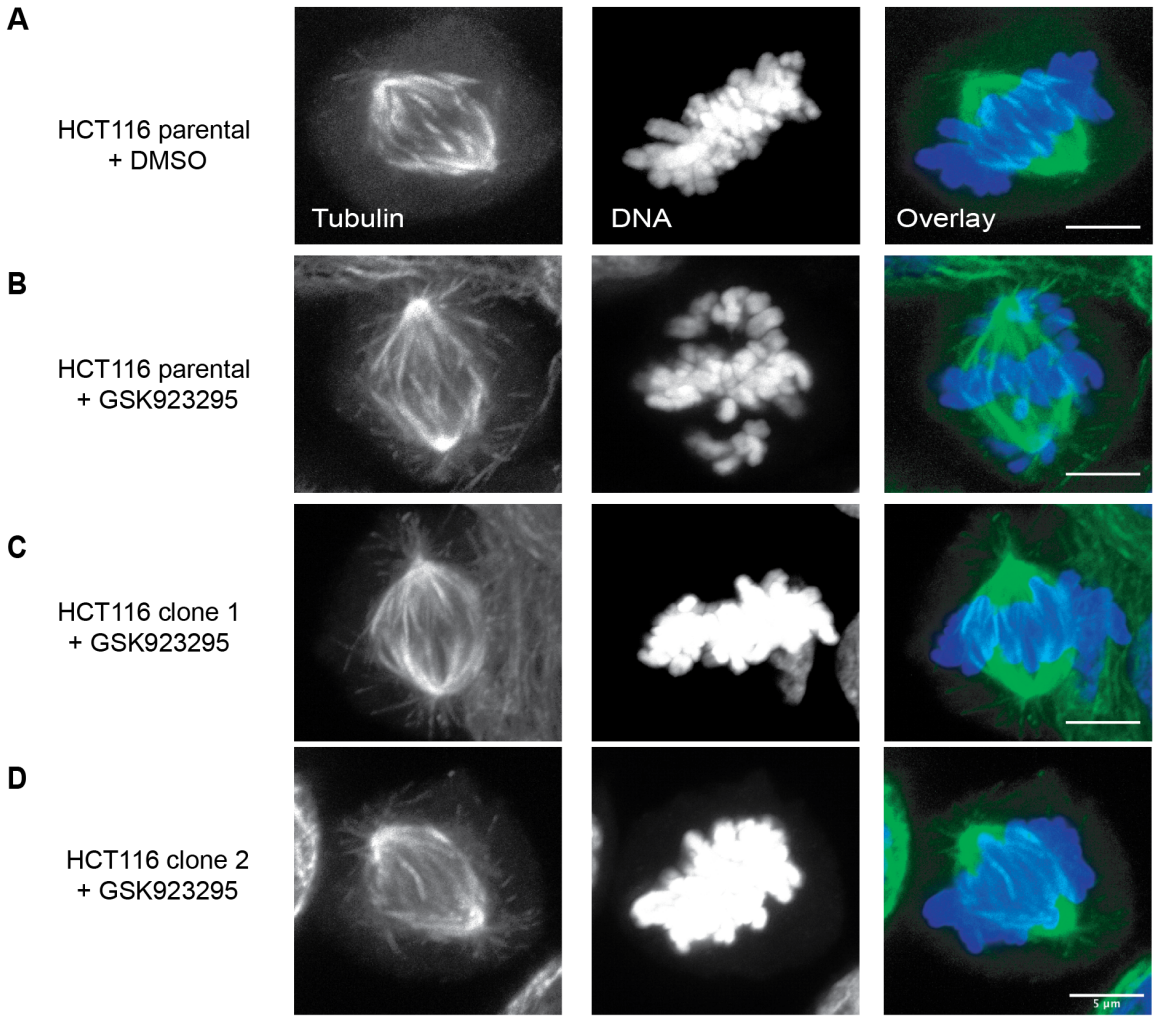


**Figure 6.3 Characterizing GSK923295-resistant clones in HCT116 cells.**
(**A-D**) Immunofluorescence images of metaphase spindles in HCT116 parental (**A,B**) and GSK923295-resistant cells (**C,D**). Maximum intensity projections of DNA, tubulin and the overlays are shown. Cells were treated with DMSO vehicle (0.1 %, parental, **A**) or inhibitor (200 nM, parental (**B**); clone 1 (**C**), clone 2 (**D**)) for 4 hours. Scale bars, 5 µm.

previously reported observations (Wood et al., 2010). In contrast, we did not observe substantial increase of uncongressed chromosomes in the resistant clones (Figure 6.3C, D).

**Examining resistance to GSK923295 in diploid HCT116 cells.**

We have found that mutations leading to chemotype-specific resistance often emerge in the direct targets of drugs (Kapoor and Miller, 2017). Therefore, we next analyzed the sequence of the CENPE gene in the GSK923295-resistant clones isolated from HCT116 cells. In particular, we sequenced genomic DNA from the GSK923295-resistant clones and the parental cells to analyze exons 1-8, which correspond to the motor domain of CENPE kinesin. Sanger sequencing did not reveal any nonsynonymous mutations in the DNA isolated from parental cells, but we found a different heterozygous mutation in each of the two GSK923295-resistant clones (clone 1, chr.4, pos.: 103195988, complement strand: ATG to GTG (M97V); clone 2, chr.4, pos.: 103194435, complement strand: AGG to ATG (R189M), Figure 6.4A). These residues map to the predicted GSK923295-binding site in a pocket near loop 5 in the CENPE motor domain (Figure 6.5A).

To characterize these mutations in CENPE we designed recombinant constructs of its motor domain. We purified wild-type and two mutant constructs (M97V and R189M) using a multistep protocol including affinity pulldown, ion exchange, and size exclusion chromatography (aa 1-341, Figure 6.4B, C and 6.5B). Next, we examined if GSK923295 inhibits the microtubule-stimulated ATPase activity of these constructs.

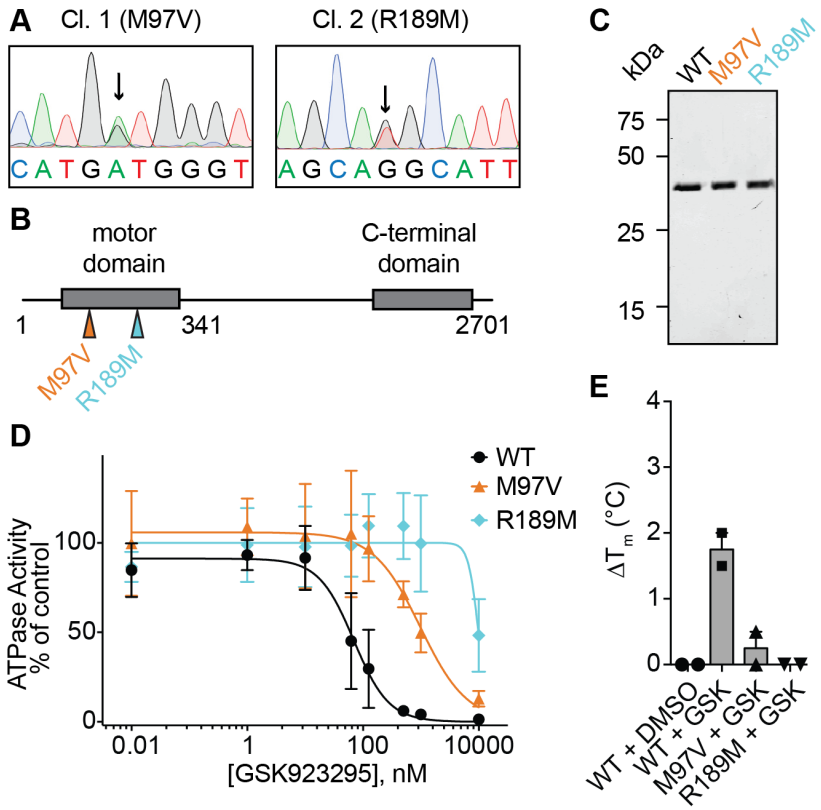


**Figure 6.4. Characterizing resistance to GSK923295 in diploid cells.**

(**A**) Sanger sequencing traces of genomic DNA encoding CENPE kinesin domain in two GSK923295-resistant clones in HCT116 cells. Positions of heterozygous mutations are indicated (black arrows). (**B**) Schematic shows kinesin motor and C-terminal domain of the CENPE protein. Positions of identified mutations are shown (colored arrows). First and last residues of the full length CENPE protein and the site of truncation to generate the recombinant kinesin motor domain construct are indicated (not to scale). (**C**) SDS-PAGE analysis of purified wild-type (WT) and mutant (M97V and R189M) CENPE con-nstructs (Coomassie Blue).

(**D**) GSK923295 concentration-dependent inhibition of microtubule-stimulated ATPase activity of recombinant CENPE kinesin motor domain constructs (aa 1-342, WT - black; M97V - orange; R189M - cyan). Graph shows values fit to a sigmoidal dose-response equation ($IC_{50}$ WT: 77 ± 60 nM, M97V: 813 ± 167 nM, R189M: $IC_{50}$ value was not deter-mined as complete inhibition at the highest drug dose was not observed, average values ± s.d., 2 mM MgATP, n=3). (**E**) Effect of DMSO (1 %) and GSK923295 inhibitor (50 μM) on the heat-induced unfolding ($\Delta T_m$) of the recombinant CENPE constructs (aa1-341, WT, M97V, R189M) analyzed using differential scanning fluorimetry assay (mean ± range, n=2). *Note - a subset of assays in this figure were performed by Donovan Phua, a summer research fellow in the Kapoor laboratory.*

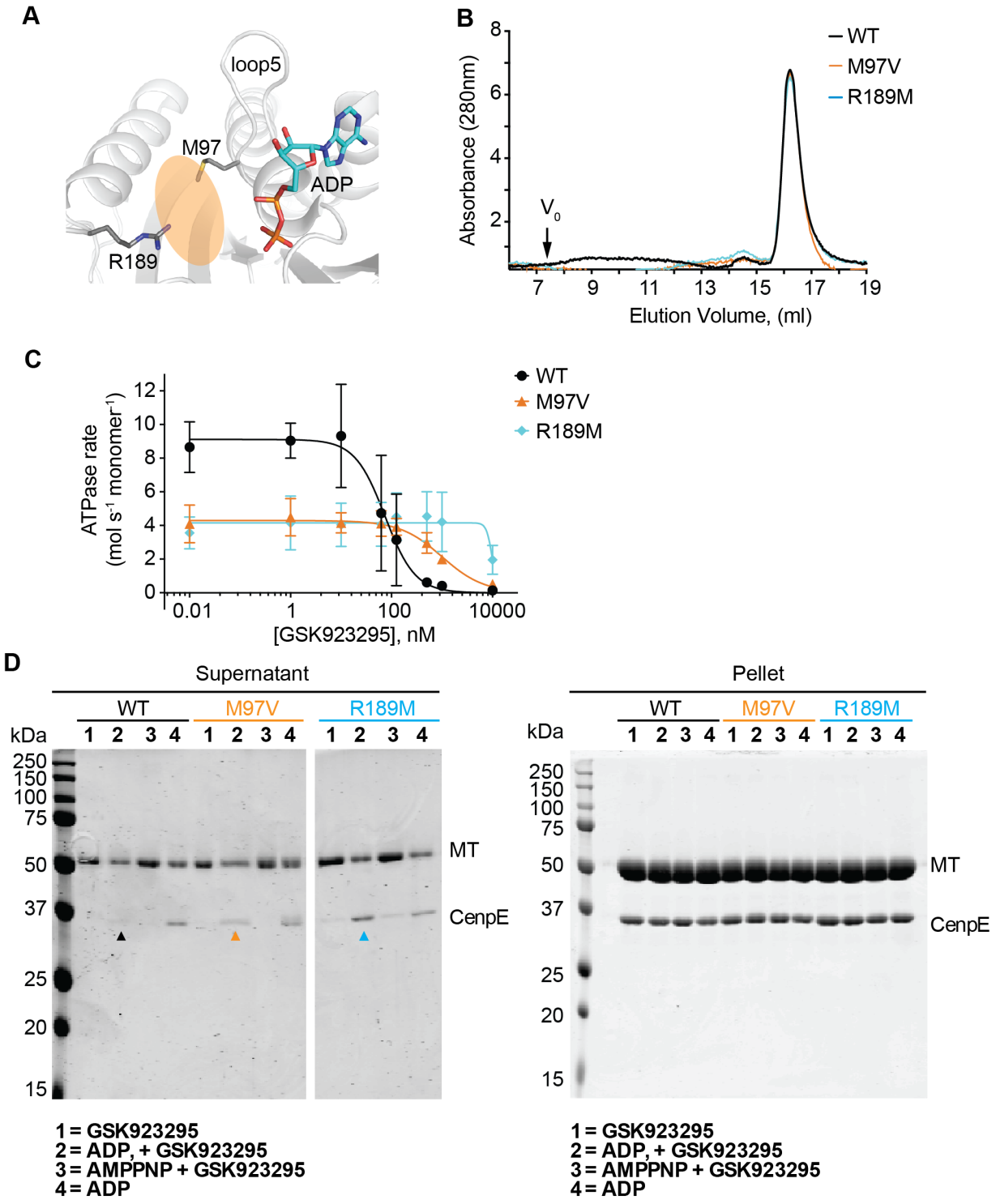


**Figure 6.5. Characterizing mutant alleles of CENPE motor domain.**

**Figure 6.5. Characterizing mutant alleles of CENPE motor domain.**

(**A**) Structural model (ribbon diagram) of human CENPE motor domain (PDB: 1T5C). Adenosine-5' diphosphate (ADP, stick representation), selected structural motif (loop 5), and side chains of selected residues (M97 and R189) are shown. Predicted binding site of GSK923295 (adapted from (Wood et al., 2010)) is highlighted (orange oval).

(**B**) Size-exclusion chromatography traces (Superdex 200 column) for WT, M97V and R189M motor domain constructs (aa 1-342). $V_0$, void volume.

(**C**) GSK923295 concentration-dependent inhibition of the steady-state ATPase activity of three CENPE motor domain constructs. $IC_{50}$: WT = 77 ± 60 nM, M97V = 813 ± 167 nM, R189M - $IC_{50}$ value was not determined as complete inhibition was not observed at the highest drug dose tested, average values ± s.d., 2 mM MgATP, 6 μM microtubules, n=3). Curves with normalized values are also shown in Figure 6.4D.

(**D**) SDS-PAGE analysis of soluble supernatant and pellet fractions from a co-sedimentation assay of CENP-E motor domain (CenpE; 3 μM) with microtubules (MT, 6 μM). The presence or absence of nucleotide (ADP or AMPPNP, 1 mM) and the presence or absence of the inhibitor (GSK923925, 20 μM) are indicated. In agreement with published data (Wood et al., 2010), the WT construct shows inhibitor-induced loss of the CENPE motor domain from the supernatant (black arrow). In contrast, the M97V and R189M constructs remain in the soluble supernatant in the presence of the compound and ADP nucleotide (orange and cyan arrows). *Note - a subset of assays in this figure were performed by Donovan Phua, a summer research fellow in the Kapoor laboratory.*

Consistent with previous reports (Wood et al., 2010), the ATPase activity of the wild-type construct was potently inhibited by the GSK923295 compound ($IC_{50}$ = 77 ± 60 nM, Figure 6.4D and 6.5C). We also found that the mutant constructs were inhibited by the GSK923295 compound with substantially lower potency (M97V: $IC_{50}$ = 813 ± 167 nM, R189M: $IC_{50}$ value was not determined as complete inhibition was not observed at the highest dose tested, Figure 6.4D and 6.5C).

The binding of kinesin motor domains to microtubules is regulated by ATP, with strong binding in the AMPPNP state and weaker binding in the ADP state (Moyer et al., 1998; Wood et al., 2010). The GSK923295 inhibitor has been proposed to stabilize the kinesin motor in a strongly-bound microtubule state even in the presence of ADP (Wood et al., 2010). Consistent with these data, we found that in the co-sedimentation assay with microtubules in the presence of ADP (1mM), the wild-type and mutant CENPE motor constructs remained in the soluble fraction but bound to microtubules in the presence of AMPPNP (1 mM) (Figure 6.5D, see Methods for details). In addition, the wild-type construct co-sedimented with microtubules in the presence of the GSK923295 inhibitor (20 μM) and ADP (1 mM) (Figure 6.5D). In contrast, the mutant motor domain constructs (M97V and R189M) remained in the soluble fraction in the presence of GSK923295 (20 μM) and ADP (1 mM) (Figure 6.5D). To further characterize binding of the GSK923295 compound to the recombinant CENPE constructs, we used differential scanning fluorimetry. These analyses revealed an increase in the melting temperature of the wild-type construct in the presence of the GSK923295 inhibitor ($\Delta T_m$ ~1.5°C, 50 μM GSK923295, Figure 6.4E). The potency of the GSK923295 inhibitor in this assay

matches the lower potency of CENPE inhibition in ATPase assays in the absence of microtubules (Wood et al., 2010). Importantly, we did not observe any changes in the melting temperature of the mutant constructs at the highest doses tested (50 μM GSK923295, Figure 6.4E). Taken together, these data suggest that single-point mutations in the CENPE motor domain confer resistance to GSK923295 by directly preventing its binding.

**Examining resistance to GSK923295 in haploid KBM7 cells.**

To examine mechanisms of resistance against the GSK923295 inhibitor in KBM7 clones we isolated, we performed transcriptome sequencing of the three GSK923295-resistant cell populations and the parental cells. We employed a pipeline using available open-source software for alignment of the reads to the human genome and gene expression and exon coverage analyses (Figure 6.6A and 6.7A, see Methods for details) (Anders et al., 2012; Koboldt et al., 2013; Liao et al., 2014). In contrast to the GSK923295-resistant clones in HCT116 cells, our analyses of single nucleotide variations and short insertions and/or deletions (indels) in the KBM7 cells did not reveal any non-synonymous mutations in the kinesin motor domain of the CENPE gene.

We next focused on gene expression analyses to compare changes in RNA expression between the parental and GSK923295-resistant cells (Figure 6.7B). First, we examined the expression of MDR efflux transporter Pgp (also known as MDR1 or ABCB1), as overexpression of this pump was reported to confer resistance to GSK923295 (Tcherniuk and Oleinikov, 2015). We observed almost no reads mapping

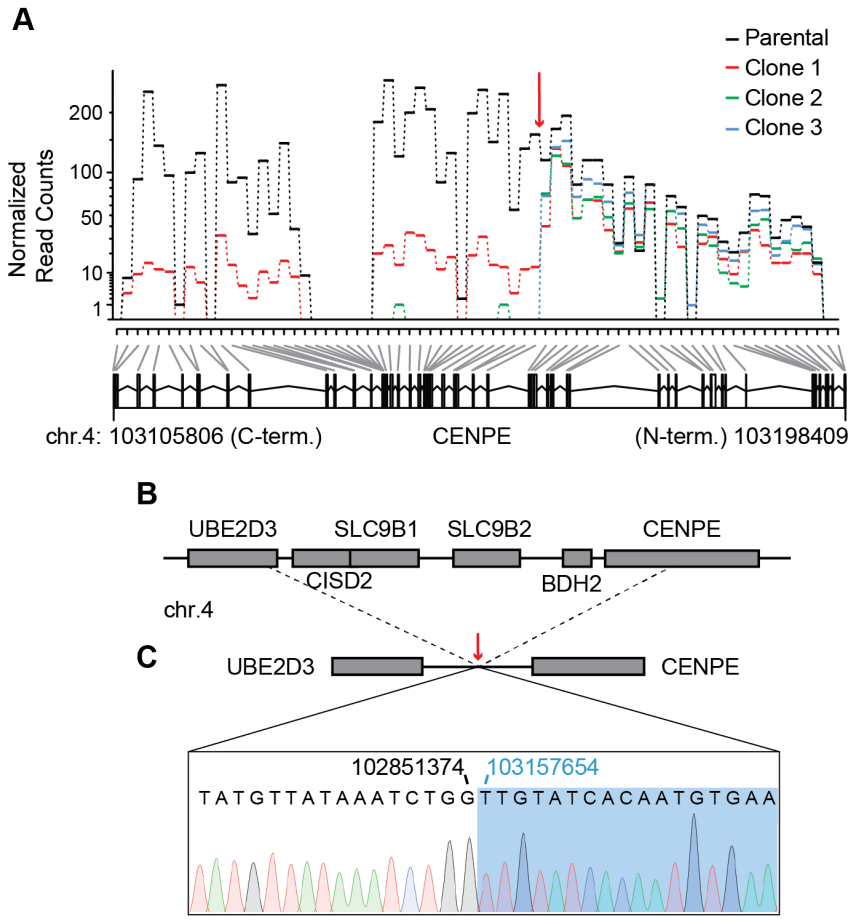


**Figure 6.6. Characterizing resistance to GSK923295 in haploid cells.**

(**A**) Exon usage over CENPE gene in parental and GSK923295-resistant KBM7 cells. Normalized read counts for each sample are shown (top panel, parental - black, clone 1 - red, clone 2 - green, clone 3 - blue). Position of the deletion site in the CENPE gene is indicated (red arrow). Gene model and first and last base pairs of the CENPE gene on chromosome 4 are shown (bottom panel, numbering from H. sapiens, genome version: GRCh38.p13). Counting bins generated by DexSeq algorithm are indicated (gray and black lines, bottom panel, see Methods and (Anders et al., 2012) for how these bins were generated). (**B**) Schematic shows UBE2D3-CENPE genomic locus. Genomic deletion identified in GSK923295-resistant KBM7 cell populations and the site of deletion/fusion event are indicated (dashed lines and red arrow). (**C**) Sanger sequencing trace of the deletion/fusion site in the genomic locus at the UBE2D3/CENPE in GSK923295-resistant KBM7 clones. Positions of the last base pair of the UBE2D3 gene (black) and the first base pair of the CENPE gene (blue) at the deletion/fusion site are indicated.

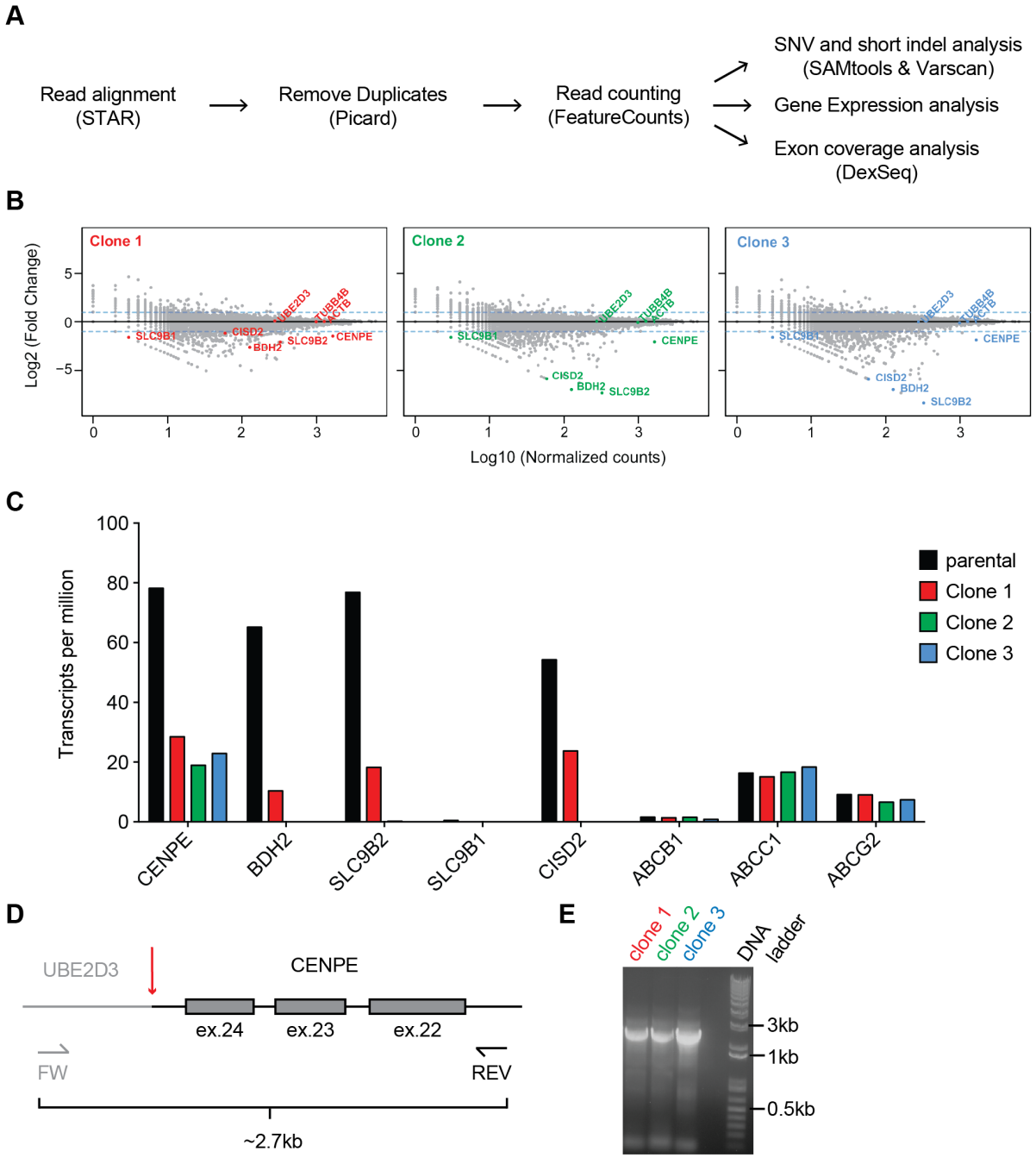


**Figure 6.7. Characterizing GSK923295-resistant clones in KBM7 cells**.

**Figure 6.7. Characterizing GSK923295-resistant clones in KBM7 cells.**

(**A**) Schematic of a pipeline for analysis of transcriptome sequencing data. Software used in each step is indicated in brackets (STAR (Dobin et al., 2013), Picard (http://broadinstitute.github.io/picard/), featureCounts (Liao et al., 2014), SAMtools (Li et al., 2009), Varscan2 (Koboldt et al., 2013), DexSeq (Anders et al., 2012))

(**B**) Plots showing normalized counts versus fold change for genes in GSK923295-resistant clones in comparison to parental cells (gray and colored dots). CENPE and the neighboring genes (BDH2, CISD2, SLC9B1, SLC9B2 and UBE2D3) are indicated (colored dots and text). Tubulin (TUBB4B) and actin (ACTB) genes are included as controls.

(**C**) Plot showing transcripts per million (TPM) values corresponding to CENPE and the neighboring genes (BDH2, CISD2, SLC9B1, SLC9B2 and UBE2D3) in parental and GSK923295-resistant cells (See Methods for details). Multi-drug resistance genes ABCB1 (also known as P-glycoprotein (P-gp) or multidrug resistance protein 1 (MDR1)) (Roninson et al., 1986; Ueda et al., 1986), ABCC1 (also known as multidrug-associated protein 1 (MRP1)) (Cole et al., 1992) and ABCG2 (also known as breast cancer resistance protein (BCRP)) (Doyle et al., 1998) are also shown.

(**D**) Schematic of the deletion/fusion region on chromosome 4 in GSK923295-resistant KBM7 cells (not to scale). UBE2D3 and CENPE genomic regions are indicated (UBE2D3 - gray, CENPE - black, deletion/fusion site - red arrow). Primers used for amplification of the genomic deletion/fusion region are indicated (FW - forward primer, REV - reverse primer).

(**E**) Agarose gel showing amplified deletion/fusion PCR products (~2.7kb) from three GSK923295-resistant KBM7 clones.

to the ABCB1 gene in parental and GSK923295-resistant cells, suggesting low or no expression of the protein (Figure 6.7B, C). Next, we performed a more extensive transcriptome-wide analysis that revealed several genes with substantially altered expression profiles, including CENPE, in GSK923295-resistant clones in comparison to the parental cells (Figure 6.7B, C). Exon coverage analyses using the DexSeq algorithm (Anders et al., 2012) revealed that the expression of exons corresponding to the N-terminal kinesin domain of CENPE was not substantially altered in the parental and GSK923295-resistant cells. But interestingly, we found nearly zero coverage for exons corresponding to the C-terminal portion of the CENPE gene in the resistant clones (exons 25-48, Figure 6.6A). We note that the residual coverage of the C-terminal exons in clone 1 (Figure 6.6A - red lines) likely represents contamination of this clone with RNA from parental cells due to incomplete separation in our dilution-based selection protocol. As the coverage of multiple adjacent genes (BDH2, SLC9B1, SLC9B2, CISD2) was also nearly zero, we suspected a possible genomic deletion (Figure 6.6A and 6.7C).

We next used PCR analyses of the CENPE genomic locus and identified the site of the deletion event (Figure 6.7D, E). Sanger sequencing confirmed a ~300kb deletion of genomic DNA that lead to a fusion between intronic regions in UBE2D3 and CENPE genes (Figure 6.6B, C). The deletion includes exons 25-48 of CENPE, spans the four adjacent genes, and extends into the first intron of the UBE2D3 gene (last base pair of the UBE2D3 gene at the fusion site: 102851374; first base pair of the CENPE gene at the fusion site: 103157654, Figure 6.6B, C). Resistance to GSK923295 in these clones

is likely CENPE-specific, as engineered CRISPR/Cas9-based deletion of CENPE in haploid mammalian cells can confer resistance to GSK923295 (Raaijmakers et al., 2018). Taken together, these data suggest that loss of the C-terminal domain of CENPE, which is needed for kinetochore targeting, is functionally equivalent to the genetic knockout that can also protect cells against GSK923295-induced toxicity.

**Discussion**

Here we report unbiased selections in diploid and haploid cells and identify mechanisms that confer resistance to GSK923295, a chemical inhibitor of the motor protein CENPE. We find that diploid HCT116 cells resistant to GSK923295 carry heterozygous, single-point mutations in the kinesin motor domain. We characterize these CENPE alleles using in vitro biochemical assays and show that the mutations directly block inhibitor binding. In contrast to diploid cells, drug-resistant haploid KBM7 cells do not carry mutations in the motor domain but have lost the kinetochore-targeting C-terminal domain of CENPE. Together, our results suggest that cancer cells with different karyotypes can lead to distinct mechanisms of resistance to GSK923295.

Our findings indicate that CENPE is the direct physiological target of GSK923295 in cells, as mechanisms of resistance to this compound in two different cell lines converge on the CENPE gene. Mutations that suppress drug binding in vitro can be introduced into drug-sensitive cells and if these mutations are sufficient to confer resistance, the “gold standard” for target validation can be achieved (Kapoor and Miller, 2017). In addition, genetically matched cells expressing the wild-type and mutant alleles

can be used in parallel experiments to examine CENPE-specific phenotypes (Kapoor and Miller, 2017). On-target inhibitor-induced phenotypes will only be observed in wild-type cells and not in cells expressing the GSK923295-resistant alleles.

The inhibition by GSK923295 leads to tight binding of CENPE's motor domain to the microtubule tracks. This likely prevents chromosome alignment at the start of cell division and leads to activation of the spindle assembly checkpoint (Putkey et al., 2002; Wood et al., 2010). In the case of haploid cells, the loss of the CENPE motor domain can be tolerated, as these cells grow in the absence of a robust spindle-assembly checkpoint (Raaijmakers et al., 2018). It has been found that many human tumors and cancer cells can have compromised spindle assembly checkpoints (Weaver and Cleveland, 2005), and loss of CENPE may be a simple strategy to overcome GSK923295-induced toxicity. In contrast, in diploid cells with robust checkpoints, the resistance mechanisms must prevent the binding of the inhibitor to CENPE through mutations that are functionally silent.

As crystal structures of compound-bound CENPE are not available, our understanding of inhibitor binding to CENPE relies on computational modelling and chemical structure-activity relationship analyses (Qian et al., 2010; Wood et al., 2010). Single-point mutations identified in this study (M97V and R189M) map adjacent to loop 5 in the kinesin motor domain of CENPE and support the predicted binding model of the CENPE-GSK923295 inhibitor complex (Wood et al., 2010). M97 and R189 residues likely form critical interactions with the GSK923295 inhibitor as mutations of these residues, which emerged in our unbiased selections, prevent binding of the compound.

Analyses of resistance-conferring mutations can not only help establish the direct physiological targets of chemical inhibitors but can also be useful during inhibitor development (Cupido et al., 2019; Pisa et al., 2019b). The single-point mutations in the CENPE motor domain we identified could therefore be valuable for the design and optimization of new potent and specific CENPE inhibitors that can overcome resistance.

Evolution of protein functions, such as ligand binding and specificity, depends on available trajectories in sequence space. These trajectories are constrained by epistasis within proteins and genetic interactions at different loci (Lehner, 2011; Starr and Thornton, 2016). These constraints can be altered in cancer cells that have aberrant gene and chromosome copy numbers. Our data reveal that distinct drug resistance mechanisms can emerge in cells with aberrant chromosomal numbers. These findings suggest that studying resistance mechanisms to drugs in cells with different karyotypes could be useful for understanding and improving the efficacy of targeted anti-cancer therapeutics.

## Chapter 6 - Methods.

### Mammalian cell culture.

HCT116 cells were obtained from ATCC (#CCL-247) and were maintained in McCoy's medium supplemented with 10% Fetal Bovine Serum (FBS), 2 mM L-glutamine and 100 U/ml penicillin/streptomycin. KBM7 cells were a kind gift from Prof. Kivanc Birsoy (Rockefeller University) and were grown in IMDM media supplemented with 10% FBS, 2 mM L-glutamine and 100 U/ml penicillin/streptomycin. All mammalian cells were incubated at 37°C and 5% $CO_2$.

### Selection of resistant clones.

Drug-resistant clones in HCT116 cells were isolated as previously described (Wacker et al., 2012). Briefly, ~$1.10^6$ cells were plated on a 10 cm culture dish in media supplemented with 2 μM GSK923295 and 0.1 - 0.5% DMSO. Medium with compound was exchanged every 2-3 days for ~2 weeks. Most cells died but a few resistant colonies emerged on the plate. Surviving colonies were picked by ring cloning, transferred to a new plate and expanded in media containing the drug (2 μM GSK923295 and 0.1 - 0.5% DMSO).

KBM7 cell populations resistant to GSK923295 were isolated by a cell dilution-based protocol in 96-well plates. Briefly, cells were grown in media supplemented with 2 μM GSK923295 and 0.1% DMSO. After 2-3 days cells were diluted ~3-fold into fresh media containing the drug (2 μM) and this process was repeated for ~3 weeks. All cells died in most wells on the plate but in a few wells we

observed a robust outgrowth of resistant clones. Cells from these wells were transferred to 10-cm dishes and expanded in media with the drug (2 μM).

**Cell proliferation assays.**

To quantify growth of HCT116 cells in the presence of drugs, cells were plated (1000-2000 cells per well) in clear flat-bottom, 96-well plates and treated with 8-9 doses of a serial dilution of the desired compound (0.5% DMSO was used as a vehicle). Growth of KBM7 cells was quantified using similar procedures (10000-20000 cells per well). 0.5% DMSO was used as a positive control and 0.1% SDS as a negative control on all plates. After 3 days, cell proliferation of both cell lines was determined using an Alamar Blue assay (O'brien et al., 2000). Briefly, 50 μl of Alamar Blue stock solution (sterile-filtered solution of 0.5 M resazurin sodium salt in DPBS) was added to each well and the plates were incubated at 37°C and 5% $CO_2$ until the ratio of fluorescent readouts between positive and negative control wells reached 5-10-fold difference. Fluorescence readout was determined using a Synergy NEO Microplate Reader (excitation: 550nm, emission: 590nm).

**Dose response analysis and $LD_{50}$ calculations.**

For each experiment, technical replicates were averaged and percent cellular growth was calculated by normalizing the background-corrected fluorescence in wells with compounds to positive control wells (0.5% DMSO). Background fluorescence was calculated as the mean of fluorescent readouts of negative control wells (0.1% SDS). To

determine the $LD_{50}$ values, percent cellular growth was plotted against concentration of compound and the data were fit using a sigmoidal dose-response curve (Equation 1) using Prism software. The values from at least three independent experiments were averaged and standard deviations were calculated.

$$Y = \%\ growth\ relative\ to\ DMSO\ control = (Y_{min}) + \frac{(Y_{max} - Y_{min})}{1 + 10^{(logLD50 - x)h}} \qquad \text{Equation 1}$$

In this equation x denotes concentration of the compound and h is the Hill coefficient.

**RNAseq and gene expression analysis.**

Parental and GSK923295-resistant KBM7 cells (~$2.10^7$) were washed once with 1X DPBS and lysed using a High-Pure RNA extraction kit followed by RNA isolation according to the manufacturer's protocol. RNA-Seq libraries were prepared at the Rockefeller University Genomics Core Facility with the Illumina TruSeq RNA Library prep kit and sequenced using the NextSeq500 system. Raw sequence reads were aligned to a human genome template (GRCh38, version 25 (Ensembl 85) provided by GENCODE, 2016-07-15) with the STAR aligner software (Dobin et al., 2013). Read groups were assigned and PCR duplicates were removed using Picard (http://broadinstitute.github.io/picard/). Aligned reads assigned to exons were counted using featureCounts (Liao et al., 2014). Normalized counts were determined as follows: first, sample normalization factors were calculated by dividing the total number of counts in each of the resistant clone samples by the total number of counts in the parental

sample. Normalized read counts were then calculated by dividing the read count value for each gene in a sample by the sample normalization factor. Fold change values were calculated as follows: first, the values of normalized read counts in all samples were augmented by 1. The fold change values were then calculated by dividing the counts value for each gene in the sample by the corresponding count value in the parental sample. Differential exon usage was determined by the DexSeq algorithm in RStudio by using the default settings (Anders et al., 2012).

**Genomic PCR analysis.**

Genomic DNA for PCR analysis was isolated from parental cells and drug-resistant clones using DNeasy Blood & Tissue Kit (Qiagen).

Primers used for amplification of CENPE motor domain in HCT116 cells:

Primers used for identifying M97V mutation in CENPE motor domain (PCR product spanning exons 3 and 4):

ATAGTTGATCATCCTACATTCTGAC

GATAAAAGTGAATCTATGCTATGCC

Primers used for identifying R189M mutation in CENPE motor domain (PCR product spanning exons 6 to 8):

TCCTACAGAATTATGGTTCCATTTGC

CCTCCCACATTTAGTTTAGTTAACAG

Primers for PCR amplification of the deletion/fusion site on chromosome 4 in KBM7 cells:

GATGACCTAGCAACTACACAGTCGA

GTTACATTTGGGGAACAGTGACAGG

Primers for Sanger sequencing of the amplified deletion/fusion site:

GAAGTTTCCAGGAATTTGCATATGG

CTAGCTATCTTTGTGACTTG

All primers are shown in 5' to 3' direction and were ordered from IDT (https://www.idtdna.com/).

**Vectors for Recombinant Protein Expression.**

Constructs for expression of CENPE motor domain were generated as described previously (Garcia-Saez et al., 2004). Briefly, the coding sequence for CENPE motor domain (aa 1-341) was PCR amplified (CloneAmp HiFi, Clontech) from pcDNA5-FRT-TO-Myc-LAP-Cenp-E plasmid and cloned into pET28 vector using NcoI and XhoI sites to generate C-terminal His6-fusion construct (XhoI site introduces leucine and glutamate residues (LE) between the CENPE motor domain (aa 1-341) and the C-terminal hexahistidine tag). M97V and R189M mutations were introduced by PCR using primers containing the mutant sequences. The coding sequences for all constructs were verified by Sanger sequencing. pcDNA5-FRT-TO-Myc-LAP-Cenp-E vector (Kim et al., 2010) was a kind gift from Dr. Ekaterina Grishchuk (University of Pennsylvania) and Dr Don Cleveland (Ludwig Institute for Cancer Research, UCSD).

**Protein Expression and Purification.**

*Escherichia coli* BL21 Rosetta (DE3) pLysS cells used for protein expression in this study were grown in Erlenmeyer flasks in Miller's LB media supplemented with 34 mg/L chloramphenicol and 50 mg/L kanamycin. Human CENPE motor domain (aa 1-341) wild-type and mutant constructs (M97V and R189M) were expressed and purified as follows. Briefly, *E.coli* Rosetta cells were grown to $O.D._{600}$ ~0.8 at 30°C, chilled to 18°C and the protein expression was induced overnight (14-16 hours, 0.5 mM IPTG). The cells were resuspended in lysis buffer (50 mM $NaH_2PO_4$ pH = 8.0, 250 mM NaCl, 20 mM imidazole, 1 mM $MgCl_2$, 1 mM β-mercaptoethanol, 0.2 mM ATP, 1 tablet of Roche cOmplete protease inhibitor cocktail per 50 ml of buffer), and lysed by sonication or using Emulsiflex-C5 homogenizer (Avestin, 5-10 cycles at 10-15 kPsi). The lysate was spun at 38,000 rpm for 40 min at 4°C in a Ti-45 rotor using Beckman Coulter Optima LE-80K ultracentrifuge. The clarified supernatant was incubated with Ni-NTA agarose resin for ~45 min. The beads were washed with ~150 ml of lysis buffer and the protein was eluted by a gradient of elution buffer (25 mM PIPES.NaOH pH = 6.8, 400 mM imidazole, 250 mM NaCl, 1 mM $MgCl_2$, 0.2 mM ATP, 1 mM β-mercaptoethanol). Eluted protein was dialyzed into low salt buffer (25 mM PIPES.NaOH pH = 6.6, 20 mM NaCl, 2 mM $MgCl_2$, 1 mM β-mercaptoethanol, 0.2 mM ATP), loaded onto HiTrap™ SP column (GE Healthcare) and eluted with a gradient of high salt buffer (25 mM PIPES.NaOH pH = 6.6, 500 mM NaCl, 2 mM $MgCl_2$, 1 mM β-mercaptoethanol, 0.2 mM ATP, 1 mM EGTA). The protein was further purified over a HiLoad 16/60 Superdex 200 or Superdex 200 Increase columns (GE Healthcare) in size

exclusion buffer (25 mM PIPES-KOH pH = 6.8, 250 mM KCl, 2 mM $MgCl_2$, 1 mM EGTA, 0.2 mM ATP, 1 mM β-mercaptoethanol) and the desired fractions were dialyzed into storage buffer (25 mM PIPES-KOH pH = 6.8, 250 mM KCl, 2 mM $MgCl_2$, 1 mM EGTA, 50 μM ATP, 1 mM DTT, 30 % sucrose) and flash frozen in liquid nitrogen.

**Microtubule co-sedimentation assays.**

Taxol-stabilized microtubules were polymerized from purified pre-cleared bovine tubulin as described (Kapitein et al., 2008). Purified CENPE motor domain constructs were incubated with microtubules in BRB80 buffer and spun in TLA 120.1 rotor (Beckman Coulter) at 90000 rpm for 10 mins at 30°C. Pelleted material was resuspended in BRB80 buffer supplemented with desired nucleotide and/or GSK923295 and incubated for 25 min at room temperature. The solution was then transferred into centrifuge tubes with a cushion of 100μl of BRB80 with 40% glycerol and subjected to sedimentation in TLA 120.1 rotor (Beckman Coulter) at 90000 rpm for 10 mins at 30°C. The soluble supernatant and the pellet were analyzed by SDS-PAGE and the gels imaged on LI-COR Odyssey scanner.

**Analyses of ATPase Activity.**

Steady-state ATPase activity of CENPE motor domain constructs was determined using the NADH-coupled assay in the presence of 6 μM taxol-stabilized microtubules. Briefly, the time course of fluorescence decrease corresponding to the consumption of NADH was measured using a Synergy NEO Microplate Reader ($\lambda_{ex}$ =

340 nm, 440 nm emission filter). Fluorescence values were plotted against time and fit by linear regression to obtain a rate of fluorescence decrease. The ATPase rate was calculated from rates of fluorescence decrease using ADP calibration curve. Percent inhibition of the ATPase activity was calculated by normalizing the rate of fluorescence decrease in the presence of compounds to DMSO control. GSK923295 compound stocks were made using DMSO. Final conditions for CENPE motor domain wild type and mutants (30-40 nM): 1x BRB80 (80 mM PIPES.KOH, 1 mM $MgCl_2$, mM EGTA, pH = 6.8), 1 mM TCEP, BSA 0.1 mg/ml, 175-200 μM NADH, 1 mM phosphoenolpyruvate, 15-30 U/ml lactate dehydrogenase, 15-30 U/ml pyruvate kinase, 2 mM MgATP, 6 μM microtubules. 0.5-1% DMSO was used as a vehicle control. Taxol-stabilized, bovine microtubules were prepared as described previously (Kapitein et al., 2008).

**Compound $IC_{50}$ Calculation**

For each experiment, technical replicates of the measured percent inhibition of ATPase activity were averaged, plotted against concentration of compound, and the data were fit using a sigmoidal dose-response curve (Equation 2) using Prism software to determine the $IC_{50}$. The values from at least three independent experiments were averaged and standard deviations were calculated.

$$Y = \%\,ATPase\ rate\ relative\ to\ DMSO\ control = (Y_{min}) + \frac{(Y_{max} - Y_{min})}{1 + 10^{(logIC50 - x)h}} \qquad \text{Equation 2}$$

In this equation x denotes concentration of the compound and h is the Hill coefficient.

**Differential Scanning Fluorimetry**

These experiments were carried out on a C1000 Touch Thermal cycler CFX-96 instrument (GE Healthcare). CENPE motor domain (WT, M97V and R189M; aa 1-342) recombinant constructs were diluted to a final concentration of 7-10 μM in 1x BRB80 supplemented with 1mM TCEP and assayed in a 96-well plate (Hard-shell® HSP9665 Bio-Rad). Compound or DMSO were added (50 μM GSK923295, 1% DMSO final concentration). SYPRO® Orange (Sigma S5692, excitation 490 nm, emission 590 nm) was used at 1:500 to 1:1000 dilution. The temperature was linearly increased with a step of 0.5°C for 55 minutes, from 25°C to 95°C and fluorescence readings were taken at each interval. Melting temperatures were determined as the minimum value of the first derivative of the fluorescence vs temperature curves.

**Immunofluorescence.**

HCT116 cells were plated on glass coverslips (Fisher Scientific) in six-well dishes 24 h before fixation. Cells were exposed to DMSO (vehicle control) or GSK923295 (200 nM) for 4 h, at 37 °C in complete medium. Cells were fixed for 10 min at 37 °C in fix solution (4% formaldehyde in 100 mM PIPES, 10 mM EGTA, 1 mM $MgCl_2$, and 0.2% Triton X-100, pH 6.9). Coverslips were washed three times with TBSTx (TBS with 0.1% Triton X-100), blocked for 30 min (2% BSA in TBSTx buffer) and incubated for 1 h at room temperature with FITC-conjugated mouse anti-tubulin monoclonal antibody (Sigma F2168; 1:2,000 dilution in blocking buffer). Coverslips were washed three times

in TBSTx, and DNA was stained with Hoechst 33342 (ThermoFisher, catalog no. H1399; 1:10,000). Coverslips were mounted in 0.5% p-phenylenediamine (Sigma, P6001) in 20 mM Tris-HCl, pH 8.8, with 90% glycerol and sealed with nail polish. A Zeiss Axio Observer.Z1 with LSM 700 confocal microscope equipped with 50 mW, 400-640 nm lasers was used for fluorescent visualizations and Zen software (Zeiss) was used for acquisition of images. Fiji software was used for brightness and contrast adjustments (Schindelin et al., 2012).

**Data and Software Availability.**

RNA sequencing data analysis was performed in R (version 1.1.423). Publicly-available packages were obtained from Bioconductor (https://www.bioconductor.org/) or as indicated in the Key Resource Table. The RNA sequencing data sets related to Figures 6.6 and 6.7 have been submitted to the SRA database and can be found under accession number: PRJNA561192.

## Chapter 7: Study Conclusions

In the preceding chapters, I have presented endeavors to determine how mutations in drug-binding sites can facilitate the design and validation of chemical inhibitors. In particular, using biochemical, structural and functional studies, I have outlined the features of the AAA active site that can be leveraged for the design of potent and selective chemical probes for spastin, a AAA protein implicated in microtubule-severing and organization of cellular organelles (e.g. endosomes). These studies showcase the features of the AAA active site that may also be relevant for development of chemical inhibitors for other proteins in the family. Together, this work provides a framework for how analyses of resistance can be useful for inhibitor design.

### Designing potent and selective chemical probes of AAA proteins.

The active site of AAA proteins is composed of a set of conserved residues, which interact with the nucleotide, and a set of less conserved residues that lie in the interior (i.e., N-loop and P-loop variability hotspots) or at the entrance of the nucleotide pocket (i.e., the sensor-II residues). Compounds that selectively inhibit spastin, such as the pyrazolylpyrrolopyrimidine-based spastazoline, interact with the N-loop and P-loop variability hotspot residues (glutamine and asparagine), which are unique to spastin in the AAA family. This indicates that selective and potent AAA inhibitors could be designed by optimizing interactions with all or subsets of these variability residues.

We speculate that selective chemical probes for AAA proteins could be designed by engineering interactions with unique combinations of variability hotspot residues. The core structures of compounds that bind conserved structural features of these ATPases can be used as starting scaffolds to which different chemical groups may be added to contact the variability hotspot residues in the target AAA protein (Figure 7.1A). For instance, in fidgetin-like 1 the P-loop and N-loop variability hot-spot residues are threonine and valine, respectively, compared with asparagine and glutamine at equivalent sites in spastin. N-loop gluamine-to-valine and P-loop asparagine-to-threonine mutations in spastin's active site confer resistance to quinazolines but not to the diaminotriazoles. Therefore, the diaminotriazole-based scaffolds are likely to be valuable starting points for developing inhibitors of fidgetin-like 1.

Our RADD analyses of allele-specific inhibitors of spastin suggest how AAA proteins with a cysteine at the P-loop variability hotspot residue could be targeted by quinazoline-based compounds. Cysteine residue at the P-loop variability hotspot site is present in ~ ¼ of the AAA family (Beyer, 1997). These proteins could be targeted by compounds that leverage the cysteine side chain interactions with electronegative substituents (e.g. fluorine) on the compound that were presented in chapter 3. For example, selectivity of the quinazoline-based VCP/p97 compound dibenzylquinazoline (DBeQ, (Chou et al., 2011)) could be optimized by engineering electronegative substituents at the C8 position of the quinazoline (Figure 7.1B, C, D). Further RADD

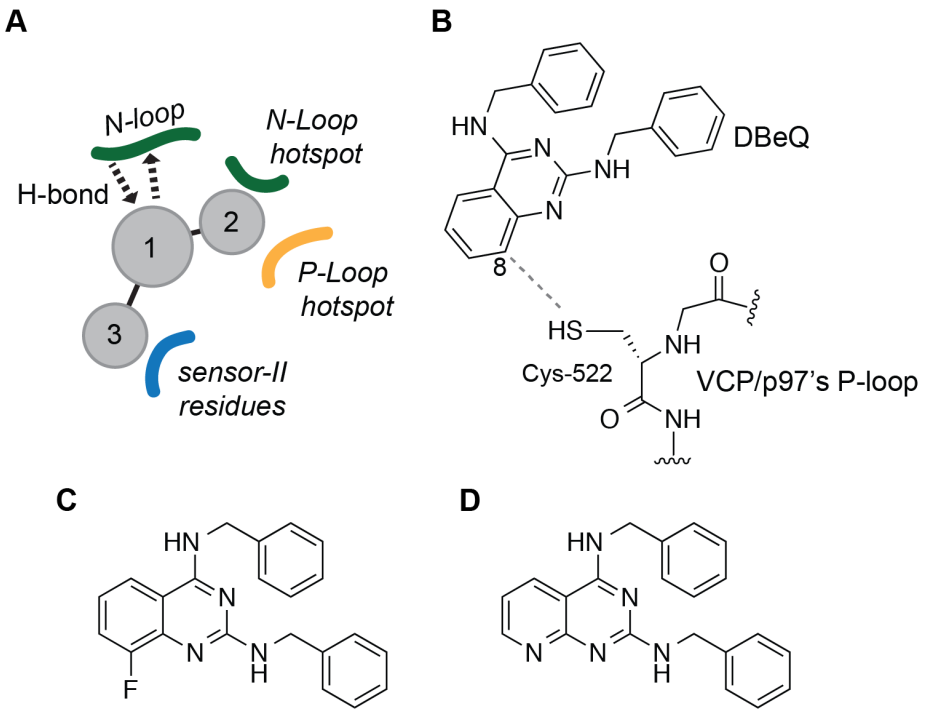


**Figure 7.1. RADD-based design of selective AAA inhibitors.**

(**A**) A schematic for designing selective ATP-competitive inhibitors of AAA proteins using RADD. Hydrogen-bonding pattern between the core scaffold (circle 1) and the N-loop backbone is shown with dotted arrows. Circles 2 and 3 correspond to modifications that interact with variability hotspot residues in the N-loop (green), P-loop (orange) and the sensor-II motif (blue) in the AAA nucleotide-binding pocket. (**B**) Schematic of predicted DBeQ (dibenzylquinazoline) interaction with native P-loop cysteine in the active site of D2 domain of VCP/p97 AAA protein (gray dashed line - predicted interaction). C8 position on DBeQ'a quinazoline is indicated. (**C-D**) Proposed analogs of DBeQ that could leverage the predicted interactions with the P-loop cysteine residue. (**C**) DBeQ analog with a fluorine moiety at quinazoline's C8 position. (**D**) DBeQ analog in which quinazoline's C8 is replaced with nitrogen.

analyses of VCP/p97 and other proteins in the AAA family will be useful for identifying strategies to target the conserved active sites in AAA proteins.

The ATP-competitive inhibitor scaffolds identified in this thesis (e.g. pyrazolylquinazoline-based compound **3.1** or the diaminotriazole-based compound **4.1**) could also serve as starting points to design allele-specific covalent compounds. These inhibitors, which have engineered electrophilic moieties, can irreversibly react with nucleophilic side chains of amino acid residues (e.g cysteine) in the target protein and can thus achieve greater occupancy in the binding site in comparison to reversible inhibitors (Johnson et al., 2010). This strategy could be generalizable to members of the AAA family of proteins if a suitable scaffold targeting the AAA active site could be identified. I propose that diaminotriazoles could be a useful starting scaffold for such studies for at least three reasons. First, diaminotriazole-based compounds such as JNJ-7706621 can bind multiple AAA proteins (e.g. spastin, fidgetin-like 1 and katanin, see Figures 2.3A, 4.1 and 4.10). Second, the inhibitor-spastin models we obtained for JNJ-7706621 indicate that the compound predominantly interacts with solvent-exposed residues at the front of the active site and does not extend inside the pocket near the variable residues in the N-loop and P-loop (Figure 7.2A). As many of the solvent-exposed residues do not directly interact with ATP, such as the sensor-II residue, they could be mutated to cysteine without disrupting ATPase activity. The inhibitor-spastin binding models developed in this thesis could also help with the rational design of electrophilic modifications on the compound (Figure 7.2B, C).

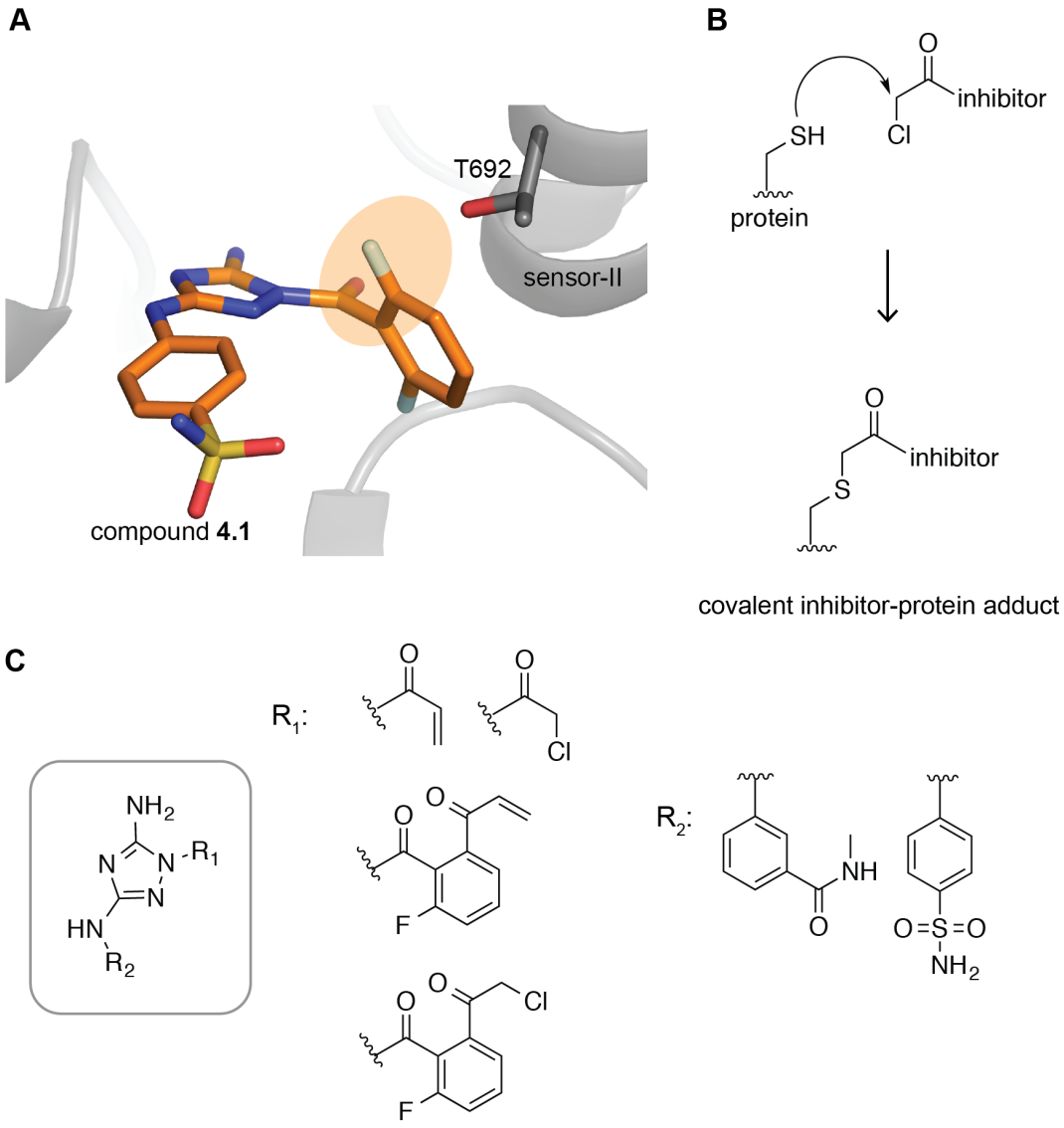


**Figure 7.2. Design of covalent inhibitors for AAA proteins.**

(**A**) View of compound **4.1** (JNJ-7706621) in the active site of spastin (pdb: 6P10). Sensor-II residue proximal to the inhibitor is shown (T692, stick representation). Proposed site for modifications of compound **4.1** to generate reactive chemical probes is indicated (orange oval). (**B**) Schematic of an irreversible modification of a cysteine side chain by a reactive α-chloroketone-based inhibitor. (**C**) Proposed chemical structures of covalent inhibitors based on the diaminotriazole scaffold (shown in gray box). α-chloroketone or vinylketone substitution at $R_1$ should lead to reactive inhibitors against alleles with cysteine mutation at the sensor-II variability hotspot site. Modifications of $R_2$ of the inhibitor can be used for tuning orientation of the inhibitor in the AAA active sites.

To engineer selective inhibitors of AAA proteins that share common N-loop and P-loop residues, compounds binding in a different orientation to quinazolines, such as the diaminotriazole-based JNJ-7706621 or quinolinone-based dovitinib, will be needed. In these cases, selectivity could be achieved by engineering interactions with other residues at the entrance of the active site (i.e., the sensor-II residues). For example, the AAA proteins katanin and VPS4B share identical N-loop and P-loop hotspots (leucine and threonine, respectively; Table 4.4) but have different residues at the entrance of the nucleotide-binding pocket (tyrosine in VPS4B in comparison with katanin's leucine; Table 4.4) and sensor-II residues (threonine in katanin and serine in VPS4B; Table 4.4). Using the RADD approach could help identify and prioritize chemical scaffolds that interact with specific residues in a desired target to guide the rational design of selective inhibitors of these ATPases.

For AAA proteins in which the shape of the nucleotide-binding site and the variability hot-spot residues diverged more substantially from spastin, other core scaffolds may be needed. Our experiments with spastin, fidgetin-like 1 and VCP/p97, suggest that mutant AAA protein alleles can be generated, and their inhibition by these other scaffolds could be tested to develop models for inhibitor–target binding and guiding compound optimization. These analyses will also help identify cognate inhibitor resistance-conferring mutations that can be used with the inhibitors to decipher target-specific phenotypes in cells.

**Using RADD to anticipate resistance to chemical inhibitors.**

Resistance to chemical inhibitors is a common complication in the clinic (e.g., cancer or HIV therapy) and mutations conferring resistance often emerge in drug targets (Gorre et al., 2001; Wensing et al., 2017). In particular, these resistance-conferring mutations commonly map to residues in drug binding sites that are in direct contact with the inhibitor (Anderson et al., 2015; Furman et al., 2014; Gorre et al., 2001; Wacker et al., 2012). For example, mutations identified in cells resistant to CB-5083 inhibitor of VCP/p97, which entered clinical trials, map to the active site in one of the two AAA domains of the protein (Anderson et al., 2015). Notably, a mutation in the sensor-II variability hotspot residue (T688A, human VCP/p97) leads to >60-fold change in compound potency (Anderson et al., 2015). Strategies to overcome resistance involve the development of compounds that retain potent binding to the mutant alleles. Our data suggest that using RADD could help identifying active site inhibitors that have different sets of resistance-conferring mutations. Therefore, integrating RADD analyses early in drug development could be used to identify compounds to overcome resistance.

Clinical studies suggest that treatment of cancers with molecularly-targeted agents with non-overlapping resistance profiles can prevent emergence of resistance (Wylie et al., 2017). Our studies indicate that RADD can help to identify compounds with non-overlapping resistance profiles. Integrating this information at early stages of compound design could guide development of drug combinations or drug “chimeras”, which have the two inhibitor scaffolds covalently attached together (e.g. via a linker),

against which resistance might be less likely to arise. It would be interesting to test whether simply linking two inhibitors that bind their target in distinct orientations could prevent the emergence of resistance and could provide therapeutic benefit.

**Overcoming resistance by targeted degradation.**

Targeted degradation of a protein of interest induced by a class of heterobifunctional compounds called PROTACs (Proteolysis Targeting Chimeras, Figure 7.3A) has recently emerged as a promising strategy to modulate protein function and to target drug resistant alleles in cancer (Lai and Crews, 2017; Salami and Crews, 2017). PROTACs are chimeric compounds composed of two functional parts connected by a covalent linker moiety. The first part of the PROTAC molecule is a ligand that can recruit E3 ligases such as von Hippel-Lindau (VHL) or cereblon (CRBN) ligases (Fischer et al., 2014; Min et al., 2002). The E3-ligase-recruiting moiety is covalently attached via an engineered linker to a second ligand that can bind a selected protein of interest (Paiva and Crews, 2019). Concomitant binding of PROTAC to the protein of interest and the E3 ligase leads to the formation of a ternary complex that promotes ubiquitination of the target protein by the E3 ligase enzyme (Figure 7.3A). This proximity-induced ubiquitylation of the protein of interest targets it for degradation by the proteasome system (Sakamoto et al., 2001; Salami and Crews, 2017). In fact, PROTACs can act sub-stoichiometrically as degradation of the ubiquitylated proteins should release the PROTAC molecule and thus allowing it to engage with another molecule of the target protein and repeating the degradation cycle. This catalytic mode of action differs from

the common occupancy-driven mechanism of inhibitor-target binding that requires high doses of the inhibitor to effectively block the target protein (Salami and Crews, 2017). Additional advantage of targeted degradation over reversible inhibition is the longer sustained blockade of the target protein since its function can only be restored by protein re-synthesis (Burslem et al., 2018). Furthermore, as PROTACs act catalytically and require a proximity-induced ubiquitination step, they can achieve exquisite selectivity. In fact, biochemical, structural and in vitro studies with PROTACs based on promiscuous kinase scaffolds indicate that selectivity of these degrader molecules can be finely tuned by engineering optimized linkers and E3 ligase ligands (Bondeson et al., 2018; Huang et al., 2018). This can be advantageous for targeting members of conserved protein families whose drug binding sites may be similar and for which selective inhibitors may be difficult to develop (e.g. kinases and AAA proteins).

Targeted degradation of AAA proteins could provide a new approach to study the function of these proteins in cells and could provide alternative approaches to test therapeutic hypotheses. For example, blocking spastin function has been proposed as a therapeutic strategy in Alzheimer's disease as knockdown of spastin can protect neuronal cells from Aβ peptide-induced toxicity (Zempel et al., 2013). However, achieving sustained inhibition of spastin using reversible inhibitors (e.g. spastazoline) may be challenging. In contrast, targeted degradation of spastin using PROTACs could provide a longer-lasting strategy to reduce spastin's activity in cells. The structural models of inhibitor-spastin complexes presented in this thesis provide a useful starting point for the design of spastin-specific PROTAC molecules. For example, our structures

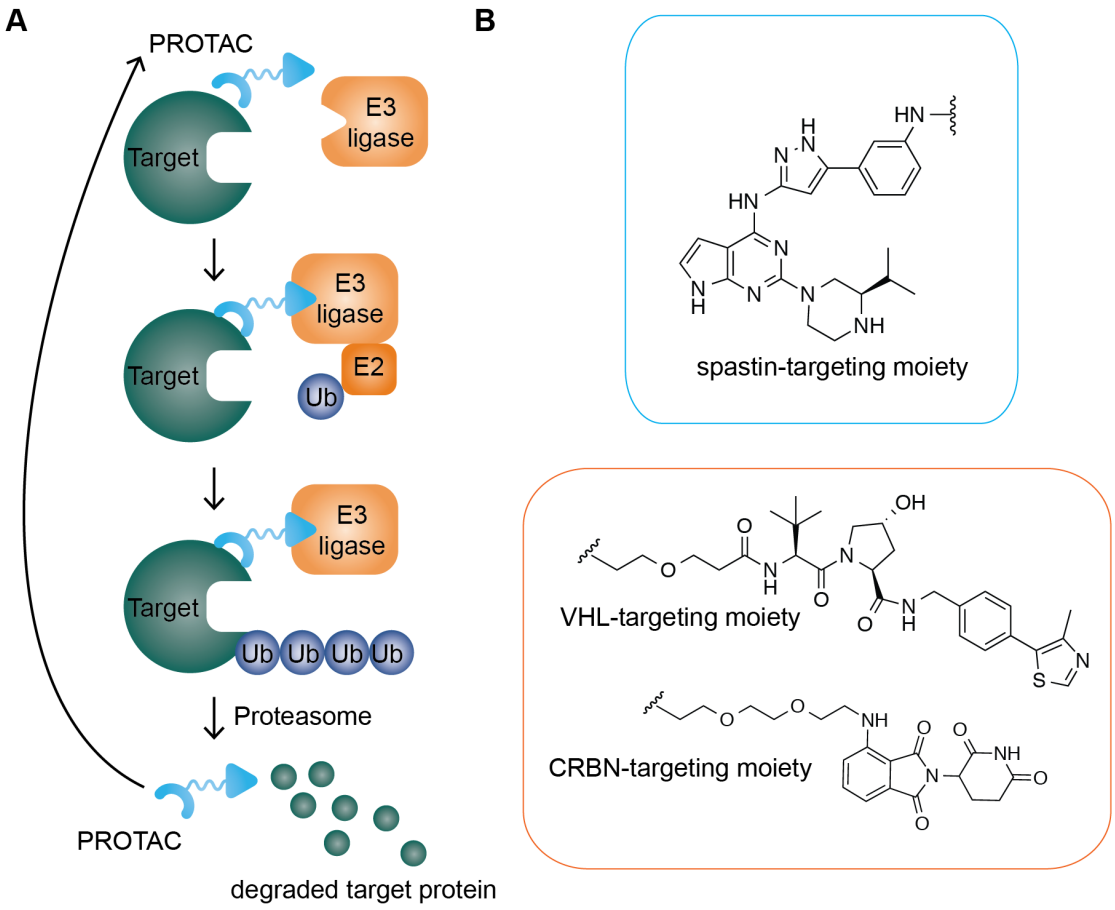


**Figure 7.3. Targeted protein degradation using PROTACs (Proteolysis-Targeting Chimeras).**

(**A**) Schematic of the PROTAC approach (adapted from Lai and Crews, Nat Rev Drug Disc, 2017) for targeted degradation of proteins. Heterobifunctional compound (PROTAC, blue) brings the target protein (green) proximal to the E3 ligase complex (orange) that can induce target ubiquitination followed by ubiquitin-dependent protein degradation by the proteasome. PROTAC molecule is released upon degradation of the target protein and can participate in the next reaction cycle. (**B**) Proposed chemical structures of spastin-targeting PROTACs. Spastazoline-based ligand that specifically interacts with spastin AAA protein (blue box) could be conjugated to E3-ligase-targeting moieties (VHL or CRBN E3 ligase, orange box) for targeted degradation of spastin.

reveal that the tert-butyl moiety of a spastazoline analog is facing into the bulk solvent (Figures 3.2D, E and 3.3C, D). Thus, modifications of spastazoline scaffold at this position may be less likely to disrupt binding of the inhibitor to spastin and could be leveraged for attachment of the E3-ligase recruiting moieties (Figure 7.3B). It will be interesting to investigate if spastazoline-based PROTACs could improve potency and specificity of blocking spastin functions in cells in comparison to the reversible inhibition by the unmodified spastazoline. Finally, the RADD approach and the structural models of distinct chemical scaffolds bound to spastin presented in this thesis could provide a starting point for the development of PROTACs for other members of the AAA family.

# REFERENCES


Adams, P.D., Afonine, P.V., Bunkóczi, G., Chen, V.B., Davis, I.W., Echols, N., Headd, J.J., Hung, L.-W., Kapral, G.J., Grosse-Kunstleve, R.W., et al. (2010). PHENIX: a comprehensive Python-based system for macromolecular structure solution. Acta Crystallogr. D Biol. Crystallogr. *66*, 213–221.

Afonine, P.V., Grosse-Kunstleve, R.W., Echols, N., Headd, J.J., Moriarty, N.W., Mustyakimov, M., Terwilliger, T.C., Urzhumtsev, A., Zwart, P.H., and Adams, P.D. (2012). Towards automated crystallographic structure refinement with phenix.refine. Acta Crystallogr. D Biol. Crystallogr. *68*, 352–367.

Agafonov, R.V., Wilson, C., Otten, R., Buosi, V., and Kern, D. (2014). Energetic dissection of Gleevec's selectivity toward human tyrosine kinases. Nat. Struct. Mol. Biol. *21*, 848–853.

Allison, R., Lumb, J.H., Fassier, C., Connell, J.W., Ten Martin, D., Seaman, M.N.J., Hazan, J., and Reid, E. (2013). An ESCRT-spastin interaction promotes fission of recycling tubules from the endosome. J. Cell Biol. *202*, 527–543.

Allison, R., Edgar, J.R., Pearson, G., Rizo, T., Newton, T., Günther, S., Berner, F., Hague, J., Connell, J.W., Winkler, J., et al. (2017). Defects in ER-endosome contacts impact lysosome function in hereditary spastic paraplegia. J. Cell Biol. *216*, 1337–1355.

Amaro, R.E., Baudry, J., Chodera, J., Demir, Ö., McCammon, J.A., Miao, Y., and Smith, J.C. (2018). Ensemble Docking in Drug Discovery. Biophys. J. *114*, 2271–2278.

Anders, S., Reyes, A., and Huber, W. (2012). Detecting differential usage of exons from RNA-seq data. Genome Res. *22*, 2008–2017.

Anderson, D.J., Le Moigne, R., Djakovic, S., Kumar, B., Rice, J., Wong, S., Wang, J., Yao, B., Valle, E., Kiss von Soly, S., et al. (2015). Targeting the AAA ATPase p97 as an Approach to Treat Cancer through Disruption of Protein Homeostasis. Cancer Cell *28*, 653–665.

Angell, R.M., Angell, T.D., Bamborough, P., Bamford, M.J., Chung, C.-W., Cockerill, S.G., Flack, S.S., Jones, K.L., Laine, D.I., Longstaff, T., et al. (2008). Biphenyl amide p38 kinase inhibitors 4: DFG-in and DFG-out binding modes. Bioorg. Med. Chem. Lett. *18*, 4433–4437.

Anstett, K., Brenner, B., Mesplede, T., and Wainberg, M.A. (2017). HIV drug resistance against strand transfer integrase inhibitors. Retrovirology *14*, 36.

Ardini, E., Menichincheri, M., Banfi, P., Bosotti, R., De Ponti, C., Pulci, R., Ballinari, D., Ciomei, M., Texido, G., Degrassi, A., et al. (2016). Entrectinib, a Pan-TRK, ROS1, and ALK Inhibitor with Activity in Multiple Molecularly Defined Cancer Indications. Mol. Cancer Ther. *15*, 628–639.

Assimon, V.A., Tang, Y., Vargas, J.D., Lee, G.J., Wu, Z.Y., Lou, K., Yao, B., Menon, M.-K.,

Pios, A., Perez, K.C., et al. (2019). CB-6644 Is a Selective Inhibitor of the RUVBL1/2 Complex with Anticancer Activity. ACS Chem. Biol. *14*, 236–244.

Awad, M.M., Katayama, R., McTigue, M., Liu, W., Deng, Y.-L., Brooun, A., Friboulet, L., Huang, D., Falk, M.D., Timofeevski, S., et al. (2013). Acquired Resistance to Crizotinib from a Mutation in CD74–ROS1. N. Engl. J. Med. *368*, 2395–2401.

Azam, M., Latek, R.R., and Daley, G.Q. (2003). Mechanisms of autoinhibition and STI-571/imatinib resistance revealed by mutagenesis of BCR-ABL. Cell *112*, 831–843.

Bakhoum, S.F., and Cantley, L.C. (2018). The Multifaceted Role of Chromosomal Instability in Cancer and Its Microenvironment. Cell *174*, 1347–1360.

Banerjee, S., Bartesaghi, A., Merk, A., Rao, P., Bulfer, S.L., Yan, Y., Green, N., Mroczkowski, B., Neitz, R.J., Wipf, P., et al. (2016). 2.3 Å resolution cryo-EM structure of human p97 and mechanism of allosteric inhibition. Science *351*, 871–875.

Basu, B., Dean, E., Puglisi, M., Greystoke, A., Ong, M., Burke, W., Cavallin, M., Bigley, G., Womack, C., Harrington, E.A., et al. (2015). First-in-Human Pharmacokinetic and Pharmacodynamic Study of the Dual m-TORC 1/2 Inhibitor AZD2014. Clin. Cancer Res. *21*, 3412–3419.

Baud, M.G.J., Lin-Shiao, E., Cardote, T., Tallant, C., Pschibul, A., Chan, K.-H., Zengerle, M., Garcia, J.R., Kwan, T.T.-L., Ferguson, F.M., et al. (2014). Chemical biology. A bump-and-hole approach to engineer controlled selectivity of BET bromodomain chemical probes. Science *346*, 638–641.

Bauer, M.R., Jones, R.N., Baud, M.G.J., Wilcken, R., Boeckler, F.M., Fersht, A.R., Joerger, A.C., and Spencer, J. (2016). Harnessing Fluorine-Sulfur Contacts and Multipolar Interactions for the Design of p53 Mutant Y220C Rescue Drugs. ACS Chem. Biol. *11*, 2265–2274.

Baym, M., Stone, L.K., and Kishony, R. (2016). Multidrug evolutionary strategies to reverse antibiotic resistance. Science *351*, aad3292.

Belshaw, P.J., Schoepfer, J.G., Liu, K.-Q., Morrison, K.L., and Schreiber, S.L. (1995). Rational Design of Orthogonal Receptor–Ligand Combinations. Angew. Chem. Int. Ed Engl. *34*, 2129–2132.

Ben-Neriah, Y., Daley, G.Q., Mes-Masson, A.M., Witte, O.N., and Baltimore, D. (1986). The chronic myelogenous leukemia-specific P210 protein is the product of the bcr/abl hybrid gene. Science *233*, 212–214.

Beyer, A. (1997). Sequence analysis of the AAA protein family. Protein Sci. *6*, 2043–2058.

Bishop, A.C., Ubersax, J.A., Petsch, D.T., Matheos, D.P., Gray, N.S., Blethrow, J., Shimizu, E., Tsien, J.Z., Schultz, P.G., Rose, M.D., et al. (2000). A chemical switch for inhibitor-sensitive alleles of any protein kinase. Nature *407*, 395–401.

Biswas, T., Pero, J.M., Joseph, C.G., and Tsodikov, O.V. (2009). DNA-dependent ATPase activity of bacterial XPB helicases. Biochemistry *48*, 2839–2848.

Blackstone, C., O'Kane, C.J., and Reid, E. (2011). Hereditary spastic paraplegias: membrane traffic and the motor pathway. Nat. Rev. Neurosci. *12*, 31–42.

Bleichert, F., Botchan, M.R., and Berger, J.M. (2017). Mechanisms for initiating cellular DNA replication. Science *355*, eaah6317.

Blencke, S. (2004). Characterization of a Conserved Structural Determinant Controlling Protein Kinase Sensitivity to Selective Inhibitors. Chemistry & Biology *11*, 691–701.

Bondeson, D.P., Smith, B.E., Burslem, G.M., Buhimschi, A.D., Hines, J., Jaime-Figueroa, S., Wang, J., Hamman, B.D., Ishchenko, A., and Crews, C.M. (2018). Lessons in PROTAC Design from Selective Degradation with a Promiscuous Warhead. Cell Chem Biol *25*, 78–87.e5.

van den Boom, J., and Meyer, H. (2018). VCP/p97-Mediated Unfolding as a Principle in Protein Homeostasis and Signaling. Mol. Cell *69*, 182–194.

Boyaci, H., Shah, T., Hurley, A., Kokona, B., Li, Z., Ventocilla, C., Jeffrey, P.D., Semmelhack, M.F., Fairman, R., Bassler, B.L., et al. (2016). Structure, Regulation, and Inhibition of the Quorum-Sensing Signal Integrator LuxO. PLoS Biol. *14*, e1002464.

Bruning, J.B., Chalmers, M.J., Prasad, S., Busby, S.A., Kamenecka, T.M., He, Y., Nettles, K.W., and Griffin, P.R. (2007). Partial Agonists Activate PPARγ Using a Helix 12 Independent Mechanism. Structure *15*, 1258–1271.

Burgess, M.R., Skaggs, B.J., Shah, N.P., Lee, F.Y., and Sawyers, C.L. (2005). Comparative analysis of two clinically active BCR-ABL kinase inhibitors reveals the role of conformation-specific binding in resistance. Proc. Natl. Acad. Sci. U. S. A. *102*, 3395–3400.

Burslem, G.M., Smith, B.E., Lai, A.C., Jaime-Figueroa, S., McQuaid, D.C., Bondeson, D.P., Toure, M., Dong, H., Qian, Y., Wang, J., et al. (2018). The Advantages of Targeted Protein Degradation Over Inhibition: An RTK Case Study. Cell Chem Biol *25*, 67–77.e3.

Chen, Y.-C. (2015). Beware of docking! Trends Pharmacol. Sci. *36*, 78–95.

Chen, Z., Suzuki, H., Kobayashi, Y., Wang, A.C., DiMaio, F., Kawashima, S.A., Walz, T., and Kapoor, T.M. (2018). Structural Insights into Mdn1, an Essential AAA Protein Required for Ribosome Biogenesis. Cell *175*, 822–834.e18.

Chou, T.-F., Brown, S.J., Minond, D., Nordin, B.E., Li, K., Jones, A.C., Chase, P., Porubsky, P.R., Stoltz, B.M., Schoenen, F.J., et al. (2011). Reversible inhibitor of p97, DBeQ, impairs both ubiquitin-dependent and autophagic protein clearance pathways. Proc. Natl. Acad. Sci. U. S. A. *108*, 4834–4839.

Chou, T.-F., Bulfer, S.L., Weihl, C.C., Li, K., Lis, L.G., Walters, M.A., Schoenen, F.J., Lin, H.J., Deshaies, R.J., and Arkin, M.R. (2014). Specific inhibition of p97/VCP ATPase and kinetic analysis demonstrate interaction between D1 and D2 ATPase domains. J. Mol. Biol. *426*, 2886–2899.

Chunduri, N.K., and Storchová, Z. (2019). The diverse consequences of aneuploidy. Nat. Cell Biol. *21*, 54–62.

Chung, V., Heath, E.I., Schelman, W.R., Johnson, B.M., Kirby, L.C., Lynch, K.M., Botbyl, J.D., Lampkin, T.A., and Holen, K.D. (2012). First-time-in-human study of GSK923295, a novel antimitotic inhibitor of centromere-associated protein E (CENP-E), in patients with refractory cancer. Cancer Chemother. Pharmacol. *69*, 733–741.

Claudiani, P., Riano, E., Errico, A., Andolfi, G., and Rugarli, E.I. (2005). Spastin subcellular localization is regulated through usage of different translation start sites and active export from the nucleus. Exp. Cell Res. *309*, 358–369.

Cohen, M.S., Zhang, C., Shokat, K.M., and Taunton, J. (2005). Structural bioinformatics-based design of selective, irreversible kinase inhibitors. Science *308*, 1318–1321.

Connell, J.W., Lindon, C., Luzio, J.P., and Reid, E. (2009). Spastin couples microtubule severing to membrane traffic in completion of cytokinesis and secretion. Traffic *10*, 42–56.

Copeland, R.A. (2004). Enzymes: A Practical Introduction to Structure, Mechanism, and Data Analysis (John Wiley & Sons).

Cravatt, B.F., Wright, A.T., and Kozarich, J.W. (2008). Activity-based protein profiling: from enzyme chemistry to proteomic chemistry. Annu. Rev. Biochem. *77*, 383–414.

Crawford, J.J., Johnson, A.R., Misner, D.L., Belmont, L.D., Castanedo, G., Choy, R., Coraggio, M., Dong, L., Eigenbrot, C., Erickson, R., et al. (2018). Discovery of GDC-0853: A Potent, Selective, and Noncovalent Bruton's Tyrosine Kinase Inhibitor in Early Clinical Development. Journal of Medicinal Chemistry *61*, 2227–2245.

Cross, D.A.E., Ashton, S.E., Ghiorghiu, S., Eberlein, C., Nebhan, C.A., Spitzler, P.J., Orme, J.P., Finlay, M.R.V., Ward, R.A., Mellor, M.J., et al. (2014). AZD9291, an irreversible EGFR TKI, overcomes T790M-mediated resistance to EGFR inhibitors in lung cancer. Cancer Discov. *4*, 1046–1061.

Cupido, T., Pisa, R., Kelley, M.E., and Kapoor, T.M. (2019). Designing a chemical inhibitor for the AAA protein spastin using active site mutations. Nat. Chem. Biol. *15*, 444–452.

Daub, H., Specht, K., and Ullrich, A. (2004). Strategies to overcome resistance to targeted protein kinase inhibitors. Nat. Rev. Drug Discov. *3*, 1001–1010.

Davis, A.M., Teague, S.J., and Kleywegt, G.J. (2003). Application and limitations of X-ray crystallographic data in structure-based ligand and drug design. Angew. Chem. Int. Ed. *42*, 2718–2736.

Davis, A.M., St-Gallay, S.A., and Kleywegt, G.J. (2008). Limitations and lessons in the use of X-ray structural information in drug design. Drug Discov. Today *13*, 831–841.

DeLaBarre, B., and Brunger, A.T. (2003). Complete structure of p97/valosin-containing protein reveals communication between nucleotide domains. Nat. Struct. Biol. *10*, 856–863.

Dobin, A., Davis, C.A., Schlesinger, F., Drenkow, J., Zaleski, C., Jha, S., Batut, P., Chaisson, M., and Gingeras, T.R. (2013). STAR: ultrafast universal RNA-seq aligner. Bioinformatics *29*, 15–21.

Drilon, A., Li, G., Dogan, S., Gounder, M., Shen, R., Arcila, M., Wang, L., Hyman, D.M., Hechtman, J., Wei, G., et al. (2016). What hides behind the MASC: clinical response and acquired resistance to entrectinib after ETV6-NTRK3 identification in a mammary analogue secretory carcinoma (MASC). Ann. Oncol. *27*, 920–926.

Drilon, A., Nagasubramanian, R., Blake, J.F., Ku, N., Tuch, B.B., Ebata, K., Smith, S., Lauriault, V., Kolakowski, G.R., Brandhuber, B.J., et al. (2017a). A Next-Generation TRK Kinase Inhibitor Overcomes Acquired Resistance to Prior TRK Kinase Inhibition in Patients with TRK Fusion-Positive Solid Tumors. Cancer Discov. *7*, 963–972.

Drilon, A., Siena, S., Ou, S.-H.I., Patel, M., Ahn, M.J., Lee, J., Bauer, T.M., Farago, A.F., Wheler, J.J., Liu, S.V., et al. (2017b). Safety and Antitumor Activity of the Multitargeted Pan-TRK, ROS1, and ALK Inhibitor Entrectinib: Combined Results from Two Phase I Trials (ALKA-372-001 and STARTRK-1). Cancer Discov. *7*, 400–409.

Drilon, A., Laetsch, T.W., Kummar, S., DuBois, S.G., Lassen, U.N., Demetri, G.D., Nathenson, M., Doebele, R.C., Farago, A.F., Pappo, A.S., et al. (2018). Efficacy of Larotrectinib in TRK Fusion–Positive Cancers in Adults and Children. N. Engl. J. Med. *378*, 731–739.

Druker, B.J., Guilhot, F., O'Brien, S.G., Gathmann, I., Kantarjian, H., Gattermann, N., Deininger, M.W.N., Silver, R.T., Goldman, J.M., Stone, R.M., et al. (2006). Five-year follow-up of patients receiving imatinib for chronic myeloid leukemia. N. Engl. J. Med. *355*, 2408–2417.

Dumas, P., Ennifar, E., Da Veiga, C., Bec, G., Palau, W., Di Primo, C., Piñeiro, A., Sabin, J., Muñoz, E., and Rial, J. (2016). Extending ITC to Kinetics with kinITC. Methods Enzymol. *567*, 157–180.

Dupeux, F., Röwer, M., Seroul, G., Blot, D., and Márquez, J.A. (2011). A thermal stability assay can help to estimate the crystallization likelihood of biological samples. Acta Crystallogr. D Biol. Crystallogr. *67*, 915–919.

Eckert, T., Link, S., Le, D.T.-V., Sobczak, J.-P., Gieseke, A., Richter, K., and Woehlke, G. (2012). Subunit Interactions and cooperativity in the microtubule-severing AAA ATPase spastin. J. Biol. Chem. *287*, 26278–26290.

Elling, U., and Penninger, J.M. (2014). Genome wide functional genetics in haploid cells. FEBS Lett. *588*, 2415–2421.

Emsley, P., Lohkamp, B., Scott, W.G., and Cowtan, K. (2010). Features and development of Coot. Acta Crystallogr. D Biol. Crystallogr. *66*, 486–501.

Endicott, J.A., Noble, M.E.M., and Johnson, L.N. (2012). The structural basis for control of eukaryotic protein kinases. Annu. Rev. Biochem. *81*, 587–613.

Engelman, J.A., Zejnullahu, K., Gale, C.-M., Lifshits, E., Gonzales, A.J., Shimamura, T., Zhao, F., Vincent, P.W., Naumov, G.N., Bradner, J.E., et al. (2007). PF00299804, an irreversible pan-ERBB inhibitor, is effective in lung cancer models with EGFR and ERBB2 mutations that are resistant to gefitinib. Cancer Res. *67*, 11924–11932.

Erlanson, D.A., Davis, B.J., and Jahnke, W. (2019). Fragment-Based Drug Discovery:

Advancing Fragments in the Absence of Crystal Structures. Cell Chem Biol *26*, 9–15.

Erzberger, J.P., and Berger, J.M. (2006). Evolutionary relationships and structural mechanisms of AAA+ proteins. Annu. Rev. Biophys. Biomol. Struct. *35*, 93–114.

Feng, B.Y., and Shoichet, B.K. (2006). A detergent-based assay for the detection of promiscuous inhibitors. Nat. Protoc. *1*, 550–553.

Ferguson, F.M., and Gray, N.S. (2018). Kinase inhibitors: the road ahead. Nat. Rev. Drug Discov. *17*, 353–377.

Firestone, A.J., Weinger, J.S., Maldonado, M., Barlan, K., Langston, L.D., O'Donnell, M., Gelfand, V.I., Kapoor, T.M., and Chen, J.K. (2012). Small-molecule inhibitors of the AAA+ ATPase motor cytoplasmic dynein. Nature *484*, 125–129.

Fischer, E.S., Böhm, K., Lydeard, J.R., Yang, H., Stadler, M.B., Cavadini, S., Nagel, J., Serluca, F., Acker, V., Lingaraju, G.M., et al. (2014). Structure of the DDB1-CRBN E3 ubiquitin ligase in complex with thalidomide. Nature *512*, 49–53.

Friesner, R.A., Murphy, R.B., Repasky, M.P., Frye, L.L., Greenwood, J.R., Halgren, T.A., Sanschagrin, P.C., and Mainz, D.T. (2006). Extra precision glide: Docking and scoring incorporating a model of hydrophobic enclosure for protein- ligand complexes. J. Med. Chem. *49*, 6177–6196.

Furman, R.R., Cheng, S., Lu, P., Setty, M., Perez, A.R., Guo, A., Racchumi, J., Xu, G., Wu, H., Ma, J., et al. (2014). Ibrutinib resistance in chronic lymphocytic leukemia. N. Engl. J. Med. *370*, 2352–2354.

Gainor, J., Dardaei, L., Yoda, S., Friboulet, L., Leischler, I., Katayama, R., Dagogo-Jack, I., Gadgeel, S., Schultz, K., Singh, M., et al. (2016). Molecular mechanisms of resistance to first- and second-generation ALK inhibitors in ALK-rearranged lung cancer. European Journal of Cancer *69*, S138.

Garcia-Saez, I., Yen, T., Wade, R.H., and Kozielski, F. (2004). Crystal structure of the motor domain of the human kinetochore protein CENP-E. J. Mol. Biol. *340*, 1107–1116.

Girard, C., Chelysheva, L., Choinard, S., Froger, N., Macaisne, N., Lemhemdi, A., Mazel, J., Crismani, W., and Mercier, R. (2015). AAA-ATPase FIDGETIN-LIKE 1 and Helicase FANCM Antagonize Meiotic Crossovers by Distinct Mechanisms. PLoS Genet. *11*, e1005369.

Glaab, W.E., and Tindall, K.R. (1997). Mutation rate at the hprt locus in human cancer cell lines with specific mismatch repair-gene defects. Carcinogenesis *18*, 1–8.

Goldstein, D.M., Gray, N.S., and Zarrinkar, P.P. (2008). High-throughput kinase profiling as a platform for drug discovery. Nat. Rev. Drug Discov. *7*, 391–397.

Gonciarz, M.D., Whitby, F.G., Eckert, D.M., Kieffer, C., Heroux, A., Sundquist, W.I., and Hill, C.P. (2008). Biochemical and structural studies of yeast Vps4 oligomerization. J. Mol. Biol. *384*, 878–895.

Gordon, D.J., Resio, B., and Pellman, D. (2012). Causes and consequences of aneuploidy in

cancer. Nat. Rev. Genet. *13*, 189–203.

Gorre, M.E., Mohammed, M., Ellwood, K., Hsu, N., Paquette, R., Rao, P.N., and Sawyers, C.L. (2001). Clinical resistance to STI-571 cancer therapy caused by BCR-ABL gene mutation or amplification. Science *293*, 876–880.

Gottesman, M.M., Lavi, O., Hall, M.D., and Gillet, J.-P. (2016). Toward a Better Understanding of the Complexity of Cancer Drug Resistance. Annu. Rev. Pharmacol. Toxicol. *56*, 85–102.

Guenther, B., Onrust, R., Sali, A., O'Donnell, M., and Kuriyan, J. (1997). Crystal structure of the delta' subunit of the clamp-loader complex of E. coli DNA polymerase III. Cell *91*, 335–345.

Han, T., Goralski, M., Gaskill, N., Capota, E., Kim, J., Ting, T.C., Xie, Y., Williams, N.S., and Nijhawan, D. (2017). Anticancer sulfonamides target splicing by inducing RBM39 degradation via recruitment to DCAF15. Science *356*, eaal3755.

Hazan, J., Fonknechten, N., Mavel, D., Paternotte, C., Samson, D., Artiguenave, F., Davoine, C.S., Cruaud, C., Dürr, A., Wincker, P., et al. (1999). Spastin, a new AAA protein, is altered in the most frequent form of autosomal dominant spastic paraplegia. Nat. Genet. *23*, 296–303.

Hendrickson, W.A. (1991). Determination of macromolecular structures from anomalous diffraction of synchrotron radiation. Science *254*, 51–58.

Hertz, N.T., Berthet, A., Sos, M.L., Thorn, K.S., Burlingame, A.L., Nakamura, K., and Shokat, K.M. (2013). A Neo-Substrate that Amplifies Catalytic Activity of Parkinson's-Disease-Related Kinase PINK1. Cell *154*, 737–747.

Hirayama, T., Okaniwa, M., Banno, H., Kakei, H., Ohashi, A., Iwai, K., Ohori, M., Mori, K., Gotou, M., Kawamoto, T., et al. (2015). Synthetic studies on centromere-associated protein-E (CENP-E) inhibitors: 2. Application of electrostatic potential map (EPM) and structure-based modeling to imidazo [1, 2-a] pyridine derivatives as anti-tumor agents. J. Med. Chem. *58*, 8036–8053.

Holohan, C., Van Schaeybroeck, S., Longley, D.B., and Johnston, P.G. (2013). Cancer drug resistance: an evolving paradigm. Nat. Rev. Cancer *13*, 714–726.

Huang, H.-T., Dobrovolsky, D., Paulk, J., Yang, G., Weisberg, E.L., Doctor, Z.M., Buckley, D.L., Cho, J.-H., Ko, E., Jang, J., et al. (2018). A Chemoproteomic Approach to Query the Degradable Kinome Using a Multi-kinase Degrader. Cell Chem Biol *25*, 88–99.e6.

Huang, W.-S., Metcalf, C.A., Sundaramoorthi, R., Wang, Y., Zou, D., Mathew Thomas, R., Zhu, X., Cai, L., Wen, D., Liu, S., et al. (2010). Discovery of 3-[2-(Imidazo[1,2-b]pyridazin-3-yl)ethynyl]-4-methyl-N-4-[(4-methylpiperazin-1-yl)methyl]-3-(trifluoromethyl)phenylbenzamide (AP24534), a Potent, Orally Active Pan-Inhibitor of Breakpoint Cluster Region-Abelson (BCR-ABL) Kinase Including the T315I Gatekeeper Mutant. Journal of Medicinal Chemistry *53*, 4701–4719.

Hwang, Y.W., and Miller, D.L. (1987). A mutation that alters the nucleotide specificity of elongation factor Tu, a GTP regulatory protein. J. Biol. Chem. *262*, 13081–13085.

Hyman, D.M., Laetsch, T.W., Kummar, S., DuBois, S.G., Farago, A.F., Pappo, A.S., Demetri, G.D., El-Deiry, W.S., Lassen, U.N., Dowlati, A., et al. (2017). The efficacy of larotrectinib (LOXO-101), a selective tropomyosin receptor kinase (TRK) inhibitor, in adult and pediatric TRK fusion cancers. J. Clin. Orthod. *35*, LBA2501–LBA2501.

Imamovic, L., and Sommer, M.O.A. (2013). Use of collateral sensitivity networks to design drug cycling protocols that avoid resistance development. Sci. Transl. Med. *5*, 204ra132.

Islam, K. (2015). Allele-specific chemical genetics: concept, strategies, and applications. ACS Chem. Biol. *10*, 343–363.

Jia, Y., Yun, C.-H., Park, E., Ercan, D., Manuia, M., Juarez, J., Xu, C., Rhee, K., Chen, T., Zhang, H., et al. (2016). Overcoming EGFR(T790M) and EGFR(C797S) resistance with mutant-selective allosteric inhibitors. Nature *534*, 129–132.

Johnson, D.S., Weerapana, E., and Cravatt, B.F. (2010). Strategies for discovering and derisking covalent, irreversible enzyme inhibitors. Future Med. Chem. *2*, 949–964.

Kamer, K.J., Choudhary, A., and Raines, R.T. (2013). Intimate Interactions with Carbonyl Groups: Dipole–Dipole or n→π*? J. Org. Chem. *78*, 2099–2103.

Kapitein, L.C., and Hoogenraad, C.C. (2015). Building the Neuronal Microtubule Cytoskeleton. Neuron *87*, 492–506.

Kapitein, L.C., Kwok, B.H., Weinger, J.S., Schmidt, C.F., Kapoor, T.M., and Peterman, E.J.G. (2008). Microtubule cross-linking triggers the directional motility of kinesin-5. J. Cell Biol. *182*, 421–428.

Kapoor, T.M., and Miller, R.M. (2017). Leveraging Chemotype-Specific Resistance for Drug Target Identification and Chemical Biology. Trends Pharmacol. Sci. *38*, 1100–1109.

Kapoor, T.M., and Mitchison, T.J. (1999). Allele-specific activators and inhibitors for kinesin. Proc. Natl. Acad. Sci. U. S. A. *96*, 9106–9111.

Kapoor, T.M., Lampson, M.A., Hergert, P., Cameron, L., Cimini, D., Salmon, E.D., McEwen, B.F., and Khodjakov, A. (2006). Chromosomes can congress to the metaphase plate before biorientation. Science *311*, 388–391.

Karaman, M.W., Herrgard, S., Treiber, D.K., Gallant, P., Atteridge, C.E., Campbell, B.T., Chan, K.W., Ciceri, P., Davis, M.I., Edeen, P.T., et al. (2008). A quantitative analysis of kinase inhibitor selectivity. Nat. Biotechnol. *26*, 127–132.

Karlberg, T., Wisniewska, M., Andersson, J., Arrowsmith, C.H., Berglund, H., Busam, R.D., Collins, R., Dahlgren, L.G., Edwards, A.M., Flodin, S., et al. (2008). Crystal structure of human fidgetin-like protein 1 in complex with ADP.

Kasap, C., Elemento, O., and Kapoor, T.M. (2014). DrugTargetSeqR: a genomics- and CRISPR-Cas9-based method to analyze drug targets. Nat. Chem. Biol. *10*, 626–628.

Kawashima, S.A., Chen, Z., Aoi, Y., Patgiri, A., Kobayashi, Y., Nurse, P., and Kapoor, T.M. (2016). Potent, Reversible, and Specific Chemical Inhibitors of Eukaryotic Ribosome

Biogenesis. Cell *167*, 512–524.e14.

Kim, Y., Holland, A.J., Lan, W., and Cleveland, D.W. (2010). Aurora kinases and protein phosphatase 1 mediate chromosome congression through regulation of CENP-E. Cell *142*, 444–455.

Kobayashi, S., Boggon, T.J., Dayaram, T., Jänne, P.A., Kocher, O., Meyerson, M., Johnson, B.E., Eck, M.J., Tenen, D.G., and Halmos, B. (2005). EGFR Mutation and Resistance of Non–Small-Cell Lung Cancer to Gefitinib. N. Engl. J. Med. *352*, 786–792.

Koboldt, D.C., Larson, D.E., and Wilson, R.K. (2013). Using VarScan 2 for Germline Variant Calling and Somatic Mutation Detection. Current Protocols in Bioinformatics 15.4.1–15.4.17.

Kressler, D., Hurt, E., Bergler, H., and Baßler, J. (2012a). The power of AAA-ATPases on the road of pre-60S ribosome maturation—molecular machines that strip pre-ribosomal particles. Biochimica et Biophysica Acta (BBA)-Molecular Cell Research *1823*, 92–100.

Kressler, D., Hurt, E., Bergler, H., and Baßler, J. (2012b). The power of AAA-ATPases on the road of pre-60S ribosome maturation — Molecular machines that strip pre-ribosomal particles. Biochimica et Biophysica Acta (BBA) - Molecular Cell Research *1823*, 92–100.

Kuo, T.-C., Li, L.-W., Pan, S.-H., Fang, J.-M., Liu, J.-H., Cheng, T.-J., Wang, C.-J., Hung, P.-F., Chen, H.-Y., Hong, T.-M., et al. (2016). Purine-Type Compounds Induce Microtubule Fragmentation and Lung Cancer Cell Death through Interaction with Katanin. J. Med. Chem. *59*, 8521–8534.

Laetsch, T.W., DuBois, S.G., Mascarenhas, L., Turpin, B., Federman, N., Albert, C.M., Nagasubramanian, R., Davis, J.L., Rudzinski, E., Feraco, A.M., et al. (2018). Larotrectinib for paediatric solid tumours harbouring NTRK gene fusions: phase 1 results from a multicentre, open-label, phase 1/2 study. Lancet Oncol. *19*, 705–714.

Lai, A.C., and Crews, C.M. (2017). Induced protein degradation: an emerging drug discovery paradigm. Nat. Rev. Drug Discov. *16*, 101–114.

Lampson, M.A., and Kapoor, T.M. (2006). Unraveling cell division mechanisms with small-molecule inhibitors. Nat. Chem. Biol. *2*, 19–27.

Lange, A., Günther, M., Büttner, F.M., Zimmermann, M.O., Heidrich, J., Hennig, S., Zahn, S., Schall, C., Sievers-Engler, A., Ansideri, F., et al. (2015). Targeting the Gatekeeper MET146 of C-Jun N-Terminal Kinase 3 Induces a Bivalent Halogen/Chalcogen Bond. J. Am. Chem. Soc. *137*, 14640–14652.

Lehner, B. (2011). Molecular mechanisms of epistasis within and between genes. Trends Genet. *27*, 323–331.

Li, D., Shimamura, T., Ji, H., Chen, L., Haringsma, H.J., McNamara, K., Liang, M.-C., Perera, S.A., Zaghlul, S., Borgman, C.L., et al. (2007). Bronchial and peripheral murine lung carcinomas induced by T790M-L858R mutant EGFR respond to HKI-272 and rapamycin combination therapy. Cancer Cell *12*, 81–93.

Li, D., Ambrogio, L., Shimamura, T., Kubo, S., Takahashi, M., Chirieac, L.R., Padera, R.F., Shapiro, G.I., Baum, A., Himmelsbach, F., et al. (2008). BIBW2992, an irreversible EGFR/HER2 inhibitor highly effective in preclinical lung cancer models. Oncogene *27*, 4702–4711.

Liao, Y., Smyth, G.K., and Shi, W. (2014). featureCounts: an efficient general purpose program for assigning sequence reads to genomic features. Bioinformatics *30*, 923–930.

Lin, R., Connolly, P.J., Huang, S., Wetter, S.K., Lu, Y., Murray, W.V., Emanuel, S.L., Gruninger, R.H., Fuentes-Pesquera, A.R., Rugg, C.A., et al. (2005). 1-Acyl-1 H-[1, 2, 4] triazole-3, 5-diamine analogues as novel and potent anticancer cyclin-dependent kinase inhibitors: synthesis and evaluation of biological activities. J. Med. Chem. *48*, 4208–4211.

Liu, Y., Bishop, A., Witucki, L., Kraybill, B., Shimizu, E., Tsien, J., Ubersax, J., Blethrow, J., Morgan, D.O., and Shokat, K.M. (1999). Structural basis for selective inhibition of Src family kinases by PP1. Chem. Biol. *6*, 671–678.

Lock, R.B., Carol, H., Morton, C.L., Keir, S.T., Reynolds, C.P., Kang, M.H., Maris, J.M., Wozniak, A.W., Gorlick, R., Kolb, E.A., et al. (2012). Initial testing of the CENP-E inhibitor GSK923295A by the pediatric preclinical testing program. Pediatr. Blood Cancer *58*, 916–923.

Lopez, M.S., Kliegman, J.I., and Shokat, K.M. (2014). The logic and design of analog-sensitive kinases and their small molecule inhibitors. Methods Enzymol. *548*, 189–213.

Loughlin, R., Wilbur, J.D., McNally, F.J., Nédélec, F.J., and Heald, R. (2011). Katanin contributes to interspecies spindle length scaling in Xenopus. Cell *147*, 1397–1407.

Magnaghi, P., D'Alessio, R., Valsasina, B., Avanzi, N., Rizzi, S., Asa, D., Gasparri, F., Cozzi, L., Cucchi, U., Orrenius, C., et al. (2013). Covalent and allosteric inhibitors of the ATPase VCP/p97 induce cancer cell death. Nat. Chem. Biol. *9*, 548–556.

Malerich, J.P., Lam, J.S., Hart, B., Fine, R.M., Klebansky, B., Tanga, M.J., and D'Andrea, A. (2010). Diamino-1,2,4-triazole derivatives are selective inhibitors of TYK2 and JAK1 over JAK2 and JAK3. Bioorg. Med. Chem. Lett. *20*, 7454–7457.

Mancuso, G., and Rugarli, E.I. (2008). A cryptic promoter in the first exon of the SPG4 gene directs the synthesis of the 60-kDa spastin isoform. BMC Biol. *6*, 31.

Maric, M., Maculins, T., De Piccoli, G., and Labib, K. (2014). Cdc48 and a ubiquitin ligase drive disassembly of the CMG helicase at the end of DNA replication. Science *346*, 1253596.

Martin, A.R., and Siliciano, R.F. (2016). Progress Toward HIV Eradication: Case Reports, Current Efforts, and the Challenges Associated with Cure. Annu. Rev. Med. *67*, 215–228.

McCoy, A.J., Grosse-Kunstleve, R.W., Adams, P.D., Winn, M.D., Storoni, L.C., and Read, R.J. (2007). Phaser crystallographic software. J. Appl. Crystallogr. *40*, 658–674.

McCullough, J., Frost, A., and Sundquist, W.I. (2018). Structures, Functions, and Dynamics of ESCRT-III/Vps4 Membrane Remodeling and Fission Complexes. Annu. Rev. Cell Dev. Biol. *34*, 85–109.

McEwen, B.F., Chan, G.K., Zubrowski, B., Savoian, M.S., Sauer, M.T., and Yen, T.J. (2001).

CENP-E is essential for reliable bioriented spindle attachment, but chromosome alignment can be achieved via redundant mechanisms in mammalian cells. Mol. Biol. Cell *12*, 2776–2789.

McNally, F.J., and Vale, R.D. (1993). Identification of katanin, an ATPase that severs and disassembles stable microtubules. Cell *75*, 419–429.

Merrill, S.A., and Hanson, P.I. (2010). Activation of human VPS4A by ESCRT-III proteins reveals ability of substrates to relieve enzyme autoinhibition. J. Biol. Chem. *285*, 35428–35438.

Min, J.-H., Yang, H., Ivan, M., Gertler, F., Kaelin, W.G., Jr, and Pavletich, N.P. (2002). Structure of an HIF-1alpha -pVHL complex: hydroxyproline recognition in signaling. Science *296*, 1886–1889.

Morgan, R.K., Carter-O'Connell, I., and Cohen, M.S. (2015). Selective inhibition of PARP10 using a chemical genetics strategy. Bioorg. Med. Chem. Lett. *25*, 4770–4773.

Moyer, M.L., Gilbert, S.P., and Johnson, K.A. (1998). Pathway of ATP hydrolysis by monomeric and dimeric kinesin. Biochemistry *37*, 800–813.

Murray, J.S., Lane, P., and Politzer, P. (2008). Simultaneous σ-hole and hydrogen bonding by sulfur- and selenium-containing heterocycles. Int. J. Quantum Chem. *108*, 2770–2781.

Murtaza, M., Dawson, S.-J., Tsui, D.W.Y., Gale, D., Forshew, T., Piskorz, A.M., Parkinson, C., Chin, S.-F., Kingsbury, Z., Wong, A.S.C., et al. (2013). Non-invasive analysis of acquired resistance to cancer therapy by sequencing of plasma DNA. Nature *497*, 108–112.

Nagar, B., Bornmann, W.G., Pellicena, P., Schindler, T., Veach, D.R., Miller, W.T., Clarkson, B., and Kuriyan, J. (2002). Crystal structures of the kinase domain of c-Abl in complex with the small molecule inhibitors PD173955 and imatinib (STI-571). Cancer Res. *62*, 4236–4243.

Nowell, P.C., and Hungerford, D.A. (1960). A minute chromosome in human chronic granulocytic leukemia. Science *132*, 1497.

Nowell, P.C., and Hungerford, D.A. (1961). Chromosome studies in human leukemia. II. Chronic granulocytic leukemia. J. Natl. Cancer Inst. *27*, 1013–1035.

O'brien, J., Wilson, I., Orton, T., and Pognan, F. (2000). Investigation of the Alamar Blue (resazurin) fluorescent dye for the assessment of mammalian cell cytotoxicity. Eur. J. Biochem. *267*, 5421–5426.

O'Hare, T., Eide, C.A., and Deininger, M.W.N. (2007). Bcr-Abl kinase domain mutations, drug resistance, and the road to a cure for chronic myeloid leukemia. Blood *110*, 2242–2249.

O'Hare, T., Shakespeare, W.C., Zhu, X., Eide, C.A., Rivera, V.M., Wang, F., Adrian, L.T., Zhou, T., Huang, W.-S., Xu, Q., et al. (2009). AP24534, a pan-BCR-ABL inhibitor for chronic myeloid leukemia, potently inhibits the T315I mutant and overcomes mutation-based resistance. Cancer Cell *16*, 401–412.

Ohashi, A., Ohori, M., Iwai, K., Nambu, T., Miyamoto, M., Kawamoto, T., and Okaniwa, M. (2015). A Novel Time-Dependent CENP-E Inhibitor with Potent Antitumor Activity. PLoS One

*10*, e0144675.

Olmos, Y., Hodgson, L., Mantell, J., Verkade, P., and Carlton, J.G. (2015). ESCRT-III controls nuclear envelope reformation. Nature *522*, 236–239.

Paez, J.G., Jänne, P.A., Lee, J.C., Tracy, S., Greulich, H., Gabriel, S., Herman, P., Kaye, F.J., Lindeman, N., Boggon, T.J., et al. (2004). EGFR mutations in lung cancer: correlation with clinical response to gefitinib therapy. Science *304*, 1497–1500.

Paiva, S.-L., and Crews, C.M. (2019). Targeted protein degradation: elements of PROTAC design. Curr. Opin. Chem. Biol. *50*, 111–119.

Pao, W., Miller, V.A., Politi, K.A., Riely, G.J., Somwar, R., Zakowski, M.F., Kris, M.G., and Varmus, H. (2005). Acquired resistance of lung adenocarcinomas to gefitinib or erlotinib is associated with a second mutation in the EGFR kinase domain. PLoS Med. *2*, e73.

Pettersen, E.F., Goddard, T.D., Huang, C.C., Couch, G.S., Greenblatt, D.M., Meng, E.C., and Ferrin, T.E. (2004). UCSF Chimera--a visualization system for exploratory research and analysis. J. Comput. Chem. *25*, 1605–1612.

Pisa, R., Cupido, T., and Kapoor, T.M. (2019a). Designing Allele-Specific Inhibitors of Spastin, a Microtubule-Severing AAA Protein. J. Am. Chem. Soc. *141*, 5602–5606.

Pisa, R., Cupido, T., Steinman, J.B., Jones, N.H., and Kapoor, T.M. (2019b). Analyzing Resistance to Design Selective Chemical Inhibitors for AAA Proteins. Cell Chem Biol *26*, 1263–1273.e5.

Podgornaia, A.I., and Laub, M.T. (2015). Pervasive degeneracy and epistasis in a protein-protein interface. Science *347*, 673–677.

Pöhler, R., Krahn, J.H., van den Boom, J., Dobrynin, G., Kaschani, F., Eggenweiler, H.-M., Zenke, F.T., Kaiser, M., and Meyer, H. (2018). A Non-Competitive Inhibitor of VCP/p97 and VPS4 Reveals Conserved Allosteric Circuits in Type I and II AAA ATPases. Angew. Chem. Int. Ed Engl. *57*, 1576–1580.

Pollock, J., Borkin, D., Lund, G., Purohit, T., Dyguda-Kazimierowicz, E., Grembecka, J., and Cierpicki, T. (2015). Rational Design of Orthogonal Multipolar Interactions with Fluorine in Protein–Ligand Complexes. J. Med. Chem. *58*, 7465–7474.

Powers, T., and Walter, P. (1995). Reciprocal stimulation of GTP hydrolysis by two directly interacting GTPases. Science *269*, 1422–1424.

Puchades, C., Rampello, A.J., Shin, M., Giuliano, C.J., Wiseman, R.L., Glynn, S.E., and Lander, G.C. (2017). Structure of the mitochondrial inner membrane AAA+ protease YME1 gives insight into substrate processing. Science *358*, eaao0464.

Putkey, F.R., Cramer, T., Morphew, M.K., Silk, A.D., Johnson, R.S., McIntosh, J.R., and Cleveland, D.W. (2002). Unstable kinetochore-microtubule capture and chromosomal instability following deletion of CENP-E. Dev. Cell *3*, 351–365.

Qian, X., McDonald, A., Zhou, H.-J., Adams, N.D., Parrish, C.A., Duffy, K.J., Fitch, D.M.,

Tedesco, R., Ashcraft, L.W., Yao, B., et al. (2010). Discovery of the first potent and selective inhibitor of centromere-associated protein E: GSK923295. ACS Med. Chem. Lett. *1*, 30–34.

Raaijmakers, J.A., van Heesbeen, R.G.H.P., Blomen, V.A., Janssen, L.M.E., van Diemen, F., Brummelkamp, T.R., and Medema, R.H. (2018). BUB1 Is Essential for the Viability of Human Cells in which the Spindle Assembly Checkpoint Is Compromised. Cell Rep. *22*, 1424–1438.

Ramadan, K., Bruderer, R., Spiga, F.M., Popp, O., Baur, T., Gotta, M., and Meyer, H.H. (2007). Cdc48/p97 promotes reformation of the nucleus by extracting the kinase Aurora B from chromatin. Nature *450*, 1258–1262.

Ren, X., Pan, X., Zhang, Z., Wang, D., Lu, X., Li, Y., Wen, D., Long, H., Luo, J., Feng, Y., et al. (2013). Identification of GZD824 as an orally bioavailable inhibitor that targets phosphorylated and nonphosphorylated breakpoint cluster region--Abelson (Bcr-Abl) kinase and overcomes clinically acquired mutation-induced resistance against imatinib. J. Med. Chem. *56*, 879–894.

Robey, R.W., Pluchino, K.M., Hall, M.D., Fojo, A.T., Bates, S.E., and Gottesman, M.M. (2018). Revisiting the role of ABC transporters in multidrug-resistant cancer. Nature Reviews Cancer *18*, 452–464.

Rodrik-Outmezguine, V.S., Okaniwa, M., Yao, Z., Novotny, C.J., McWhirter, C., Banaji, A., Won, H., Wong, W., Berger, M., de Stanchina, E., et al. (2016). Overcoming mTOR resistance mutations with a new-generation mTOR inhibitor. Nature *534*, 272–276.

Roll-Mecak, A., and McNally, F.J. (2010). Microtubule-severing enzymes. Curr. Opin. Cell Biol. *22*, 96–103.

Roll-Mecak, A., and Vale, R.D. (2005). The Drosophila homologue of the hereditary spastic paraplegia protein, spastin, severs and disassembles microtubules. Curr. Biol. *15*, 650–655.

Roll-Mecak, A., and Vale, R.D. (2008). Structural basis of microtubule severing by the hereditary spastic paraplegia protein spastin. Nature *451*, 363–367.

Rouiller, I., DeLaBarre, B., May, A.P., Weis, W.I., Brunger, A.T., Milligan, R.A., and Wilson-Kubalek, E.M. (2002). Conformational changes of the multifunction p97 AAA ATPase during its ATPase cycle. Nat. Struct. Biol. *9*, 950–957.

Rowley, J.D. (1973). Letter: A new consistent chromosomal abnormality in chronic myelogenous leukaemia identified by quinacrine fluorescence and Giemsa staining. Nature *243*, 290–293.

Russo, M., Misale, S., Wei, G., Siravegna, G., Crisafulli, G., Lazzari, L., Corti, G., Rospo, G., Novara, L., Mussolin, B., et al. (2016). Acquired Resistance to the TRK Inhibitor Entrectinib in Colorectal Cancer. Cancer Discovery *6*, 36–44.

Sakamoto, K.M., Kim, K.B., Kumagai, A., Mercurio, F., Crews, C.M., and Deshaies, R.J. (2001). Protacs: Chimeric molecules that target proteins to the Skp1–Cullin–F box complex for ubiquitination and degradation. Proc. Natl. Acad. Sci. U. S. A. *98*, 8554–8559.

Salami, J., and Crews, C.M. (2017). Waste disposal—An attractive strategy for cancer therapy. Science *355*, 1163–1167.

Sawyers, C.L. (1999). Chronic Myeloid Leukemia. New England Journal of Medicine *340*, 1330–1340.

Scheffzek, K., Ahmadian, M.R., Kabsch, W., Wiesmüller, L., Lautwein, A., Schmitz, F., and Wittinghofer, A. (1997). The Ras-RasGAP complex: structural basis for GTPase activation and its loss in oncogenic Ras mutants. Science *277*, 333–338.

Schindelin, J., Arganda-Carreras, I., Frise, E., Kaynig, V., Longair, M., Pietzsch, T., Preibisch, S., Rueden, C., Saalfeld, S., Schmid, B., et al. (2012). Fiji: an open-source platform for biological-image analysis. Nat. Methods *9*, 676–682.

Schindler, T., Bornmann, W., Pellicena, P., Miller, W.T., Clarkson, B., and Kuriyan, J. (2000). Structural mechanism for STI-571 inhibition of abelson tyrosine kinase. Science *289*, 1938–1942.

Schoepfer, J., Jahnke, W., Berellini, G., Buonamici, S., Cotesta, S., Cowan-Jacob, S.W., Dodd, S., Drueckes, P., Fabbro, D., Gabriel, T., et al. (2018). Discovery of Asciminib (ABL001), an Allosteric Inhibitor of the Tyrosine Kinase Activity of BCR-ABL1. J. Med. Chem. *61*, 8120–8135.

Scott, A., Chung, H.-Y., Gonciarz-Swiatek, M., Hill, G.C., Whitby, F.G., Gaspar, J., Holton, J.M., Viswanathan, R., Ghaffarian, S., Hill, C.P., et al. (2005). Structural and mechanistic studies of VPS4 proteins. EMBO J. *24*, 3658–3669.

Shah, K., Liu, Y., Deirmengian, C., and Shokat, K.M. (1997). Engineering unnatural nucleotide specificity for Rous sarcoma virus tyrosine kinase to uniquely label its direct substrates. Proc. Natl. Acad. Sci. U. S. A. *94*, 3565–3570.

Shah, N.P., Nicoll, J.M., Nagar, B., Gorre, M.E., Paquette, R.L., Kuriyan, J., and Sawyers, C.L. (2002). Multiple BCR-ABL kinase domain mutations confer polyclonal resistance to the tyrosine kinase inhibitor imatinib (STI571) in chronic phase and blast crisis chronic myeloid leukemia. Cancer Cell *2*, 117–125.

Shah, N.P., Tran, C., Lee, F.Y., Chen, P., Norris, D., and Sawyers, C.L. (2004). Overriding imatinib resistance with a novel ABL kinase inhibitor. Science *305*, 399–401.

Sharp, D.J., and Ross, J.L. (2012). Microtubule-severing enzymes at the cutting edge. J. Cell Sci. *125*, 2561–2569.

Shoichet, B.K., and Kobilka, B.K. (2012). Structure-based drug screening for G-protein-coupled receptors. Trends Pharmacol. Sci. *33*, 268–272.

Siddiq, M.A., Hochberg, G.K., and Thornton, J.W. (2017). Evolution of protein specificity: insights from ancestral protein reconstruction. Curr. Opin. Struct. Biol. *47*, 113–122.

Smurnyy, Y., Cai, M., Wu, H., McWhinnie, E., Tallarico, J.A., Yang, Y., and Feng, Y. (2014). DNA sequencing and CRISPR-Cas9 gene editing for target validation in mammalian cells. Nat. Chem. Biol. *10*, 623–625.

Song, C., Wang, Q., and Li, C.-C.H. (2003). ATPase activity of p97-valosin-containing protein (VCP). D2 mediates the major enzyme activity, and D1 contributes to the heat-induced activity.

J. Biol. Chem. *278*, 3648–3655.

Starr, T.N., and Thornton, J.W. (2016). Epistasis in protein evolution. Protein Sci. *25*, 1204–1218.

Statsuk, A.V., Maly, D.J., Seeliger, M.A., Fabian, M.A., Biggs, W.H., 3rd, Lockhart, D.J., Zarrinkar, P.P., Kuriyan, J., and Shokat, K.M. (2008). Tuning a three-component reaction for trapping kinase substrate complexes. J. Am. Chem. Soc. *130*, 17568–17574.

Steinman, J.B., Santarossa, C.C., Miller, R.M., Yu, L.S., Serpinskaya, A.S., Furukawa, H., Morimoto, S., Tanaka, Y., Nishitani, M., Asano, M., et al. (2017). Chemical structure-guided design of dynapyrazoles, cell-permeable dynein inhibitors with a unique mode of action. Elife *6*, e25174.

Tanaka, A., Cleland, M.M., Xu, S., Narendra, D.P., Suen, D.-F., Karbowski, M., and Youle, R.J. (2010). Proteasome and p97 mediate mitophagy and degradation of mitofusins induced by Parkin. J. Cell Biol. *191*, 1367–1380.

Tang, W.K., Odzorig, T., Jin, W., and Xia, D. (2019). Structural Basis of p97 Inhibition by the Site-Selective Anticancer Compound CB-5083. Mol. Pharmacol. *95*, 286–293.

Taylor, J.L., White, S.R., Lauring, B., and Kull, F.J. (2012). Crystal structure of the human spastin AAA domain. J. Struct. Biol. *179*, 133–137.

Tcherniuk, S.O., and Oleinikov, A.V. (2015). Pgp efflux pump decreases the cytostatic effect of CENP-E inhibitor GSK923295. Cancer Lett. *361*, 97–103.

Thress, K.S., Paweletz, C.P., Felip, E., Cho, B.C., Stetson, D., Dougherty, B., Lai, Z., Markovets, A., Vivancos, A., Kuang, Y., et al. (2015). Acquired EGFR C797S mutation mediates resistance to AZD9291 in non-small cell lung cancer harboring EGFR T790M. Nat. Med. *21*, 560–562.

Tiefenbrunn, T., Forli, S., Happer, M., Gonzalez, A., Tsai, Y., Soltis, M., Elder, J.H., Olson, A.J., and Stout, C.D. (2014). Crystallographic Fragment-Based Drug Discovery: Use of a Brominated Fragment Library Targeting HIV Protease. Chem. Biol. Drug Des. *83*, 141–148.

Tokarski, J.S., Newitt, J.A., Chang, C.Y.J., Cheng, J.D., Wittekind, M., Kiefer, S.E., Kish, K., Lee, F.Y.F., Borzillerri, R., Lombardo, L.J., et al. (2006). The structure of Dasatinib (BMS-354825) bound to activated ABL kinase domain elucidates its inhibitory activity against imatinib-resistant ABL mutants. Cancer Res. *66*, 5790–5797.

Trudel, S., Li, Z.H., Wei, E., Wiesmann, M., Chang, H., Chen, C., Reece, D., Heise, C., and Stewart, A.K. (2005). CHIR-258, a novel, multitargeted tyrosine kinase inhibitor for the potential treatment of t(4;14) multiple myeloma. Blood *105*, 2941–2948.

Twomey, E.C., Ji, Z., Wales, T.E., Bodnar, N.O., Ficarro, S.B., Marto, J.A., Engen, J.R., and Rapoport, T.A. (2019). Substrate processing by the Cdc48 ATPase complex is initiated by ubiquitin unfolding. Science *365*, eaax1033.

Uphoff, C.C., and Drexler, H.G. (2013). Detection of mycoplasma contaminations. Methods Mol.

Biol. *946*, 1–13.

Urban, D.J., and Roth, B.L. (2015). DREADDs (designer receptors exclusively activated by designer drugs): chemogenetic tools with therapeutic utility. Annu. Rev. Pharmacol. Toxicol. *55*, 399–417.

Vietri, M., Schink, K.O., Campsteijn, C., Wegner, C.S., Schultz, S.W., Christ, L., Thoresen, S.B., Brech, A., Raiborg, C., and Stenmark, H. (2015). Spastin and ESCRT-III coordinate mitotic spindle disassembly and nuclear envelope sealing. Nature *522*, 231–235.

Vivanco, I., and Sawyers, C.L. (2002). The phosphatidylinositol 3-Kinase–AKT pathway in human cancer. Nat. Rev. Cancer *2*, 489–501.

Wacker, S.A., Houghtaling, B.R., Elemento, O., and Kapoor, T.M. (2012). Using transcriptome sequencing to identify mechanisms of drug action and resistance. Nat. Chem. Biol. *8*, 235–237.

Wagle, N., Grabiner, B.C., Van Allen, E.M., Hodis, E., Jacobus, S., Supko, J.G., Stewart, M., Choueiri, T.K., Gandhi, L., Cleary, J.M., et al. (2014a). Activating mTOR mutations in a patient with an extraordinary response on a phase I trial of everolimus and pazopanib. Cancer Discov. *4*, 546–553.

Wagle, N., Grabiner, B.C., Van Allen, E.M., Amin-Mansour, A., Taylor-Weiner, A., Rosenberg, M., Gray, N., Barletta, J.A., Guo, Y., Swanson, S.J., et al. (2014b). Response and acquired resistance to everolimus in anaplastic thyroid cancer. N. Engl. J. Med. *371*, 1426–1433.

Wang, Q., Song, C., Yang, X., and Li, C.-C.H. (2003). D1 ring is stable and nucleotide-independent, whereas D2 ring undergoes major conformational changes during the ATPase cycle of p97-VCP. J. Biol. Chem. *278*, 32784–32793.

Weaver, B.A.A., and Cleveland, D.W. (2005). Decoding the links between mitosis, cancer, and chemotherapy: The mitotic checkpoint, adaptation, and cell death. Cancer Cell *8*, 7–12.

Wells, J.A., and McClendon, C.L. (2007). Reaching for high-hanging fruit in drug discovery at protein-protein interfaces. Nature *450*, 1001–1009.

Wendler, P., Ciniawsky, S., Kock, M., and Kube, S. (2012). Structure and function of the AAA+ nucleotide binding pocket. Biochim. Biophys. Acta *1823*, 2–14.

Wensing, A.M., Calvez, V., Günthard, H.F., Johnson, V.A., Paredes, R., Pillay, D., Shafer, R.W., and Richman, D.D. (2017). 2017 Update of the Drug Resistance Mutations in HIV-1. Top. Antivir. Med. *24*, 132–133.

Whitehead, E., Heald, R., and Wilbur, J.D. (2013). N-terminal phosphorylation of p60 katanin directly regulates microtubule severing. J. Mol. Biol. *425*, 214–221.

Wilson, C., Agafonov, R.V., Hoemberger, M., Kutter, S., Zorba, A., Halpin, J., Buosi, V., Otten, R., Waterman, D., Theobald, D.L., et al. (2015). Kinase dynamics. Using ancient protein kinases to unravel a modern cancer drug's mechanism. Science *347*, 882–886.

Witte, O.N., Dasgupta, A., and Baltimore, D. (1980). Abelson murine leukaemia virus protein is

phosphorylated in vitro to form phosphotyrosine. Nature *283*, 826–831.

Wood, K.W., Sakowicz, R., Goldstein, L.S.B., and Cleveland, D.W. (1997). CENP-E Is a Plus End–Directed Kinetochore Motor Required for Metaphase Chromosome Alignment. Cell *91*, 357–366.

Wood, K.W., Lad, L., Luo, L., Qian, X., Knight, S.D., Nevins, N., Brejc, K., Sutton, D., Gilmartin, A.G., Chua, P.R., et al. (2010). Antitumor activity of an allosteric inhibitor of centromere-associated protein-E. Proc. Natl. Acad. Sci. U. S. A. *107*, 5839–5844.

Wu, X., and Rapoport, T.A. (2018). Mechanistic insights into ER-associated protein degradation. Curr. Opin. Cell Biol. *53*, 22–28.

Wylie, A.A., Schoepfer, J., Jahnke, W., Cowan-Jacob, S.W., Loo, A., Furet, P., Marzinzik, A.L., Pelle, X., Donovan, J., Zhu, W., et al. (2017). The allosteric inhibitor ABL001 enables dual targeting of BCR-ABL1. Nature *543*, 733–737.

Yang, D., Rismanchi, N., Renvoisé, B., Lippincott-Schwartz, J., Blackstone, C., and Hurley, J.H. (2008). Structural basis for midbody targeting of spastin by the ESCRT-III protein CHMP1B. Nat. Struct. Mol. Biol. *15*, 1278–1286.

Yelin, I., and Kishony, R. (2018). Antibiotic Resistance. Cell *172*, 1136–1136.e1.

Yuan, J., and Chen, J. (2013). FIGNL1-containing protein complex is required for efficient homologous recombination repair. Proc. Natl. Acad. Sci. U. S. A. *110*, 10640–10645.

Yun, C.-H., Mengwasser, K.E., Toms, A.V., Woo, M.S., Greulich, H., Wong, K.-K., Meyerson, M., and Eck, M.J. (2008). The T790M mutation in EGFR kinase causes drug resistance by increasing the affinity for ATP. Proc. Natl. Acad. Sci. U. S. A. *105*, 2070–2075.

Zempel, H., Luedtke, J., Kumar, Y., Biernat, J., Dawson, H., Mandelkow, E., and Mandelkow, E. (2013). Amyloid-β oligomers induce synaptic damage via Tau-dependent microtubule severing by TTLL6 and spastin. EMBO J. *32*, 2920–2937.

Zhao, B., Sedlak, J.C., Srinivas, R., Creixell, P., Pritchard, J.R., Tidor, B., Lauffenburger, D.A., and Hemann, M.T. (2016). Exploiting Temporal Collateral Sensitivity in Tumor Clonal Evolution. Cell *165*, 234–246.

Zhou, T., Commodore, L., Huang, W.-S., Wang, Y., Thomas, M., Keats, J., Xu, Q., Rivera, V.M., Shakespeare, W.C., Clackson, T., et al. (2011). Structural mechanism of the pan-BCR-ABL inhibitor ponatinib (AP24534): lessons for overcoming kinase inhibitor resistance. Chem. Biol. Drug Des. *77*, 1–11.

Zhou, W., Ercan, D., Chen, L., Yun, C.-H., Li, D., Capelletti, M., Cortot, A.B., Chirieac, L., Iacob, R.E., Padera, R., et al. (2009). Novel mutant-selective EGFR kinase inhibitors against EGFR T790M. Nature *462*, 1070–1074.

Zimmermann, J., Buchdunger, E., Mett, H., Meyer, T., and Lydon, N.B. (1997). Potent and selective inhibitors of the Abl-kinase: phenylamino-pyrimidine (PAP) derivatives. Bioorg. Med. Chem. Lett. *7*, 187–192.

Ziółkowska, N.E., and Roll-Mecak, A. (2013). In vitro microtubule severing assays. Methods Mol. Biol. *1046*, 323–334.

Zuccotto, F., Ardini, E., Casale, E., and Angiolini, M. (2010). Through the “Gatekeeper Door”: Exploiting the Active Kinase Conformation. J. Med. Chem. *53*, 2681–2694.